

[ EDITORS ]

J.M. DESANTES | CMT-Motores Térmicos, Universitat Politècnica de València, Spain

G. PANIAGUA | Von Karman Institute for Fluid Dynamics, Belgium

J.R. SERRANO | CMT-Motores Térmicos, Universitat Politècnica de València, Spain

# XXI BIENNIAL SYMPOSIUM ON MEASURING TECHNIQUES IN TURBOMACHINERY

Transonic and Supersonic Flow in Cascades and Turbomachines

Proceedings of the conference held at VALENCIA, SPAIN • March 2012

EDITORIAL  
UNIVERSITAT POLITÈCNICA DE VALÈNCIA

# **XXI BIENNIAL SYMPOSIUM ON MEASURING TECHNIQUES IN TURBOMACHINERY**

**VALENCIA, SPAIN • March 2012**

## **EDITORS**

**J.M. Desantes**

CMT-Motores Térmicos, Universitat Politècnica de València, Spain

**G. Paniagua**

Von Karman Institute for Fluid Dynamics, Belgium

**J.R. Serrano**

CMT-Motores Térmicos, Universitat Politècnica de València, Spain

**EDITORIAL**

**UNIVERSITAT POLITÈCNICA DE VALÈNCIA**

First edition, 2013

© Editors:  
J.M. Desantes  
G.Paniagua  
J.R. Serrano

© of the present edition: Editorial Universitat Politècnica de València

© All commercial names, brands, or distinctive marks of any kind included in this piece of work are protected by law.

ISBN: 978-84-8363-966-5 (Versión impresa Ref. editorial: 6074)

Any unauthorized copying, distribution, marketing, editing, and in general any other exploitation, for whatever reason, of this piece of work or any part thereof, is strictly prohibited without the authors' expressed and written permission.

The XXI edition of the biennial symposium on Measuring Techniques in Turbomachinery has been held for the first time in Spain. The research institute CMT-Motores Térmicos which belongs to Universitat Politècnica de València has had the honor to host such a traditional symposium which first took place in 1970 in the von Karman Institute.

Although originally this symposium mainly focused on Transonic and Supersonic Flows in Turbomachinery, it expanded over the years into a meeting where researchers discuss the most up-to-date aerodynamic and heat transfer measurement techniques in turbomachinery from low speed to supersonic regimes, using intrusive as well as optical techniques, including micro-sensors, and designing innovative experimental facilities. In XXI edition, the scope has been opened to combustion topics and turbochargers, linking closer the original symposium concept with the gas turbine engines and introducing the turbocharged reciprocating engines from which turbomachinery components are essential.

The present edition has focused on following topics:

- Acoustics
- Aerodynamic probes
- Temperature measurement
- Optical techniques
- Novel facilities

CMT-Motores Térmicos and other world leading experts have chaired each session. The two days program had 16 speakers who have been a good representation of the leading European companies and research public centers working in experimental activities associated with the conference scope. Interesting discussions were held during the conference and as a result 16 high level papers have been elaborated and distributed in the present edition according to previous list of topics.

The objective of the symposium remains to provide a forum for researchers from universities, research institutes and industry to get together, discuss problems and share experiences involved in making measurements in turbomachines.

**G. Paniagua**

Von Karman Institute for Fluid Dynamics, Belgium

**J.R. Serrano**

CMT-Motores Térmicos, Universitat Politècnica de València, Spain



## ACOUSTICS

### **EXPERIMENTAL CHARACTERIZATION OF ACOUSTIC PRESSURE WAVES PROPAGATING IN CIRCULAR DUCTS ..... 1**

Giovanni Ferrara, Lorenzo Ferrari, Giulio Lenzi, Sergio Stecco

### **THE USE OF CAUSALITY METHOD FOR DETECTING NOISE SOURCES IN ISOLATED TURBOMACHINERY AIRFOILS AND CASCADE ..... 13**

Stefano Bianchi, Alessandro Corsini, Anthony G. Sheard

## AERODYNAMICS PROBES

### **DUAL HOT WIRE PROBES WITHOUT CROSSED PRONG-WIRE INTERFERENCE EFFECTS ..... 21**

Katia María Argüelles Díaz, Mónica Galdo Vega, Jesús Manuel Fernández Oro, Eduardo Blanco Marigorta

### **RESONANCES INFLUENCE IN RECESSED-MOUNTED TRANSDUCERS USED FOR UNSTEADY PRESSURE MEASUREMENTS ..... 35**

Antonio Sanz Luengo, Damian M. Vogt, Torsten H. Fransson

### **INTEGRATED PRESSURE AND VELOCITY MEASUREMENTS USING A SINGLE PRESSURE SENSOR ON THE CONE OF A WIND TURBINE ..... 47**

Konstantinos N. Antivachis, Anestis I. Kalfas

## TEMPERATURE MEASUREMENTS

### **AEROTHERMAL ANALYSIS AND CHARACTERIZATION OF SHIELDED FINE WIRE THERMOCOUPLE PROBES ..... 61**

Laura Villafañe, Guillermo Paniagua

### **INFLUENCE OF THERMOCOUPLE THERMAL INERTIA IN IMPINGEMENT HEAT TRANSFER EXPERIMENTS USING TRANSIENT TECHNIQUES ..... 75**

Alexandros Terzis, Jens von Wolfersdorf, Guillaume Wagner, Bernhard Weigand, Peter Ott

### **TOTAL TEMPERATURE PROBES FOR TURBINE EFFICIENCY MEASUREMENTS IN TRANSONIC ROTATING RIGS ..... 89**

Victor Pinilla, Raúl Vázquez, Andoni Puente

### **EXPERIMENTAL ANALYSIS MEANS OF THE TURBINE PARTS THERMAL STATE ..... 105**

D.V. Karelin, S.D. Mukhina

## OPTICAL TECHNIQUES

### **ON MEASUREMENT AND EVALUATION OF FLOW CONDITIONS AT LIMIT LOAD OF TURBINE BLADE CASCADES..... 109**

Pavel Šafařík, Martin Luxa, Helena Picmausova, David Šimurda

### **COMPARISON OF TWO OPTICAL TECHNIQUES TO OBSERVE TURBOCHARGER SHAFT MOTION ..... 115**

J.V. Pastor, J.R. Serrano, V. Dolz, M.A. López, F. Bouffaud

### **APPLICATION OF SPECTROSCOPY FOR ANALYSIS OF ADVANCED COMBUSTION MODES IN COMPRESSION IGNITION ENGINES ..... 135**

J.V. Pastor, J. M. García-Oliver, A. García, C. Micó

### **A DECISION MAKING ALGORITHM FOR AUTOMATIC SHOCK WAVES DETECTION IN SCHLIEREN IMAGING..... 139**

Flora Tomasoni, Bayindir H. Saracoglu, Guillermo Paniagua

## NOVEL FACILITIES

### **MEASUREMENT OF THE AERODYNAMICS IN THE PRIMARY ZONE OF A LOW-NO<sub>x</sub> COMBUSTOR AT ATMOSPHERIC AND ISOTHERMAL CONDITIONS ..... 151**

Christian Faustmann, Andreas Lang, Fabrice Giuliani

### **CHARACTERIZATION OF A HIGH SUBSONIC WIND TUNNEL TEST SECTION TO DEVELOP A STUDY APPROACH TO SOLVE THE INVERSE HEAT CONDUCTION PROBLEM..... 163**

Ir. F. Baldani, Ir. Dr. Prof. W. Bosschaerts, Ing. R. Wagemakers

### **A NEW LINEAR CASCADE TEST FACILITY FOR USE IN ENGINEERING EDUCATION ..... 185**

Monaco, L., Vogt, D.M., Fransson, T.H.

## EXPERIMENTAL CHARACTERIZATION OF ACOUSTIC PRESSURE WAVES PROPAGATING IN CIRCULAR DUCTS

Giovanni Ferrara<sup>1</sup>, Lorenzo Ferrari<sup>2\*</sup>, Giulio Lenzi<sup>1</sup>

<sup>1</sup> "Sergio Stecco" Department of Energy Engineering, University of Florence  
Via S. Marta 3, 50139, Firenze (FI) , Italy

<sup>2</sup> ICCOM CNR, National Research Council of Italy

Via Madonna del Piano 10, 50019, Sesto Fiorentino (FI), Italy

\* *Contact Author: Ph. +39 055 4796 570 - Fax +39 055 4796 342; e-mail: ferrari@iccom.cnr.it*

### ABSTRACT

The increasing interest in thermoacoustic phenomena in turbomachinery components prompted a detailed analysis of acoustic field propagation in ducts. The numerical codes for the prediction of the acoustic behavior of complex system are still in a developing phase and an experimental validation is still necessary. The wall acoustic pressure could be easily measured whereas very few examples of radial measurement, necessary for a 3D analysis, are present in the literature. In this paper, several simple remote probes mounting a 1/4" pressure microphone are characterized. The one, performed best, is used to map the acoustic pressure field of a wave propagating in a circular duct with different modes. The experimental set up and the calculation methodology are shown in detail in the paper.

### INTRODUCTION

New generation combustors, based on a lean combustion technology, are very sensitive to thermoacoustic phenomena. For this reason the analysis of acoustic pressure wave propagation and interaction with boundary walls are gaining increasing interest. Since the behavior of an acoustic pressure wave is strongly dependent on its mode, many experimental activities are now focused on the characterization of wave pressure distribution during its propagation in ducts [1, 2]. In turbomachinery applications, for example, many investigations are carried out on the interaction between the combustion chamber liner (acting as acoustic dumping device) and the thermo-acoustic instability of the flame [3]. The typical approach is limited to the analysis of the wall pressure distribution by means of flush mounted microphones. This methodology allows the measurement of the planar and tangential distribution only and does not give any information on the radial pressure trend. This lack of data makes a 3D reconstruction of the acoustic pressure wave difficult. Only few limited examples of indirect estimation of pressure distribution can be found in the literature. These are based on the acoustic velocity estimation by PIV [4] and LDV [5] measurement techniques. Another solution, much simpler to set up, could be the adoption of a wave guide probe. This is generally made up of a transmitting duct and a sensor housing placed at one of its ends. This system would allow the direct estimation of the acoustic pressure values along the span even in presence of hot flow. The main issue limiting the wave guide probe application is the high number of peaks and valleys of their frequency response function. This trend is due to the duct resonances and the reflected wave generated by the variation of diameter between the duct and the measurement chamber. The adoption of a long dumping duct behind the sensor (about 30 m) [6] or a dissipating chamber ([7] and [8]) are typical solutions to these problems. The common applications of these systems are the dynamic pressure measurement in turbomachinery components ([9] and [10]). For the radial acoustic pressure measurement, the probe has to be much smaller than the duct diameter and then also smaller than the microphone diameter (typically 1/4" in order to have high sensitivity). Therefore the adoption of a dumping element would not solve the presence of a reflected wave since a chamber for the microphone housing is inevitably present.

Within this context, several wave guide probes, with different geometries and housing a 1/4" microphone, are designed and tested to identify which solution has the best frequency response function. The range of interest is limited to a frequency below 5 kHz in order to investigate the first radial mode. The probe with the best frequency response function is used to estimate the acoustic pressure map in three different propagating conditions in a straight circular duct. The pressure maps are estimated measuring the acoustic pressure in twelve circumferential and nine radial positions. The experimental procedure, the numerical analysis and an estimation of the error related to the measurement approach (e.g. the probe tip positioning) are discussed in this paper.



### ACOUSTIC WAVE FIELD PROPAGATION IN CIRCULAR DUCTS

The propagation of a sound wave field in a circular infinite duct is described by the convective wave equation that for a hard wall duct is expressed as in Eq. 1.

$$\left( \frac{D^2}{Dt^2} - c^2 \nabla^2 \right) p(x, \theta, r, t) = 0 \quad \text{Eq. 1}$$

The solution of Eq. 1 by the variables separation method in a cylindrical duct with radius  $R$  without mean flow, gives the acoustic pressure distribution along the duct (Eq. 2) for a given acoustic pressure source ( $p_{mf}$ ). The acoustic pressure distribution turns out to be the sum of several acoustic modes (indicated with a  $m$  and  $n$  index pairs). Index  $m$  describes the circumferential pressure distribution, typically sinusoidal. Index  $n$  indicates the radial pressure distribution. This follows a first order Bessel function whose argument  $\kappa_{mn}$  is related to the pressure gradient calculated on the duct wall (Fig. 1). In the axial direction, each mode decays independently with an exponential law with coefficient  $\Gamma$ .

$$p(\theta, r, x, t) = \sum_{m=0}^M \sum_{n=0}^N p_{mf} J_m(\kappa_{mn} r) \times \exp[i\Gamma x + im\theta + i\omega t] \quad \text{Eq. 2}$$

$$\Gamma^{\pm} = \mp \sqrt{\frac{\kappa_{mn}^2}{\eta^2} - 1}$$

The coefficient  $\kappa_{mn}$  is also involved in the calculation of the axial decay coefficient  $\Gamma$  which determines if the acoustic mode propagates through the duct or not. If the axial index ( $\Gamma$ ) is real, the acoustic mode propagates otherwise, if it is imaginary, the acoustic field decays. The frequencies for which a mode starts to propagate are named cut-on frequencies; on the contrary the ones for which a mode decays are named cut-off frequency. For the  $m=0$  mode, the cut on frequency is 0Hz.

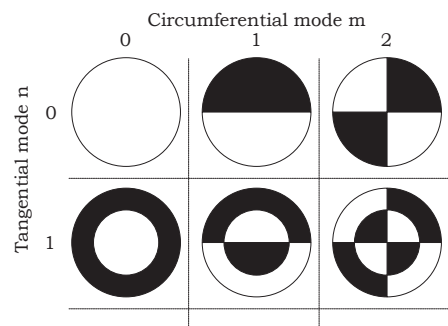


Fig. 1 Schematic shapes of acoustic modes

If one considers a 150 mm diameter duct, the cut on and off frequencies of an acoustic wave are reported in Table 1. The total acoustic wave field for a given frequency is the superposition of the propagating modes. For example, in a frequencies range between 1.39 and 2.28 kHz both planar wave field ( $m=0$ ,  $n=0$ ) and first mode ( $m=1$ ,  $n=0$ ) propagate: the total acoustic field is given by the complex sum of the two modes.

		m					
		0	1	2	3	4	5
n	0	2892 Hz	1390 Hz	2280 Hz	3171 Hz	3949 Hz	4784 Hz
	1	5229 Hz	4005 Hz	5006 Hz	5952 Hz	6898 Hz	7844 Hz

Table 1. Cut-on and cut-off frequencies for a 150 mm diameter duct.

When the frequency increases the acoustic wave field becomes more and more complex; if one considers a frequency range between 3.95 and 4.78 kHz, the acoustic pressure field turns out to be made up of three modes: the fourth tangential ( $m=4$ ,  $n=0$  Fig. 2-a), the zero radial ( $m=0$ ,  $n=1$  Fig. 2-b) and first radial ( $m=1$ ,  $n=1$  Fig. 2-c) modes.

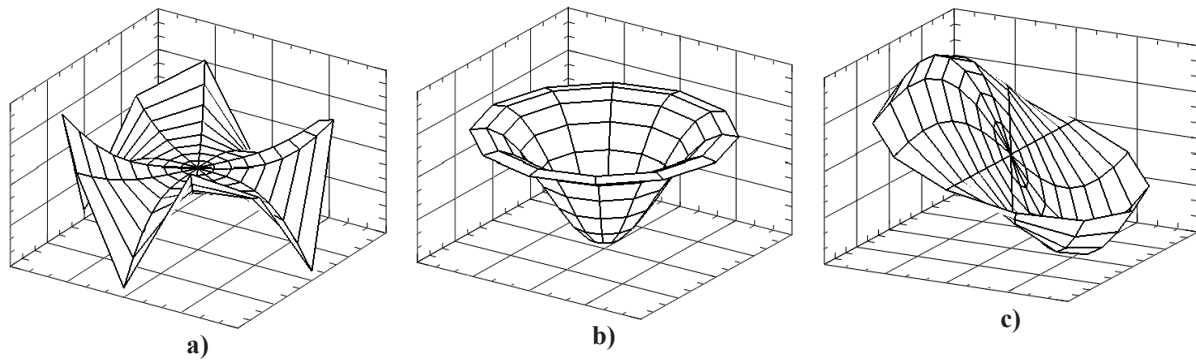


Fig. 2. Theoretical single modes at 4.1 kHz

In case of a semi-infinite duct, with an acoustic source at one end, only one travelling wave with characteristics described before propagates. In case of a finite length duct or in presence of discontinuities, the global pressure field is made up of two travelling waves that propagates in opposite direction: the one from the acoustic source (incident wave) and that reflected by the discontinuity (reflected wave). Along the duct, the superposition of the two travelling wave fields is a standing wave. In a generic section of the duct, the combination of the incident and reflected waves generates an oscillating field, instead of a rotating one, with the distribution of the incident wave.

### EXPERIMENTAL SET UP

The experimental activity (acoustic wave field mapping and probe calibration) is performed on a circular duct of Silere which is an acoustic dumping material. On one hand, the acoustic source is made up of four compressor drivers (Monacor® KU616T), mounted in radial direction and equally spaced; on the other hand the duct is open to air. The source signal is generated by a waveform generator (Agilent® 33220A) and amplified with a power amplifier (Monacor® PA-940). The duct has a diameter of 150 mm and a total length of 6 m. The measurement section is placed at five diameters from acoustic source, the rest of the duct is used to dump both incident and reflected waves to make the acoustic field in the measurement section as close as possible to the one of semi-infinite condition (Fig. 3). Twelve microphones are used to measure the tangential acoustic wave field. They are flush mounted and equally spaced in the circumferential direction. A microphone placed 60 mm upstream to the measurement section is used as a reference to clock the signals in different measurement sessions. The radial acoustic pressure measurement for different angular positions is performed replacing one of the twelve microphones with the wave guide probe. All the acoustic pressure measurements are carried out with G.R.A.S.® 1/4" pressure type microphone. The acquisition software is developed in Labview® and the signals are acquired by a National Instruments® device with a maximum sampling rate of 51,2 kSamples/.

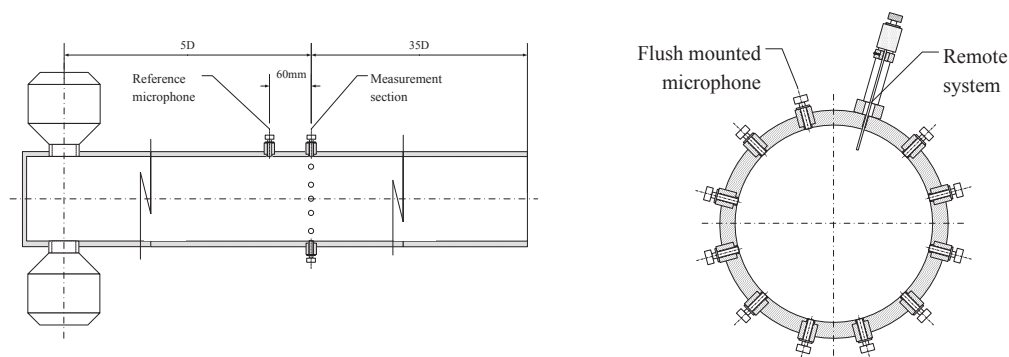
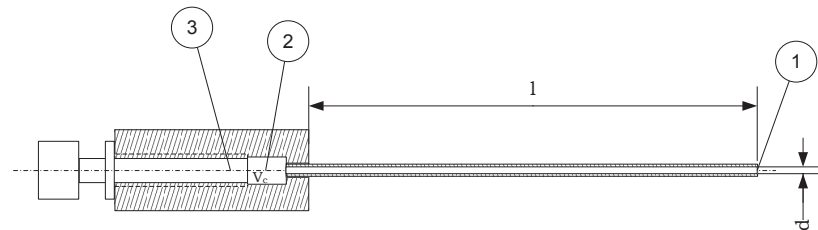


Fig. 3. Scheme of test rig for probe characterization and wave field mapping

### REMOTE PROBE DESIGN AND CALIBRATION

The measurement of wave fields with tangential distribution is commonly performed with flush mounted microphones placed on the duct wall. To perform a radial pressure measurement it is necessary to estimate the acoustic pressure at different radii without interference with the field itself. For this reason it is generally used a probe instead of a local direct measurement. A typical probe for this application is reported in Fig. 3. This device is made up of a transmitting duct and a sensor housing placed at one of its ends.

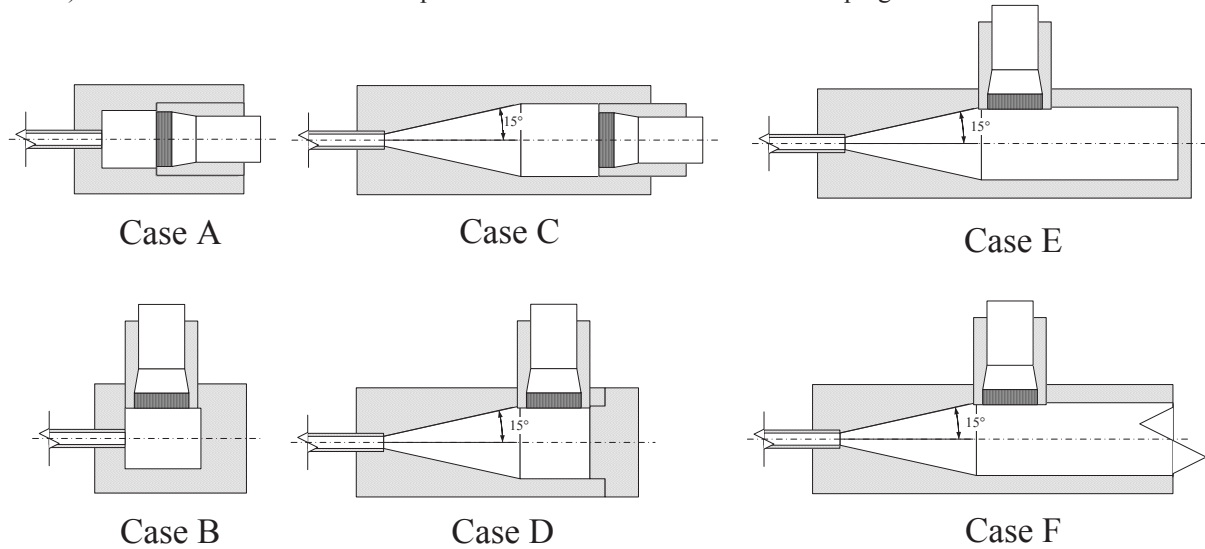


**Fig. 3. Scheme of remote probe; 1) Transmission duct; 2) Chamber; 3) Microphone ¼"**

The main issue limiting the application of this kind of probes is their frequency response that is characterized by several peaks and valleys. Such distortion are due to the transmitting duct resonances and to the reflected wave generated by the variation of diameter between the duct and the measurement chamber. Therefore, the geometry of the connection between the transmitting duct and the chamber, the microphone dimension and the cavity of sensor housing play a key role.

In order to choose a probe geometry that could minimize the frequency distortion, an extended experimental campaign is performed. A transmission duct with a diameter of 2 mm and 120 mm long is considered. The housing chamber is 10 mm long and, due to the microphone dimensions, has a diameter of 8 mm. The probe geometries investigated are (Fig. 4):

- 1) Case A: back mounted microphone with abrupt connection (baseline)
- 2) Case B: flush mounted microphone with abrupt connection
- 3) Case C: back mounted microphone with conical connection
- 4) Case D: flush mounted microphone with conical connection
- 5) Case E: flush mounted microphone with conical connection and extended chamber (30 mm)
- 6) Case F: flush mounted microphone with conical connection and damping duct of 30 m



**Fig. 4. Schemes of the probes realized**

The comparisons between the probes are performed with a planar wave field (up 1.3 kHz) because this distribution is characterized by an equal amplitude and phase in every point of the measurement section. For greater frequencies the presence of additional modes would have made the calibration procedure too complex for the comparison purposes. The probe is moved back so that the transmission duct end is aligned with the inner duct wall. The acoustic pressure measured by the microphone is compared with the one of a flush mounted microphone in the same section. Microphone signals are acquired for 1 second and analyzed with a FFT approach. The main results are reported in Fig. 5 to Fig. 8 in terms of Frequency Response Function (FRF), Eq. 3. This is the ratio between the pressure measured by the reference microphone on the one measured by the probe both considered as complex quantities and then having a modulus and a phase.

$$FRF = \frac{\hat{P}_{mic}}{\hat{P}_{probe}} \quad \text{Eq. 3}$$

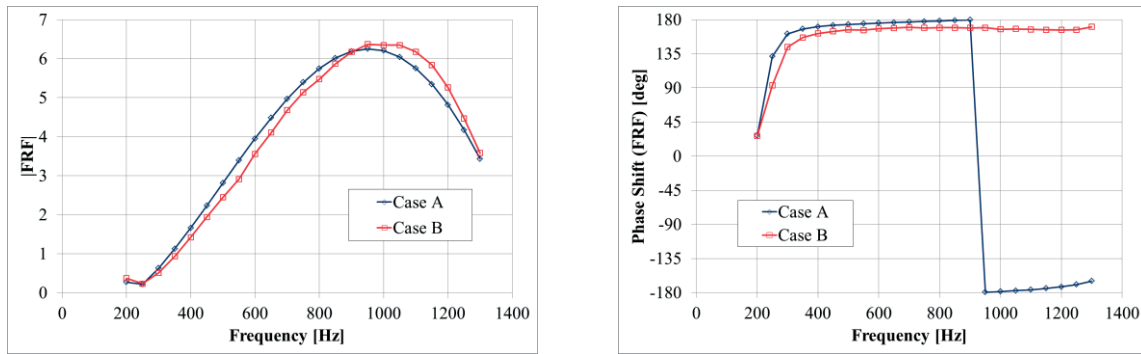


Fig. 5. Comparison of frequency response function for Case A and B

The comparison of the plots in Fig. 5 (Case A and B) shows that the position of the microphone does not deeply affect the frequency response of the probe. The difference in frequency response due to the sensor position increases when a conical connection is considered (Case C and D, Fig. 6).

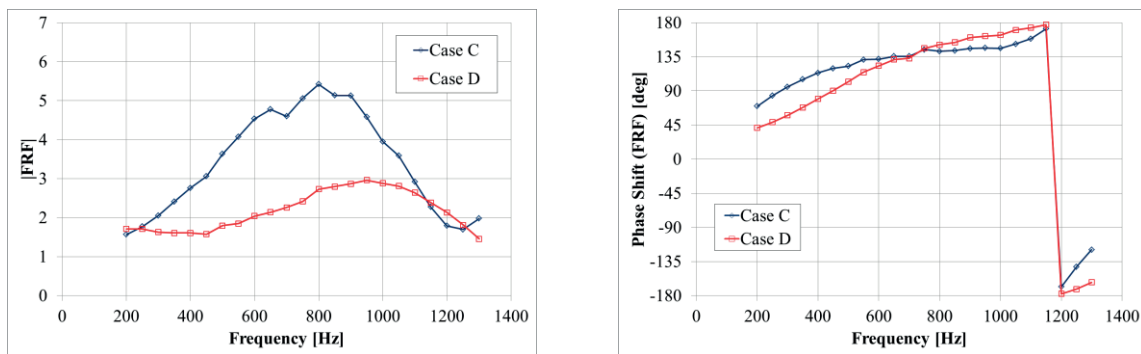


Fig. 6. Comparison of frequency response function for Case C and D

As a general trend, the conical connection reduces the pressure losses in the transition between the transmission duct and the housing chamber. In particular the best results are achieved with the flush mounted configuration.

A common practice to reduce the detrimental effects of the transmission duct resonance is the use of a damping duct several meters long placed at the end of the housing chamber [1]. The influence of a 30 m long damping duct and of an extended housing chamber dimension are reported in Fig. 7 (Case D, E and F). As expected, the increasing of the chamber dimension has a detrimental effect on the probe FRF. An unexpected result is the worsening of the FRF in case of a dumping duct. This result confirms the relevance of the housign chamber dimension on the probe FRF.

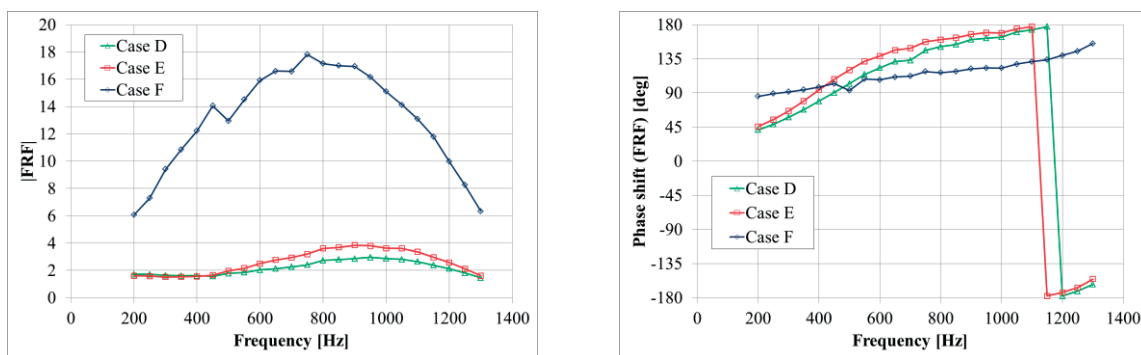


Fig. 7. Comparison of frequency response function for Case D, E and F.

From the comparison of all the results, the probe with a conical connection, a small housing chamber and a flush mounted microphone has the best FRF. For that probe, the experimental calibration is extended up to 4.5 kHz (as depicted in Fig. 8) because the dependence of acoustic pressure on radial position starts, for the described test rig, from 4.0 kHz.

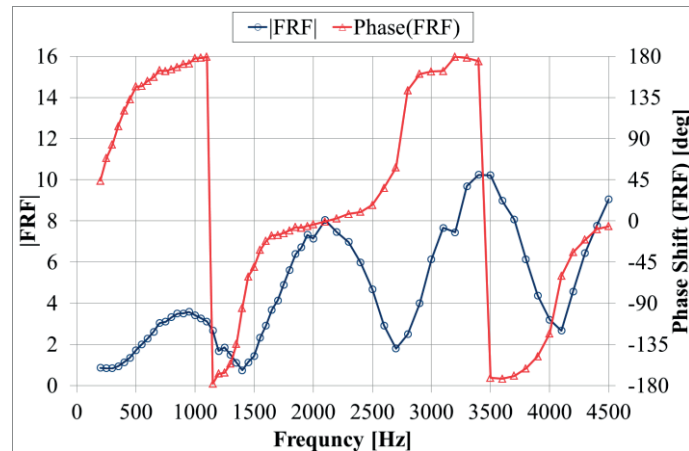


Fig. 8. Extended characterization

For frequencies higher than the first cut-on frequency, the acoustic pressure on the duct wall is no more uniform but changes with the position ( $x'$ ,  $r$ ,  $\theta$ ). To estimate the FRF of the probe at high frequency, the measurement of acoustic pressure at wall radius has to be made in two times (1 and 2) in the same measurement position ( $x'$ ,  $R$ ,  $\theta$ ). In the first session the acoustic pressure field is measured by the reference microphone (*ref*) and the probe. In the second session the same condition of session 1 on the reference microphone is reproduced and the probe is replaced by a flush mounted microphone. The FRF is therefore calculated as the ration between the second and the first measurement (Eq. 4).

$$FRF = \frac{\hat{p}_{mic}^{(1)}(x', R, \theta) \Big|_{ref(1)}}{\hat{p}_{probe}^{(2)}(x', R, \theta) \Big|_{ref(2)}} \quad \text{Eq. 4}$$

## ACOUSTIC FIELD MAPPING

### Data analysis methods

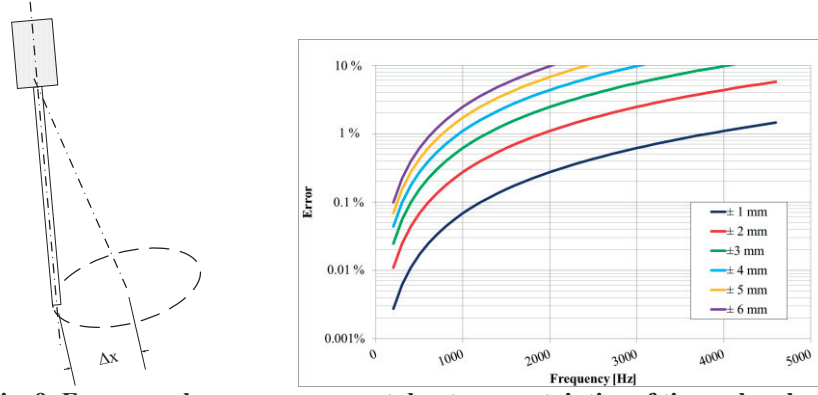
The acoustic pressure distribution in the duct cross section is the result of two waves moving in opposite directions. In each measurement point the pressure field is characterized by an amplitude and a phase, the two parameters depending on the geometrical set up of the test rig (distance from the acoustic the source, the sound pressure level of the source, measurement section and duct termination).

The description of acoustic wave fields needs several measurement points. In this activity the pressure distribution is measured by twelve measurement points in tangential direction and nine positions along twelve radii. As consequence, the wave field reconstruction involves twelve measurement sessions, where both the tangential distribution and the one along a radius are acquired. In addition to the previous ones, also the reference microphone signal is recorded. These data are used to clock the twelve measurement sessions and scale the amplitude (Eq. 5).

$$p_{map}(r, \theta) = \frac{|p_{r\theta}|}{|p_{ref}|} \cos(\varphi_{r\theta} \Big|_{mic_{ref}}) \quad \text{Eq. 5}$$

### Data fitting procedure

The pressure measurements are used to create a map of the acoustic field. Raw data are fitted with an interpolation procedure. The residuals of the fitting procedure need to be compared with the errors related to the measurement procedure and in particular they have to be lower than the errors due to the probe tip positioning. The position of the probe strongly affects the measurement of acoustic pressure. By making the hypothesis that pressure amplitude change is negligible for small axial variations, a wrong positioning of probe tip causes a shift in signal phase and consequently an error on the estimation of acoustic wave field pressure. The relevance of this error, that depends on the frequency, is estimated for different tip positioning and depicted in Fig. 9.



**Fig. 9. Error on phase measurement due to uncertainties of tip probe plating**

To estimate the placing error experimentally, the characteristics of the first tangential mode ( $m=1, n=0$ ) is exploited. This mode has a linear pressure distribution along the radial span. Due to the presence of the planar wave field the linear distribution has a finite value in the middle of the duct (instead of a null value). This value can be calculated as the mean value between the maximum and minimum acoustic pressure measured by the flush mounted microphones in the measuring section (Eq. 6).

$$|p_{00}| = \frac{\max[|\hat{p}_\theta| \cos(\varphi_\theta)] + \min[|\hat{p}_\theta| \cos(\varphi_\theta)]}{2} \quad \text{Eq. 6}$$

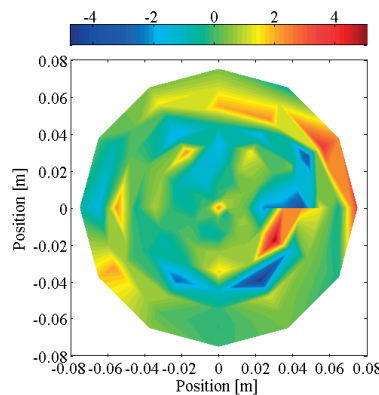
If one subtracts the amplitude of planar wave field calculated by Eq. 6 from the acoustic pressure distribution in the duct, the first tangential mode distribution is obtained. This distribution has a null value in the middle of the duct at measurement section; if the probe measures a pressure different from zero for that span, probably a tip displacement error is present, this causing a  $\delta p$ . To estimate the tip displacement from the theoretical position is assumed the hypothesis that the variation in the axial direction of planar acoustic field amplitude between the theoretical and actual probe position can be neglected. Since a standing wave has a sinusoidal trend in the axial direction it is possible to calculate the phase difference corresponding to the pressures estimated in the measurement section at tip probe position. The phase difference can be related to the axial displacement by considering the wave length (Eq. 7).

$$\Delta \bar{x} = \arcsen\left(\frac{p(\theta)|_{r=0} - |p_{00}|}{|p_{00}|}\right) * \frac{c}{2\pi f} \quad \text{Eq. 7}$$

Since the wall positioning of the probe is geometrically verified and all the measurement points lay on the same plane, the displacement error can be estimated as a linear distribution along the radius (Eq. 8).

$$\Delta x(r) = r * \text{arctg}\left(\frac{\Delta \bar{x}}{r_{\text{duct}}}\right) \quad \text{Eq. 8}$$

The same procedure is carried out for all the twelve circumferential positions and the estimation of the radial measurement is carried out (Fig. 10). The pressure at the middle of the duct considered for the calculation of the distribution map is the one with the minimum displacement error among the twelve measurement.



**Fig. 10. Probe tip positioning error (%) estimated for Case D probe, flush mounted microphone with conical connection.**

### Experimental wave field mapping

The pressure distribution maps are measured for three propagating wave field of increasing complexity:

- 1) From 1.39 to 2.28 kHz, complex sum of planar mode ( $m=0$ ,  $n=0$ ) and first tangential mode ( $m=1$ ,  $n=0$ );
- 2) From 2.28 to 3.17 kHz, complex sum of planar mode ( $m=0$ ,  $n=0$ ) and the second tangential mode ( $m=2$ ,  $n=0$ );
- 3) From 3.95 to 4.78 kHz 4.1 kHz, complex sum of three modes, the fourth tangential ( $m=4$ ,  $n=0$ ), the zero radial ( $m=0$ ,  $n=1$ ) and first radial ( $m=1$ ,  $n=1$ ).

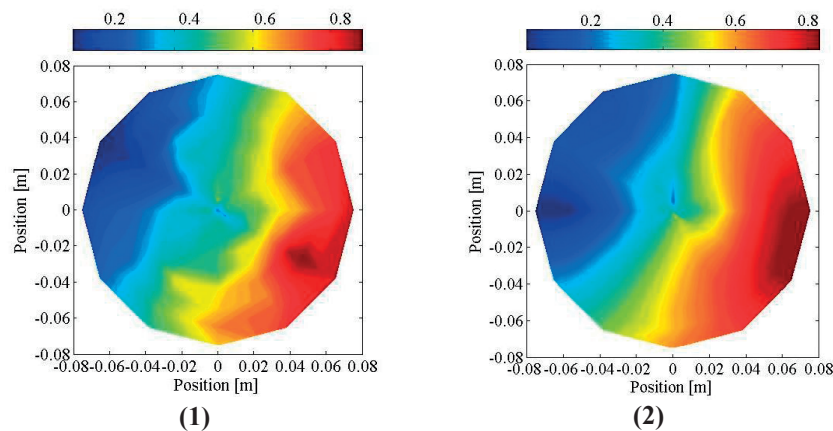
The frequencies for which the propagating fields are investigated are the ones where the frequency response function of the probe has a minimum. The measurement are carried out with both Case D and Case A probes with the aim of comparing the FRF influence on the results. The calibration coefficient for the two probes are reported in Table 2.

Field type	Case A			Case D		
	Frequency [kHz]	Gain	Phase Shift	Frequency [kHz]	Gain	Phase Shift
<b>n. 1</b>	1.8	4.29	-17°	1.5	1.40	-50°
<b>n. 2</b>	2.8	4.61	100°	2.7	1.79	58°
<b>n. 3</b>	4.1	3.49	-81°	4.1	2.66	-60°

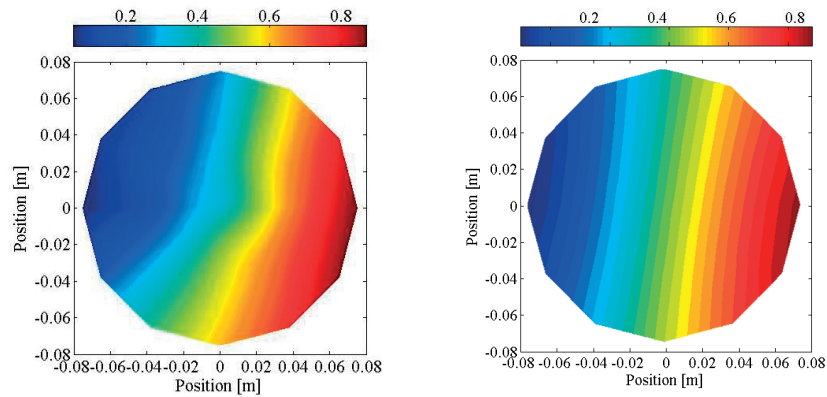
**Table 2. comparison of best calibration of the two probe in each propagation mode range**

All the pressure maps are referred to the reference microphone pressure and reported in Fig. 11 to Fig. 16. In order to compare the results, the data raw for the two probes (linear interpolation), the fitted values (lower cubic) for Case D probe and the theoretical distributions are reported for the three propagating fields. The theoretical maps considers both the incident and reflected wave in analogy with what is measured by the probes. For the theoretical distributions it is not possible to know the phase difference between the incident and reflected wave for non-planar modes since it is not possible to characterize the duct end behavior. In the Figures below the same phase shift is considered for the planar wave and all the other modes.

In Fig. 11 and Fig. 12, the pressure distribution for condition 1, are reported. The overall acoustic pressure distribution has a linear trend in the radial direction. The map measured with the Case D probe has a more uniform distribution than the one measured by the other. The fitted distribution turns out to be in good agreement with the theoretical one.

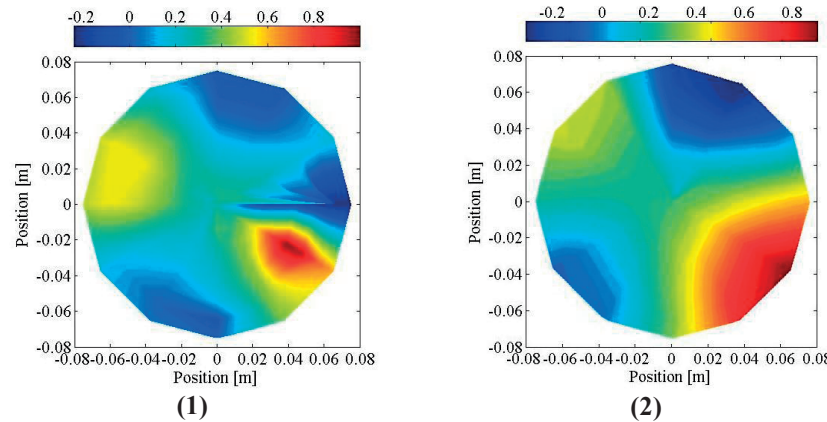


**Fig. 11. Comparison of experimental maps of first tangential mode ( $m=1$ ,  $n=0$ ) measured with probe Case A, back mounted microphone with abrupt connection (1) and D, flush mounted microphone with conical connection (2)**

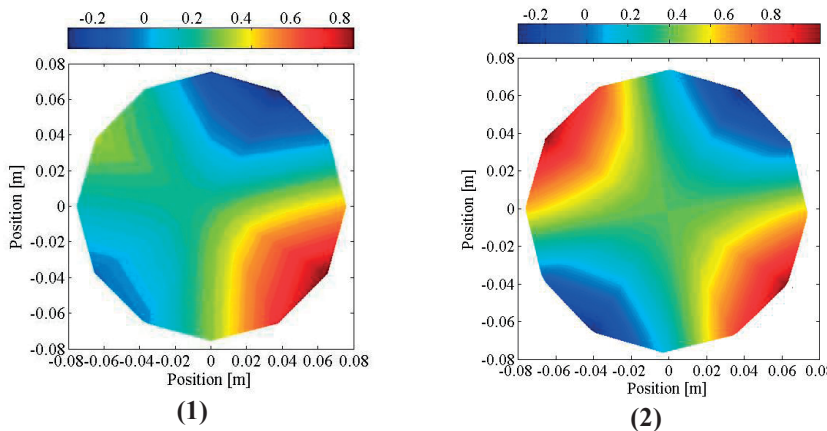


**Fig. 12. Comparison of first tangential mode ( $m=1, n=0$ ) with theoretical wave field**

In Fig. 13 and Fig. 14, the pressure distribution for condition 2, are reported. The results are similar to those of the previous case. The distribution is not symmetrical as in theoretical distribution (Fig. 14), because the phase of the tangential second mode is not the same that in the theoretical map.



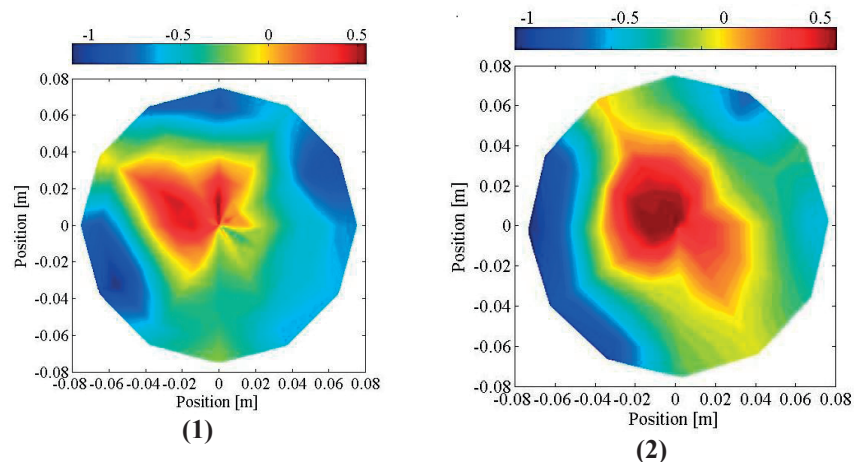
**Fig. 13 Comparison of experimental maps of second tangential ( $m=2, n=0$ ) mode measured with probe Case A, back mounted microphone with abrupt connection (1) and D, flush mounted microphone with conical connection (2)**



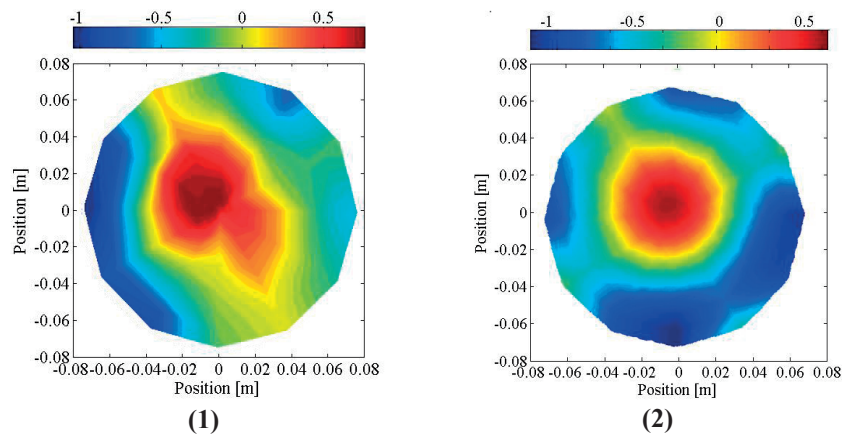
**Fig. 14 Comparison of second tangential mode ( $m=2, n=0$ ) with theoretical wave field**

In Fig. 15 and Fig. 16, the pressure distribution for condition 3, are reported. Even for this test case probe Case D needs lesser gain and consequently has lesser error amplification. Also in this case a good agreement with the theoretical distribution is achieved.





**Fig. 15. Comparison of experimental maps at 4.1 kHz measured with probe Case A, back mounted microphone with abrupt connection (1) and B, flush mounted microphone with conical connection (2)**



**Fig. 16 Comparison of experimental maps at 4.1 kHz with theoretical map**

## CONCLUSION

In recent years, the analysis of acoustic wave propagation in ducts has become more and more important thanks to the relevant effects of acoustic perturbations on flame stability. Many numerical tools can be adopted for the investigation of acoustic wave propagation, whereas from the experimental point of view, only a few solutions are available, especially if a 2D characterization of the wave is sought. A common practice is the adoption of a wave guide probe, made-up of a transmitting duct and a housing chamber for a microphone. The larger the microphone diameter is the higher its sensitivity. On the other hand, larger diameters involve greater discontinuity between the transmission duct and the microphone housing and then more distorted frequency response functions. Several geometries of microphone housing have been investigated in this paper. Among them the one with a conical connection between the transmission duct and sensor housing and the microphone mounted orthogonally to the cone axis shows the best results. This probe is used for the measurement of the acoustic wave field propagating in a semi-infinite circular duct considering twelve circumferential positions and nine radial displacements. An procedure is developed for the estimation of the errors due to probe tip placing. The acoustic pressure map is experimentally reconstructed for three different propagating acoustic field with increasing complexity: the first and the second tangential modes characterized by the complex sum of planar wave field and the tangential one, and the acoustic field at 4.1kHz which is made up of three different field the forth tangential and the zero and first radial. Experimental data are compared with theoretical acoustic fields taking into account that the experimental map is made up of both incident and reflected waves. A good agreement is found between the experimental and the theoretical results.

The results achieved with this work demonstrate that with a properly calibrated probe it is possible to reconstruct also the radial acoustic pressure distribution of a propagating acoustic field. This is a quite new result in the field of acoustic pressure wave propagation analysis.

**NOMENCLATURE**

$c$	Sound velocity
$FRF$	Frequency response function
$J$	Bessel first order function
$i$	Time index
$L$	Duct length
$m$	Tangential mode index
$n$	Radial mode index
$p_{mnf}$	Acoustic pressure for $mn$ mode
$\hat{p}$	Complex pressure
$p_{mn}$	Pressure evaluated for mode $m,n$
$R$	Radius of the duct
$r$	radial coordinate
$x$	Axial position
$\lambda$	Wave length
$\Gamma$	Axial decay coefficient
$\theta$	Position on circumference
$\varphi$	Phase shift
$\kappa_{mn}$	Roots of square root of decay coefficient
$\eta = \frac{\omega r}{c}$	
$\omega$	Angular frequency

**AKNOWLEDGMENTS**

Thanks are due to Prof. Ennio Antonio Carnevale of the University of Florence for supporting this study.

**REFERENCES**

- [1] J. M. Verdon, M. D. Montgomery e K. A. Kousen, «Developmento of linearized unsteady Euler analysis for tubomachinery blade rows,» NASA, East Hartford, Connecticut, 1995.
- [2] D. L. Sutliff, «Rotating Rake Turbofan Duct Mode Measurement system,» NASA, Cleveland, Ohio, 2005.
- [3] A. Andreini, B. Facchini, L. Ferrari, G. Lenzi, F. Simonetti e A. Peschiulli, «Experimental investigation on effusion liner geometry for aero-engine combustors: evaluation of global acoustic parameter,» Accepted for *ASME Turbo Expo 2012*, Copenhagen, Denmark, 2012.
- [4] A. Fischer, E. Sauvage e I. Röhle, «Acoustic PIV: Measurements of the acoustic particle velocity using synchronized PIV-technique,» in *14th Int Symp on Applications of Laser Techniques to Fluid Mechanics*, Lisbon, 2008.
- [5] G. Souchon, B. Gazengel, O. Richoux e A. L. Duff, «Characterization of a dipole radiation by Laser Doppler Velocimetry,» 2004.
- [6] G. Ferrara, L. Ferrari e G. Sonni, «Experimental characterization of a remoting system for dynamic pressure sensors,» in *ASME TURBO EXPO*, Reno-Tahoe, Nevada, USA, 2005.
- [7] H. Tijdeman, «Investigation of the transonic flow around oscillating airfoils,» National Aerospace Laboratory (NLR), Amsterdam, 1977.
- [8] J. R. v. Ommen, J. C. Schouten, M. L. v. Stappen e C. M. v. d. Bleek, «Response characteristics of probe-transducer systems for pressure measurements in gas-solid fluidized beds: how to prevent pitfalls in dynamic pressure measurements,» *Powder Technology*, vol. 106, p. 199–218, 1999.
- [9] D. H. Zinn e D. M. Habermann, «Developements and experiences with pulsation measurements for heavy-duty gas turbines,» in *ASME Turbo Expo*, 2007.
- [10] M. A. White, M. Dhingra e J. Prasad, «Experimental analysis of a wave guide pressure measuring system,» *Journal of Engineering for Gas Turbines and Power*, vol. 132, n. 041603-1, 2010.



## THE USE OF CAUSALITY METHOD FOR DETECTING NOISE SOURCES IN ISOLATED TURBOMACHINERY AIRFOILS AND CASCADE.

Stefano Bianchi\*  
Alessandro Corsini

University of Roma – Sapienza, Department of  
Mechanical and Aerospace Engineering.  
Roma, Italy.

\*bianchi@dma.ing.uniroma1.it  
corsini@dma.ing.uniroma1.it

Anthony G. Sheard

Flakt Woods Ltd  
Axial way, CO4 5ZD  
Colchester, UK.

geoff.sheard@flaktwoods.com

\*corresponding author

### ABSTRACT

This paper describes an experimental investigation on the interaction noise from a jet investing isolated airfoils. The region of interest focused on the tip region of an isolated cambered airfoil, in use in subsonic axial fans. The Mach number, Reynolds number and blade incidence angles are set in the static frame of reference in order to reproduce flow field condition kinematically similar to that in the rotating frame. Far-field noise measurements were correlated to simultaneous near field pressure measurements taken at different chord-wise positions on the blade surface. The aim was to find, through the use of a cross correlation technique, a causal relationship between the aerodynamic sources and noise emissions to establish the role of airfoil self-noise associated with turbulent structures produced by interaction of the turbulent inflow and highly cambered blade tip geometry. Because the importance of the noise originating from the interaction of unsteady disturbances in fan or compressor blades, as a fundamental contributor to rotors' overall acoustic emission, there is interest also in the development of an estimation of the noise sources by the mean of experimental surveys not directly dedicated to the noise measurements. The technique of cross-correlation represents a good compromise in the study of the blade noise sources, especially when the rig set-up is not dedicated to a proper noise investigation (*i.e.* HPC compression tube facilities).

### INTRODUCTION

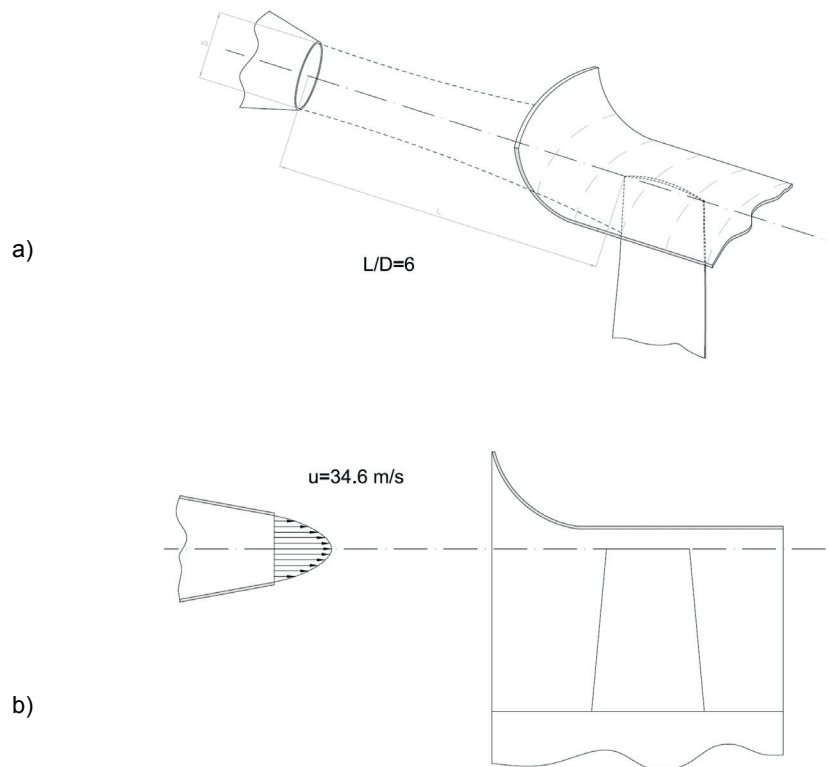
There is an historical interest on developing physical understanding for the problem of a solid body invested by a steady flow, but in practice, propellers and fans operate under non-uniform inflow. When a turbulent eddy passes the sharp edge of a solid body, the turbulent fluctuations radiate even more strongly, scaling with the Mach number's fifth power as Ffowcs Williams and Hawkins<sup>1</sup> showed. Therefore, due to this scaling, in absence of other noise-generating mechanisms, the trailing edge and the tip gap are the most significant aerodynamic noise source, especially at low Mach number. In stationary tests, engineers have deduced that the dominant noise component arises from the interaction between ingested turbulence and the rotor blades, as demonstrated by Magliozzi and co-authors<sup>2</sup>. These authors worked on understanding the physical mechanisms that are responsible for the noise due to unsteadiness in the impinging flow.

The base for this approach is the linearised aerodynamic theory of an isolated airfoil<sup>3</sup>. The far-field noise, which an airfoil radiates, is related to the turbulent velocity field by transfer function independent of the aerodynamic flow characteristics; when determined for an isolated airfoil to rotating blades. The only limitation in this case, being the neglecting for the blade aerodynamic interaction among the other blades. Winkler *et al.*<sup>4</sup> first proposed this approach for the trailing edge noise study of a highly cambered NACA five digit airfoil at zero degrees angle of attack with and without a boundary layer tripping.

### Measurement technique

The data analysis in this paper came from a comprehensive broadband noise experiment for stationary airfoil. Testing parameters included flow average velocity, blade pitch angle, and angle of incidence of the incoming flow and the tip leakage flow control through a new aerodynamic tip end-plates compared with a *datum* impeller geometry.

The authors tested the airfoil in the core of a round free jet blowing into an anechoic chamber at the Fläkt Woods facility in Colchester, UK. They blew the jet through a circular nozzle at the end of a convergent duct onto the airfoil. They aligned the jet's upper part 50 mm from the fan's inlet bell-mouth edge which blew the jet centreline approximately to the blade's tip region (Figures 1.a and 1.b). The relative position of the round jet to the blade assured an aerodynamic behaviour as close as possible to the rotating conditions. The authors used two microphone types for the far-field and the near-field measurements. They obtained the measured time series from positioned probes to give an acceptable trade-off between signal-to-noise ratio and directivity according to Winkler et al.<sup>4</sup> and Bianchi et al.<sup>5</sup>.



**Fig. 1: schematic arrangement of the sector rig.**

The far-field microphone was a free-field standard Bruel & Kjaer 1/3" protected with a foam-ball. The microphone was located in the anechoic chamber 1.2 fan diameters off the blade trailing edge, with an angular anomaly  $\theta = 30^\circ$  from the centreline of the jet plume as recommended by Bianchi et al.<sup>5</sup>, Winkler et al.<sup>4</sup> and by Leggat and Siddon<sup>6</sup>. The probes in the near-field unsteady pressure measurements on the blade surface are GRAS Type 40PS surface microphones (Figure 2), designed for measurements on planar and curved surfaces. These probes are 2.8 mm thick with a useful frequency range up to 20 kHz and a dynamic range topping at around 136 dB. The signals from all microphones were acquired using a dBFA-AREVA Symphonie acquisition card. The authors used the near- and far-field signals to compute auto- and cross-spectra. They obtained all the spectral data with 3.125 Hz bandwidth where normalised under the impinging jet parameters to the St number; defined as.

$$St = fL / U_j$$

Where  $f$  is the considered frequency,  $L$  is the airfoil chord and  $U_j$  is the jet average velocity.

The airfoil under investigation is representative of a fan blade section which the engineers had previously developed and which the authors refer to as the *datum* blade configuration. The *datum* blade in the tip region was a modified ARA-D 6% airfoil, British Aeronautical Research type D for subsonic tip propellers. Table 1 provides the *datum* fan's specifications and airfoil section.

The authors present the experimental results '*as measured*', whilst the theoretical aeroacoustics on the turbulence/airfoil interaction include correction to account for the jet shear layer presence through which the sound must pass before reaching the far-field microphone. Note that there were no adjustable parameters in the theory, which the authors could have used to improve the agreement between theory and experiments for the tested airfoil type.

After the measurement, the authors appropriately processed the instantaneous pressure data in order to derive some quantitative data on the the tip noise. The authors recorded all measurements at a sampling rate of 50 kHz, thus the Nyquist frequency was  $f = 25$  kHz. To avoid signal aliasing, they filtered all data at 20 kHz and analysed it in the range below 20 kHz. The resulting Nyquist-Rate was 2 kHz which was largely below the sampling frequency, thus verifying the second condition in the Nyquist problem on signal aliasing.

The authors estimated the overall uncertainty on unsteady pressure measurements as: i)  $\Delta V = 1000 \text{ mV} \pm 12 \text{ mV}$  (20:1) on the voltage and ii)  $\Delta G = 200 \text{ dB} \pm 2.4 \text{ dB}$  (20:1) for the row signal gain in the frequency ranges. The error in the Fourier transform was in the range of 0.1-0.2 dB at 1 kHz and 2 dB at 10 kHz, as given by the calibration certification on the microphones and the acquisition system.

The authors processed the auto- and cross-spectra using a signal post-process suite in the frequency range 25 Hz to 20 kHz with a constant bandwidth of 3.15 Hz. A 01-dB Symphonie digital signal processor acquired the signals from the far-field microphone and performed the cross correlation with the near-field blade surface pressure.

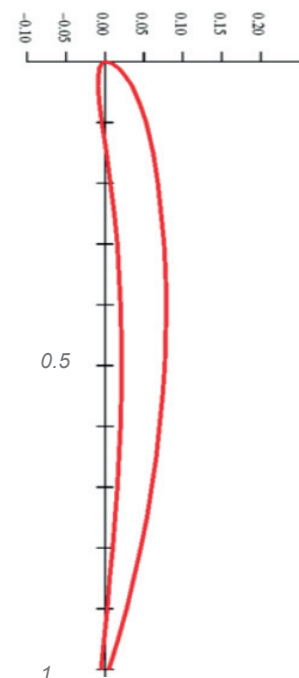
### Causality Method Analysis

A transfer function that couples the pressure fluctuation (due to the unsteady flow in the near- field) with perceived noise in the far-field (which constitutes the response of the system) governs aeroacoustics emissions. Pseudo sound can degrade the results; however, in an anechoic chamber, the pseudo sound's transfer function has a shorter decay time than the same function transmitting the genuine noise emission to the far-field.<sup>7</sup> In accordance with Leggat and Siddon's<sup>6</sup> method, the authors chose the distance of the far-field probe from the fan as the optimum to avoid pseudo sound becoming coherent.

In the present study, the authors correlated the tip pressure measurements of the near-field with the measured noise at the far-field. In diagnosing acoustic sources, engineers find identification of the proper correlation domain useful for assigning flow regions in the near-field controlling the sound in the far-field. The cross-correlation between near- and far-field signals reveals a causal relationship between individual noise-source phenomena and the overall radiated sound in a given direction, thereby yielding quantitative information about acoustic source distribution, their local spectra and the scale of their coherence. If a strong harmonic coupling between a source in the near- field and far-field spectra exists, the resulting correlation function does not decay quickly, but is periodic in nature.

**Table 1: ARA-D 6% rotor metrics.**

<i>AC90/6 fans</i>		
<b>blade geometry</b>	<i>hub</i>	<i>Tip</i>
<i>ℓ / t</i>	1.32	0.31
<i>pitch angle (deg)</i>	36	28
<i>camber angle (deg)</i>	46	41
<i>solidity</i>	1.24	0.3
<b>fan rotor</b>		
<i>blade number</i>	6	
<i>blade tip pitch angle (deg)</i>	16 ÷ 28	
<i>hub-to-casing diameter ratio v</i>	0.22	
<i>tip diameter (mm)</i>	900.0	
<i>rotor tip clearance τ (% span)</i>	1.0	
<i>rated rotational frequency (rpm)</i>	935	



Thus, the authors derived a coherence function for the data set. In accordance with Mile's suggested procedure<sup>8</sup>, the authors set the threshold for signal coherence at 95% of the calibrated noise source and used this to confirm the anechoic chamber's acoustic performance. The authors used a white noise Brüel & Kjør Type 4204. This

procedure ensured that only coherent sources contributed to the cross-spectra; whereas, the auto-spectra remained as a consequence of coherent and incoherent sources. Correlating near- and far-field data was a good solution for facilitating an improvement in pseudo sound correction.

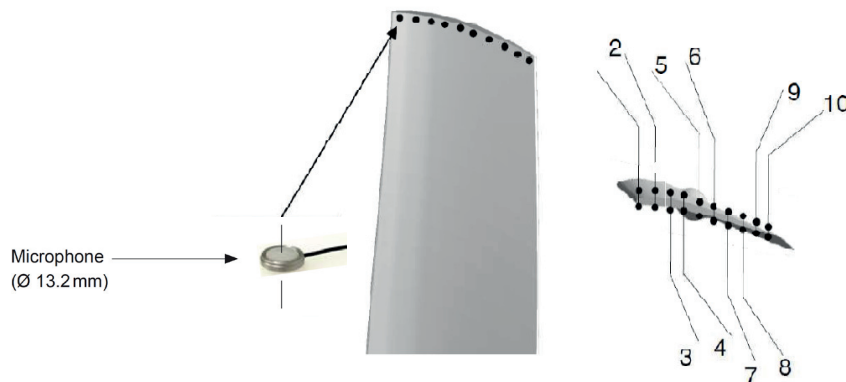


Fig. 2: arrangement of the near-field pressure probes.

### REMARKS ON THE METHODOLOGY

The measurement of instantaneous pressure in the airfoil near field raises questions about the consequences of using such measurements to dissect noise-source activity. Previous work<sup>3</sup> has established that, in addition to the ‘purely hydrodynamic’ contributions, the near-field also comprises an ‘acoustic’ component limited to the progressive pressure fluctuations put towards the reach of the far field. Several studies on subsonic jet noise have reported on near field pressure measurements under similar velocity gradients to those in the outflow from fan rotor<sup>8</sup>. With regard to the relationship between the near field pressure and noise-source dynamics, Ribner<sup>9</sup> observed that the first-order approximation of the Lighthill source term is formally related to the pressure Laplacian in incompressible flows. Moreover, Laurendeau *et al.*<sup>6</sup> noted that the spectrum in the near-field combines a low frequency range dominated by the aerodynamic signature and a high frequency range that senses acoustic-pressure fluctuations. The pressure in the near-field senses both the ‘aerodynamic cause’ and the ‘acoustic effect’ in different frequency ranges. Applied far field filtering provides insights into the source-noise emission coupling mechanisms. From this perspective, the paper aims to correlate the local pressure fluctuations on the blade surface, measured for three chord positions in the tip zone, with the noise at the far-field measured in the different azimuthal angles which the experiments considered. This ‘causality method’ is no less than a high precision source localisation technique, which identifies the coupling mechanism’s structure via which the largely redundant wall pressure dynamic drives the far-field pressure field.

### Cross-Correlation Method

Generally speaking, cross-correlations help identify variables (*e.g.* wall pressure) which are leading indicators of other variables (*e.g.* noise) or how much one variable is predicted to change in relation the other variable. This analysis will provide a correlation between two time series or two waveforms. The cross-correlation of two complex functions  $f(t)$  and  $g(t)$  of a real variable  $t$ , denoted  $f * g$  is defined by:

$$f * g \equiv \bar{f} = (-t) \otimes g(t)$$

where  $\bar{f}$  is the complex conjugate and  $\otimes$  denotes here the convolution of the function.

It follows that

$$[f * g](t) = \int_{-\infty}^{\infty} \bar{f}(-\tau)g(t - \tau)d\tau = \int_{-\infty}^{\infty} \bar{f}(\tau)g(t + \tau)d\tau$$

We can use the relation above to determine the relative sizes of sound field intensities radiated from given blade surface positions at given flow speeds. It is understood that the results from the cross-correlation function are to be interpreted as the fraction of the overall intensity radiated from the eddy located at the position of the pressure probe measuring wall static pressure in the near-field.

As the flow velocity ratio increases to higher Mach numbers, since a finite averaging time is employed in the calculation of the cross-correlation function, there exists a noise fluctuation riding on the function itself which

gives the uncertainty in the true value of the cross-correlation function. Different studies<sup>12, 14</sup> reported very little difference in the magnitude of peaks pressure of the fundamental tones, but these peaks are shifted to higher frequency. Twofold elements contributed to this evidence: the background tunnel noise, which is greater at high frequencies, and the distance between the near-field and the far-field probes. This effect is partly due to the semi-reverberation environment of the wind tunnel. This increase in frequency for the shear region as compared with that for the mixing region, is supported by other work<sup>14</sup>, as the present survey represents a first attempt with the simple case-study of low Mach number flow. In that work<sup>14</sup> a relatively slow jet is disturbed by high intensity sound fields produced at various frequencies, it is found that the maximum instability within the shear layer occurred for a Strouhal number of 18 to 20. If we compare this with the typical Strouhal number for the mixing region,  $St = 0.3$ , one obtains a ratio of approximately  $St = 6-7$  for the critical frequencies for these two regions, agreeing qualitatively with our observations of the actual pressure fluctuations. Because of the increased importance of the shear layer in cross-flow sound-radiation, this has the effect of increasing the frequency of the spectrum maximum for the radiated sound under cross-flow conditions. This frequency shift should be accounted for in any experiment of confined supersonic flow. The reflected correlation pulses can be found experimentally; they will be separated from the first arrival— sound travelling directly from the source position to the far field position — so long as the far field probe is more than a wavelength from the nearest wall of the tunnel. The important measurement is the maximum of the correlation function. The 'noise' evident in this theoretical sketch is composed, depending on test condition, of:

- a) Wind tunnel noise.
- b) Flow self-noise at the  $i^{\text{th}}$  microphone.
- c) Higher order reflections of jet noise from the tunnel walls.

All of these noises are uncorrelated (for small values off) with the main aerodynamic noise of airfoils — which is what we want to measure.

The authors chose the position of the near-field microphones at ten positions along the airfoil's chord to cover the three most important regions responsible for the tip noise emission: the leading edge (LE), the mid-chord (MD) and the trailing edge (TE). This is an important point given the aforementioned difficulty associated with identify the radiating part of a source in the near-field. Because the formal identity between the source far-field correlation and the integral solution of the Lighthill's equation, the filtering operation by which the said solution sorts and extracts acoustically matched source activity, is inherently present in the source far-field correlation. This is most effective when the source fluctuation frequency matches with the far-field noise pressure. Other researchers have reported the same deduction in past studies on the jet noise source correlations<sup>10</sup>.

The second important consequence of using near-field pressure is that we are dealing with more than just the signature of a causal pressure dynamic. We also sense the beginnings of the acoustic response for certain frequencies, as the radiation extent of the airfoil wall pressure field's 'hydrodynamic' component is a function of frequency. The authors could sense low frequency 'hydrodynamic' pressure fluctuations further in the airfoil surface than the high frequencies due to their reflection on the rigid wall surface. The spectrum of the near pressure field thus comprises a low frequency range where the perturbations are largely dominated by the hydrodynamic signature of the largest scale of the jet turbulence and a high frequency range dominated by progressive, acoustic, fluctuations. So, the same near-field measurement both senses the cause and the effect, in different frequency ranges. When we correlate them with the far-field measurements, which are sensitive only to the acoustic effects, it is possible to obtain valuable information related both to the mechanism by which the hydrodynamic cause couples with the far-field, but also to how the new-born far-field sound field at higher frequency radiates to the various far-field microphones. This also provides insight into the sound waves' directional character issuing from the airfoils rigid surface.

Certain difficulties exist, however, concerning physical interpretation of the pressure field in this near-field region, and in particular when relating it to the sound production mechanisms. On one hand, the near pressure field is dominated by dynamics which are best described by a linear hyperbolic differential equation; whereas, it is essentially driven by a nonlinear hydrodynamic pressure field which is well approximated by elliptic equations. There is, however, a further difficulty related to the hyperbolic dynamics of the near field, and which hinders clear interpretation of near-field measurements. Nevertheless, together with the hydrodynamic signature of the turbulence in the high rotational region, as it is for an airfoil near wall region, the near-field also contains the beginnings of a sound field which is destined to reach the far-field. As we are dealing with a jet investing an airfoil, in addition to those discussed above, we have further complications which arise on account of the existence of different shear layers. We characterise these by different velocity gradients, turbulence scales, and characteristic convection velocities.



Guitton *et al.*<sup>11</sup> presented an empirical model which accounted for both the different flow velocity dependence, and the different spectral decay of the hydrodynamic and acoustic components of the near pressure field. They proposed the following criterion to predict the point at which we can observe transition from hydrodynamic to acoustic dominance.

On the base of the above model, Laurendeau<sup>6, 12</sup> convincingly showed that for a jet flow with similar aerodynamic characteristics with the one that the authors used in this measurement campaign, the transition region, from the hydrodynamic and the acoustic regime, lie somewhere in the region of  $St = 1.3$  for a near-field to far-field microphone distance equal to the one that the authors used in these experiments. With respect to the most amplified frequency of the transition region, Laurendeau<sup>12</sup> clearly indicated this value as  $St = 0.7$ . This means that, in terms of cause-effect relationship, we seek to probe the limit of  $St=5$ , imposed for the similarity of the noise emission of a static airfoil invested by a round jet with respect to a real rotating blade. This limited the value in understanding the details of source dynamic in providing information of the *cause-effect* regime, but informed to the directivity of the high frequency sound field emanating from the three locations at which the authors performed the near-field measurements. Nevertheless, this is strictly true for the cross-correlation analysis, as the tool of coherence analysis is still useful in order to highlight the *cause-effect* relationship. Indeed, because the coherence function involves a normalisation by frequency band, it tends to highlight events that are highly coherent even if their energy is low, also inside the hydrodynamic regime. On the other hand, an analysis using the correlation coefficient, such as cross-correlation, will tend to suppress the low energy events and to highlight the *effect-effect* relationship that we associate with the most energetic events. The coherence analysis is better suited to highlight the near-field acoustic relationship to the far-field domain and gives a feel for the directivity of the sound field issuing from different regions of the airfoil tip. In addition, the cross-correlation analysis informs with regard to that precious information related to the subtle details of the coupling mechanism via which the airfoil wall pressure energy excites the far-field in a particular direction.

### EXAMPLES OF RESULTS

The authors applied the sequence of signal processing techniques, which the previous sections illustrated, to the pressure transducer signal located on the tip region's blade surface, and the far-field microphone noise signal. As already discussed, the complexity of the experimental set-up makes it impossible to use analytical Green's functions tailored to the actual geometry. Moreover, the authors expect that the noise sources distributed along the airfoil become non-compact around  $St = 6$ , thus a derivation of the Green's function is practically impossible for the frequency range of our interest. It is worth reminding that the conventional *dictum*: "*correlation does not imply causation*" means that we cannot use correlation to infer a strict causal relationship between the variables. As the introduction explains, do not interpret this *dictum* to mean that correlations cannot indicate the potential existence of causal relations for an aerodynamically produced noise. However, the causes underlying the correlation, if any, may be indirect and unknown, and high correlations also overlap with identity relations, where no causal process exists. For example, if the coefficient of the cross correlation is  $r = 0.1$ , as mainly occurs for the peak values in the emission of the studied airfoil, then the coherence  $g^2 = 0.50$ , which means that we can explain 50% of the total variation in noise by the linear relationship between this noise and the airfoil wall pressure (as described by the regression equation). The other 50% of the total variation in the noise remains unexplained.

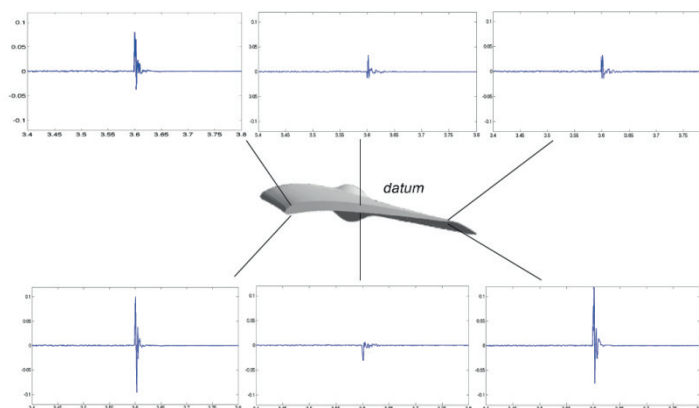
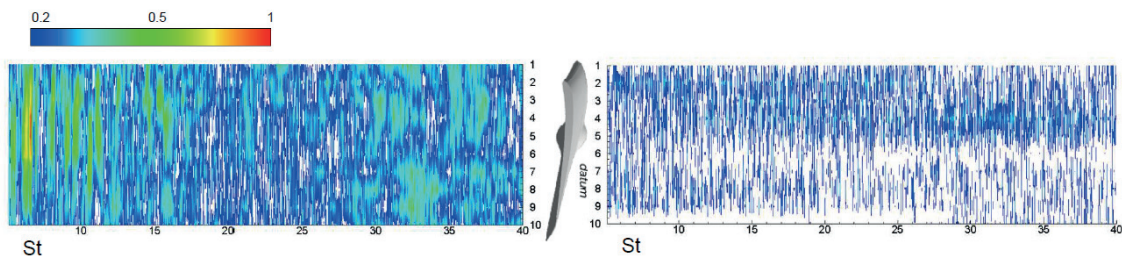


Fig. 3: Cross correlation coefficients of the airfoil in three different chord positions.

Bearing in mind the above stated limitations, the authors use cross-correlation and coherence analyses to discuss the causal relationship between the near-field wall pressure and the far-field sound domain. Figure 3

presents the coefficients of the cross-correlation. As usual for this analysis, if there is a perfect match of the two sets for the given near- to far-field time delay, a peak appears in the correlation function.

The plots in Figure 3 show the correlation coefficients in the time region from  $3.4 \times 10^{-3} s$  to  $3.8 \times 10^{-3} s$ , which contains the peak value. Turning our attention to the coefficients of the correlation function in Figure 2, a number of interesting observations drop off about the airfoil pressure side's source mechanisms. As Miles<sup>8, 13</sup> recently proved, the correlation coefficient's peak region in a near- to far-field cross correlation, is representative of different *cause-effect* and *effect-effect* mechanisms. The left side of the peak is determined by the direct correlated noise, which dominates the considered source and moves at acoustic speed along its full path to the far-field probe (Miles<sup>8</sup> dealt with the combustor pressure correlated noise in jet engines). The right side of the peak is in the region controlled by the indirect aerodynamic noise, which initially propagates with the mean flow velocity. Consequently, one might expect to see in Figure 3 a correlation function with one smeared peak, due to the direct wall pressure noise, and a smaller smeared peak due to indirect aerodynamic noise. From the examination of the correlation functions of Figure 3, it drops off that this is generally the case encountered.



**Fig. 4: chord-wise map of near-to-far-field coherence.**

Figure 4 shows the chord-wise map of near-to-far-field coherence ( $\gamma^2$ ) in the *datum* fan blade. The pressure measurements on blade pressure side (PS) indicate a significant coherence level distributed along the chord in a range of St up to 11. The tones of coherence produced at the leading edge region ( $1 < c < 3$ ), in the frequency range  $St = 5$  to  $St = 11$ , are due to the flow impingement as a result of the inflow's turbulent nature affecting the structures of the flow/leading-edge interaction. On the blade LE, the near-field probe merged in the boundary layer and was sensitive to the oscillatory pressure field mechanism. We can associate this highly fluctuating source with the Kelvin-Helmholtz mixing-layer structure, which became less efficient as the near-field probe position approached the airfoil's fully developed region.

In case the investigated blade might be placed inside a transonic jet, the derivation of the correlation factors from the measurement should be carefully evaluated, looking at the considerations discussed above and the experimental procedure should be designed properly<sup>14</sup>. The aerodynamic noise generated by a cascade of turbomachinery airfoils is generally 10 to 15 dB higher to the tunnel noise, except for the fundamental peak, which rises at about 19 dB. It is found that the presence of local overpressure due to the shock waves increases the fundamental peaks noise by 10 dB. Many of our measurements could have been improved (if the scope of the work had permitted) by such increased averaging times.

### CONCLUSIVE REMARKS

The primary purpose of this work was to determine the effect on sound levels when a high cambered airfoil is immersed in a subsonic turbulent flow. A secondary purpose has been to develop, in a preliminary way, the concept for a measurement process employing correlation techniques, which could be used in a reverberant wind tunnel environment, for transonic cascade or rotors.

The cross correlation function and the coherence function methods provided a procedure to detect the presence of coherent indirect and direct aerodynamic noise, when both are present. However, the inherent smearing of the cross correlation that occurs as a consequence of the turbulence filtering renders the determination of the relative contribution of the indirect and direct noise to the total airfoil noise difficult.

The frequency of the full developed local turbulence of the datum airfoil is  $St=32$ . The components in the vicinity of the local mixing-layer frequency are at  $St=7.5$ . We can associate this highly directional source with the Kelvin-Helmholtz mixing-layer structure, which became less efficient as the near-field probe position approaches the airfoil's fully developed region.

Finally a comment concerning the cross-correlation measurement technique in a reverberant environment, like a pressure tube. The difficulties experienced in making sound measurements in high reverberant wind

tunnel facilities are sufficiently known<sup>14</sup>, but have not been investigated extensively. The pressure to noise correlation process has the advantage to eliminate background noise and the unwanted reflection noise. However, the smaller the signal to noise, referred to the direct radiated noise as the signal and all other sounds whether reflection or otherwise as noise, the greater is the averaging time needed in order to obtain a valid correlation function.

## REFERENCES

- 1 Ffowcs Williams, J.E. and Hawkings, D.L., Sound Generated by Turbulence and Surfaces in Arbitrary Motion, Philosophical Transactions of the Royal Society, 1969, A264, 321–342.
- 2 Magliozzi, B., Hanson, B., Johnson, D.B. & Metzge, F.B. (1973), Noise and Wake Structure Measurements in a Subsonic Tip Speed Fan. Report NASA CR-2323.
- 3 Blake, W.K. and Gershfeld, J.L., The Aeroacoustics of Trailing Edges, in: Gad-el-Hak, M., ed., Frontiers in Experimental Fluid Mechanics, Springer-Verlag, Berlin, 1989, 457–532.
- 4 Winkler, J., Temel, F.Z. and Carolus, T., Concepts, Design and Characterization of a Small Aeroacoustic Wind Tunnel Facility with Application to Fan Blade Measurements, Proceedings of Fan Noise, 3rd Symposium, Lyon, 2007.
- 5 Bianchi, S., Corsini, A., Rispoli, F. and Sheard, A.G., Experimental Aeroacoustic Studies on Improved Tip Geometries For Passive Noise Signature Control in Low-Speed Axial Fan, ASME Journal of Vibration and Acoustics, 2009, 131(6).
- 6 Leggat, L.J. and Siddon, T.E., Experimental Study of Aeroacoustic Mechanism of Rotor-vortex Interactions, Journal of the Acoustical Society of America, 1978, 64, 1070–1077.
- 7 Laurendeau, E., Jordan, P., Delville, J. and Bonnet, J., Nearfield-farfield Correlations in Subsonic Jets: What Can They Tell Us?, 28th AIAA Aeroacoustics Conference, 2007, AIAA 2007-3614,
- 8 Miles, J.H., Procedure for Separating Noise Sources in Measurements of Turbofan Engine Core Noise, 2006, NASA/TM-2006214352.
- 9 Ribner, H., S., The generation of sound by turbulent jets, Adv. Appl. Mech. Vol. 8, 1964.
- 10 Jordan, P., and Gervais, Y., Subsonic jet aeroacoustics: associating experiment, modelling and simulation, Exps. Fluids Vol. 44, 2008.
- 11 Guitton, A., Jordan, P., Laurendeau, E. and Delville, J., Velocity Dependence of the Near Pressure Field of Subsonic Jets, 2007, AIAA-2007-3661.
- 12 Laurendeau, E., Jordan, P., Delville, J. and Bonnet, J., Nearfield-farfield Correlations in Subsonic Jets: What Can They Tell Us?, 28th AIAA Aeroacoustics Conference, 2007, AIAA 2007-3614.
- 13 Miles, J.H., Core Noise Diagnostics of Turbofan Engine Noise Using Correlation and Coherence Functions, 2009, AIAA 2009-1237.
- 14 Meecham, W. C.; Hurdle, P. M., Measurements of V/STOL aircraft noise mechanisms using pressure cross-correlation techniques in a reverberant wind tunnel, NASA report 19750008475, October 1974.

## DUAL HOT WIRE PROBES WITHOUT CROSSED PRONG-WIRE INTERFERENCE EFFECTS

**Argüelles Díaz, Katia María**

University of Oviedo, Fluid Dynamics Group  
Viesques, 33271, Gijón (Asturias), Spain  
[arguelleskatia@uniovi.es](mailto:arguelleskatia@uniovi.es)

**Fernández Oro, Jesús Manuel**

University of Oviedo, Fluid Dynamics Group  
Viesques, 33271, Gijón (Asturias), Spain  
[jesusfo@uniovi.es](mailto:jesusfo@uniovi.es)

**Galdo Vega, Mónica**

University of Oviedo, Fluid Dynamics Group  
Viesques, 33271, Gijón (Asturias), Spain  
[galdomonica@uniovi.es](mailto:galdomonica@uniovi.es)

**Blanco Marigorta, Eduardo**

University of Oviedo, Fluid Dynamics Group  
Viesques, 33271, Gijón (Asturias), Spain  
[eblanco@uniovi.es](mailto:eblanco@uniovi.es)

### ABSTRACT

Dual Hot Wire (DHW) probes are widely used for the measurement of two-dimensional velocity flows. Typically, the two wires of this kind of probes are placed either orthogonal or with a larger angle between them (i.e.  $120^\circ$ ) in order to increase the measurement angular range of the probe. For both orthogonal and non-orthogonal probes, certain angular ranges of the incident flow imply that the inner wire is found in the wake of one of the prongs of the outer wire, causing significant interference effects and a practical limitation of the measurement angular range of the probes. This angular range may be insufficient when trying to measure flows with sudden and notable changes of direction. This work proposes new designs of DHW probes without cross prong-wire interference effects for a significant angular interval. As a consequence, the measurement angular range of these enhanced probes is significantly extended, allowing a reliable determination of flows with important recirculation effects, such as those found in turbomachinery environments.

### INTRODUCTION

Thermal anemometry is a measuring technique that retrieves the flow velocity through heat transfer variations in a small sensor that it is electrically heated while exposed to a moving fluid. It is a reliable method, extremely accurate and with a high frequency response.

The most common thermal anemometer is the hot wire thermal device, which it is composed by a single or multiple tiny wires mounted on the probe tip. Tungsten is typically considered as the wire material due to its electrical resistance which is particularly suitable to be heated under regular values of intensity or voltage. Every wire is weld to a couple of prongs, usually of stainless steel, incrustated to the probe support, which are also employed as electrical contacts to heat the wire to a temperature in the range of 200-300 °C.

Wire's diameter must be extremely reduced so the signal-to-noise ratio at high frequencies may be amplified, the spatial resolution and frequency response increased, and the heat conduction losses and interferences with the flow minimized. Additionally, the diameter size must be large enough to increase the wire resistance and reduce aging effects provoked by particles transported by the flow. It is accepted that optimal wire diameters must be ranged between 2 to 5  $\mu\text{m}$ , resulting in extremely low Reynolds numbers which lead to consider the incident flow over the wires as symmetric and quasi-steady.

On the other hand, the wire's length must be also quite reduced to enlarge the probe's spatial resolution and minimize the aerodynamic load, while keeping a minimum size to control conduction losses and preserve a uniform temperature distribution. Optimal values are found when the length-to-diameter ratio is about 200 ([1]), although it must be kept in mind that the spatial resolution is also conditioned by the existing distance between the wires ([2]).

When the flow impinges on a hot wire, part of its heat energy is advected by the flow (forced convection [3]) due to the relative difference between the temperatures of the sensor (hot) and the fluid flow (cold). Because of the wire thermal inertia, its frequency response to flow velocity variations is damped, so the final measured changes in voltage turn to be lesser than the real ones. As a consequence, the wire self-response is excessively low and needs to be electronically compensated using, for instance, a constant temperature anemometer (CTA). This kind of equipment is an amplifier device that feeds back the wires to maintain its temperature independent of the variations in the flow velocity ([4]). Using this technique, the frequency limit can be significantly raised, up to 1000 times higher ([5], [6]).

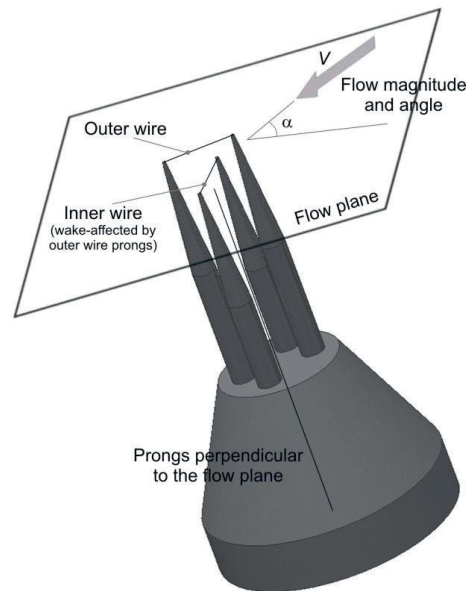
Every probe must be calibrated before it can be used to measure a particular flow. The calibration determines a relationship between the output voltage of every single wire and the magnitude and direction of the flow velocity vector. The electrical current in the wires provokes a heat release that must be transferred to the surrounding fluid to restore the thermodynamic equilibrium. If the flow velocity is modified, then the heat transfer changes so the wire temperature must evolve until a new equilibrium situation is reached. The heat transfer rate is directly related to the flow velocity impinging on the sensor. The feedback control of the CTA acts to modify the intensity of the electrical current so the wire temperature remains constant overtime. Consequently, the flow velocity can be determined through the measurement of the intensity or voltage modifications needed to keep the wire at constant temperature.

The most popular method to calibrate hot wire probes consists in keeping them steadily in a moving fluid. This calibration, known as “static calibration”, is completed in a two-step sequence. In the first one, the probe is located in the calibration facility, with both yaw and pitch angles set to zero, so one can obtain the relationship between the effective velocity in every wire and the CTA output voltage, including a correction factor for the temperature difference. Such relationship is given by the well-known King’s law ([7]) and represents the transfer function to be used when transforming voltage data into flow velocities. The second step is to complete the angular calibration, required for two and three-wire probes, to determine its directional sensitivity, that is, the relationship between the effective voltage and the components of the velocity field. Such relationship can be approximated via analytical functions, or can be obtained by means of a direct calibration procedure, which comprises the derivation of three coefficients to represent the flow angle and the change in velocity magnitude ([8]-[10]). For that purposes, the pitch angle is set to zero while the yaw angle is ranged from a minimum to a maximum value, obtaining the value of the calibration coefficients for every angular position. Thus, the resulting distributions are employed instead of the analytical functions, giving more precise results because all the geometrical effects and manufacturing imperfections are considered inherently.

Ref. [11] describes in detail a direct calibration procedure for a three-wire probe, including the uncertainty transmitted to the measurements; while references [12] and [13] provide an in-depth review of the different calibration methods available for hot wire probes.

Using dual hot wire (DHW) probes, we can obtain in-plane velocity components of the flow. The most common configuration is the so-called X-probe, consisting in a hot wire anemometer with two crossed wires, either in an orthogonal or a non-orthogonal disposition. If the wires are orthogonal to each other, the maximum angular range cannot exceed 90 deg, while higher angle between the wires (i.e. 120 deg) may provide and extended angular range ([14], [15]). Anyway, whatever the angle selected, if the X-probes are built with the supporting prongs in a perpendicular orientation respect to the measuring plane (figure 1a), there are certain angular positions where interference effects between the first wire and the prongs of the second wire arise. These effects are superimposed to the self interference of one wire with its own prongs, which is clearly less important than crossed interferences ([16]).

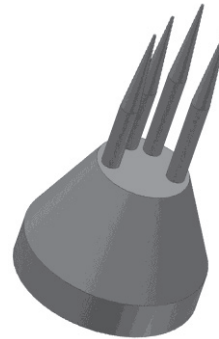
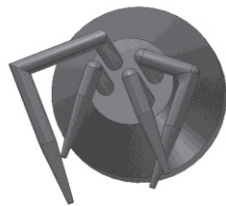
The crossed interference effect appears for certain yaw angles when one of the probe’s wires is found in the wake of a prong of the other wire. This effect, which has been already identified and studied by several authors ([17], [18]), can be called as “wake interference effect”, and implies that the wire affected by the prong wake (i.e. in a region with a notable velocity deficit) is measuring flow velocities significantly lower than those of the real flow. The direct consequence is a reduction in the measuring angular range of the probe. Furthermore, it is expected the appearance of an artificial induced turbulence which may limit the wire frequency response and affect negatively the accuracy of the velocity measurements. Concerning this point, it is possible that if the velocity to be measured differs significantly respect to the calibration conditions, this effect could lead to a considerable error in the final measurements.



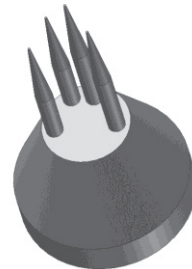
**Fig. 1a. Typical 120 deg, non-orthogonal X-type DHW probe with prong-wire interference.**



**Fig. 1b. 120 deg, Z-type DHW probe without wake interference effects.**



**Fig. 1c. 120 deg, V-type DHW probe without wake interference effects.**



To overcome these problems, the probes can be designed with the supporting prongs placed in a plane parallel to the one of the incident flow. Hence, the wake interference effect vanishes, remaining exclusively the interference effect of the wires with their own prongs, and increasing the angular range accordingly. A wide catalog of commercial designs for DHW probes with or without wake interference effects can be found in the technical literature. As an example, figure 2 shows some of these designs from leading manufacturers of hot wire probes like DANTEC and TSI.

For the present investigation dealing with interference effects, two DHW probes have been built, denoted as Z-type and V-type, with the wire prongs placed in a parallel plane to the flow pattern (figure 1b and 1c respectively). These probes have been calibrated in an aerodynamic calibration facility and compared with the results obtained for a classic 120 deg X-type probe. It is found that both Z-type and V-type calibrations are similar (for probes with identical geometrical characteristics in terms of wires diameter, wires lengths and overall probe size), presenting accurate calibration coefficients without severe interference irregularities.

Following sections present the conclusions obtained in terms of accuracy gained with free-wake interference probes. Both angular ranges and influences of the Reynolds number, as well as turbulence levels, are explored in order to provide a comprehensive overview of the interference impact over those parameters for developers and users of hot-wire measuring devices.

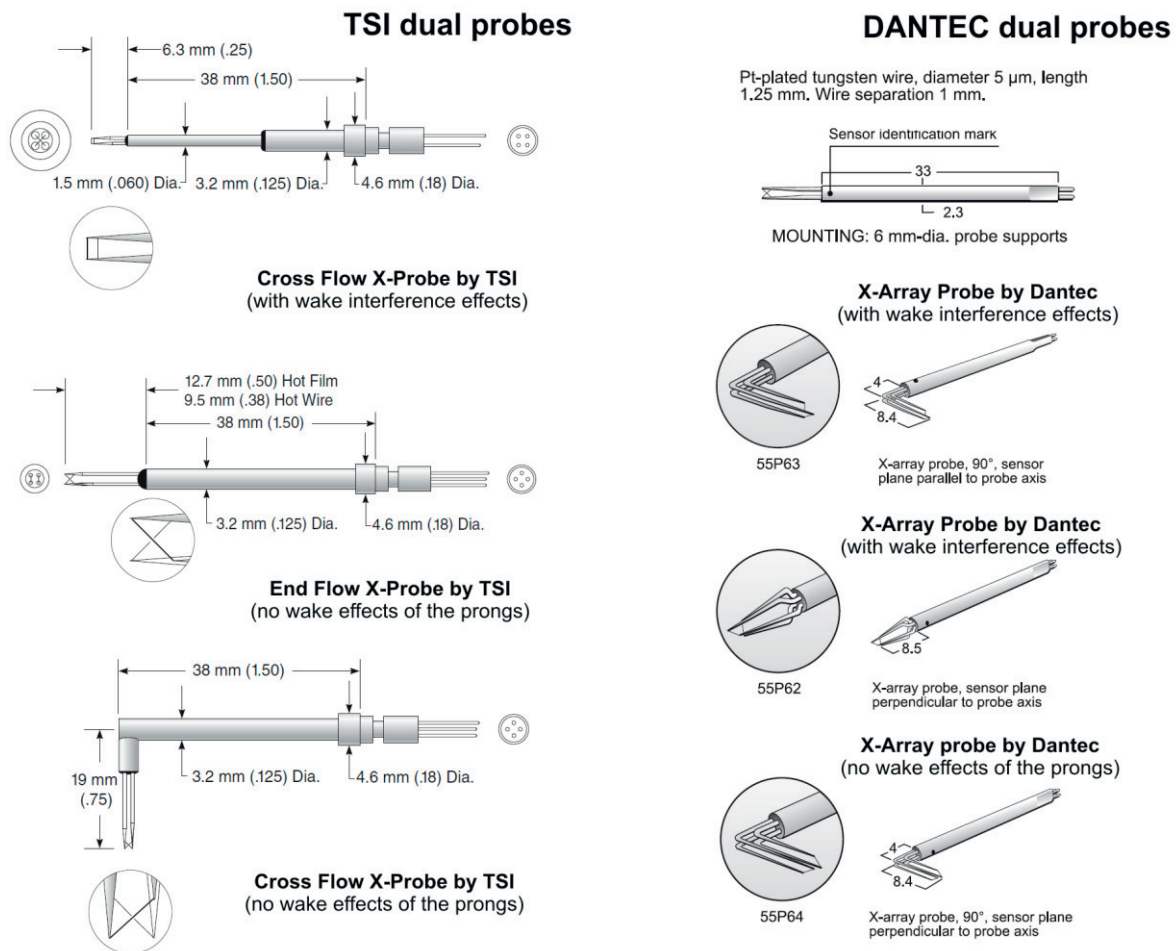


Fig. 2. Commercial designs of DHW anemometers by leading manufacturers TSI and Dantec.

## PROBES GEOMETRY AND EXPERIMENTAL SETUP

Three different probe geometries have been considered for the present investigation. The original design is a classical X-type probe with the supporting prongs perpendicular to the flow plane. This means that the inner wire suffers wake interferences coming from the prongs of the outer wire. The remaining probes, designated as Z-type and V-type probes, are improved versions developed to eliminate interference effects, with the prongs placed in a plane parallel to the flow. All the probes were in-home manufactured, with tungsten wires of 5  $\mu\text{m}$  and 1 mm long, in a 120 deg crossed arrangement. The wire prongs are stainless steel needles with 0.4 mm diameter. Figure 1 presents a schematic view of the geometrical characteristics of the probes.

Both Z-type and V-type probes should present analogous calibration coefficients and similar measurements results. For practical reasons, we have employed intensively the V-type probe for the experimental characterization of flow fields due to its higher compactness and simplicity to be manufactured or repaired.

The calibration facility is an opened nozzle with a circular discharge section of 1.5 cm dia. This nozzle supplies a uniform incident flow over the hot-wire probes when mounted in the test section. The flow rate can be regulated with a throttling valve placed on the compressed air supply, so the velocity can be ranged from 0 to 70 m/s approximately.

The probes are typically placed 20 mm downstream of the nozzle discharge, aligned with the jet axis. For a fixed angular position, the velocity is progressively increased from zero to the maximum velocity, obtaining the King's law for every wire. One single wire can only measure the normal velocity component, which is usually

known as effective velocity. When probes with more than one unique wire are employed, the proximity between the different wires and the supporting prongs provokes that effective velocities of the wires differ from the case when every wire is isolated. This is traduced in the need for an additional angular calibration, changing the incidence angle of the calibration flow for a fixed velocity magnitude. This angular repositioning is carried out by means of a two-axis mechanical gear, driven by a couple of step-by-step motors controlled via PC. For two-wire anemometers, only one axis rotation is needed (yaw angle), while three-wire probes require both yaw and pitch angles relocations. Finally, the effective velocity of every wire is monitored as a function of the flow angle and the angular calibration coefficients of the probe are determined to complete the procedure.

During the calibration, the probe wires are connected to a four channel, TSI IFA-100, CTA anemometer. The measured data is acquired with a NIDAQ PCI device, 16-bit A/D converter, which are following stored in a PC using MATLAB routines and specific libraries. For every measuring point, up to  $10^4$  samples, at a low-frequency response of 100 Hz, are recorded. The surrounding environmental conditions of the calibration facility are controlled and the temperature variations within the calibration room are also registered. Additionally, calibration measurements have been also conducted modifying the inlet turbulence of the incident flow (with a perturbing grid mounted on the nozzle) to analyze the impact of this additional parameter on the wake interference effect.

## RESULTS AND DISCUSSION

A direct calibration procedure ([11]) has been applied with these three DHW probes, ad hoc manufactured in the Fluid Mechanics Lab of the School of Engineering at the University of Oviedo, to confirm the characteristics explained above. For every probe, the King's law has been experimentally determined, and the angular calibration for a reference velocity has been completed. Finally, an angular calibration coefficient has been defined from the output voltage of the wires as follows:

$$\text{Acf} = U_{e1} - U_{e2} \quad (1)$$

where  $U_{e1}$  y  $U_{e2}$  correspond to the effective velocities of both external (wire 1) and internal (wire 2) wires.

### Calibration distributions of the X-type probe (with wake interference effects)

Figure 3 shows angular distributions of the output signals (in voltage) in the wires, obtained during calibration. Though not shown here, an angular discretization of 2.5 deg has been chosen for the entire data sets, which has been found accurate enough to determine the angular variations.

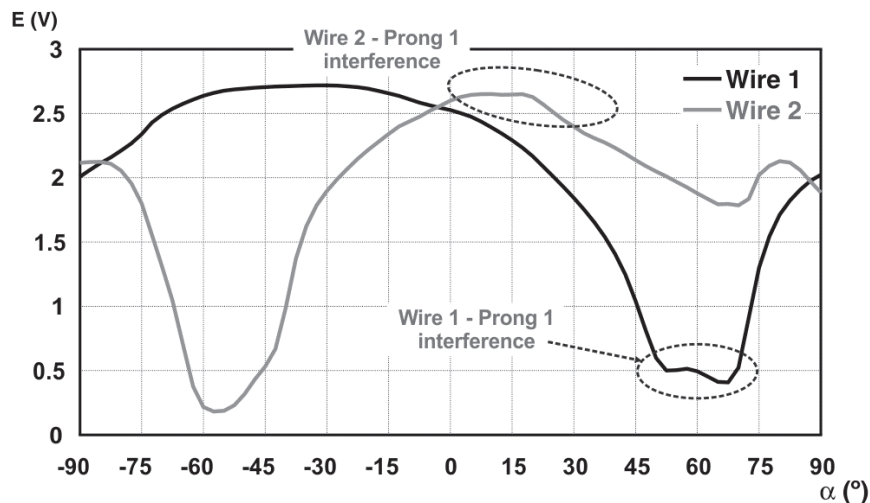


Fig. 3: Angular distributions of wires output voltage for a 120 deg DHW X-probe.



Interference effects between the wires and their own prongs or between the wires and the wake fluid coming from adjacent prongs are manifested as oscillations in the output signals of the probe. Such perturbations may lead to the appearance of two different detrimental effects. In the one hand, they can induce the arising of double points in the distribution of the angular calibration, which implies the impossibility for a unique determination of the angle and a practical reduction in the operative angular range of the probe. On the other hand, if the flow angle to be measured is placed within the angular interval of the calibration affected by interference effects, the measurement accuracy drops severely and consequently the error in the determination of the velocity and flow angle increases.

In the case of the present X-type probe, the wire interference with their own prongs appears when the incident flow angle is high. In particular, wire 1 suffers self-interference between 50 and 70 deg (see annotations in fig. 3); while wake interferences are observed earlier exclusively in the second wire (the inner wire) for small yaw angles. In this case this effect modifies the probe performance for the angular interval between 0 and 30 deg, being maximum at 20 deg approximately.

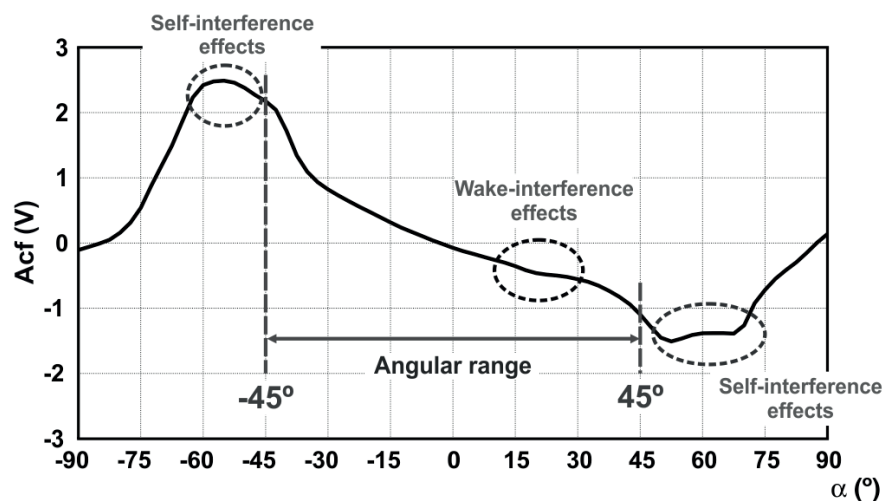


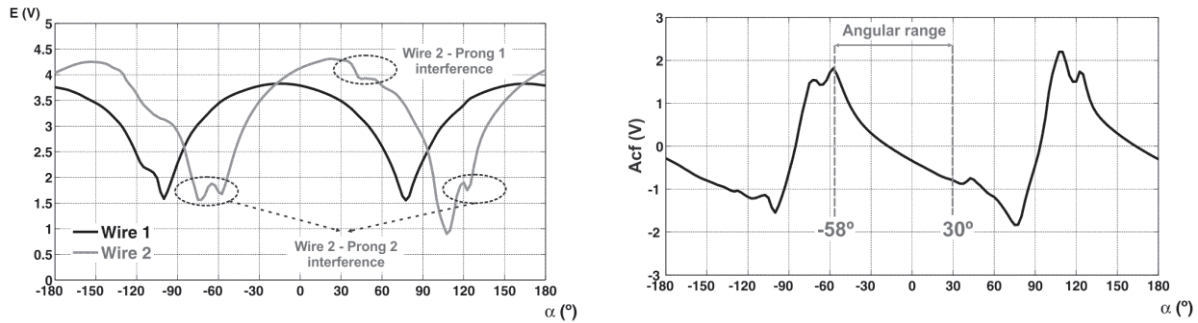
Fig. 4: Angular coefficient for a 120 deg DHW X-probe.

Figure 4 shows the angular coefficient of the X-type probe, in terms of output voltage, obtained using equation 1. The overall angular range of the probe turns to be 90 deg, being operative for angular measurements between  $-45$  and  $45$  deg. Note that in this case, the limits of the angular range are established by the self-interference effects of the wires with their own prongs. The wake-interference effect is manifested as a perturbation in the angular coefficient at  $20$  deg, which will surely lead to a lower precision of the flow measurements for flow angles in that zone. Moreover, it is expected that irregularity in the angular calibration could lead in practice to a further reduction of the angular range to the  $(-45, 0)$  deg interval. Depending on the application, this angular range can be not sufficient to describe flow angle variations overtime.

The appearance of wake interference effects for positive flow angles close to  $0$  deg is due to the equal length of the wires in the X-type design. Hence, when misalignment of the yaw angle towards positive values comes across, the inner wire is automatically placed in the wake of a prong of the outer wire. This characteristic can be retarded if the probe wires are built with different lengths, so the outer wire is made larger than the inner one. Figure 5 shows how the wake effect is effectively displaced towards higher yaw angles with non-equal wires.

Precisely, such a figure represents the wires output signals and the corresponding angular calibration for X-type probes with wires of different length. Note that self-interference of a wire with its own prong is more pronounced for the second wire than for the first one, because it results to be shorter due to the  $120$  deg X-type design. These interference effects are manifested at  $-58$  deg and  $110$  deg approximately for wire 2, and only at  $-110$  deg for wire 1. As expected, the wake interference effect is only experienced in the inner wire, as a consequence of the deficit velocity induced by the outer wire prongs for yaw angles ranged between  $30$  and  $65$  deg.

The wake interference effect is now fixed as the limitation for positive values of the angular range, so the operative zone of the angular calibration (88 deg) is established between -58 and 30 deg. Due to the wires asymmetry, the wake interference is now more severe (see the worse response marked with a dashed oval in the figure) and turns to be a real limit for the angular calibration; but on the contrary, it has been possible to extend the practical angular range from 45 to 88 deg.



**Fig. 5: Angular distributions of wires output voltage and angular calibration coefficient for a 120 deg DHW X-probe with different length wires.**

In order to study how wake interference impact have a detrimental effect on the measurements accuracy, several tests with the classic X-type probe of equal length wires have been conducted. For that purpose, the starting point has been the determination of the angular calibration for an averaged incident flow velocity of 40 m/s, already reported in figures 3 and 4.

After calibration, the tests facility is employed for measurements acquisition. In particular, measurements have been performed for several flow velocities (differing from the calibration conditions) ranging from 20 to 60 m/s at intervals of 10 m/s. Additionally, for every Reynolds number, we have gone through a wide number of angular positions including free-wake positions and also locations susceptible of wake interference. The incidence flow angle has been ranged from -40 to 40 deg in a 10 deg interval between consecutive positions.

### Error in the determination of the velocity magnitude with the X-type probe

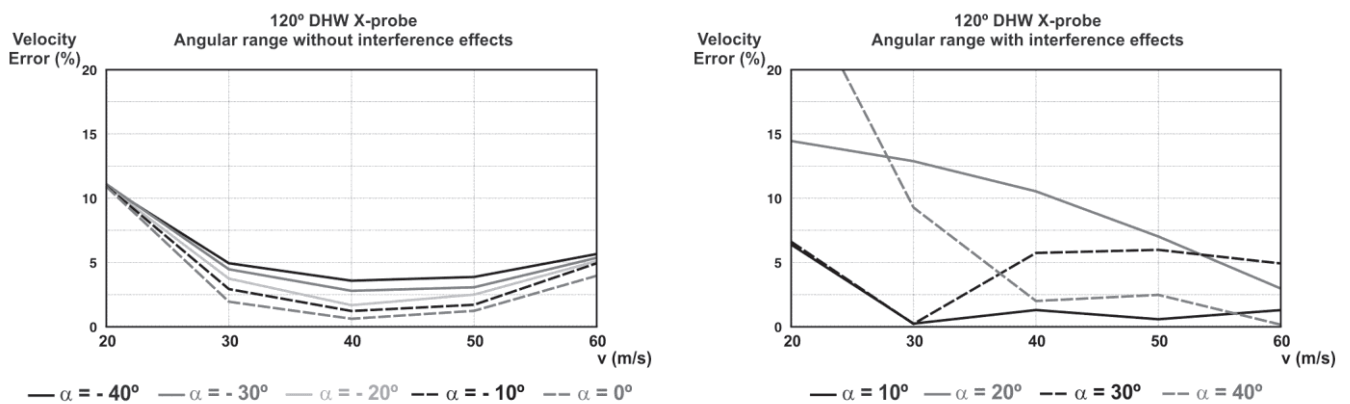
Figure 6 represents the error associated to flow velocity retrieval when the 40 m/s calibration is employed to reduce data coming from measurements taken at other flow velocities. The error is expressed in a percentage basis according to the following formula:

$$\text{Velocity error} = 100 \times \frac{|v_{\text{real}} - v_{\text{measurement}}|}{v_{\text{real}}} \quad (2)$$

where  $v_{\text{measurement}}$  is the velocity registered with the hot-wire probe and  $v_{\text{real}}$  is the real velocity magnitude measured by means of a pressure transducer connected to the NIDAQ acquiring card in the nozzle discharge.

The results have been split in two different figures for clarity. Figure 6a shows the error distributions corresponding to flow angles for -40 to 0 deg out of the wake-affected region (in this case, negative yaw angles). It is observed how the errors in velocity are increased as the incident flow angles are closer to the limits of the angular calibration. For 40 m/s incident flow, the error is minimum at 0 deg (around 1%) and maximum at extreme -40 deg (around 4%).

As expected, the errors are also intensified as the incident flow velocity is progressively separated from calibration conditions. All the angular positions present their relative minimum at 40 m/s, revealing the overall coherency of the present data set. Also, it is observed a slight trend to obtain higher error for lower velocities than for higher velocities respect to the calibration reference. In particular, all the flow angles present their maximum errors around a significant 12%, at 20 m/s.



**Fig. 6. Error associated to the determination of the velocity magnitude at different operating conditions.**  
 a) zone without wake interferences; b) zone with wake interferences.

Figure 6b reveals analogous results now for flow angles between 10 and 40 deg within the wake-affected region. First of all, the error evolution is not as clear as in previous figure 6a. The minimum values are no longer obtained at 40 m/s, but it can be reasonably accepted a similar trend than before with higher errors for lower velocities. Additionally, the error is generally the largest for 20 deg angular positions, where the wake interference effect is maximum.

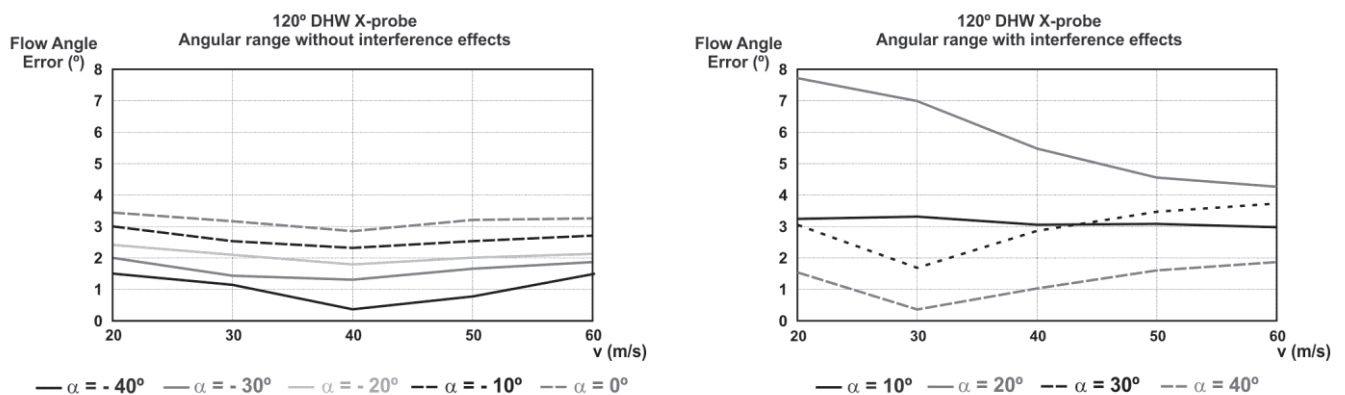
The conclusion from results shown in figure 6b is that when an incident flow angle is measured with the probe working under wake-interference conditions, the error involved in the determination of the velocity magnitude is excessive to validate that intermediate angular interval, so the operative range has to be limited to the free-wake regions as previously warned.

#### Error in the determination of the flow angle with the X-type probe

Following, similar considerations for the flow angle determination are presented below. Now, the error in the angle retrieval when measuring for Reynolds numbers out of the calibration conditions is calculated according to:

$$\text{Flow Angle Error} = |\alpha_{\text{real}} - \alpha_{\text{measurement}}| \quad (3)$$

where  $\alpha_{\text{measurement}}$  represents the flow angle retrieved with the X-type probe and  $\alpha_{\text{real}}$  corresponds to real misalignment of the probe, respect to the incident jet, determined from the repositioning system of the calibration facility (step-by-step motor) and confirmed with a goniometer.



**Fig. 7. Error associated to the determination of the flow angle at different operating conditions.**  
 a) zone without wake interferences; b) zone with wake interferences.

In a similar fashion, the results are shown in two complementary figures (7a and 7b). Figure 7a includes the results from free-wake angular zones. Now, the general trend is opposite to the one analyzed in figure 6a, so the error associated to the flow angle retrieval turns to be higher for yaw angles close to 0 deg, being progressively reduced as we move towards the angular limits of the calibration (-40 deg). Typical errors are found to be of 3 deg at  $\alpha=0^\circ$  and 1 deg at  $\alpha=-40^\circ$ . On the contrary, concerning discrepancies in the flow velocity respect to calibration conditions, relative minima appear once again at 40 m/s, with similar deviation at both high and low velocities (note that error distributions as a function of the yaw angle seem to be quite constant for the whole of velocities tested).

To conclude this section, figure 7b completes the analysis with results from the wake-affected region. As in previous figure 6b, no clear trend can be derived from the obtained distributions. When the yaw angle is set to 10 deg (black solid line), the error is almost constant (around 3 deg), whatever incident flow velocity considered. In the case of  $\alpha=30^\circ$  and  $\alpha=40^\circ$ , the error in angle is minimum at 30 m/s and maximum at 60 m/s. Alternatively, for the angle with the maximum wake interference ( $\alpha=20^\circ$ ), the error is progressively increased as the flow velocity slows down with the maximum error reaching 7.5 deg. Also note that for this particular angle, the errors are notably higher than any other angle considered.

All these considerations confirm, also for the flow angle retrieval, that X-type probes should not be operated when the incident flow angle induces wake interference effects on the wires.

### Wake interference effect on the determination of turbulence intensities with the X-type probe

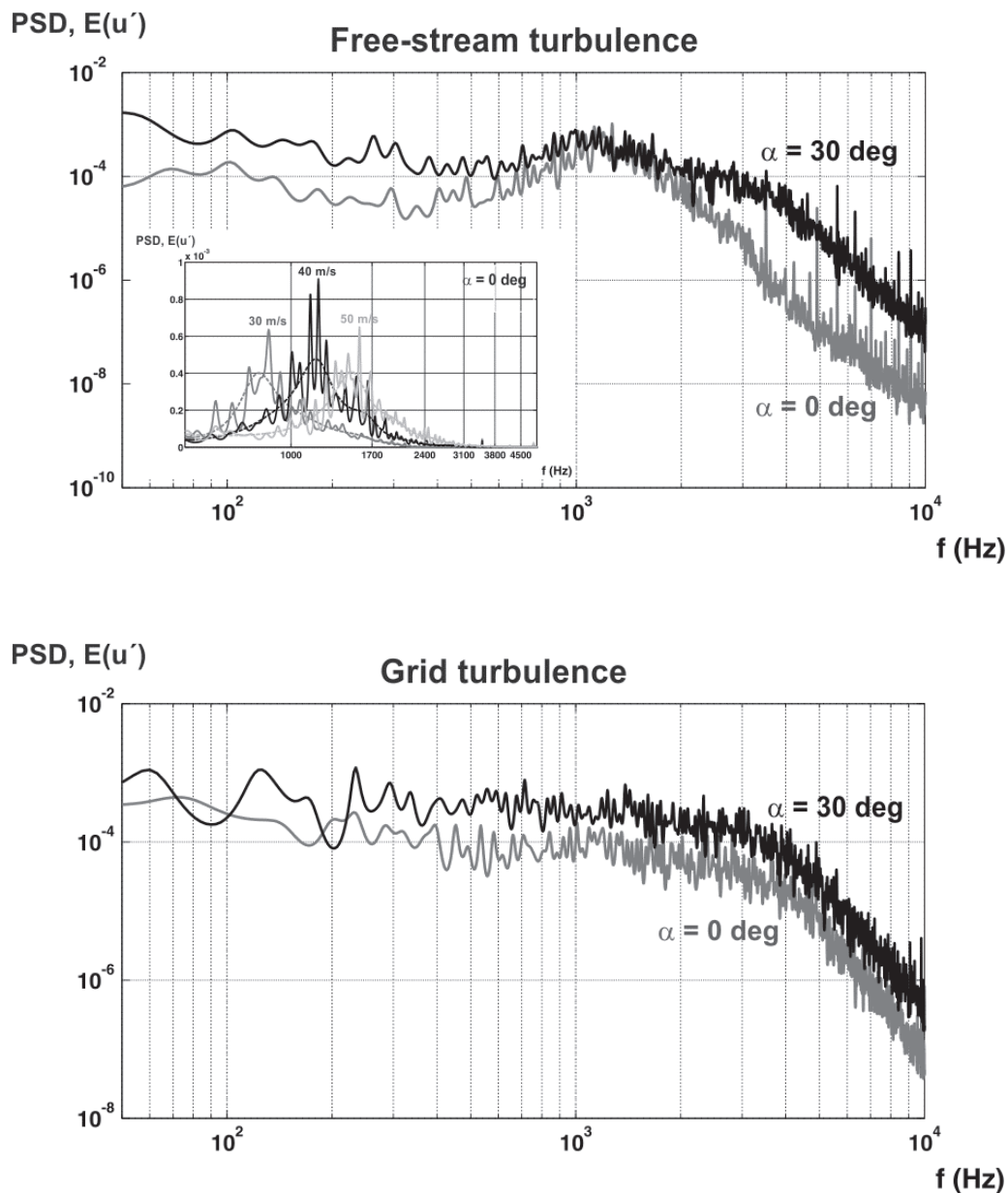
Additionally, the impact of measuring with the X-type probe in the wake-affected region of the calibration has been analyzed in terms of turbulence prediction. Notice that when wake interference effects are perturbing the inner wire, there must be superimposed an additional, fictitious turbulence provoked by the vortex shedding of the outer prongs, that may lead to an overestimation in the quantification of real flow turbulence levels.

In order to study such hypothesis, additional tests at full high-frequency response of the X-type probe have been conducted. In particular, every measuring point has been sampled at 30 kHz (close to the maximum frequency response of the probe), recording 10000 instantaneous values during 0.3 seconds. Two different datasets have been considered for the analysis. Firstly, measuring in an incident flow with identical levels of inlet turbulence to those experienced during calibration (denoted as free-stream turbulence). Secondly, placing the probe in a flow with a slightly higher inlet turbulence (denoted as grid turbulence), which has been generated with a perturbing grid at the nozzle discharge of the facility. Measurements for impinging velocities of 30, 40 and 50 m/s have been performed in both settings, ranging the yaw angle of the probe from -40 to 40 deg in a 10 deg interval. The angular calibration at 40 m/s has been systematically applied for data reduction of all the measured points.

Figure 8 shows power spectra of the time series corresponding for measurements obtained at 0 yaw angle (no interference with outer prongs) and 30 deg yaw angle (wake affected region) for an incident velocity of 40 m/s. Since they have been derived with the 40 m/s calibration, they are free of inaccuracies related to Reynolds number deviations. Upper plot includes results from free-stream turbulence condition, while lower plot reproduces similar results for grid turbulence database. Both figures represent in the y-axis, in a logarithmic scale, the power spectrum density (PSD) of the axial velocity fluctuation from the instantaneous traces. These spectra have been post-processed with a smoothed periodogram based on a parametric algorithm (autoregressive 800th order) in order to reduce spurious scatter. Additionally, a high-pass filter of 300 Hz has been used for signal conditioning to eliminate low-frequency oscillations of the supplying compressed air.

Both situations (free-stream and grid turbulence) reveal that the energetic contents corresponding to wake-affected regions (30 deg) are higher for all the turbulent scales (throughout the whole frequency range) than out-of-wake locations (0 deg), clearly indicating that the probe is measuring an overestimated turbulence intensity at 30 deg yaw angle. It is also remarkable that for those spectra corresponding to free-stream conditions (figure 8a), there is a peak of turbulent kinetic energy around 1 kHz for all the angular ranges tested. This phenomenon is reproduced for all the different velocities analyzed, as it can be seen in the small plot of the lower left corner in the figure. Note that this frequency signature is shifted along the x-axis as the mean incident velocity is increased. The linear displacement observed indicates that this phenomenon must be related to vortex shedding in the nozzle discharge because when the grid is installed, this effect is vanished. In particular, considering a

typical Strouhal number around 0.2, it has been estimated a 7 mm length scale as representative for vortex shedding, in reasonable accordance with the real blunt thickness of the nozzle endwall at the calibration facility.



**Fig. 8: Power spectrum density (PSD) of the axial velocity fluctuation (incident flow of 40 m/s).**  
 a) Free-stream turbulence conditions; b) Grid turbulence conditions.

Figure 9 shows the angular distribution of turbulence levels (in percentage) for the incident flow angle of 40 m/s. This intensity has been computed from the instantaneous fluctuation of the axial velocity. Note that these results are again free of errors from Reynolds number deviations. Whatever configuration considered, free-wake regions (from -40 to 0 deg) present quite uniform, low values, ranging between 1.5 and 2%. Conversely, from 0 deg on, due to the effect of interference, there is a significant increase in the turbulence intensity, reaching up to 3.5% for extreme angles of 40 deg. It is also remarkable the slight difference between turbulence levels for both datasets at free-wake regions, as a direct consequence of the extremely thin grid employed in these measurements.

These results confirm the overestimation in the measurement of the turbulence level when the probe is operated under wake-interference effects. Considering that hot-wire anemometry technique is widely used to characterize turbulent variables in real flows, it is quite reasonable to affirm that wake-affected regions are not valid ranges for measurements requiring high-frequency response.

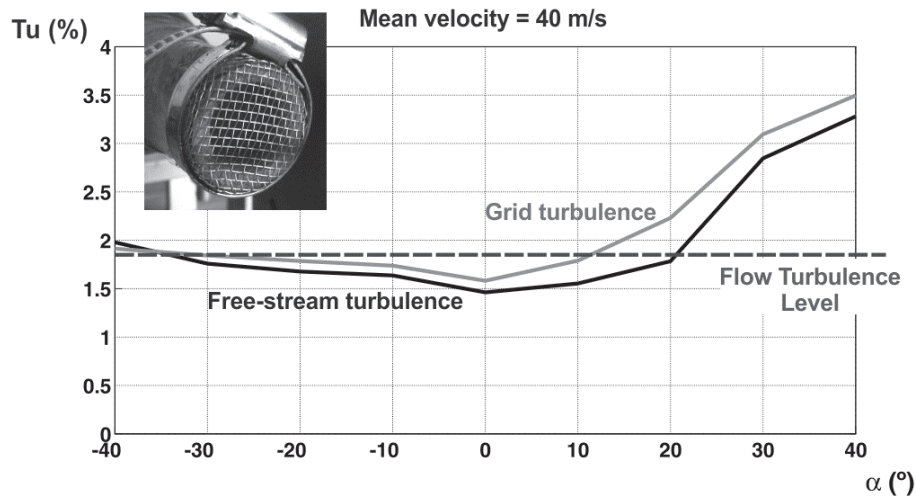


Fig. 9: Turbulence intensity as a function of the angular incidence (baseline conditions at 40 m/s).

Finally, figure 10 shows the effect of Reynolds number deviations from calibration conditions over the turbulence intensities measured from the instantaneous axial velocity. The shaded regions represent the angular distribution of the dispersion of the results, when reducing data with out-of-velocity calibrations, which somehow corresponds to the maximum associated errors. Dark grey band identifies the dispersion in the turbulence level estimation for the grid turbulence setting, while light grey band represents dispersion associated to free-stream conditions. Obviously, higher intensity levels throughout the whole angular range are obtained for the perturbed conditions of the grid turbulence setting. Dashed lines are turbulence intensity levels for the 50 m/s inlet flow, while solid lines represent those levels for the 30 m/s case. The overall trend is that when the mean velocity is increased, the turbulence level seems to be progressively reduced. For no interference zones, the evolution of the turbulence intensity is similar for all the considered velocities, with maximum discrepancies of a 0.5%. On the contrary, for wake-affected regions between 0 and 40 deg, changes in the intensity trends seem to be more pronounced with velocity variations, with typical errors in the order of 1%. Hence, it is not recommended the use of data obtained under wake interferences to characterize turbulence levels.

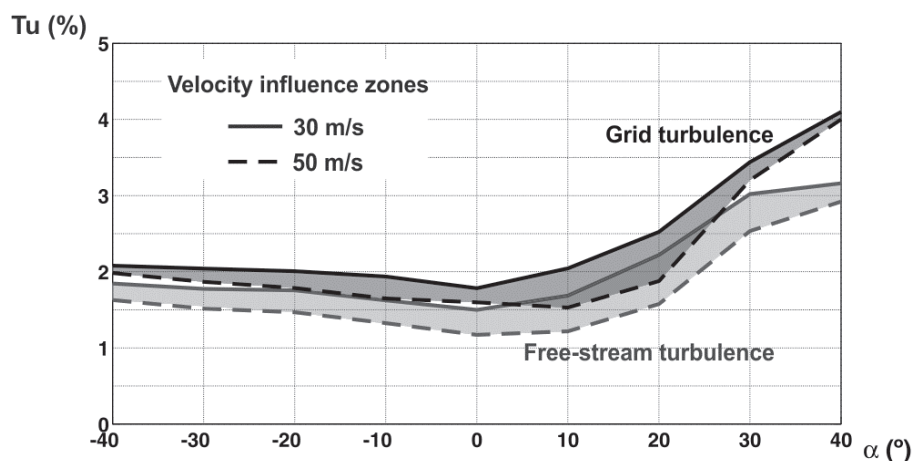
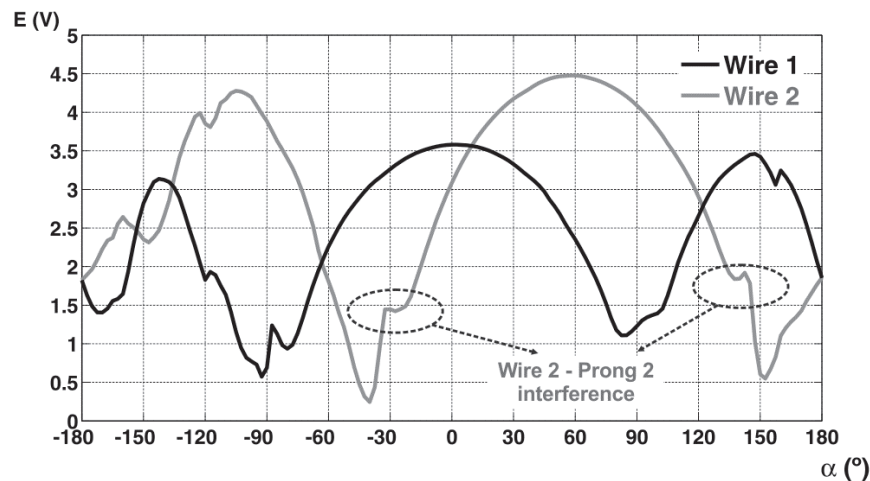


Fig. 10: Evolution of the turbulence intensity as a function of the probe yaw angle and deviations in the operative Reynolds number.

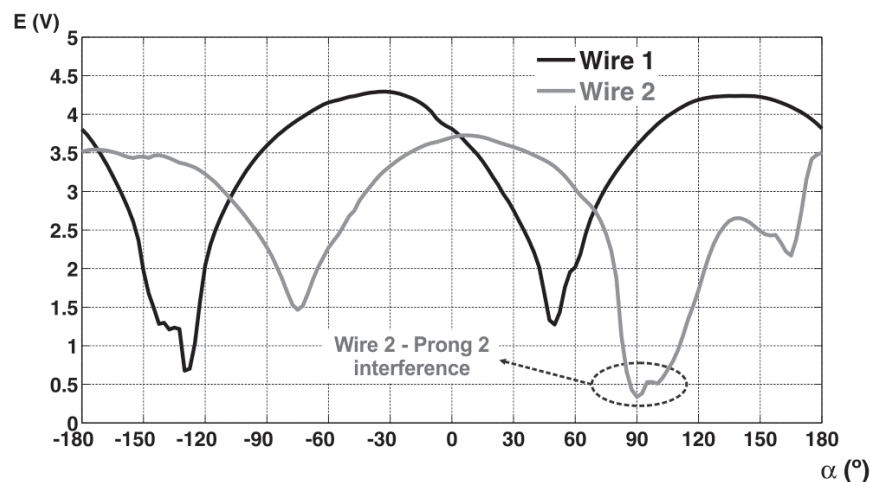
**Calibration distributions of the Z-type and V-type probes (no wake effects of the prongs)**

Following, figure 11 shows the angular distributions of the wire's output signals corresponding to the Z-type probe. As expected, there are no wake interference effects throughout the whole angular span. Only self-interactions with their own prongs arise, being more evident for both wires than in the case of the X-type probe. Such effects are observed at -75 and 80 deg for the first wire and around -22 and 135 deg for the second wire. Also, angular distributions for both wires are notably different between them, especially if they are compared with the results for the X-type probe.



**Fig. 11: Angular distributions of wires output voltage for a DHW Z-probe.**

Additionally, figure 12 shows analogous results to figure 11, but now in the case of the V-type probe. Note that wake interference effects are missing again. The angular distribution for the outer wire is smoother than previous one for the Z-type, presenting less pronounced effects of self-interference which are now set off at 90 deg for wire 2 and -130 and 60 deg for wire 1.



**Fig. 12: Angular distributions of wires output voltage for a DHW V-probe.**

Figure 13 represents the angular coefficients of both Z and V-type probes obtained after using equation 1. The angular range for the Z-type probe turns to be 102 deg, while the V-type is extended to 125 deg. In both cases, the significant increment in the operative angular range is a direct consequence of the absence of wake interference effects over the inner wire of the probes, as discussed in the introduction. For these free-wake

interference probes, the limitation in the angular range comes from the self-interaction of the wires with their own prongs. Therefore, it is reasonable to find a reduced angular range for the Z-type probe respect to the V-type because their self-interactions are more evident. The angular coefficient of the Z-type probe presents a higher slope than the one from the V-type, so it is presumable that the uncertainties and errors in the flow determination will be slightly higher in the case of the V-type probe.

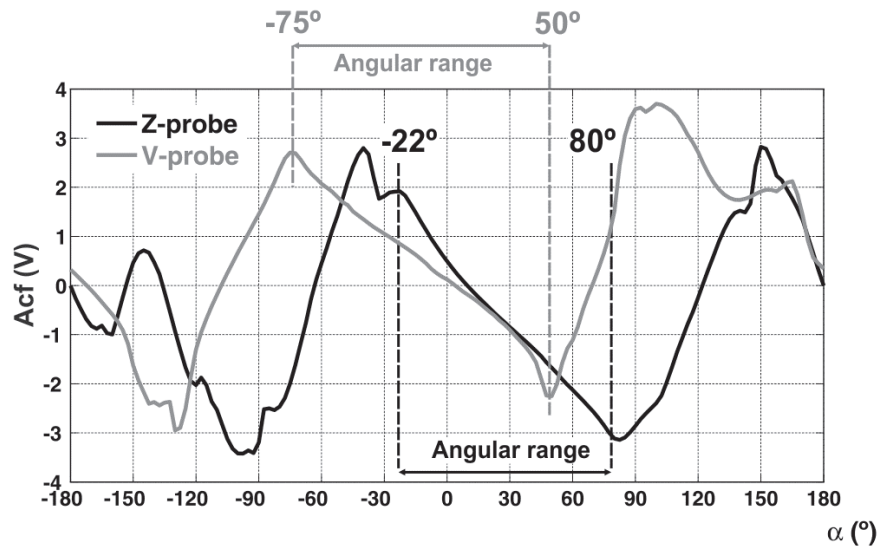


Fig. 13: Comparison of angular calibration coefficients for DHW Z- and V-probes.

Nevertheless, it can be assumed as a first approach that the angular distributions of the wires response are quite similar, so it is expected that both Z and V-type probes will provide identical results with comparable levels of error. The major difference would be placed in the operative angular range, 23 deg higher for the V-type. This fact, and the higher compactness and simplicity of V-type designs, makes them preferable to be manufactured and employed for measuring real flows.

## CONCLUSIONS

In the present investigation, three different DHW probes have been manufactured and calibrated to analyze the impact of wake interference effects coming from adjacent prongs in the wire response of simple X-type probes. In particular, Z-type and V-type designs have been employed as free-wake interferences probes to quantify this detrimental phenomenon.

It has been confirmed that the existence of cross wire-prong interferences has a notable impact on the angular calibration of the probe and, therefore, in the accuracy of the measurements performed within real flows. For that purpose, the influence of these interferences on the errors associated to the retrieval of the flow angle and velocity magnitude when measuring at Reynolds numbers that differ notably from calibration conditions has been carried out.

Additionally, it has been explored the relevance of this effect over the determination of turbulent variables in DHW probes, which is really convenient since their high-frequency response is the strongest characteristic of these hot-wire anemometers.

Finally, it has been confirmed that these probe designs, manufactured without cross wire-prong effects, may present operative angular ranges up to 35 deg higher than classical X-type probes. This enhancement can be especially desirable for the characterization of unsteady flows with large angular variations (i.e. jet-wake patterns in turbomachinery environments). Besides, with these free-wake effects probes, the measurement errors associated to inaccuracies in the data reduction technique performed with calibration out of real flow conditions will be reduced.



## REFERENCES

- [1] Turan O and Azad RS. 1989. Effect of hot-wire probe defects on a new method of evaluating turbulence dissipation *J. Phys. E: Sci. Instrum*, **24**, 254–61.
- [2] Cameron JD, Morris SC, Bailey S and Smith A. 2010. Effects of hot-wire length on the measurement of turbulent spectra in anisotropic flows. *Meas. Sci. Technol*, **21**, 105407 (10 pp).
- [3] Sanitjai S and Goldstein RJ. 2004. Forced convection heat transfer from a circular cylinder in crossflow to air and liquids. *International Journal of Heat and Mass Transfer*, **47**, 4795-4805.
- [4] Jorgensen FE. 1996. The computer-controlled constant-temperature anemometer. Aspects of set-up, probe calibration, data acquisition and data conversion. *Meas. Sci. Technol*, **7**, 1378-1387.
- [5] Freymuth P. 1977. Frequency response and electronic testing for constant-temperature hot-wire anemometers. *Journal of Physics E*, **10**, 705-710.
- [6] Freymuth P. 1997. Interpretations in the control theory of thermal anemometers. *Meas. Sci. Technol*, **8**, 174-177.
- [7] King LV. 1914. On the convection of heat from small cylinders in a stream of fluid: determination of the convection constants of small platinum wires with applications to hot-wire anemometry. *Philosophical Transactions of the Royal Society of London*, **214**, 373-432.
- [8] Brunn HH, Khan MA, Al-Kayiem HH and Fardad AA. 1988. Velocity calibration relationships for hot-wire anemometry. *J. Phys. E: Sci. Instrum*, **21**, 225-232.
- [9] Brunn HH. 1971. Interpretation of a hot-wire signal using a universal calibration law. *J. Phys. E: Sci. Instrum*, **4**, 225-232.
- [10] Brunn HH and Tropea C. 1985. The calibration of inclined hot-wire probes. *J. Phys. E: Sci. Instrum*, **18**, 405-413.
- [11] Blanco-Marigorta E, Ballesteros-Tajadura R and Santolaria C. 1998. Angular range and uncertainty analysis of non-orthogonal crossed hot wire probes. *Journal of Fluids Engineering*, **120**, 90-94.
- [12] Stainback PC and Nagabushana KA. 1997. Review of hot-wire anemometry techniques and the range of their applicability for various flows. *Electronic Journal of Fluids Engineering*, **119**.
- [13] Lekakis I. 1996. Calibration and signal interpretation for single and multiple hot-wire/hot-film probes. *Meas. Sci. Technol*, **7**, 1313-1333.
- [14] Brunn HH, Nabhani N, Al-Kayiem HH, Fardad AA, Khan MA and Hogarth E. 1990. Calibration and analysis of X hot-wire probe signals. *Meas. Sci. Technol*, **1**, 782-785.
- [15] Brunn HH, Nabhani N, Fardad AA and Al-Kayiem HH. 1990. Velocity component measurements by X hot-wire anemometry. *Meas. Sci. Technol*, **1**, 1314-1321.
- [16] Comte-Bellot G, Strohl A and Alcaraz E. 1971. On aerodynamic disturbances caused by single hot-wire probes. *J. Appl. Mech*, **38**, 767-774.
- [17] Strohl A and Comte-Bellot G. 1973. Aerodynamic effects due to configuration of X-wire anemometers. *J. Appl. Mech*, **40**, 661-666.
- [18] Adrian RJ, Johnson RE, Jones BG, Merati P and Tung ATC. 1984. Aerodynamic disturbances of hot-wire probes and directional sensitivity. *J. Phys. E: Sci. Instrum*, **17**, 62-71.

## RESONANCES INFLUENCE IN RECESSED-MOUNTED TRANSDUCERS USED FOR UNSTEADY PRESSURE MEASUREMENTS

**Antonio Sanz Luengo**

Royal Institute of Technology  
Chair of Heat and Power Technology  
S-100 44 Stockholm, Sweden  
[ansl@kth.se](mailto:ansl@kth.se)

**Damian M. Vogt**

Royal Institute of Technology  
Chair of Heat and Power Technology  
S-100 44 Stockholm, Sweden  
[damian.vogt@energy.kth.se](mailto:damian.vogt@energy.kth.se)

**Torsten H. Fransson**

Royal Institute of Technology  
Chair of Heat and Power Technology  
S-100 44 Stockholm, Sweden  
[torsten.fransson@energy.kth.se](mailto:torsten.fransson@energy.kth.se)

### ABSTRACT

The present paper analyzes the influence of resonances in recessed mounted transducers for measuring unsteady pressures in turbomachinery related test facilities. Due to the difficulties of the unsteady measurements in this kind of setups, recessed mounted technique allows increasing the resolution of measurement points, transducer exchangeability, fair operation conditions, and cost reduction with respect to other procedures. However the intrinsic nature of this procedure requires a duct which connects the control volume to be measured and the transducer, producing damping and phase lagging of the signal due to the pipe. In consequence a dynamic calibration is required for being able to evaluate these effects through a transfer function. This dynamic calibration can show up the presence of resonances due to the duct properties. These resonances are studied in this paper for determining its influence on the measuring capabilities, as well as an overview of the different tuning capabilities at the interest frequency bands.

### NOMENCLATURE

$f$	frequency
$D$	dynamic calibration damping
$P$	pressure
$\hat{P}$	unsteady pressure (complex)
$t$	time
$V$	voltage
$\delta$	infinitesimal increment
$\Delta$	associated uncertainty
$\varphi$	signal phase
$\emptyset$	dynamic calibration phase lag

### Subscripts and Superscripts

$n$	specific frequency
$pos$	related to the positioning error
$ref$	related to the reference transducer
$stc$	related to the stochastic error
$std$	steady
$sys$	related to the systematic error
$td$	related to the recessed mounted transducer

## Abbreviations

FFT                      fast fourier transformation

## INTRODUCTION

In turbomachinery aeromechanics, the correct measurement techniques and measurement uncertainties are of crucial importance for the correct understanding of unsteady aerodynamic interactions. Among these phenomena the aerolastic interactions show up as the most challenging from the experimental point of view due to the complex working conditions. Flutter is one of this phenomena, it is produced by a structural, fluid dynamic interaction which generates a self-excited and self-sustained instability. This can lead to high vibration amplitudes, producing ultimately, machine failure due to high cycle fatigue. The instability is generated due to the unsteady pressures applied on the blade surface, interacting with the blade movement. This fact makes this unsteady pressure the fundamental objective of the measurements.

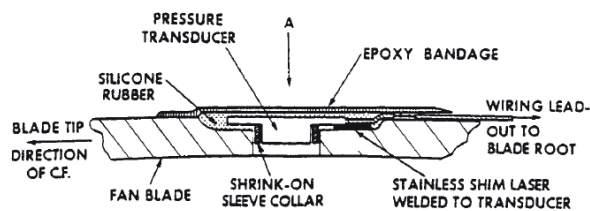


Figure 1 Embedded Transducer assembly

The interaction of the structural and fluid dynamics implies that the instrumentation should not interfere both in the fluid and in the blade structure. Normally the instrumentation is mounted inside the blade modifying the structural performance, in addition the evolution of turbomachines lead to more slender blades with high 3D shapes. This fact complicates the instrumentation and shows up the needing off less invasive procedures.

Furthermore flutter is a phenomenon extremely sensible to unsteady pressures, in consequence the measurements require highly time-accuracy which implies fast response transducers and high sensitivity due to the low pressures that can initiate the self-excitation.

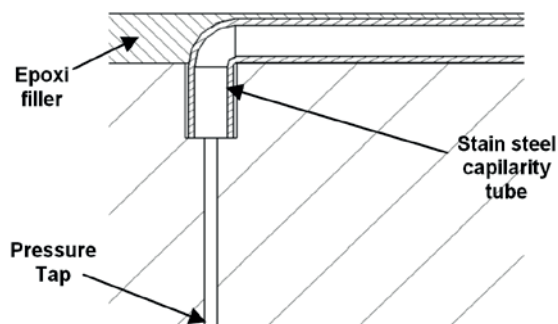


Figure 2 Recessed mounted pressure tap

Traditionally these measurements have been done using embedded miniature transducers (Figure 1), which provides a direct pressure measurement. This kind of assembly provides very good results while properly calibrated for the working conditions but with high limitations regarding cost, physical embedding, measuring resolution, inertial effects, thermic effects, and other operating problems produced by the structure-transducer interaction.

As an alternative recessed-mounted transducers consist on the assembly of the transducer outside the test object, linking it with the flow domain using capillarity tubes between 50mm and 150mm (Figure 2).

This procedure presents some interesting advantages with respect to the traditional one. It is cheaper because of the inter exchangeability of the transducers, and in consequence de reduction on the transducer number. It allows detailed measurement resolution, the instrumentation can be highly noninvasive but depending on the number of measuring points. On the other hand, the duct properties produce signal attenuation and a phase lagging of the signal, which implies a bigger postprocessing of the data.

For being able to obtain an accurate measurement it is necessary to calibrate dynamically the complete setup. The dynamic calibration analyzes the behavior of the system regarding amplitude and phase of the complex pressure at different frequencies. This procedure is done using an in-house calibrating procedure which compares the response obtained by a pressure pulse train on a reference transducer (direct measurement), and on the recessed-mounted one. With this information is possible to generate a transfer function that corrects the response of the transducer with reality.

The present study shows up the presence of system resonances and analyzes the possible consequences along the processing system regarding uncertainty.

## CALIBRATION SET UP

The calibration system is composed of 3 different parts:

- Pressure pulse generator
- Calibration probe (miniature reference cavity)
- High-speed data acquisition system.

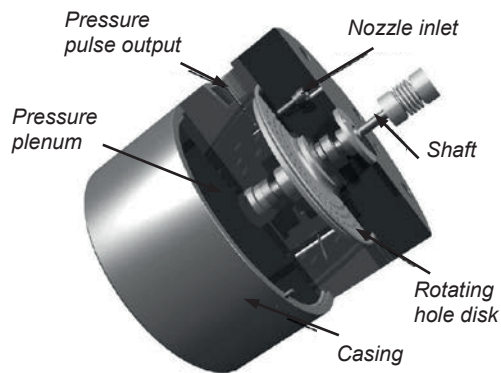


Figure 3 Pressure pulse generator set up

The pressure pulse generator is siren type, consisting on a miniaturized nozzle that generates a fluid jet (air) which collides with a three row hole perforated disk. This disk is driven by a speed controlled DC motor so setting a determined rotational speed of the disk will interfere the pressure jet a number of holes times the rotational frequency. The presence of 3 hole rows on the rotating disk produces the presence of different harmonics into the pressure signal but with dominating influence of the first harmonic which will be the one used for the dynamic calibration. The pressure pulse is driven outside through an output tube collinear with the nozzle that connects with the calibration probe. The disk is isolated in a pressure chamber connected to a pressure plenum. Modifying the plenum pressure the disk gets pressurized and in consequence output mean pressure intensity level can be set. The relation between the nozzle inlet pressure and the plenum pressure will define the intensity of the unsteady pulse generated.

The reference cavity consist on a cylindrical control volume (1.8mm  $\varnothing$  x 3mm h) with a reference fast response piezoelectric pressure transducer (Kulite XCQ-062, 1.6bar abs) on one extreme of the volume, the pressure tap to calibrate is set on the other extreme of the cavity being the cavity sealed with an O-ring. The pressure pulse is transferred form the pressure pulse generator with a capillarity tube. The pulse enters through a side hole in the mid-section of the cavity. For being able to ensure the flow channel symmetry, in the opposite position, an outlet tube has been introduced, connected to a long capillarity tube which ensures no reflections. In this way the reference cavity is completely symmetric defined, and the wave symmetry is guarantee.

The pressure taps to calibrate are connected with capillarity tubes to the recessed mounted transducers (Kulite XCQ-062, 1.6bar abs). These transducers are statically calibrated using a Druck DPI-603(100Pa accuracy) to minimize uncertainties. The high-speed data acquisition is done with the system Kayser-Threde KT8000, which also provides a stabilized sensor excitation (10VDC). The system provides 32 channels with programmable amplifiers and 14bit A/D conversion for a maximum sampling rate of 200kHz.

The system featured 32 channels with programmable amplifiers, 14bit A/D conversion for each channel and a maximum sampling rate for all 32 channels simultaneously of 200kHz. Each channel could be programmed individually such as to set gain and a low-pass filter with variable cut-off frequency. The present tests were performed with a gain of 10, no low-pass filtering and at a sampling rate of 20kHz.

The standard calibration procedure consists of 3 steps:

- Reference cavity positioning and centering
- Data acquisition (KT8000)
- Postprocessing. Frequency spectrum, signal attenuation, phases lagging, transfer function acquisition.

## TEST OBJECT (Baseline configuration)

The blade used in this experiment is a low pressure turbine with a high lift profile. The test tap was situated in the suction side at 90% of the span. The instrumentation has been done using a stainless-steel tube of 0.5mm of internal diameter embedded on a groove that communicates the tap with the root of the blade. The pressure tap of 0.4mm diameter is perpendicular to the surface, the connection with the stainless-steel pipe can be done in many different ways but the most interesting for our case due to the simplicity and the leak-free robustness is the procedure shown in

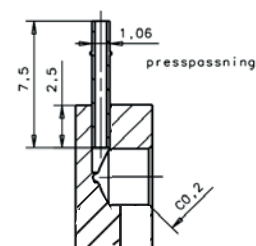


Figure 4 Transducer housing

Figure 2. This procedure uses an L-bended pipe that smoothly conduits the pressure signals. The length of the pipe from tap to root is 150mm.

The blade is connected to the transducers housing through a vinyl pipe (50mm), a fast connector and another vinyl pipe (25mm). The first vinyl pipe length and shape will be studied later as a possible way of modifying the response of the overall system response.

The fast response transducers are accommodated on a brass housing (Figure 4). This housing consists on a signal intake that communicates the cavity, where the transducer membrane lies, with the tap pipe line.

## RESONANCE INFLUENCE, UNCERTAINTY ASSESSMENT

For analyzing the influence of the resonance influence on the system it has been necessary to set up an uncertainty model of the system. This model, is divided principally between the errors due to calibration and the raw measurement own errors.

### RAW Measurement Uncertainty

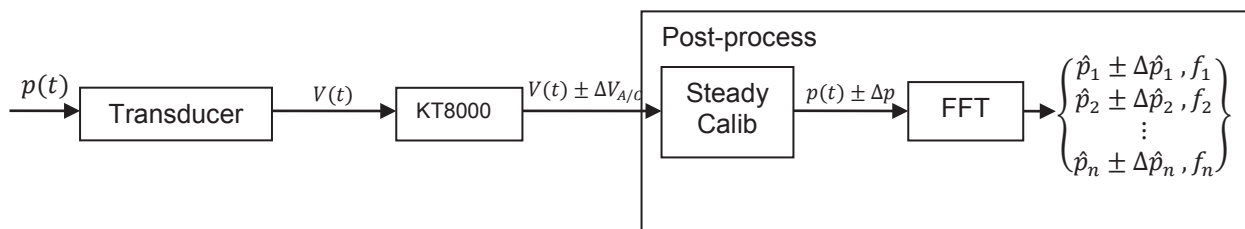


Figure 5 Pressure measurement diagram. Uncertainty propagation

As shown in Figure 5, the fast response transducer transforms the pressure into a voltage in the time domain the error introduced in the measurement by the transducer is not considered stochastic, which implies that the possible offset remains constant for all the measurement along the time and in conclusion can be neglected while analyzing the unsteady part. Due to the amplification of the signal and the A/D converter, the high-speed acquisition system (KT8000) introduces a new error in the measurement. This error depends on the gain set. For the present paper all the analysis has been done with the calibration settings determined in Table 1.

Table 1

Unsteady Intrinsic System error		
A/D converter(100mV, gain=10)	$\pm \Delta V_{A/D}$	$\pm 6.1 \mu V$
TD sensibility(Pa)	$\pm \Delta p_{TD}$	$\pm 10 Pa$

For translating the electric signal into pressure, the voltage is multiplied by the steady calibration parameter. The pressure error is obtained applying the “root-sum-square error linear approximation” [x]

$$p = k_{td \text{ std } calib} \cdot V \quad \text{Eq. 1}$$

$$\Delta p = \sqrt{\left(\frac{\partial p}{\partial k} * \delta k\right)^2 + \left(\frac{\partial p}{\partial V} * \delta V\right)^2} + \Delta p_{TD} = \sqrt{(V * \Delta k)^2 + (k * \Delta V)^2} + \Delta p_{TD} \quad \text{Eq. 2}$$

Due to the nature of the steady calibration the deviation transformation will produce an offset in the calibration curve not modifying its slope, as the objective is the analysis of the unsteady behavior, the  $k_{td \text{ std } calib}$  error can be depreciate, being the error reduced to the equation x.

$$\Delta p = k_{td \text{ std } calib} * \Delta V + \Delta p_{TD} = 1698.7882 \frac{kPa}{V} \cdot \pm 6.1 \mu V + \pm 10 Pa = \pm 20.3626 Pa \quad \text{Eq. 3}$$

The pressure signal is transformed into the frequency domain using a FFT (Fast Fourier Transformation). For avoiding signal truncation problems, a preliminary FFT has been applied on the original signal with the

frequency obtained it has been defined the period of the signal, and the signal has been delimited by a multiple of the period. At this point is very important to keep in mind that the error associated with the pressure measurement not only depends on its absolute value but on the distribution pattern along the signal. This means that for a sinusoidal signal with a frequency  $f$  the most prejudicial error pattern corresponds to an error signal with the same frequency. While translating to the frequency domain the signal error will be decomposed into a modulus error and phase error.

For calculating the error progression along the FFT the time-domain pressure has been perturbed with an error signal with the error amplitude and the main harmonics of the original signal. These 2 elements can be expressed as phasors, Figure 6

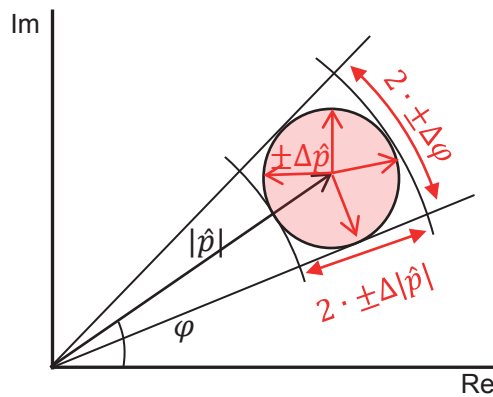


Figure 6 Complex pressure uncertainty propagation scheme

The uncertainty subjected to an unsteady pressure measurement using the described set up, reveals that the modulus uncertainty remains constant and only depends on the transducer characteristics. The phase uncertainty depends both on the intrinsic characteristics of the transducer but also on the pressure measured as shown in Figure 6. This implies that the bigger the measurement amplitude the smaller the phase error.

Calibration Uncertainty

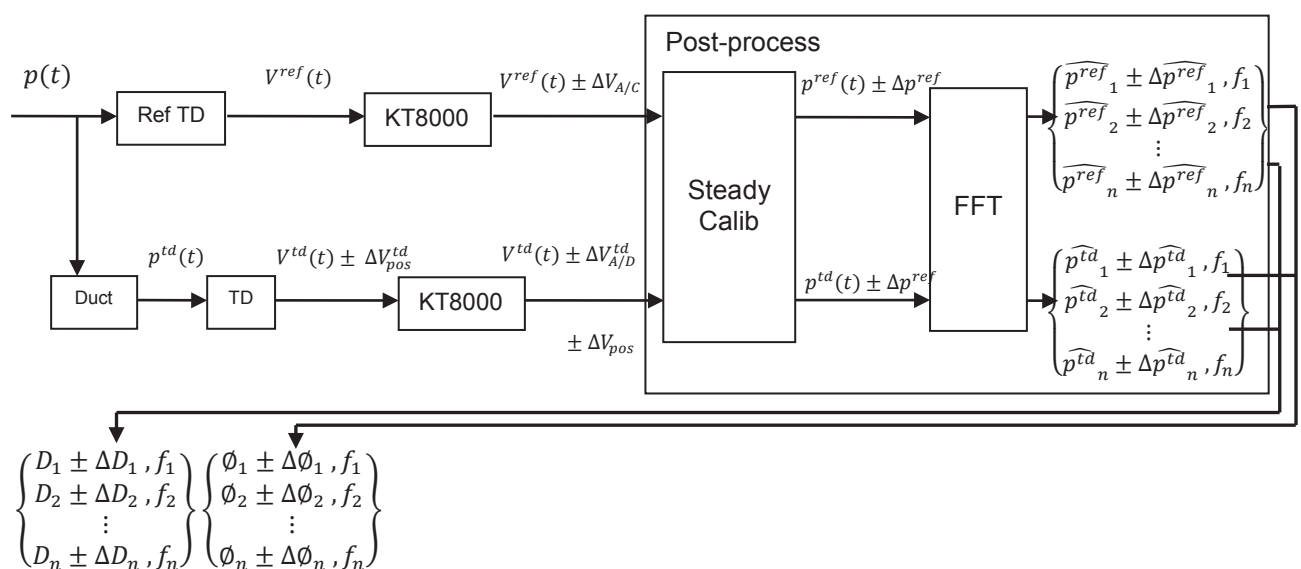


Figure 7 Calibration process diagram. Uncertainty propagation

The calibration procedure can be modeled as shown in Figure 7. The pressure signal  $p(t)$  generated by the pressure pulse generator reach the reference cavity where is captured by the reference transducer. The same pulse is communicated to the pressure tap, and depending on the position of this tap with respect to the reference cavity a positioning uncertainty is introduced. The pulse travel along the duct to the transducer connected to the piping modifying in the way its characteristics. Both transducers transform the pressure into an analogic electric signal within the transducer sensibility. In the high speed acquisition module the analog signal is amplified and transformed into a digital signal, this introduces another uncertainty source.

Both signals are post-processed and correct with the steady calibration and transformed into the frequency domain, where the damping coefficient and phase lag values are determined for each frequency, allowing to estimate the reference signal with the one measured in the tap transducer.

The calibration procedure uncertainty analysis has been done from 2 different perspectives, from the theoretical point of view using 2 raw pressure measurement uncertainty progression lines that end with the determination of the signal damping and lagging. Form the statistical point of view for determining the influences of other parameters on the overall uncertainty, as for example the error in the probe positioning or the random error inherent to the system. There are other possible sources of error that have not been included as the sampling frequency error, this will be studied in future experiments.

The error of the vectors  $D$  and  $\phi$  can be decomposed into a systematic error of the procedure itself, an stochastic error of unknown source, and a positioning error depending on the position of the reference cavity with respect to the tap .

$$\Delta D = \Delta D_{sys} + \Delta D_{stxc} + \Delta D_{pos} \quad \text{Eq.4}$$

For determining these errors different methods have been used:

-The calibration systematic error, assumed as the error inherent to the system accuracy, has been determined through the “root-sum-square error linear approximation”.

$$D_n = \frac{|p_n^{td}|}{|p_n^{ref}|} \quad \text{Eq.5}$$

$$\Delta D_n = \sqrt{\left(\frac{\partial D_n}{\partial |p_n^{td}|} * \delta |p_n^{td}| \right)^2 + \left(\frac{\partial D_n}{\partial |p_n^{ref}|} * \delta |p_n^{ref}| \right)^2} = \sqrt{\left(\frac{1}{|p_n^{ref}|} * \Delta |p_n^{td}| \right)^2 + \left(\frac{|p_n^{td}|}{|p_n^{ref}|^2} * \Delta |p_n^{ref}| \right)^2} \quad \text{Eq.6}$$

$$\phi_n = \varphi_n^{ref} - \varphi_n^{td} \quad \text{Eq.7}$$

$$\Delta \phi_n = \sqrt{\left(\frac{\partial \phi_n}{\partial \varphi_n^{ref}} * \delta \varphi_n^{ref} \right)^2 + \left(\frac{\partial \phi_n}{\partial \varphi_n^{td}} * \delta \varphi_n^{td} \right)^2} = \sqrt{\Delta \varphi_n^{ref}^2 + \Delta \varphi_n^{td}^2} \quad \text{Eq.8}$$

-The positioning error has been determined, experimentally. The probe has been positioned in 6 different positions 2 centered and 4 eccentric and equally spaced around the reference cavity. As the set-up is identical for each position, it can be assumed that the stochastic error and the systematic as identical, so the positioning error can be estimated as the standard deviation of the experiments set.

-The sampling error has been determined with the same procedure as the one used for the positioning error. 6 different sampling frequencies have been used for estimating this error. As indicated before the truncation of the signal has been prevented, for avoiding possible disturbances. (Figure 8 blue dots)

-The Stochastic error has been determined with the following criteria. 20 different measurements have been done, with exactly the same set up, same probe position, same sampling frequency, and in the same

measurement campaign. Under this conditions it is assumed that the standard deviation of the experiment test correspond to the stochastic error. (Figure 8 red dots).

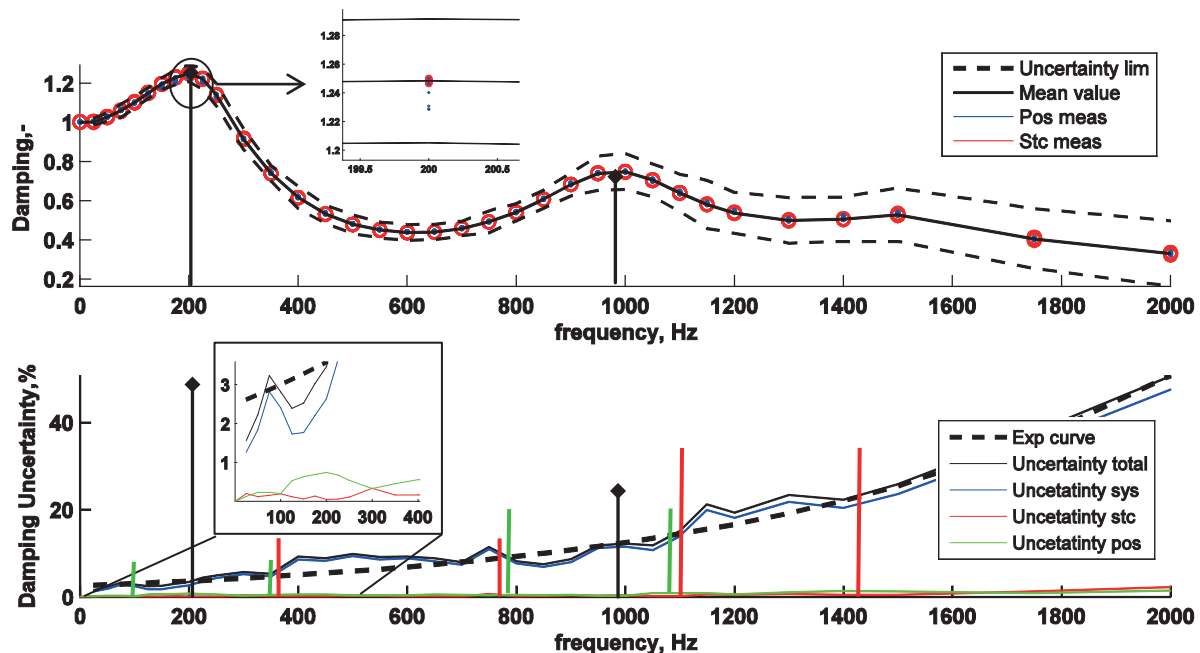


Figure 8 Damping and Damping uncertainty. Calibration diagram

With the data obtained in the experiments, the transducer-duct, damping and phase lag characteristic curves have been obtained, up to a frequency of 2000Hz that is very far away of the interest band that goes from 0 to 300Hz. The reason is to obtain a wide perspective of the behavior along the frequency band.

In the studied band 3 resonances have appeared being the first harmonic directly in the area of interest (Figure 8 up). The calculated uncertainty lies down a 6% for the band of interest. It is also observed that the dispersion of the data apparently is very small which indicates a priori that the determination of the damping is very stable. The uncertainty of the measurement has been introduced with the dashed lines in Figure 8 up.

Analyzing the influence of the each source of error it is evident that the bigger uncertainty source is the theoretical systematic error with respect to the positioning and random experimental uncertainties. Analyzing the overall uncertainty of the damping, an exponential uncertainty increase with the frequency (dashed line Figure 8 down) has been assumed. On this curve it can be appreciated that the overall uncertainty it is not spoiled due to the resonance peaks. Focusing on the 200Hz and 800Hz surroundings the uncertainty is increased with respect to the exponential while decreasing the resonance effect (400-800Hz). The uncertainty decreases again while starting the second resonance and quickly increased while its effect is minor (1100-1400Hz).

The influence of the resonance onto the damping is a high nonlinear process. If the resonance presence tends to reduce from a general point of view the uncertainty, it affects in a different way to the different error sources. In Figure 8 can be observed how the system uncertainty tends to be reduced with the resonances. Apparently a bigger damping should affect negatively the uncertainty according to the Eq.6, but the percentual uncertainty shows a bigger amplification of the signal than the amplification of the uncertainty. The systematic uncertainty is subjected to the data acquisition system, and directly dependent on the reference and transducer modulus of the unsteady pressure and its associated error. Therefore for transducer and reference constant associated errors, the uncertainty tends to be reduced while increasing the unsteady pressures.

On another hand the positioning errors are increased around the resonances. The origin of this effect lies in the fact that the geometrical properties of the reference cavity are slightly modified. This necessarily affects the tuning of the system varying the position of the resonance. This induces an uncertainty increase around these points.

In the end the random uncertainty does not seem to be significantly influenced by the resonances.



For the phase lag between signals a similar behavior is observed. But it is interesting to remark that the presence of a resonance increase the phase lag slope.

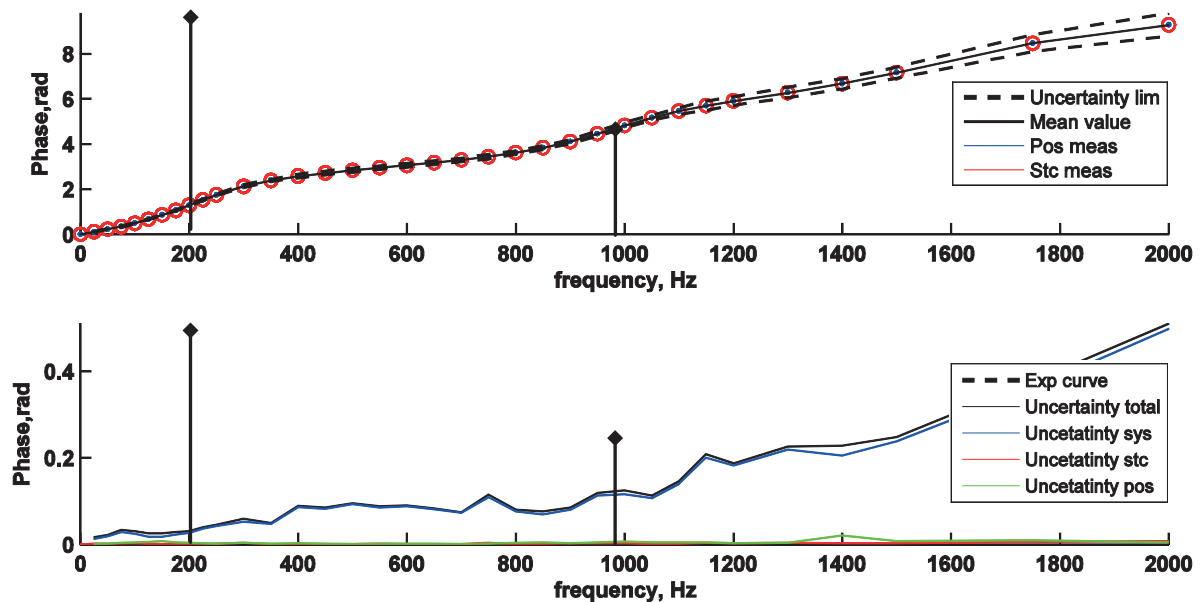


Figure 9 Phase lag and Phase lag uncertainty. Calibration diagram

For the set up used the main uncertainty source corresponds to the systematic one due to the range of measurements which defines the gain of the amplifier, the transducers... etc. The importance of the different uncertainty sources will change depending on the set up.

The pressure measured by the transducer is decomposed in its main frequencies modulus and phase. This pressure measurement is corrected with the damping and phase lag (equations XX and XX) and recomposed back for obtaining the estimation of the real unsteady pressure in the pressure tap inlet. The damping and phase lag deviation will be defined by the contribution of each uncertainty source taken into account, systematic, stochastic and position.

The uncertainty of the measurement is ultimately determined by the “root-sum-square error linear approximation” of the correction procedure shown below (Eq.9 and Eq.11).

$$|\hat{p}_n| = \frac{|p_n^{td}|}{D_n} \quad \text{Eq.9}$$

$$\Delta|\hat{p}_n| = \sqrt{\left(\frac{\partial|\hat{p}_n|}{\partial|p_n^{td}|} * \delta|p_n^{td}|\right)^2 + \left(\frac{\partial|\hat{p}_n|}{\partial D_n} * \delta D_n\right)^2} = \sqrt{\left(\frac{1}{D_n} * \Delta|p_n^{td}|\right)^2 + \left(\frac{|p_n^{td}|}{D_n^2} * \Delta D_n\right)^2} \quad \text{Eq.10}$$

$$\varphi_n = \varphi_n^{td} + \phi_n \quad \text{Eq.11}$$

$$\Delta\varphi_n = \sqrt{\left(\frac{\partial\varphi_n}{\partial\varphi_n^{td}} * \delta\varphi_n^{td}\right)^2 + \left(\frac{\partial\varphi_n}{\partial\phi_n} * \delta\phi_n\right)^2} = \sqrt{\Delta\varphi_n^{td^2} + \Delta\phi_n^2} \quad \text{Eq.12}$$

The result of this procedure is shown in Figure10. The overall uncertainty of the unsteady pressure modulus has an increase in general maintaining the shape of the damping uncertainty trend. Analyzing how each source

of uncertainty contributes to the overall uncertainty,  $\Delta|\widehat{p}_n^{td}|$  seems to be the dominating factor which induces the uncertainty increase.

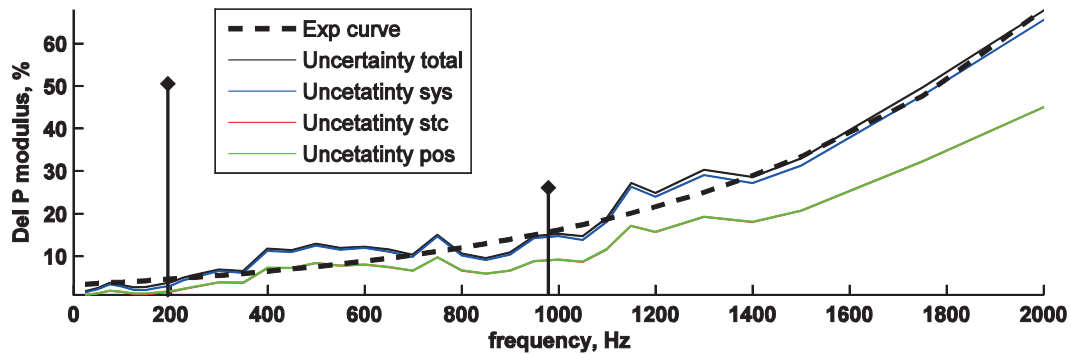


Figure 10 Unsteady pressure uncertainty graph

On the unsteady pressure phase uncertainty point of view as happened before with the modulus keeps the same trend of the phase lag but with an increase in the slope. The mayor contribution to the uncertainty is the one introduced by the transducer  $\varphi_n^{td}$ .

### FLUTTER TEST SIGNAL RECONSTRUCTION, AND PROCEDURE IMPLICATIONS

At this point is interesting to have a clear perspective of the usage of this procedure. This system is used for measuring the unsteady pressures on the blade surface due to a controlled oscillation. With this set up a controlled flutter is modeled in the influence coefficient domain, measuring the unsteady pressures produced by the oscillation of one blade on itself and on the adjacent blades. From this point of view the analysis of the measurement uncertainty becomes complex due to the fact that for each frequency there is a modulus and phase measurement uncertainty. While reconstructing the wave depending on the number of harmonics used the uncertainty will change. The more harmonics involved the bigger the uncertainty associated with the estimated unsteady pressure.

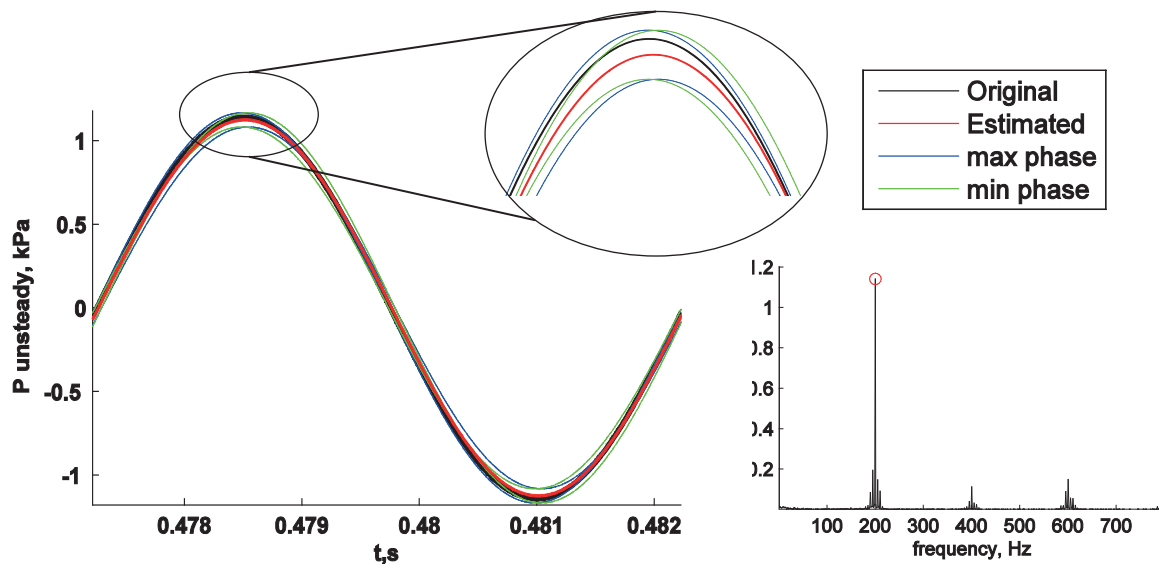


Figure 11 1st Harmonic reconstruction

For this specific case the blade is moved by a mechanical device which provides a harmonic motion at specific frequency (From 0 to 260Hz). It can be assumed that the mayor influence on the blade unsteady pressure will be produced by the motion frequency. This implies that analyzing the main harmonic of the unsteady pressure (that corresponds to the motion frequency), will provide a good approximation of the unsteady performance of the blade. This fact simplifies substantially the measurement uncertainty analysis,

because the uncertainty associated with the measurement only correspond to the pressure modulus and phase uncertainty of the first harmonic.

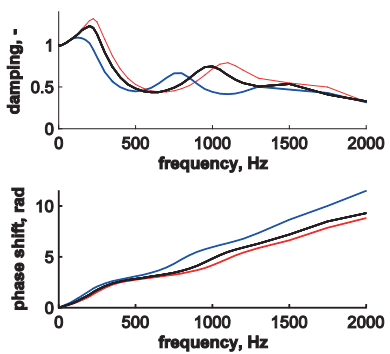

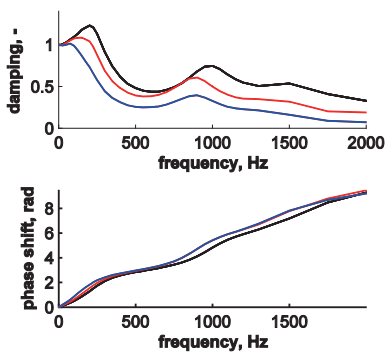

For analyzing how is the reconstruction is affected a 200.2Hz signal obtained with the pressure pulse generator has been analyzed. The unsteady pressure measured by the transducer has been decomposed into the frequency domain and applying the correction procedure has been obtained the estimated pressure in the tap and phase corresponding to the first harmonic. The same procedure has been done with the reference transducer situated in the reference cavity. The result shown in figure() shows a good agreement of the signals (reference and estimated) and the uncertainty window of the measurement, that in this specific case shows an uncertainty in pressure modulus of 4% and a phase uncertainty of 0.01rad. This represented by the curves in blue and green that show the maximum and min amplitude and max and min phase, defining in this way the uncertainty enclosure.

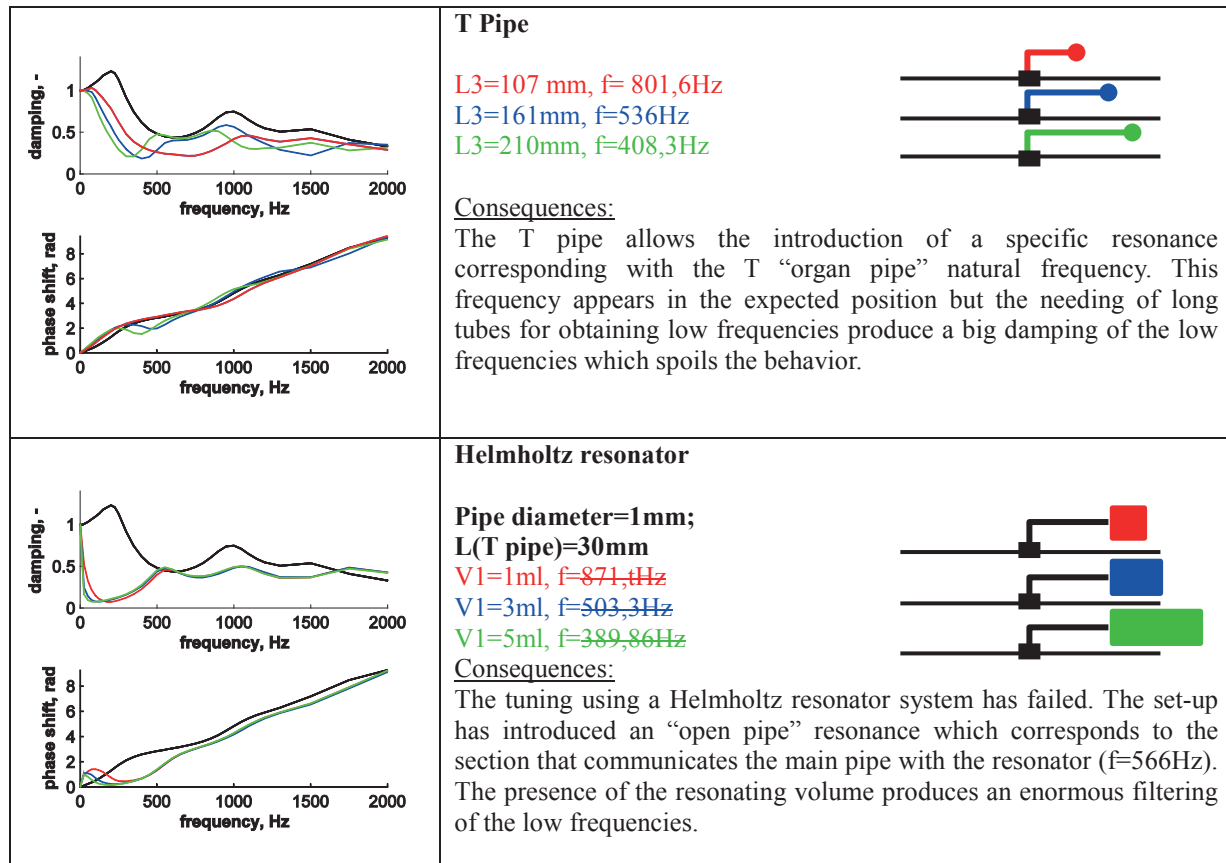
The natural continuation of this work will be the analysis of how is this uncertainty transmitted onto the unsteady blade loading, the subsequently will allow the determination of the aerodynamic damping of the system.

In consequence the modulus and phase uncertainty at can be directly applied into an unsteady blade loading, this will provide the blade unsteady loading uncertainty enclosure that after an integration the imaginary force obtained will provide de aerodynamic damping and its uncertainty.

### SYSTEM TUNING PROCEDURES OVERVIEW

The calibrating set up resonances have shown up to be interesting for measuring the unsteady pressure in recessed mounted transducers. At this point the question is if using different piping systems can be tuned the system for introducing the resonance at specific positions. With this purpose different experiments have been done:

 <p>The top graph shows damping vs frequency (0-2000 Hz) for three pipe lengths: L1=48mm (red), L1=68mm (black), and L1=118mm (blue). The bottom graph shows phase shift (rad) vs frequency (0-2000 Hz) for the same three lengths. As pipe length increases, the resonance frequency decreases and the damping increases.</p>	<p><b>Pipe length</b></p> <p>L1=48mm L1=68mm (baseline) L1=118m</p>  <p><u>Consequences:</u> A pipe length reduction, increase the main resonance frequency which leads to a mayor influence of the resonance. The phase lag is smaller as well, so in conclusion this is an interesting way for increasing the resonances.</p>
 <p>The top graph shows damping vs frequency (0-2000 Hz) for two section increases: L2=10mm (red) and L2=30mm (blue). The bottom graph shows phase shift (rad) vs frequency (0-2000 Hz) for the same two lengths. The introduction of a section increase significantly increases damping and shifts the resonance frequency.</p>	<p><b>Pipe section increase</b></p> <p>L2=10mm L2=30mm</p>  <p><u>Consequences:</u> The introduction of a section increase module produces a reduction of the resonance reducing the appearance frequency, so the overall behavior is spoiled due to the big damping of the signal produced.</p>



## CONCLUSIONS

The present paper has analyzed the key aspects which are influenced by a resonance in the calibration set up as well as the possible techniques for resonance manipulation.

The recessed-mounted transducer system and the calibration procedure have shown a big robustness from the point of view of uncertainty assessment and detection of possible uncertainty sources. The capability of detecting the uncertainty sources allows the error tracing along the processing chain providing a good overview of how do each source is affected by the resonances in the calibration.

The results show up interesting reduction of the overall relative uncertainty of the damping determination with respect to the trend (in the frequency band of interest, and in higher frequency resonances) which is translated into an uncertainty reduction of the unsteady pressure estimation. The sources of error analyzed, in this case have revealed a different behavior from the uncertainty point of view. On the one hand, the systematic uncertainty is reduced due to the resonance because the amplification of the signal is bigger than the amplification of the uncertainty. On the other hand the positioning uncertainty that is physically ligated to the duct geometrical properties induces an increase of the uncertainty in the resonant zones due to the change in the resonant properties. At last the random error can be assumed that is not affected by the resonance and its order of magnitude makes it the least significant.

As conclusion, the most significant uncertainty source is the systematic, which only depends on the transducer properties and the analog digital converter and amplification. A good improvement could be to reduce as much as possible the amplification of the signal for increasing the number analog to digital sampling points or to modify acquisition system to be able to set the full resolution of the A/D converter on the unsteady signal. This second improvement is not possible at the present time but is considered to be the best procedure for reducing the uncertainty. It could be also interesting to select the transducers and use the ones with the smallest steady calibration factor (Eq. 3). This will reduce significantly the uncertainty associated with the “measurement steady correction”.

The uncertainty of the estimated pressure will depend directly on the uncertainty of the reference transducer pressure. This fact has shown up as the leading factor for the high frequencies uncertainty. Being the damping uncertainty the most influential for the low frequencies and especially the systematic. The phase lag shows a similar behavior.

For analyzing the unsteady pressures on the blade surface produced by a blade controlled oscillation, only the first harmonic is needed. This fact indicates that the unsteady loading uncertainty is only subjected to the uncertainty associated with the first harmonic of the unsteady pressure.

For other applications in which a mayor number of harmonics are needed to be taken into account, the uncertainty of the measurement will be subjected to the number of harmonics. As the wave reconstruction is based on the assembly of sinusoidal signals at the frequencies indicated by each harmonic and with the corresponding phase, the uncertainty of each harmonic will contribute to the final measurement uncertainty. This fact is needed to be taken into account for determining which harmonics keeps the uncertainty into acceptable limits providing a good agreement with the original signal.

In the end different tuning procedures have been used for adjusting the damping resonances. Among the different test the only one with interesting application is the reduction of the piping system length. Unfortunately the length of this pipe is limited by the physical set up; the blade length, the connector, and the needing of a smooth transition between the stainless steel pipe and the connector. All the rest of the procedures introduce a big fluid volume to the system and increase the internal surface extension, which ultimately spoils damping response at low frequencies. As a final remark the usage of the set up so called Helmholtz, provides a low frequency signal filter that can be used in other applications.

## REFERENCES

*A Technique For Using Recesed-Mounted Pressure Transducers To Measure Unsteady Pressure.*  
Vogt, D. M., Fransson, T. H., 2004

*Measurement techniques for unsteady flows in turbomachines*  
C. H. Sieverding, T. Arts, R. DeÂnos, J.-F. Brouckaert, 2000

*Measurement Systems, application and design*  
Ernest O. Doebelin, ISBN 0-07-017336-2

*Describing the Uncertainties in Experimental Results*  
Robert J. Moffat, 1988

*HANDBOOK. UNCERTAINTY IN GAS TURBINE MEASUREMENTS*  
Dr. R. B. Abernethy, Pratt & Whitney, J. W. Thompson, Jr., 1973

# INTEGRATED PRESSURE AND VELOCITY MEASUREMENTS USING A SINGLE PRESSURE SENSOR ON THE CONE OF A WIND TURBINE

**Konstantinos N. Antivachis and Anestis I. Kalfas**

Department of Mechanical Engineering,  
Aristotle University of Thessaloniki,  
GR-54124 Thessaloniki, Greece

## ABSTRACT

A new method of measuring 3D flow with a single pressure transducer mounted on the head of a wind turbine's nose cone is presented in this paper. The principal of the proposed method is based on the five-hole probe calibration methodology. The novelty of the proposed method lies in the fact that a single rotating pressure tap on the wind turbine's nose cone is used. Evidently, simplicity, functionality and applicability can be combined in industrial standard machines.

The pressure tap is directly connected to the transducer, which obtains four pressure measurements in four distinctive angular positions of the cone predefined by the calibration model. Thus the above measurements in the appropriate calibration coefficients obtain the flow field quantities such as yaw and pitch angle as well as total and static pressure. Pressure taps have been made and calibrated on five distinctive diameters on the cone of a small-scale wind turbine in order to investigate the influence of the taps mounting on the calibration results. In addition, the effects of the wind turbine blades have been investigated. The proposed calibration coefficients results have been compared to results of an alternative model with an additional pressure tap located at the tip of the cone. While the precision of the model may improve, it may also increase the complexity of the measuring process. The coefficients of different structural parts have been compared too, giving interesting conclusions about their impacts on the coefficients' behaviour. The aforementioned process was implemented inside the low-pressure section of a wind tunnel. The results of this paper were acquired, using the above-mentioned wind turbine's nose cone, but they can easily be applied to any rotating single pressure probe.

The most spectacular outcome of this paper is the fact that, instead of using a probe with at least five-holes in order to obtain the full vector of a 3D flow, it is possible to achieve the same goal by using a single pressure probe, which has the ability to rotate. Therefore, the proposed method leads to a much smaller probe, which disturbs the flow a lot less, providing for a reduced measurement error. In addition, the calibration method becomes far less complicated. The cost reduction of the measuring process may be approximated by the difference between the manufacturing and running cost of a 5-hole probe and manufacturing and running cost of a single-hole pressure probe.

## INTRODUCTION

In 3D flow measurements and especially in turbomachinery applications, the necessity of manufacturing probes as small as possible with the highest sensitivity and biggest angular range of operation have always been pursued. The most commonly used pressure probe until today has been the five-hole pressure probe, which has the least number of holes by which the full vector of any 3D flow can be defined using the classical calibration coefficients. Unfortunately, in most cases those probes are often larger than ideal, inducing errors that cannot be neglected in measuring results.

On the other hand, single sensor pressure probes can be typically made to be a half to a third of the size of multi-sensor probes [1] [2] [3]. Furthermore, when a single sensor is employed, the calibration is a lot simpler to define as well as more accurate as it does not involve multi-sensor accuracy issues. In addition, the manufacturing complexity and the total construction costs are reduced. The results of this paper were acquired using a small-scale wind turbine's nose cone in the low-pressure section of a wind tunnel. Nevertheless, the same method can be implemented to any single pressure probe that has the ability to rotate.

Firstly, the behaviour of a dual pressure-sensor rotating probe is being analysed but the calibration method used is the classical five-hole probe method [4]. The basic difference lies in the fact that the measurements are being conducted in predefined angular positions, while the probe is rotating simulating a virtual five-hole probe. Secondly, new calibration coefficients are being presented requiring only one pressure sensor mounted on the nose cone. Those methods simplify a lot the measuring process but have also some disadvantages, which will be discussed in this paper. Thirdly, the impacts of the blades' existence are examined too, showing that they cannot be neglected since they induce large variations in the coefficients' results.

## EXPERIMENTAL SETUP

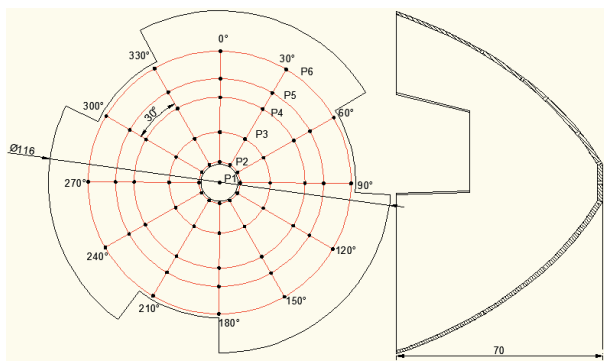
In order to investigate the ability of a wind turbine's nose cone to estimate a flow's vector by the way a pressure probe does, the nose cone of the small-scale wind turbine presented in Fig.1 was detached from its main construction and studied separately in laboratory conditions. In Fig.2 the cone's drawing with its pressure tapings for several mounting diameters is presented.



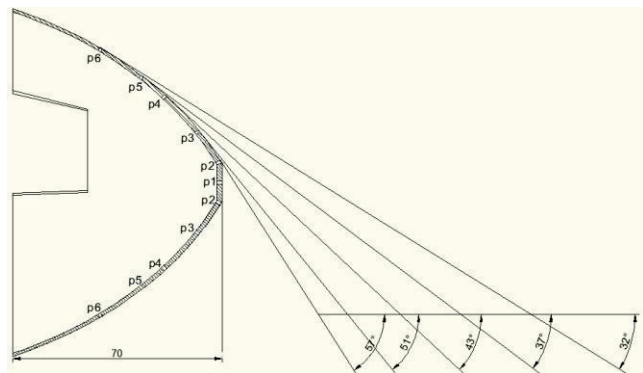
**Fig. 1: Small scale wind turbine**

The tapings were made in various diameters, in order to investigate the pressure conditions on the cone's surface. Another reason was to examine their mounting place effects on the calibration coefficients. Fig. 3 shows a significant variation on the tapings' construction angle as the mounting diameter changes due to the geometry of the cone. Despite the fact that the measuring techniques presented in this paper are applicable for single pressure tapping arrangements, twelve pressure tapings have been made on each measuring diameter. An additional tapping had been made at the tip of the cone. This arrangement has been chosen in order to reduce the large amount of measurements required for the calibration procedure. In case there was only one pressure tapping on each diameter the calibration procedure would last much longer, since except for the angular motion in the pitch and yaw angles the cone would also have to rotate. Using the currently proposed method, the calibration coefficients for a virtual  $30^\circ$  roll angle step can be obtained.

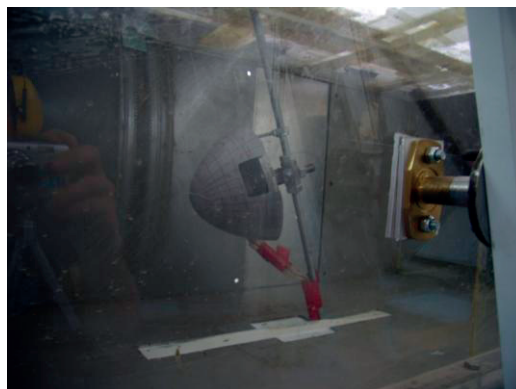
Two stepper motors were responsible for the motions of the cone in yaw and pitch angles and a digital pressure meter would register the pressure measurements. A fully automated program written in Labview programming language was used to conduct the process. The outcome of the measuring process was a set of 11,532 pressure measurements.



**Fig. 2 : Nose cone dimensions and tapings**



**Fig. 3 : Probe construction angles and diameters**



**Fig. 4 : Nose cone inside the wind tunnel**

In Fig. 4 the cone is depicted inside the wind tunnel during the measuring process. The range used for both yaw and pitch angles, is  $\pm 30^\circ$  and the angular step used is  $2^\circ$ . As a result, for each diameter of the cone, a file with 961 different combinations of yaw and pitch angles was produced. Each set of calibration data contains 12 pressure measurements intended for the reconstruction of a virtual single rotating pressure tap acquiring pressure data every  $30^\circ$ , for each diameter. All of the measurements took place under the same free stream velocity of 10.5m/s in steady state conditions. The air density was  $1.225\text{kg/m}^3$  and the Reynolds number was stable at  $8.2 \cdot 10^4$ .

## CALIBRATION METHODOLOGY

### TWO PRESSURE SENSOR ROTATING PROBE CALIBRATION METHOD

The distribution of the calibration coefficients are presented in the following figure 5.

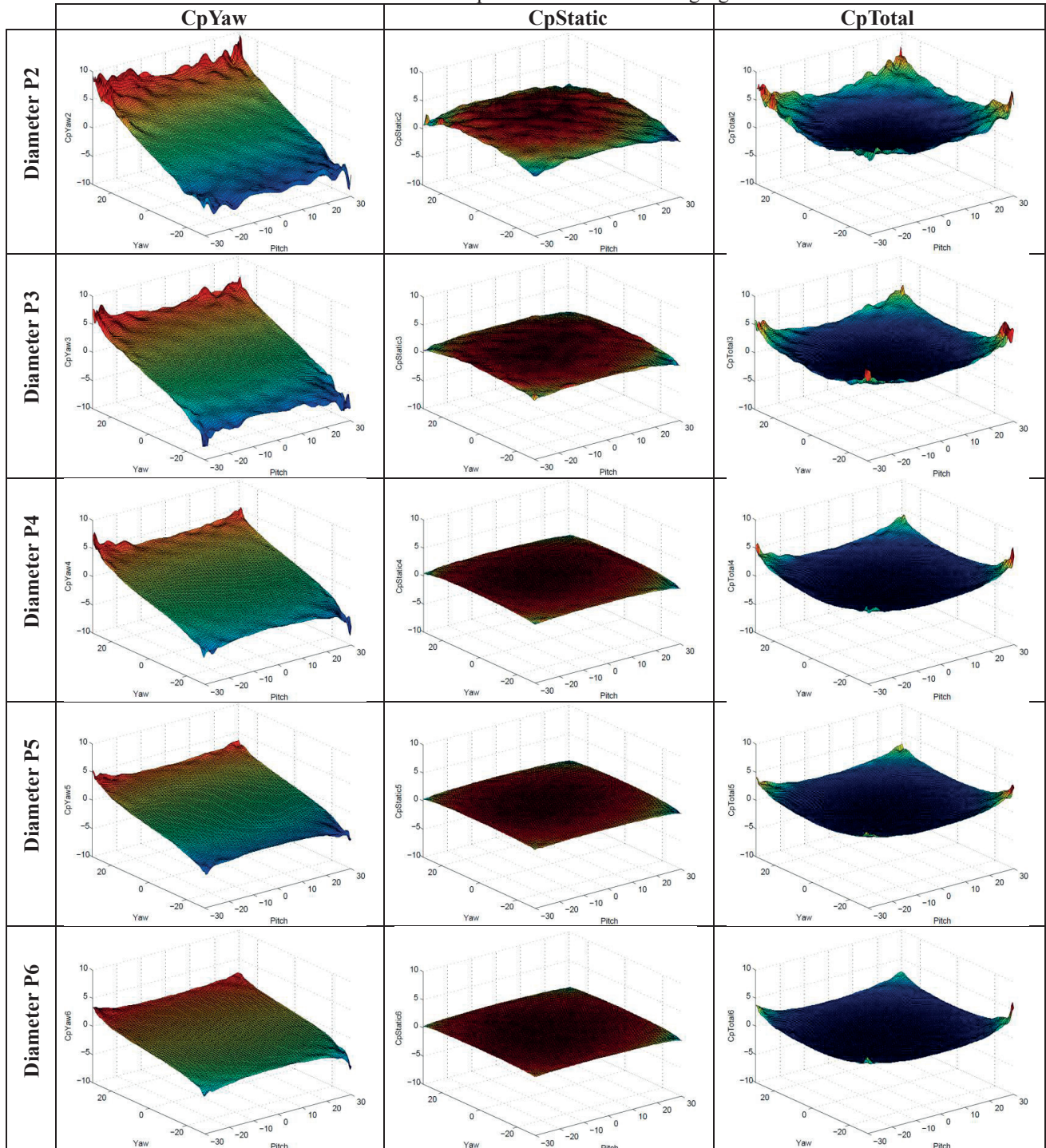


Fig. 5: Calibration coefficients variations according to pressure sensors taping diameter.



In this section, the coefficients of a two pressure sensor probe related to the yaw and pitch angles as well as the total and static pressure are presented.

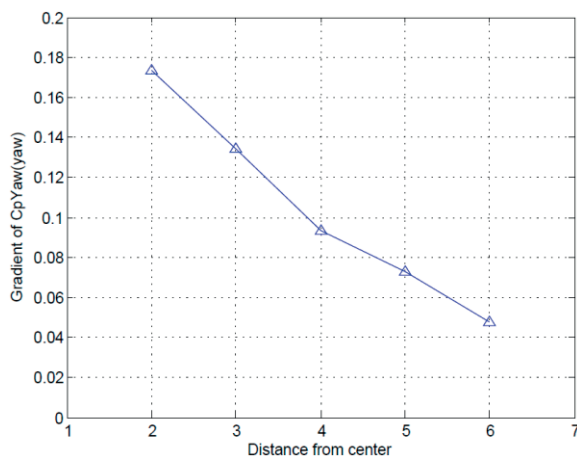
$$\begin{aligned} & \text{-----} & (1) \\ & \text{-----} & (2) \\ & \text{-----} & (3) \\ & \text{-----} & (4) \end{aligned}$$

The “i” indicator stands for the pressure sensors tapping diameter according to Fig. 2. The behaviour of each coefficient varies according to the diameter in which the pressure sensor is mounted. Those variations are presented in Fig. 5 for the coefficients of yaw angle, total and static pressure. The coefficient of pitch angle is not presented since it is almost identical with the yaw angles one. This happens because of the axial symmetry of the nose cone. The coefficients behaviour depends strongly on the pressure sensors tapping diameter, which has a direct impact on the tapings construction angle.

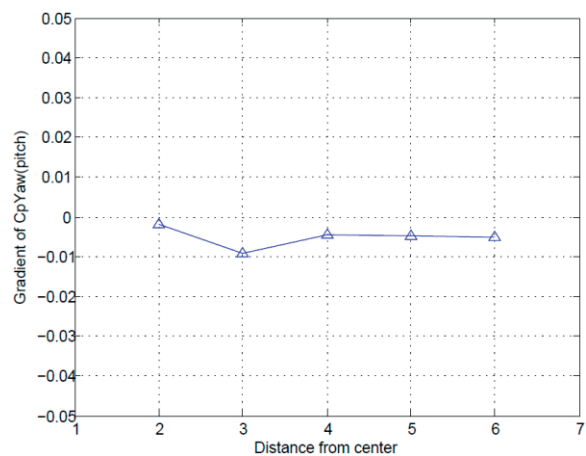
In larger diameters the coefficients distinctiveness-sensitivity diminishes but the operational angular range of reliability raises. On the other hand in smaller diameters the coefficients sensitivity raises but the operational angular range of reliability diminishes. The diagrams of static and total pressure coefficients are smoother for larger diameters leading to much more trustworthy results. In addition their dependence from angular variations diminishes too. The behaviour of the pitch angle coefficient is approximately the same with yaw one but for some minor differences caused by construction errors in the symmetry of the cone. The above facts can be clearly observed, in the following four diagrams in which the reliable angular range and the gradient in both yaw and pitch angles of the yaw coefficient are presented.

In Fig. 6 the mean gradient of CpYaw is presented, which is the coefficient responsible for the yaw angles changes and its dependence from the sensors mounting diameter. It is clear that in smaller diameters which correspond to larger construction angles, such as p2 this gradient can be larger than four times the gradient in larger diameters such as the p6 one which corresponds to smaller construction angles.

In Fig. 7, the dependence of the CpYaw gradient from the sensors mounting diameter is presented. In this case, the focus is the pitch angle, which would be zero in the ideal case. In fact, there are construction errors, as well as measuring errors. This figure shows that there is some sensitivity-gradient, which is almost two orders of magnitude smaller than the gradient of the previous case. This is expected and, in any other case, it may be taken as a warning against systematic error, either with the measurements or the structural parts chosen for the specific coefficient.

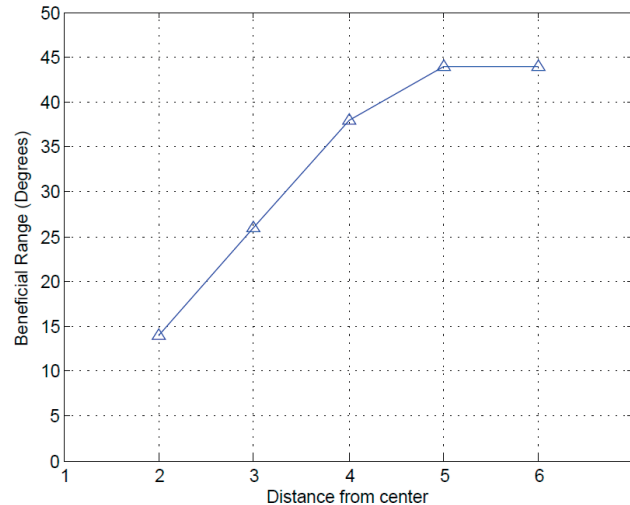


**Fig. 6 : Gradient of CpYaw depending on the yaw angle for each diameter**



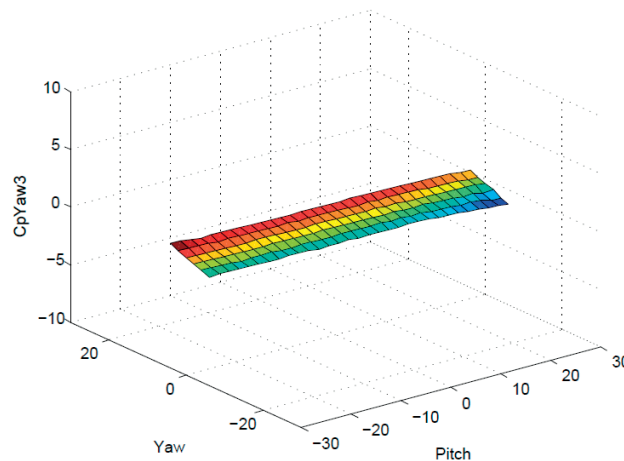
**Fig. 7 : Gradient of CpYaw depending on the pitch angle for each diameter**

In Fig. 8, the trustworthy range of the yaw coefficient is presented for each examined diameter. As trustworthy or beneficial range, in which a coefficient is operational is called the angular range in which this coefficient is considered capable to determine the angle of the flow with which it is charged for. This means that this range depends in its wholeness on the application in which the probe is going to be used in as well as the researcher’s scope. So any method that tries to determine that range is a totally empirical method such as the one presented here.



**Fig. 8 : Trustworthy range for CpYaw for each diameter**

More specifically, the proposed empirical method excludes from the trustworthy angular range the angles for which the yaw coefficient experiences intensive gradient variations for two consecutive pitch angles. The CpYaw coefficients values for the diameter p3 after the implementation of the aforementioned empirical method is presented in Fig. 9, which in comparison with the corresponding diagram of Fig. 5, provides further clarification in terms of the method as well as its application.



**Fig. 9 : Trustworthy angular range for CpYaw coefficient**

**SINGLE PRESSURE SENSOR ROTATING PROBE CALIBRATION METHOD**

In this section, four single pressure sensor probe calibration models are presented. The experimental part of the calibration process, is identical to the one used in the previous section for the two pressure sensor calibration probe. Each yaw and pitch angle combination (Fig.10) has a different impact on the nose cone’s surface pressures. As a result, the characteristics of those unique contours for each angular combination could be captured by a single rotating pressure sensor mounted on the nose cones surface.

The reasons why the contours are not completely symmetric are structural and depend on the cone’s geometry. As can be seen in Fig. 4 the cone is made out of casted plastic which obviously is not a very accurate treatment.

It has to be clear that the pressure results are differences between the atmospheric pressure and each pressure sensors measurement. This results to positive quantities since the experiment took place in the low pressure section of a wind tunnel. Hence the blue regions refer to higher pressures and the red ones to lower pressures. As mentioned before the pressure measurements were obtained for every 30°. Hence for the construction of those diagrams a mathematical model of Fourier polynomial was used, which extrapolated those measurements.

Fig. 11 presents the same information with Fig. 10 for a specific pitch and yaw angle combination (30°, 30°), while it is also, presenting the pressure tapings diameters. Obviously, each taping is subjected to a different combination of pressures in a full rotation This can be clearly seen in Fig 12.

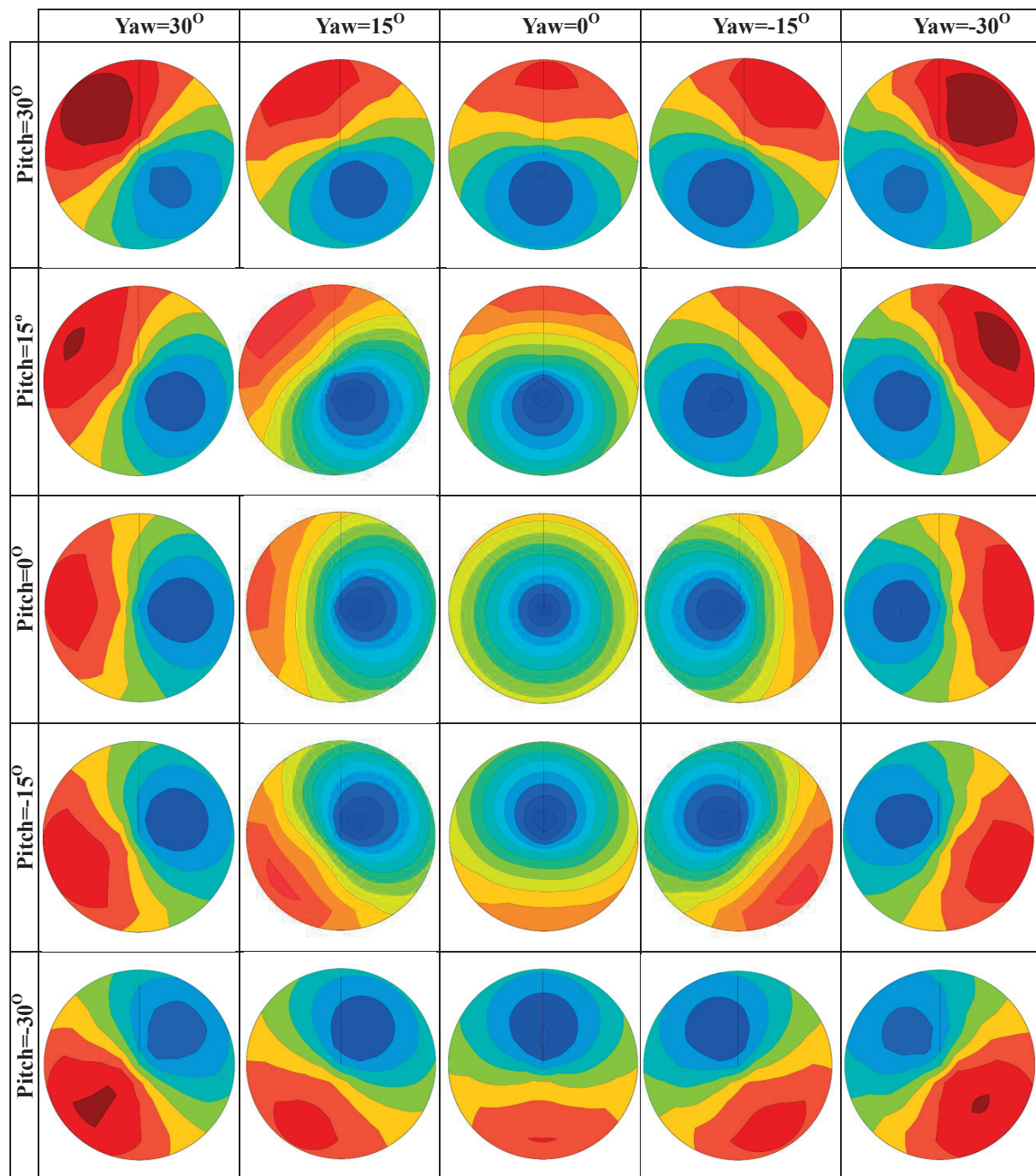


Fig. 10 : Pressure contours on the nose cone's surface

Except for the taping that belongs to the largest diameter p6 all the other tapings pressure measurements have very little differences between them. Each of the pressure lines in Fig.12 is unique for the particular yaw and pitch angle combination and its shape depends also on the flows total and static pressure and consequently on the flows velocity. The last observation clarifies that there is a non linear functional dependence between the pressure readings of each sensor and the flows velocity, as expected from the energy equation. This means that if a measurement takes place for the same yaw and pitch angle but for a different flow velocity, the pressure measurements will vary significantly. This issue has always been overcome by non-dimensionalisation methods as shown in the previous section for the two pressure sensor probe by estimating the velocity of the flow. That method requires at least two pressure tapings, even for the rotating pressure probe. In the methods presented in this section, only one pressure sensor is necessary.

In order to identify the most appropriate way to build the best calibration model, four variations of the model have been set up and tested with respect to their effectiveness.

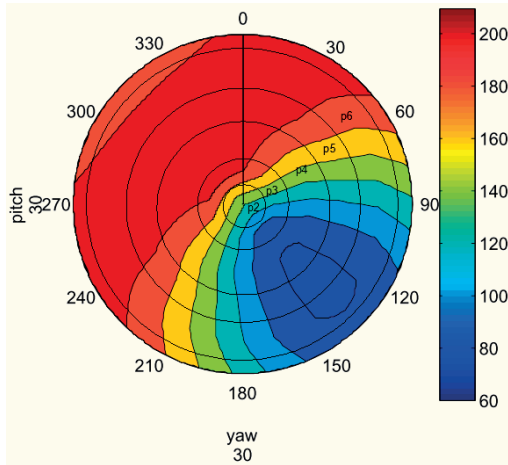


Fig. 11: Pressure contours on the nose cones surface and pressure tapings diameters

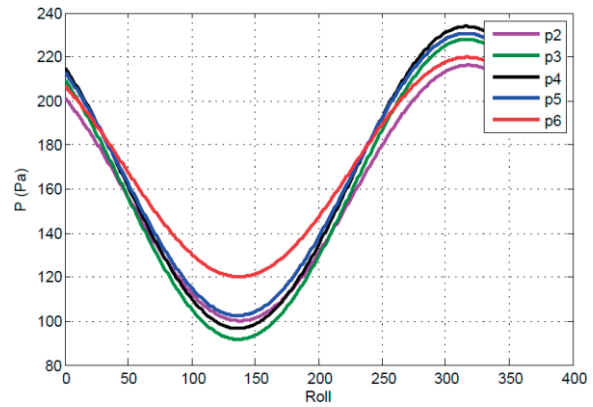


Fig. 12: Pressure readings of pressure tapings mounted on each one of the five selected diameters

**1<sup>st</sup> model**

The first model uses the sum of two pressure measurements with angular distance equal to  $180^\circ$ . In the equations presented, the pressure measurements in  $0^\circ$  and in  $180^\circ$  are used, but the coefficients behaviour would be the same if the ones in  $90^\circ$  and  $270^\circ$  were to be used, instead.

$$\text{_____} \tag{5}$$

$$\text{_____} \tag{6}$$

$$\text{_____} \tag{7}$$

$$\text{_____} \tag{8}$$

**2<sup>nd</sup> model**

The second model uses the maximum pressure estimated by the four pressure measurements, which occur at  $0^\circ$ ,  $90^\circ$ ,  $180^\circ$  and  $270^\circ$ . For example, in the case of the angular combination presented in Fig. 12 the pressure sensor mounted on the fourth diameter would give an estimation of the maximum pressure on that diameter, equal to 95 Pa approximately and the equivalent on the second diameter would give an estimation of 100 Pa.

$$\text{_____} \tag{9}$$

$$\text{_____} \tag{10}$$

$$\text{_____} \tag{11}$$

$$\text{_____} \tag{12}$$

In Fig. 13 and Fig.14 the above calibration coefficients results can be observed. In the first figure, the  $C_p$ Pitch and  $C_p$ Static coefficients for the 1<sup>st</sup> model are presented and in the second the same coefficients for the 2<sup>nd</sup> model that makes use of the maximum pressure estimation. The mounting locations examined, are the first three diameters, as the corresponding results have been found to provide sufficient information for a full view on changes invoked by the sensors mounting position. Figs. 13 and 14 present diagrams on the same scale, in order to facilitate direct comparison. Also, the diagrams presented in Fig. 5 can be compared with them, too, despite the fact that they are plotted on different scale. The behaviour of the pitch coefficient is identical to the yaw coefficient, so the same conclusions can be drawn from both angle coefficients.

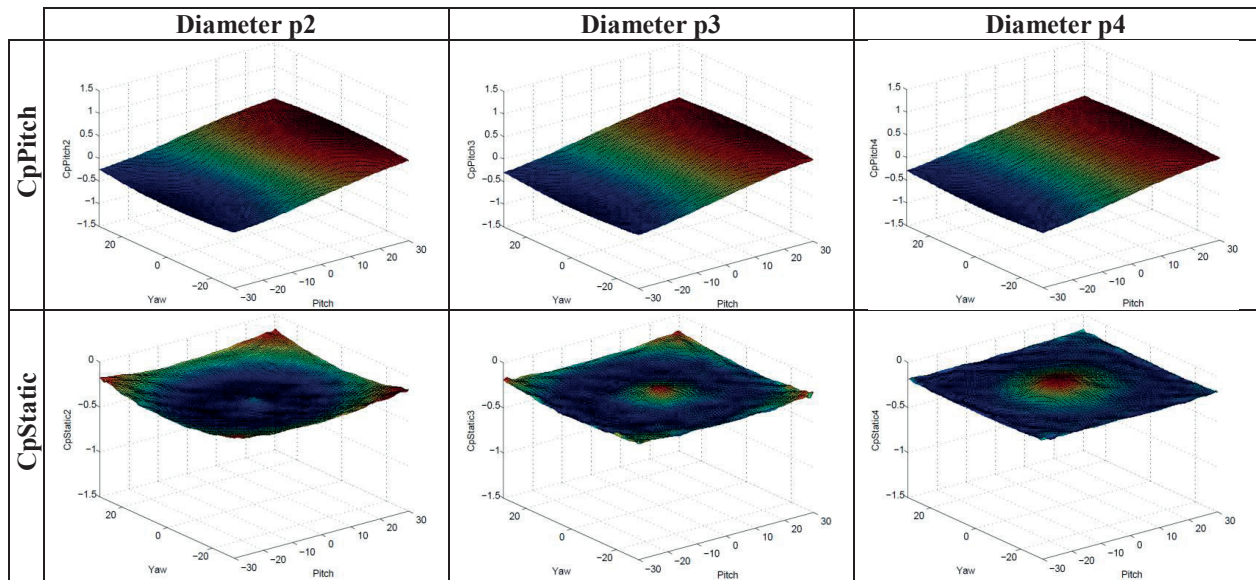


Fig. 13: Single pressure sensor calibration coefficients -CpPitch, CpStatic- model with the 1<sup>st</sup> model

Firstly, the sensitivity of these models differs, where the highest sensitivity belongs to the two sensor model presented earlier in this paper. Right next to that is the single sensor model with the maximum pressure estimation and the last is the single sensor model with no estimations. Secondly, regarding the coefficient variations according to the sensors mounting diameter, the single sensor models do not seem to have significant variations, whereas the variations of the two sensor model presented in the previous section were very intense with their sensitivity increasing as the diameter grows smaller. An important outcome of this observation is that the choice of the mounting place of the pressure transducer for those single pressure sensor models does not affect the coefficients behaviour. Hence, this choice can be made based on alternative criteria, such as the accommodation of the probes construction process. Thirdly, the reliability range for both last models presented is maximized since the coefficients behaviour, especially, for the first one is very smooth. This characteristic shows reliable results especially in comparison to the two pressure sensor model presented earlier, specifically for the smaller diameters. So according to the above analysis the maximum pressure estimating calibration method is the most efficient since it has the highest sensitivity.

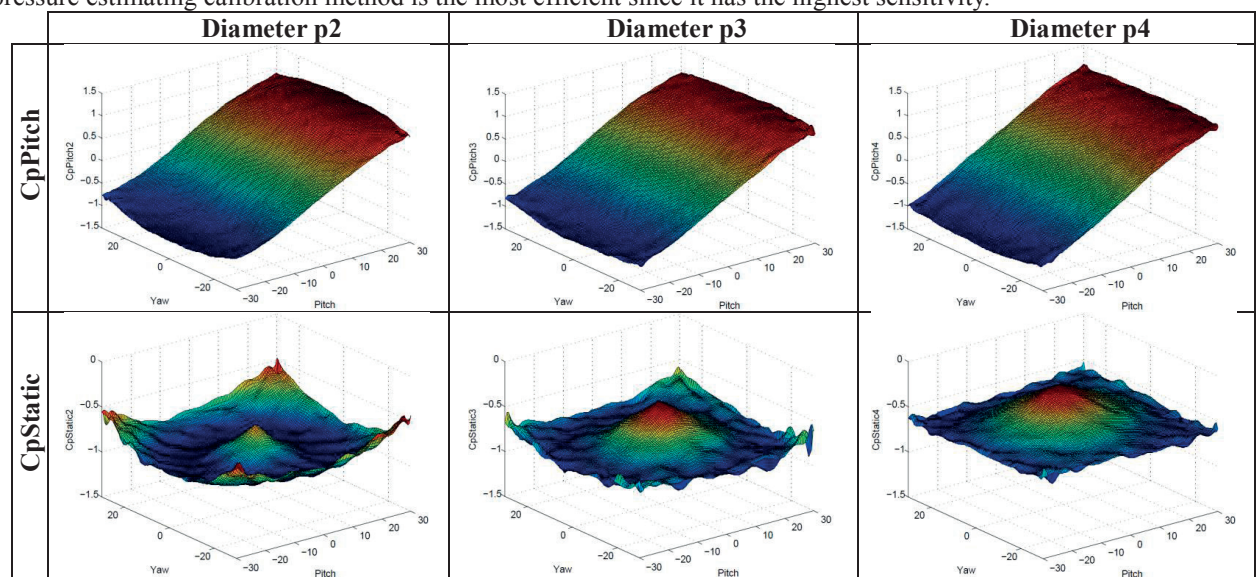


Fig. 14: Single pressure sensor calibration coefficients -CpPitch, CpStatic- model with the 2<sup>nd</sup> model

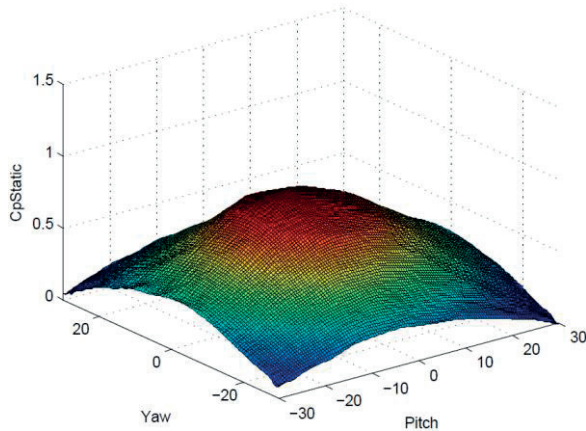
**3<sup>rd</sup> model**

In this model the yaw and pitch coefficients are the same with the ones presented in 2<sup>nd</sup> model, but for the determination of the total and static pressure the following coefficients are used (eq.13 and 14).

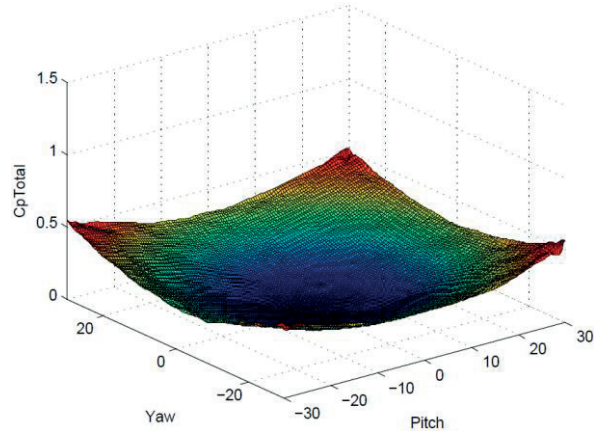
$$(13)$$

(14)

Where,  $P_1$  is the pressure on the tip of the nose cone while the  $P_{\max}$  and  $P_{\min}$  are the maximum and minimum pressures over the whole surface of the cone, for each particular combination of yaw and pitch angles, respectively. The static and total pressure coefficients behaviour is presented in Fig. 15 and 16.



**Fig. 15: Static pressure coefficient (eq. 13)**



**Fig. 16 : Total pressure coefficient (eq. 14)**

This calibration method requires the non-dimensionalization of the surfaces pressure contours with a specific pressure that belongs to a certain diameter. So, if the pressure sensor chosen belongs to, e.g., the diameter p4, for each angular combination, the maximum pressure of this diameter is used for the division of all pressures on the surface. Thus a new index similar to the one presented in Fig. 10 is formed. In this case, the maximum pressure occurring on the diameter p4 for each particular angular combination is used to divide each pressure on the surface.

#### 4<sup>th</sup> model

This method is based on the diagram of Fig. 12 and the fact that each pressure sensor after a full rotation gives a unique combination of pressure measurements for a predefined combination of yaw and pitch angles. Hence, the calibration method is very similar to the 3<sup>rd</sup> model. The difference is that no angular coefficients are used. In their place, for each angular combination all five different pressure sensors measurements for a full rotation are saved. Then a certain sensor is chosen, e.g., the one belonging to p4 whose maximum pressure measured in each angular combination after a full rotation is used for the non-dimensionalisation of all the pressure measurements occurred in this angular combination, as in the previous model. This sensor is essentially the one that will be used in the actual measuring process. The total and static pressures are estimated using the same coefficients and methodology as with the 3<sup>rd</sup> model.

### **MEASURING METHODOLOGY WITH THE PRESENTED CALIBRATION MODELS**

In all cases, the measuring process is similar to a three or a five hole-probe, except for the necessity for the probe's rotation. Each calibration method has its own measuring methodology, by which all the necessary characteristics of the flow are obtained. As in every measuring process, the absolute barometric pressure has to be determined by a barometer in order to calculate the exact total pressure of the flow.

For each specific measurement there must be a certain sample of measurements the average of which is extracted. The sample should be at least larger than 5 so that uncertainties will be minimized. The stability of the flow as well as the accuracy of the measuring equipment is critical for the sampling range required.

In the case of using those models with a wind turbine nose cone, the determination of the angular position can be made firstly by noticing mechanically a specific angle as the 0<sup>o</sup> angle. Then, the amount of time required for covering a single degree is known by automatically dividing the amount of time required for a full rotation by 360<sup>o</sup>. So, every actual angular position can be determined.

#### Two pressure sensor probe, 1<sup>st</sup> model

Firstly the probe enters a flow according to the calibration axes and obtains a measurement. Then it bears a 90<sup>o</sup> rotation and the second measurement takes place. This partial rotation is repeated three times in order to obtain all the necessary measurements for the calibration coefficients.

When all the necessary measurements are obtained, the yaw and pitch angles can be determined. Through them the total and static pressure can be extracted from their calibration diagrams. Hence, the flows velocity can be determined.

The appropriate mounting diameter for the second transducer may be chosen according to the goal. If high sensitivity is required for a small angular range, the diameter should be small. On the other hand, if larger angular range combined with larger reliability is required, a larger diameter should be chosen.

#### **Single pressure sensor probe, 1<sup>st</sup> model**

This model is very similar to the previous one. It only differs in the use of a single pressure sensor instead of two. Firstly, the angular coefficients are determined, which combined with the calibration diagrams provide the flow angles. Then, total and static pressures are determined through the total and the static coefficients. The nose cone's tip sensor is disabled. The mounting of the sensor can be anywhere between the five diameters presented in Fig.2 since, as shown in the diagrams of Fig.13, there is no particular variation in them.

#### **Single pressure sensor probe, 2<sup>nd</sup> model**

For the single pressure probe with the maximum pressure estimation, an extra step will be necessary in order to complete the measuring process. This step requires the estimation of the maximum pressure, by a certain mathematical model, such as a Fourier polynomial. The sensor may be taken as if it would obtain measurements continuously for a whole rotation. The remaining procedure is the same as for the previous models.

#### **Single pressure sensor probe, 3<sup>rd</sup> model**

In this model the angular coefficients used are the same with the last model. After the determination of the flow's angles, the index that contains the nondimensionalised pressures of the whole cones surface can be obtained through the calibration process. Thus if that index gets multiplied with the maximum pressure estimated from the sensor that belongs to the chosen pressure tapping diameter e.g.  $p_4$ , the actual pressures on the whole cone's surface will come up as result. After that, the maximum and minimum pressure on the surface are acquainted as well as the pressure on the cones tip, which by now can determine through eq.13 and eq.14 the total and static pressure of the flow and hence its velocity. Since in this model no matter which mounting diameter is chosen, the static and total pressures coefficients are the same, the only difference is in the angular ones, which as mentioned before have no significant influences by changes in the sensors mounting place.

#### **Single pressure sensor probe, 4<sup>th</sup> model**

The basic difference between this model and all the others is that the measurements to be taken do not have to be in specific angular positions, except for the first one and also they don't have to be of a certain number. According to the Nyquist theorem for the determination of every periodical signal only two values of it are necessary. In this case it is best if at least three values are obtained after a full rotation with the first one to be made in a known angular position, which should be the  $0^{\circ}$ .

The next two or more measurements can take place in any other angular position in the same rotation. This flexibility in the measuring positions makes this model the most easy to handle and also the most easy to accomplish, since no angular position recognition mechanism in every  $90^{\circ}$  is necessary, except for the recognition of the  $0^{\circ}$  angular position.

Hence, a simple way to make sure that all the measurements take place in the same rotation is to compute the time required for a full rotation and then to take all the required measurements in a smaller amount of time.

Having obtained the required measurements, the pressure combinations of the chosen sensor are estimated e.g. the sensor in the  $p_4$  diameter and a specific curve is produced, similar to the ones presented in Fig. 12, by which the maximum pressure can be estimated.

All pressures are divided by the maximum pressure, in order to produce the previous curve in a nondimensionalised form. All possible combinations of angles have been saved nondimensionalised and so a pattern recognition can be developed, by which the pitch and yaw angles can be defined. Finally, the total and static pressure of the flow can be defined by eq. 13 and eq. 14 as presented earlier.

### **WING BLOCKAGE EFFECT ON THE CALLIBRATION COEFFICIENTS**

The until now the presented models and measurements, refer to a wind turbines nose cone without its wings mounted, as it is shown in Fig.4. In order to investigate their possible effects on the pressure combinations that the cones surface bears, three simulation wings were constructed and mounted on it.

Then the same measurements took place for the diameter  $p_4$ , so that a comparison between them could be made. In Fig. 17 and Fig 18 can be seen that the two angular coefficients are strongly affected by the existence of the wings. This means that for the use of this cone as a dynamically measuring pressure probe, the calibration coefficients have to be recalculated.

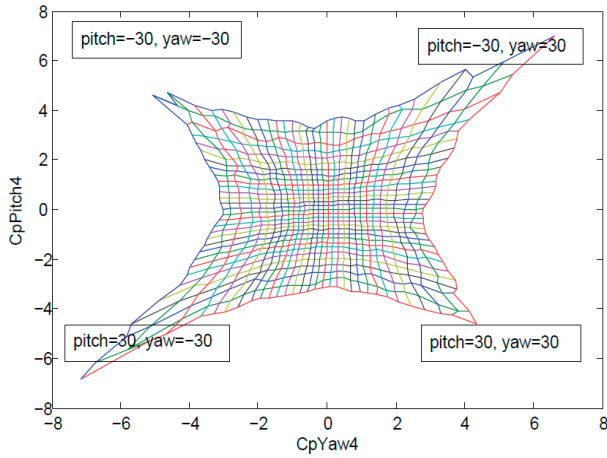


Fig. 17 : CpPitch-CpYaw coefficients for p4 diameter without wings

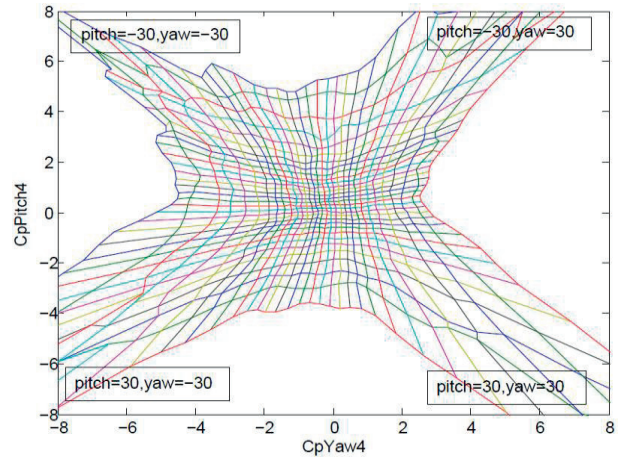


Fig. 8 : CpPitch-CpYaw coefficients for p4 diameter with wings

### INVESTIGATION OF THE NONDIMENSIONALISATION QUANTITIES

In the previous pages, five different calibration models were presented for the same pressure probe with four different sets of calibration coefficients. Regardless of the fact that each set of coefficients had a different behaviour, all of them had parts that were the same. In this section, the basic parts (numerator-denominator) of those coefficients will be analysed separately in order to obtain conclusions about the influences of each one in each coefficient's result.

#### Coefficients numerator

Each coefficient presented has a numerator whose role is to react in any changes occurring in the variable that this coefficient is responsible for.

$$(15)$$

$$(16)$$

No matter which calibration model is used the numerators of the angular coefficients are the same differential quantities that maximize the sensitivity in any angular changes of the flows vector presented by the quantities of eq.15 and eq.16 and can be seen in Fig.19.

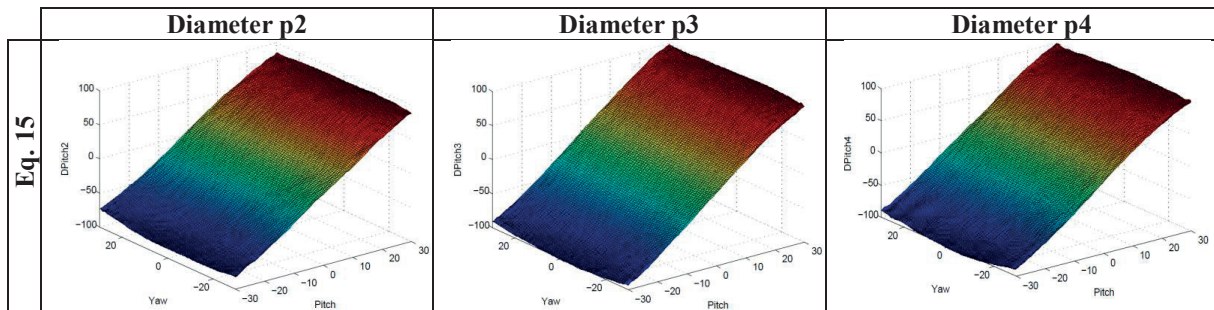


Fig. 19: Equation 15 results for three different diameters

The 17 to 22 quantities represent the numerator of static and total pressure coefficients respectively and in Fig. 20 and Fig. 21 the behaviour of the first two is presented. The basic difference and at the same time drawback of them comparing to the angular ones is the fact that they are not differential. This happens because in a certain flow the total and static pressures are dimensionless constants.

$$(17)$$

$$(18)$$

$$(19)$$

$$(20)$$

$$(21)$$

$$(22)$$



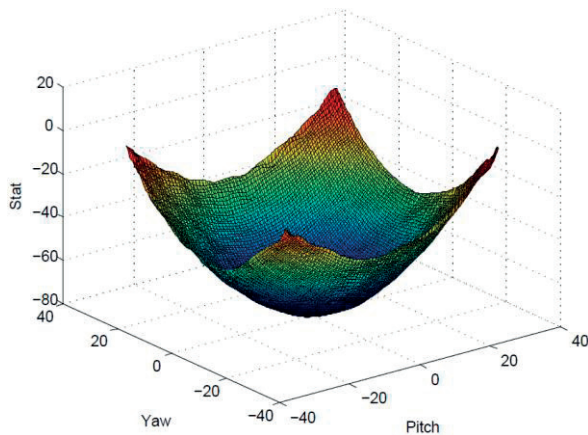


Fig. 20: Equation 17 results

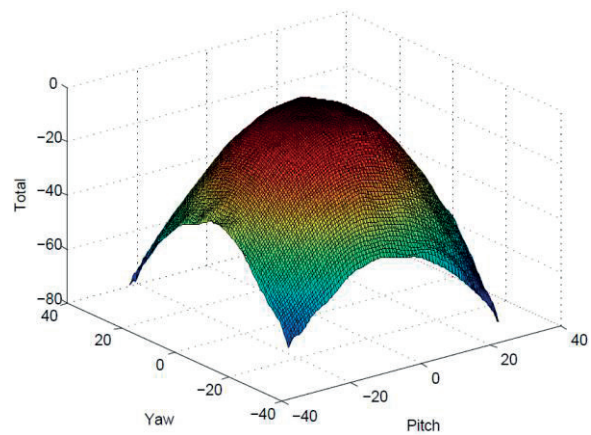


Fig. 21: Equation 18 results

### Coefficients denominator

The ability to use each coefficient in flows with different static and total pressure from the flow used for the calibration of the probe depends on nondimensionalisation process. This process takes place by adding a denominator to the quantity that calculates the situation of the flows characteristic it has been charged with.

Bellow four different nondimensionalisation quantities are presented where eq. 23 belongs to the two sensor model while eq. 24 to 27 belong to the single sensor model. The results of eq. 24 and eq.25 are actually the same, since they measure pressures with angular distance equal to  $180^{\circ}$ .

(23)

(24)

(25)

(26)

(27)

In Fig.22 the behaviour of the non-dimensionalisation quantities is presented providing a complete survey of the impact of each one on the coefficient it is used in. The first conclusion that can easily be conducted is that each quantity has a different scale. Hence, the smallest one belongs to eq.23 which belongs to the two sensor probe and follows the eq. 26 for the single pressure probe with the maximum pressure estimation. The largest scale belongs to eq. 24, which corresponds to the single pressure probe without estimations.

Observation and comparison of Fig. 5, Fig. 13 and Fig. 14 show that the smaller the scale of the non-dimensionalisation quantity, the larger is the sensitivity of the coefficient according to changes in the flows characteristic it is charged with. Thus, the two sensor probe has the largest sensitivity, and the single sensor pressure probe follows, with the least sensitivity belonging to the model without the estimation of the maximum pressure.

The second characteristic of the coefficients besides their sensitivity is their reliability, a characteristic that concerning the two sensor calibration model was shown to decrease as the coefficients sensitivity increased. The same behaviour can be noticed in Fig. 22 for eq. 23, which obviously is responsible for the two sensor model coefficients behaviour, since their numerator is very smooth for all the diameters.

Although the denominators of the other two models, have in some cases a very smooth behaviour, this cannot be seen in the counterpart of their coefficients. This is, also, because of the scale of the denominators, which in this case are much smaller compared to the two sensor calibration method. e.g. for the two sensor case an alteration from 5 Pa to 10 Pa is a 100% change which strongly determines the coefficients result. On the other hand for the single sensor case an alteration from 330 Pa to 340 Pa is an about 3% alteration which does not have much of an influence in the smoothness of the coefficients diagram.

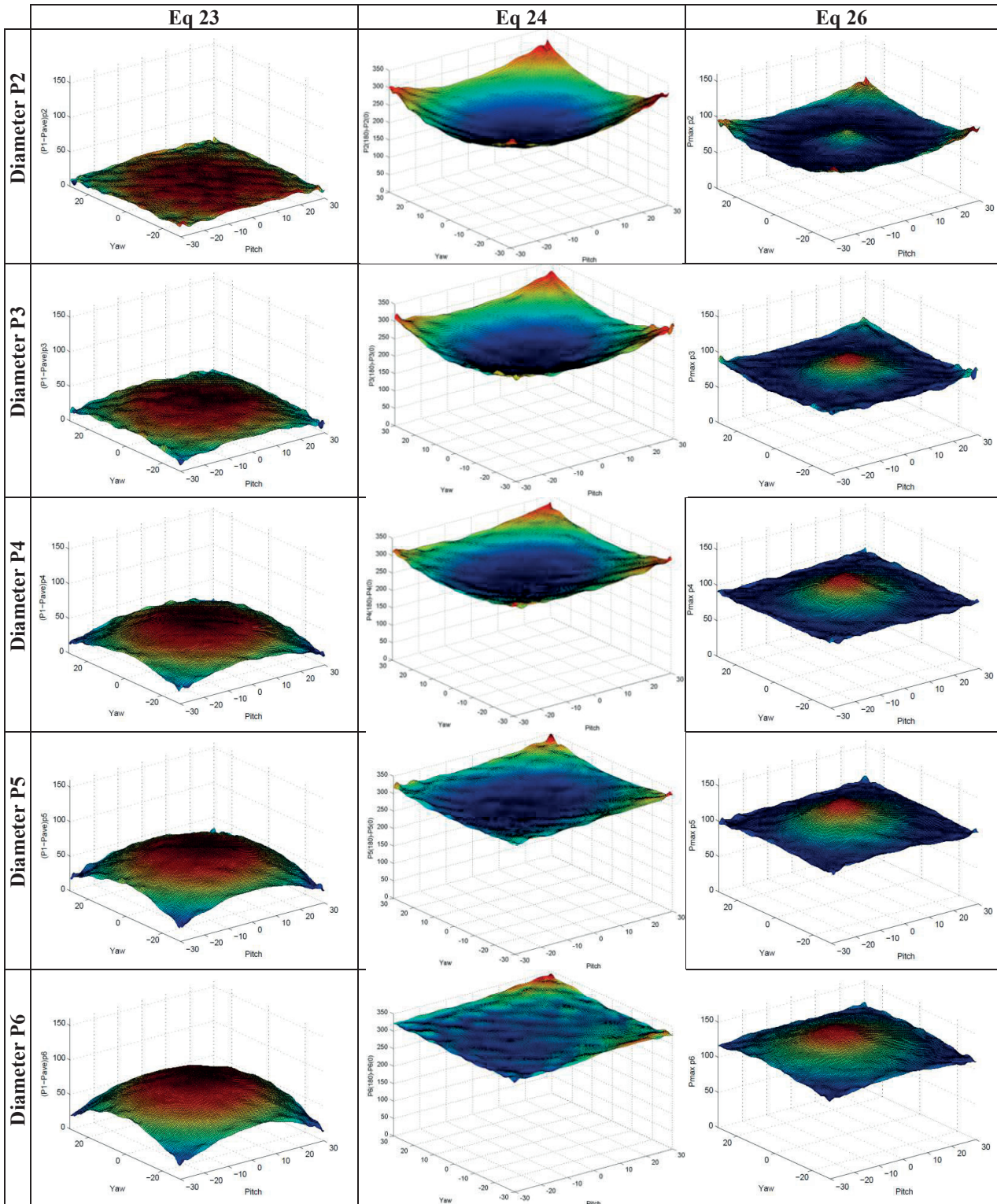
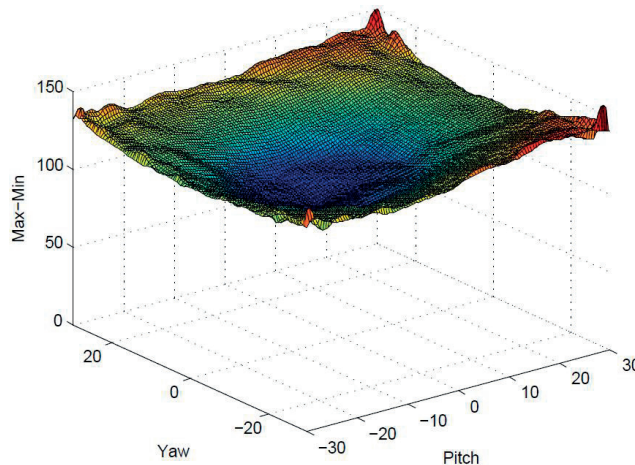


Fig. 22 : Coefficients denominator dependency on yaw and pitch angles

Therefore, in order to achieve the same range of sensitivity in flow changes between the two sensor model and the single sensor model, there will be necessary a much more sensitive-accurate pressure meter as well as more stable flow. Finally, Fig. 23 presents the quantity of eq. 27, which is used as a denominator in the total and static pressure coefficients of the 3<sup>rd</sup> and 4<sup>th</sup> calibration models.



**Fig. 23 : Coefficients denominator Eq 27**

## CONCLUSIONS

A small wind turbines cone was aerodynamically examined and successfully calibrated as a rotating single pressure probe which has the ability to define all the characteristics of a 3D flow by four distinctive single pressure probe calibration methods. In order to compare those models with a commonly used five-hole probe a rotating two pressure sensor calibration model was implemented for the same cone.

The two pressure sensors coefficients behaviour depended strongly on the peripheral sensors mounting diameter, leading to growth of their sensitivity and diminishing of their reliability as expected. On the contrary as concerns the single sensor models, the mounting diameter of the measuring sensor induced such small changes to the coefficients that they could be neglected. The above facts depend on the innovative normalization quantities that were used for each single sensor model, which were separately examined from the coefficients for further understanding. From the models used the best was the one that made use of the maximum pressure estimation during a whole rotation of the probe. Furthermore, the alterations that the blockage effect of the blades causes to the calibration coefficients were investigated proving that they are considerable.

The presented calibration models are appropriate for use not only by any wind turbine nose cone but with any pressure probe that has the ability to rotate and has axial symmetry. This leads to revolutionary calibration models that have similar capabilities with a common five-hole probe but require smaller and easier to construct probes with simplified calibration methods and most important of all a single pressure sensor mounted anywhere on the probes surface. Those characteristics result to a cost reduction in a 3D flow measurement equal to at least the manufacturing cost difference between the two mentioned probes.

## REFERENCES

- [1] J. Schlienger, A. Pfau, A.I. Kalfas, R.S. Abhari (2002) "Single pressure transducer probe for 3d flow measurements" 16th Symposium on Measuring Techniques in Transonic and Supersonic Flow in Cascades and Turbomachines Cambridge, UK September 2002.
- [2] Tanaka, K, Kalfas, AI, and Hodson, HP (2000), Development of Single Sensor Fast Response Pressure Probes, XVth Symposium on Measuring Techniques in Transonic and Supersonic Flows in Cascades and Turbomachines, Florence, Italy.
- [3] Babinsky H., Kuschel U., Hodson H. P., Moore D. F. Welland M. E. (2000) "The Aerodynamic Design and Use of Multi-Sensor Pressure Probes for MEMS Applications" XV Symposium on measuring techniques in turbomachinery Sep 21-22 Firenze Italy.
- [4] Antivachis K.N., (2011) "Wind flows vector determination through a single pressure sensor mounted on a wind turbines nose cone" Diploma thesis, Dep. of Mechanical Engineering Aristotle University of Thessaloniki.
- [5] Gossweiler C. (1993) On Probes and Measuring Techniques for Fast-Response Flow Measurement Using Piezo-Resistive Pressure Transducers, Dissertation ETH No. 10253, ETH Zurich, Switzerland
- [6] Gossweiler C. (1996) Unsteady Measurements with Fast Response Probes, Von Karman Institute for Fluid Dynamics, Bruxelles, Lecture series 1996-01.
- [7] Kupferschmied P., Gossweiler C. (1992), Calibration, Modelling and Data Evaluation Procedures for Aerodynamic Multihole Pressure Probes on the Example of a Four Hole Probe, Proc. 11th Symp. on Meas. Tech. for Transonic and Supersonic Flows in Cascades and Turbomachines, Munich, Germany.
- [8] Barigozzi G., Dossena V., Gaetani P., Development and First Application of a Single Hole Fast Response Pressure Probe, 15th Symposium on Measuring Techniques for Transonic and Supersonic Flows in Cascades and Turbomachines, Florence, Italy, Sep 28-29.

# AEROTHERMAL ANALYSIS AND CHARACTERIZATION OF SHIELDED FINE WIRE THERMOCOUPLE PROBES

**Laura Villafañe, Guillermo Paniagua**

Turbomachinery and Propulsion Department  
von Karman Institute for Fluid Dynamics  
Chaussée de Waterloo 72  
Rhode-Saint-Genèse, 1640, Belgium  
Email: laura.villafane@vki.ac.b

## ABSTRACT

Thermocouple probes for high accuracy gas temperature measurements require specific designs optimized for the application of interest and precise characterization of the uncertainty. In the present investigation a numerical procedure is proposed that outperforms previous experimental approaches to analyze the thermocouple response and the different sources of temperature error. The results presented from conjugate heat transfer simulations on different shielded thermocouples provide information of the influence of the design parameters on the different error sources. These outcomes could help experimentalists to better design future instrumentation.

*Keywords:* thermocouples, conjugate heat transfer (CHT), recovery factor, conduction effects, response time, transfer function

## 1. INTRODUCTION

In transonic intake research [1] high fidelity in the total temperature is needed. In the present investigation numerical simulations were performed to study the steady and unsteady heat fluxes within a temperature probe to evaluate both the temperature during a transient and at equilibrium.

Multiple attempts to provide correction factors for standard thermocouple designs were found in the literature [2],[3],[4]. Traditionally over-all recovery factors were experimentally determined as an indicator of the temperature error of a thermocouple. Such global recovery factors accounted for the total effect of radiation, conduction and convection on the probe for a given flow environment. The variability of the heat fluxes balance within the probe with the environment and probe design, required each thermocouple to be carefully designed and calibrated for the required application. However, precise corrections from experimental probe calibrations are impractical. During such calibration not only the flow conditions need to be replicated but also the thermal interactions between the probe and the test bench. Furthermore, the precision to reproduce and to characterize the calibration environment determines the accuracy of the corrections.

The numerical characterization of the probes excelled previous experimental experiences in accuracy. The presented numerical methodology allowed understanding and quantifying the effects of the design parameters, required to achieve precise gas temperature measurements. Adiabatic recovery factors, conduction error estimations and response time characteristics were determined for a shielded probe with different values of thermocouple wire diameter, wire materials and boundary conditions at the thermocouple wire support. The presented numerical approach may be coupled with optimizers to design the best probe for any specific application.

## 2. THERMOCOUPLE PROBE DESIGN

### 2.1. Application

A transonic wind tunnel with a distorted annular sector, helicoidal test section was manufactured to study a novel heat exchanger [1]. Total flow temperature measurements were to be performed in this intermittent wind tunnel discharging to the atmosphere from a pressurized vessel. The flow temperature decreased during a test run

due to the flow expansion in the reservoir. Flow temperature traverses were to be recorded along the test section of about 0.013 m<sup>2</sup> transversal area. High-frequency response was required in order to allow fast traverses. A rake of temperature probes allowed to maximize the measurement locations in a test. Precise characterization of the probe response was necessary to synchronize all readings, as well as to accurately analyze the heat exchanger efficiency.

## 2.2. Pre-existent design rules

The temperature of a thermocouple junction is the result of the energy balances including the convective heat flux between the junction and the surrounding gas, radiation to the walls, and conductive flux to the wire. The balance is different for each probe and each condition. The measured temperature would be equal to the total flow gas temperature in the absence of radiative heat fluxes, conductive flux to the thermocouple support and dissipation of kinetic energy in the boundary layer.

General design rules provide advises to reduce the temperature error sources. A shield is recommended in order to decrease the error caused by the dissipation of kinetic energy in the boundary layer around the junction (often called velocity error). The shield also provides structural resistance in high velocity flows and reduces radiation effects. However decreasing the velocity of the flow decreases the convective heat transfer, penalizing the conduction error and the response time. Thus, the internal velocity must be kept as high as allowable. The internal velocity is function of the vent hole to inlet ratio. The junction position within the shield is a compromise between non-aligned entrance flow effects, and flow alteration due to convective heat transfer to the shield. Recommended values are given by Rom and Kronzon [3], Saravanamuttoo [5] and Glawe et al. [2]. The wires within the shield can be placed parallel or perpendicular to the flow. In the first case, the length of the wires is limited to prevent wire bending. In the second, the length is limited by the shield diameter.

Conduction errors can be estimated from the simplified solution of the 1D energy equation for a wire element  $dx$ , (Eq.1), considering symmetry boundary condition  $\partial T/\partial x = 0$  at the junction ( $x = 0$ ), and isothermal temperature  $T_w = T_{sp}$  at the support of the wire ( $x = l$ ). Eq. 2 provides a simplified solution particularized for the junction. The assumption of constant gas temperature and constant convection coefficient  $h$ , neglects the effect of the real flow temperature differences along the wire.

$$h(T - T_g)\pi d_w dx = k \frac{\partial^2 T}{\partial x^2} \pi \frac{d_w^2}{4} dx \quad (1)$$

$$T_{ad} - T_j = \frac{T_{ad} - T_{sp}}{\cosh(l \sqrt{\frac{4h}{k_w d_w}})} = \frac{T_{ad} - T_{sp}}{\cosh(l/l_c)} \quad (2)$$

Let us consider the total temperature of the gas  $T_g$ , equal to the junction recovery temperature  $T_{ad}$ , namely the total temperature in the absence of velocity error. Design rules derived from this simplified solution recommend to have high values of  $h$  (high velocities), high  $l/d_w$  ratios, low conductivity wire materials, and support temperatures close to gas temperature. Petit et al. [6] suggest that the ratio  $l/l_c$  should not be smaller than 5.

The contribution of the error due to radiation is generally important at high flow temperatures. The simplified relationship (Eq.3) considering the most adverse conditions with unity view factor and equal conductive and radiative areas yielded a negligible error, lower than  $4 \cdot 10^{-4}\%$ , about 1 mK.

$$T_0 - T_j = \frac{K_R \sigma \epsilon A_R (T_j^4 - T_w^4)}{h A_c} \quad (3)$$

In flow temperature transients the energy balance at the thermocouple junction or on a  $dx$  at any position along the wire can be expressed by Eqs. 4. As in the steady case,  $T_g$  is considered equal to  $T_{ad}$  in the absence of velocity errors.

$$\begin{aligned} S_j h_j (T_g - T_j) + \frac{\pi}{2} d_w^2 k_w \left( \frac{\partial^2 T_w}{\partial x^2} \right) |_{x=0} &= \rho_j C_{p,j} V_j \frac{\partial T_j}{\partial t} \\ h_w (T_g - T_w) + \frac{d_w}{4} k_w \left( \frac{\partial^2 T_w}{\partial x^2} \right) &= \rho_w C_{p,w} \frac{d_w}{4} \frac{\partial T_w}{\partial t} \end{aligned} \quad (4)$$

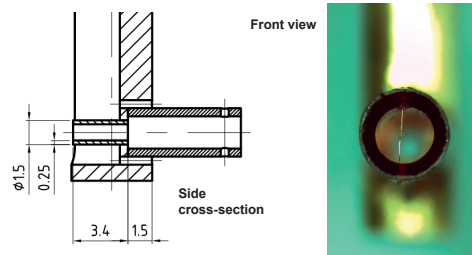


Figure 1: Shielded thermocouple probe.

In the case of uniform temperature on the junction, constant heat transfer coefficient independent with time, and no heat transfer by conduction between the junction and the adjacent wire, the thermocouple response to a temperature step is a first order system, Eq. 5. The assumption of first order system would be also valid for the assembly wire and junction if their diameters are identical, there are no radial or longitudinal temperature gradients, no conductive heat transfer to the supports, and the heat transfer coefficient is constant in time and along the length of the wire. Eq. 5, provides the time constant.

$$T_g = T_j + \tau \frac{\partial T_j}{\partial t}, \quad \text{with} \quad \tau_j = \frac{\rho_j C_{p_j} V_j}{h_j S_j}; \quad \tau_w = \frac{\rho_w C_{p_w} d_w^2}{4k_g N u_w} \quad (5)$$

### 2.3. Shielded probe design

The temperature probe consists of a rake of five shielded thermocouples. Minimization of blockage effects given the small transversal area of the test section is considered, while preserving the structural resistivity of the whole rake. The geometric characteristics of the temperature probe heads are sketched in Fig. 1.

A type T thermocouple (copper-constantan) is placed perpendicular to the flow with a total length equal to the internal shield diameter, 2 mm. This wire configuration is intended to avoid wire bending at high velocities. Ratios  $(l/d)_w$  of 79 are obtained with wires of  $25.4 \mu\text{m}$  diameter. The ratio weld-bead to wire diameter measured after probe manufacturing is about 2.7. The shield diameter is a compromise between the blockage minimization, wire structural resistivity and limitation of conduction errors. The shield is made of polycarbonate, chosen for its low conductivity. In agreement with the values recommended in the literature [2], [3], [5], the inlet/outlet area ratio is 4 and the junction is placed at  $1/2$  internal shield diameters from the entrance.

## 3. METHODOLOGY OF THE AEROTHERMAL STUDY.

The transfer function of the thermocouple probe was numerically obtained by evaluating the response to a temperature step. Experimentally, the accuracy of the temperature corrections required a precise control of the gas temperature excitation and test conditions.

At the transonic conditions of interest, the characteristic time for the flow to develop around the thermocouple is two orders of magnitude smaller than the characteristic time of the thermal transient in the thermocouple wires. This allows performing simulations in two stages. First, a steady simulation is solved to establish the flow around the probe considered isothermal. The flow-field solution of this first step is imposed as initial condition for the simulation of the second step. In the second step, the solid boundary conditions are changed and a conjugate heat transfer (CHT) simulation is performed, solving the energy balances within the thermocouple. This second stage is ran in steady or transient state depending on whether the interest is focused on the steady temperature errors or on the transient behavior. In the latter case, the result is the response of the thermocouple to a temperature step. The decomposition in two stages highly reduces the computational cost.

This methodology allows the detailed analysis of the heat fluxes within the thermocouple probe, and the evaluation of the influence of the flow environment, probe geometry and wire materials.

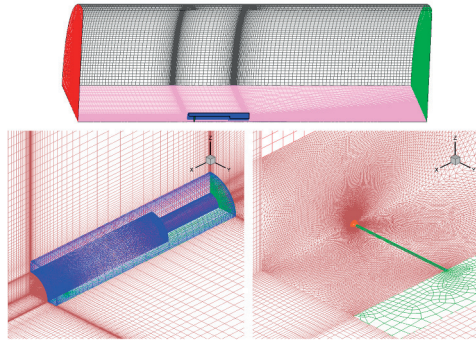


Figure 2: Computational domain. Left: TC shield view. Right: TC wire and junction.

Table 1: Probe geometric configurations.

	<i>Geom 1</i>	<i>Geom 2</i>	<i>Geom 3</i>
$l, [mm]$	1	1	1
$d_w, [mm]$	0.0254	0.0508	0
$d_j, [mm]$	0.07	0.14	0.07

## 4. NUMERICAL TOOLS.

### 4.1. Computational domain and solver

The shielded thermocouple head is modeled in a 3D domain constituted by a quarter of a cylinder thanks to the existence of two symmetry planes on the probe geometry. The grid extends 6 shield diameters in the radial direction and in the axial direction upstream of the probe, and 10 diameters downstream. The three solid parts (shield, wire and junction) are meshed independently and concatenated to the gas domain mesh in the used NS solver. The gas hybrid 3D mesh composed by about 1.75 million cells is shown in Fig. 2-b. The grid is refined along the walls of the solid parts and specially around the thermocouple wire and junction (Fig. 2-c).

The Reynolds Averaged Navier Stokes solver employed was CFD++ (v.8.1). The k-epsilon turbulence model was considered. The initial values of k and epsilon were estimated in function of the free stream nominal velocity, with a free-stream turbulence level of 1% and a turbulence length scale based on the tube inner diameter. Values of  $y^+$  in the vicinity of the thermocouple junction are lower than 0.3, and lower than 0.5 along the wire. For the steady simulations on both stages, convergence was achieved after 1000 iterations, 5.5 hours CPU time in 8 parallel Intel Core 2 Quad Q9400 (2.66 GHz) machines. For the transient CHT simulations the number of iterations required to achieved convergence varied depending on the wire material simulated. As an average 1000 iterations with different time steps were required, involving 51 hours CPU time running in 8 parallel machines. The integration time step was adjusted as function of the rate of evolution of the junction temperature, starting from 0.1ms.

### 4.2. Numerical test conditions

Nominal flow conditions for the simulations correspond to inlet boundary conditions  $T_s = 273.22K$ ,  $P_s = 101325Pa$ ,  $V_\infty = 231.12m/s$ , and  $P_s = 101325Pa$  at the domain outlet. Different Mach and Reynolds numbers were tested for the geometrical configuration corresponding to the design geometry, Table??.

Three geometrical configurations were analyzed: *Geom 1, 2 and 3*, (ref. 1). The shield is the same in the three cases. *Geom 1* corresponds to the design geometry. The modified parameter is the wire diameter, doubled in *Geom 2* where the ratio junction to wire diameter has been kept constant. *Geom 3* refers to the test case of a junction with infinitely thin wires.

Heat loss through the wires to the support is function of the wire dimensions and flow conditions (convection), but also of the material conductivity, and the support temperature. Different wire materials and boundary conditions at the support were analyzed for the configurations *Geom 1* and *Geom 2*. In all cases the shield material is polycarbonate and the junction properties are the average of the two materials of type T thermocouple. Other two materials of lower conductivity were considered: Nicrosil and an ideal material with conductivity equal to one, Tab. 2. The different support boundary conditions tested were:

- (a) The shield-support behaves as an adiabatic solid,
- (b) the shield is isothermal at 300 K,
- (c) CHT on the shield.

Table 2: Material properties of thermocouple wires. Evaluated at 23

	Copper	Constantan	Nicrosil	Ideal	Polycarbonate
$K$ , [ $\text{W m}^{-1} \text{K}^{-1}$ ]	401	19.5	13	1	0.2
$\rho$ , [ $\text{kg m}^{-3}$ ]	8930	8860	8530	8860	1210
$C_p$ , [ $\text{J kg}^{-1} \text{K}^{-1}$ ]	385	390	460	390	1250

## 5. STEADY TEMPERATURE EFFECTS.

### 5.1. Global Temperature Correction

The junction temperature results from the balance between the convective heat fluxes gas-junction and gas-wire, and conductive flux junction-wire and wire-support. If those effects were decoupled, individual error equations could be used to estimate the deviation of the measured temperature. However, in practical applications the junction temperature must be evaluated by the simultaneous solution of the different heat flux rates [7].

The overall recovery factor  $Z$  (Eq. 6), the difference between the measured temperature ( $T_j$ ) and the total gas temperature ( $T_0$ ), can be decomposed into several contributions. The first term (a) is the velocity error, related to the adiabatic recovery factor. The second term (b), takes into account the temperature error due to conduction and convection along the wire, for a given support-shield temperature, ( $T_{sp}$ ). The last term (c) collects the velocity error of the support-shield and the conduction effects between the shield, probe stem, and external probe support. The numerical method applied allows analyzing separately each contribution.

$$(1 - Z) = \frac{T_0 - T_j}{T_0 - T_\infty} = \overbrace{\frac{T_0 - T_{ad}}{T_0 - T_\infty}}^a + \overbrace{\frac{T_{ad} - T_j}{T_{ad} - T_{sp}}}^b \cdot \overbrace{\frac{T_{ad} - T_{sp}}{T_0 - T_\infty}}^c \quad (6)$$

### 5.2. Velocity error

Temperature probes are intended to measure the gas total temperature, i.e. the temperature that the gas would attain if it is brought to rest through an isentropic process. However, in real gases frictional heat is generated within the boundary layer, hence the conversion of kinetic energy into thermal enthalpy is not perfect. The recovery factor, Eq. 7, represents the amount of kinetic energy recovered by the gas, where  $T_{ad}$  is the temperature of the surface of the junction if it would behave as an adiabatic body, and  $V$  is the reference upstream flow velocity. The recovery factor is function of the geometry of the immersed body and the Prandtl number of the fluid. Experimental values of adiabatic recovery factor determined by different authors [8],[9],[10] were presented by Moffat [11].

$$r = \frac{T_{ad} - T_s}{V^2/2C_p} = 1 - \frac{T_0 - T_{ad}}{V^2/2C_p} \quad (7)$$

For shielded thermocouples behaving as adiabatic bodies, the term (a) in Eq. 6 represents an overall adiabatic recovery factor, related to  $r$  by Eq.8. The velocity upstream of the junction within the shield ( $V$ ) is different from the free stream flow velocity ( $V_\infty$ ).



$$Z_a = \frac{T_{ad} - T_s}{V_\infty^2/2C_p} = 1 - \frac{T_0 - T_{ad}}{V_\infty^2/2C_p} = 1 - (1 - r) \frac{V_{int}^2}{V_\infty^2} \quad (8)$$

Experimental determination of recovery factors was impractical since the junction temperature has to be determined with great accuracy, and ensuring negligible influence of conduction to the supports, so the junction behaves as an adiabatic body. Steady simulations at different flow velocities allowed determining both  $r$  and  $Z_a$  and their sensibility to flow Mach and Reynolds numbers. Wire and shield were considered adiabatic solids in the computations and CHT was solved at the junction, at  $T_{ad}$ .

Computations were also performed considering all the solid boundaries adiabatic, junction included. The average temperature on the junction adiabatic surface  $T_{ad,m}$  was compared with the junction temperature obtained when CHT was applied. Temperature differences were observed to be lower than 0.004 % ( $T_{ad,m} - T_{ad}/T_{ad,m}$ ). These small differences were explained by the junction heat capacity.

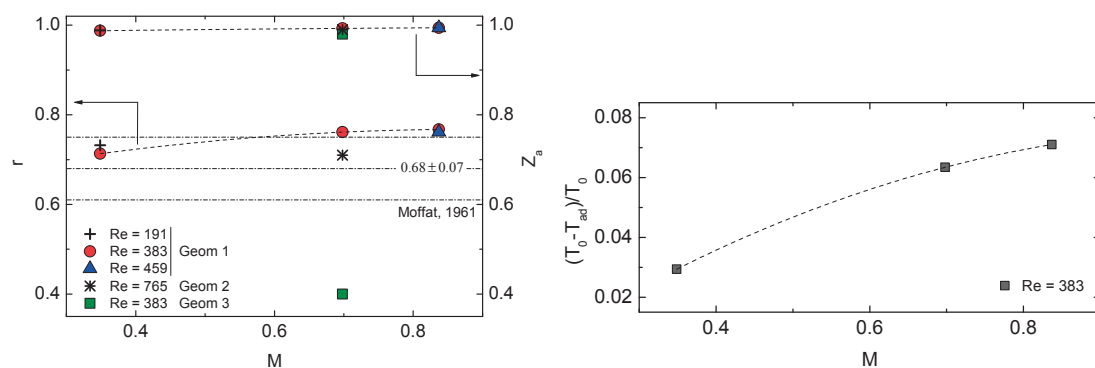


Figure 3: a) Recovery factors for different probe geometries, Mach and Reynolds numbers, b) Temperature error due to no isentropic flow deceleration

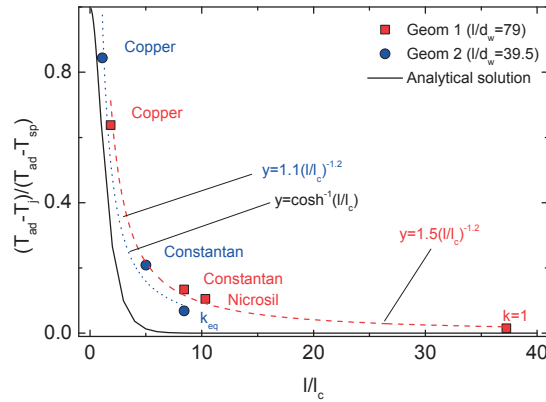
Figure 3(a) shows the evolution of the recovery factor ( $r$ ), and the overall recovery factor ( $Z_a$ ), for different Reynolds and Mach numbers. The adiabatic recovery factor slightly increases with the flow Mach number, and thus with the velocity within the shield (about six times slower than the external flow). The results are in good agreement with the recovery values compiled by Moffat [11]. For the same probe geometry *Geom 1*, at constant temperature and Mach number, an increase in the Reynolds number achieved through an increase in static pressure, results in a slightly decrease of the recovery factor. An increase of the Reynolds number at nominal flow conditions due to the increase of the wire and junction diameter (*Geom 2*), yields to an analogous decrease of the recovery factor. The overall recovery factor shows the same trend but less sensitive to Mach and Reynolds variations.

Recovery factors were computed likewise for *Geom 3*, providing lower values. The flow behavior around a sphere is not similar to that around a thermocouple junction, neither to the flow parallel to a cylinder [11]. Comparison of the flow fields around the junction for *Geom 1* and *Geom 3*, showed a stronger flow deceleration in the first case forced by the presence of the wires, and hence, a thicker thermal boundary layer. Consequently the transformation of the flow kinetic energy into thermal energy is more efficient.

Although the recovery factor increases with the Mach number, the kinetic velocity rises in a higher amount, thus the temperature error represented in Fig. 3(b) also increases with velocity.

### 5.3. Conduction error

Free of velocity errors, the difference between the real junction temperature and the total temperature is the error due to conduction, namely the product of terms (b) and (c) in Eq.6. In a well designed thermocouple the junction temperature should be little sensitive to the support temperature, i.e. the term (b) is close to zero. In that case the overall contribution of conduction would be negligible whatever is the value of term (c). In real applications term (b) is different to zero.



**Figure 4: Ratio junction to support temperature deviations with respect to total temperature in function of the parameter  $l/l_c$ . Results from CHT simulations.**

Term (b) reflects the influence on the junction of the balance conduction-convection along the wire and the conduction with the support. Its contribution can be estimated by the solution of the one dimensional energy equation, Eq.2, that predicts an exponential decrease with the increase of the parameter  $l/l_c$  (for  $x \geq 5$ ,  $\cosh x \approx 0.5e^x$ ). Term (c) indicates the strength of the conduction heat transfer between the thermocouple and the support. The lower temperature of the shield-support with respect to the total gas temperature ( $T_{ad}$  in the absence of velocity error),  $T_{ad} - T_{sp}$ , drives the conduction to the wire. In the case the support would be perfectly isolated from external sources, it is function of the recovery factor of the complete shield/support. In real applications it is also function of the depth of immersion of the support in the flow, the support geometry and thermal properties, and the external boundary conditions of the probe.

The values of the parameter  $l/l_c$  for each material and the geometries *Geom 1 and 2* are indicated in Tab. 3. For the computation of  $l/l_c$ , Eq. 9, air conductivity is evaluated at the gas total temperature [7], and the Nusselt number is derived from a correlation for wires perpendicular to the flow [11]:  $Nu = (0.44 \pm 0.06)Re^{0.5}$ .

$$\frac{l}{l_c} = l \sqrt{\frac{4h}{k_w d_w}} = \frac{2l}{d_w} \sqrt{\frac{Nuk_g}{k_w}} \quad (9)$$

**Table 3: Material parameters of thermocouple wires affecting conduction.**

	Constantan	Copper	Nicrosil	Ideal	Equivalent
$k$ , [kW m <sup>-1</sup> K <sup>-1</sup> ]	19.5	401	13	1	6.89
$l/l_c$ (Geom 1)	8.43	1.86	10.33	37.24	
$l/l_c$ (Geom 2)	5.01	1.11	n.a.	n.a.	8.43

Fig. 4 shows the non-dimensional conduction temperature error corresponding to term(b) in Eq.6. All results correspond to complete CHT simulations. The temperatures difference ratio is plotted versus the parameter  $l/l_c$ , which for a given probe geometry is only varied by a change in the wire material. The error decreases as the parameter  $l/l_c$  increases indicating that the junction temperature is less influenced by the conduction effects. The results show two slightly distinct trends for each  $l/d_w$  case that are best fitted by power laws with a common exponent coefficient of -1.2. The equivalent material,  $k_{eq}$ , corresponds to an hypothetical material with a conductivity such that the  $l/l_c$  value for *Geom2* is equal to the  $l/l_c$  value for constantan wire and *Geom1* ( $k_{eq} = k_{const} \sqrt{2}/4$ ). At this  $l/l_c$  value (8.43), the contribution of conduction of term (b) is slightly smaller for *Geom2*. The analytical prediction (Eq.2) underestimates the results when compared with the numerical results. This discrepancy can be explained by the simplifications introduced in the analytical solution, especially the assumption of homogeneous gas temperature and heat transfer coefficient along the wire, and equal to the conditions and geometry at the junction. The parameter  $l/l_c$  is a good estimator of the conduction error, but inappropriate to establish a unique relation with the temperature error.

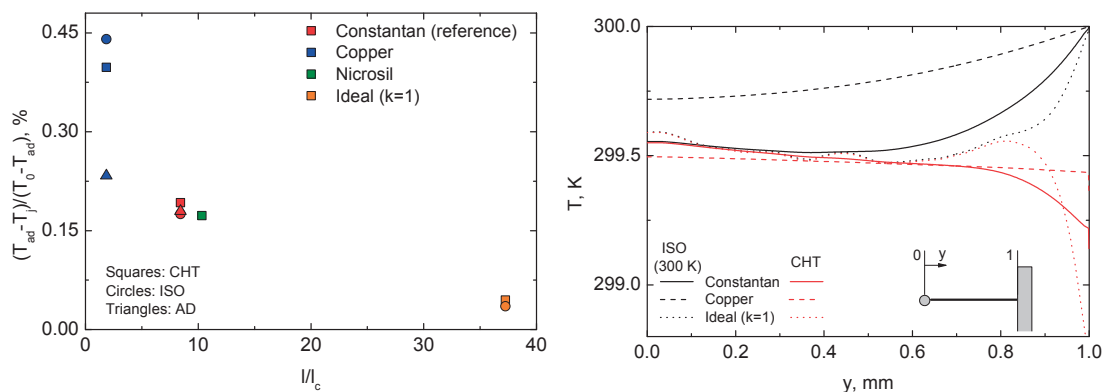


Figure 5: a) Overall temperature errors due to conduction in function of  $l/l_c$ , b) Wire temperature distributions

Figure 5(a) represents the global contribution to the conduction error computed for the reference probe geometry (*Geom1*) for different materials. The figure compares for a given wire material and geometry, thus a given  $l/l_c$ , the variability of the temperature error due to the conditions at the shield/support. Fig. 5(b) displays the temperature distribution along the wire in the same conditions for three of the materials and two of the boundary conditions, adiabatic support and CHT within wire and support. The junction temperature ( $y = 0$ ) is the same for the ideal wire ( $l/l_c = 37$ ) independently of the conduction at the shield, with an overall conduction error about 0.04%. The temperature at each position along the wire is less affected by the longitudinal conduction, hence by the shield temperature, and more by the convective heat flux. Thus the temperature distribution is able to reflect the non homogeneity of the gas temperature around the wire. The junction is only influenced by the wire temperature adjacent to it, and the effect of the shield temperature penetrates until the last 20% of the wire. In the case of constantan wire the temperature along the wire is affected by conduction to the shield to a higher extent. However, the temperature at the junction converges to almost the same value for the different boundary conditions. Overall conduction errors vary between 0.18 and 0.19%. In the copper wire case, with a  $l/l_c$  about 2, conduction with the support influences the junction temperature in a higher degree. Errors vary between 0.23 and 0.45% depending on the support conditions.

The reference adiabatic temperature considered for the analysis of the conduction errors is that of the junction. However, due to the strong flow deceleration taking place around the wire in the vicinity of the junction, there is a less efficient flow deceleration in this region. Thus, the temperature recovered is lower when compared to the junction. This effect can be observed in Fig. 5(b) for the ideal wire distribution in which the temperatures at 10 to 20% from the junction are slightly lower than at the junction. It explains also the slight difference between the junction temperatures for constantan and ideal material wires. The higher conductivity of constantan forces the junction to stabilize at the lower temperature of the wire in the vicinity, while for the ideal material the temperature at the junction rises to almost the adiabatic temperature.

## 6. TRANSIENT TEMPERATURE EFFECTS.

The diffusion of the heat fluxes within the probe introduce a temperature lag on the junction temperature with respect to the gas temperature. The properties and geometry of the thermocouple wires affect the junction temperature evolution.

The numerical methodology applied in this study allowed analyzing the temperature evolution on the complete probe in response to a temperature step. All the results correspond to the nominal flow conditions, with an initial probe temperature equal to  $T_i = 300$  K.

The temporal evolution of the temperature along the constantan wire for *Geom1* is displayed in Fig.6. At each position along the wires, the rate of temperature change is different. The response time of the shield is much

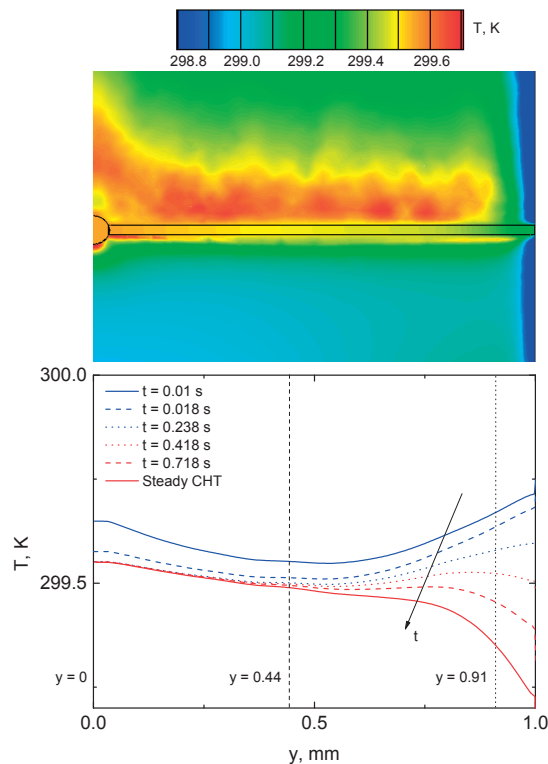


Figure 6: a) 2D temperature contour, steady conditions. b) Evolution of constantan wire temperature distribution. CHT result

higher than that of the junction or wire due to its larger thermal inertia and lower thermal diffusivity  $a$ . Thus the part of the wire closer to the junction  $y = 0$  reached the final temperature faster than the part of the wire close to the shield/support due to its influence by conduction. Figure 7 shows the time temperature history at three wire positions and a point within the shield, for constantan and copper materials. The temperature traces are made non dimensional with their steady value in order to compare the response times, not taking into account the differences on the final temperature achieved.

All the temperature distributions, except that of the shield, showed a fast initial temperature change, followed by a slower evolution. The fast initial temperature rise is dictated by the inertia of the junction or wire elements. The slow down is accentuated by the influence of the support at a certain position. In the constantan case the junction overpassed the conventional threshold of the 63.2 % of the response in 6.5 ms, and achieved the 90% of the final temperature in 18 ms. The temperature at  $y = 0.44$  mm showed a faster initial rise due to the lower thermal inertia of a wire element when compared with the junction, of bigger volume. However the convergence to the final temperature takes longer than in the junction due to the influence of the evolution of the shield at this point. The same behavior was observed at  $y = 0.91$ , but influenced in a higher degree by the shield temperature evolution.

The comparison of the temperature evolutions in the copper wire case, is analogous. When compared with the constantan results, the initial response of the copper is slightly slower, and the temperature evolutions at the different points closer in terms of the temperature rate evolution. It is explained by the higher conductivity of the copper, that implies higher diffusivity along the wire, and thus smoother temperature gradients between the different positions. Whereas in the constantan case, the effect of the support is little felt close to the junction but greatly affecting the opposite wire extreme.

In the ideal case of no existence of conductive heat between junction and wire, or if equal wire and junction diameters and no conduction flux with the support, the response of the thermocouple would be that of a first order system, Eq. 5. The characteristic would be the time required to complete 63.2 % of its response to a

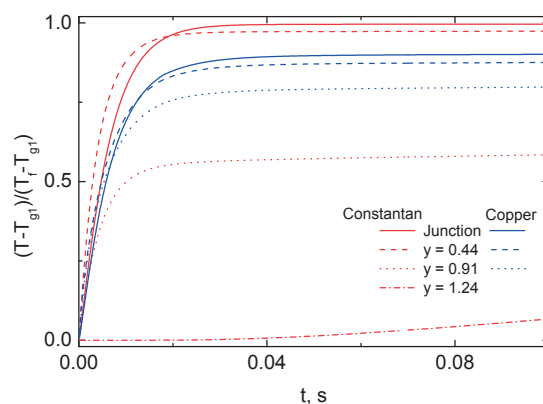


Figure 7: Temperature evolution at four control points on constantan and copper wires

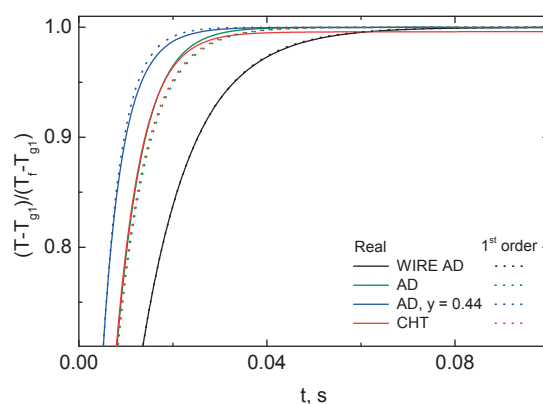


Figure 8: Comparison junction temporal evolutions with the correspondent first order.

gas temperature step. None of the wire temperature evolutions represented in Fig.7 corresponds to a first order response due to the influence of the support.

Non dimensional junction temperature evolutions are represented in Fig. 8 for the ideal case of adiabatic wire, and constantan wire with two different support conditions: CHT and adiabatic. For each evolution the time to reach 63.2% of the final temperature was used to evaluate the correspondent first order response. When the wires are considered adiabatic, the junction evolution collapses to the first order response. The presence of the wires modifies the temperature response whatever the condition at the support. When no flux occurs between shield and wires the junction reach the final temperature without the delay caused by the support but it does not correspond to a first order. This result is in agreement with the works of Yule [12] and Petit [6]. The influence of the wires causes an acceleration of the junction response if compared with the adiabatic wire result. It is instigated by conductive effects from the faster response of a wire element. The evolution at  $y = 0.44$  is included in the graph for comparison. A simple decomposition in two first order systems expressing the response of the wire and support as done in cold wires [13] does not accurately reproduce the junction response in the presence of conductive effects.

Figure 9 displays the non dimensional junction temperature evolutions for different wire materials and the two wire diameters (*Geom1* and *Geom2*). All cases correspond to complete CHT simulations with the consequent possible influence of the slower response of the support. For the cases in which the conductive effects on the junction are not too noticeable ( $l/l_c \geq 5$ ), the higher the wire conductivity the faster the response of a wire element and therefore the faster the response of the junction. Increasing the wire and junction diameters introduces a delay in the response due to the increase of the thermal inertia, and a decrease of the parameter  $l/l_c$ , hence an increase of the conductive fluxes.

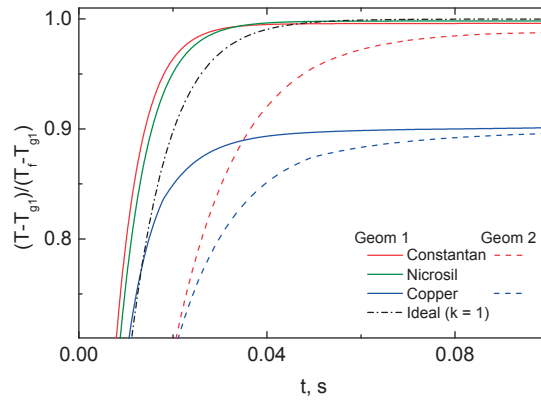


Figure 9: Junction temporal evolution. CHT simulations

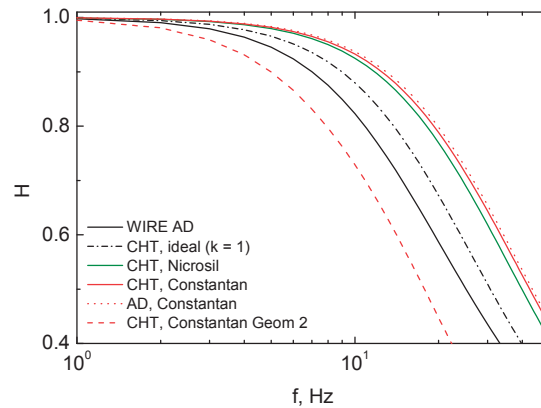


Figure 10: Transfer functions for different wire materials, wire diameter, and support conditions

Assuming the response of a thermocouple can be expressed as linear system model of  $m$ -order, the transfer function of the thermocouple in the  $Z$  domain can be expressed by the ratio of two  $m$ -order polynomials, Eq. 10. A digital procedure [14] was used to determine the invariant transfer function that reproduces better the junction response in each case.

$$H(z) = \frac{b_0 \cdot z^{-d} + b_1 \cdot z^{-1-d} + \dots + b_m \cdot z^{-m-d}}{1 + a_1 \cdot z^{-1} + a_2 \cdot z^{-2} + \dots + a_m \cdot z^{-m}} \quad (10)$$

A first order response was found for *Geom1* with adiabatic wires and for *Geom3*, in accordance with the temporal analyses. A second order system fitted the junction response when the support is adiabatic. A second order system represented likewise the complete CHT simulation in the case of the ideal wire material, where the conductive effects are negligible. For the case of the nicrosil wire, a third order response was found. The higher the effect of the support, the higher the order of the system found to represent the transfer function. The response was found to be that of a 5<sup>th</sup> order system, for both *Geom1* and *Geom2* and constantan wire. For copper wires the response could be considered 5<sup>th</sup> or 6<sup>th</sup> order, although the fitting was less accurate. The transfer functions representing the junction responses for several test cases are shown in Fig. 10. The faster response corresponded to constantan wires with cutting frequencies slightly higher than 10 Hz.

## 7. CONCLUSIONS.

A new methodology was proposed to numerically resolve the evolution of the heat transfer balances within a thermocouple probe. This procedure was applied to a shielded thin wire thermocouple, providing valuable information of the effect of the design parameters on the different error sources. This method overcame the experimental difficulties providing detailed information of the performances of a given probe in the range of flow conditions of interest.

Results from conjugate heat transfer simulations were analyzed at different values of the main non dimensional parameters driving the heat fluxes within the thermocouple probe. This approach allowed dissecting the commonly described experimental "recovery factor" into two steady error sources: flow velocity effects and conductive-convective errors. Radiation effects were shown to be negligible for the flow environment of interest.

Recovery factors for the shielded probe were computed at different Mach and Reynolds numbers. The temperature error increase due to velocity effects was evaluated, confirming the benefit of shield designs against bare thermocouples at high velocities.

Temperature errors due to conduction were analyzed for different test cases. The influence of conductive errors on the junction temperature is mainly dictated by the parameter  $l/l_c$ , which collects the effects of the wire conductivity, length and diameter and flow convective heat transfer, and by the support characteristics. The decrease of the temperature error with increasing values of  $l/l_c$  is reported. When values of the parameter  $l/l_c$  higher than 5 cannot be achieved, the junction temperature error is dominated by the wires support.

Time resolved CHT simulations allowed analyzing the temporal temperature evolution within the probe. The effect of the design parameters on temperature change rate was analyzed. The transfer function of the junction temperature response was obtained for the different tests simulated. The order of the lineal differential equation modeling the response was shown to increase with the influence of the conductive effects from the support on the junction. The response could be that of a second or third order differential linear system for  $l/l_c$  values higher than 10.

The presented methodology coupled with optimizers would provide a tool to design the best probe for a specific application.

## ACKNOWLEDGMENTS.

This work was sponsored by TechSpace Aero in the frame of INTELLIGENT COOLING SYSTEM project. The financial support of the Region Wallone and the pole of competitiveness Skywin is acknowledged. The authors are grateful to V. Van der Haegen for his valuable contribution on the numerical work.

## REFERENCES.

- [1] L. V. ne, G. Paniagua, M. Kaya, D. Bajusz, S. Hiernaux, Development of a Transonic Wind Tunnel to investigate Engine Bypass Flow Heat Exchangers, Proc. IMechE, Part G: J. Aerospace Engineering 225, 8 (2011) 902–914.
- [2] G. E. Glawe, R. Holanda, L. N. Krause, Recovery and Radiation Corrections and Time Constants of Several Sizes of Shielded and Unshielded Thermocouple Probes for Measuring Gas Temperature, Tech. rep., Lewis Research Center, Cleveland, Ohio (1978).
- [3] J. Rom, Y. Kronzon, Small shielded thermocouple total temperature probes, Tech. rep., Institute of Technology, Israel (1967).
- [4] T. M. Stickney, Recovery and time-response characteristics of six thermocouple probes in subsonic and supersonic flow, NACA TN 3455, Tech. rep., Lewis Flight Propulsion Laboratory, Cleveland Ohio (1955).
- [5] H. I. H. Saravanamuttoo, Recommended practices for measurement of gas path pressures and temperatures for performance assessment of aircraft turbine engines and components, Advisory Report 245, AGARD Advisory Report No. 245 (1990).
- [6] C. Petit, P. Gajan, J. C. Lecordier, P. Paranthoen, Frequency response of fine wire thermocouple, J. Phys. E: Sci. Instrum 15 (1982) 760–764.
- [7] M. D. Scadron, I. Warshawsky, Experimental determination of time constants and Nusselt numbers for bare wire thermocouples in high velocity air streams and analytic approximation of conduction and radiation errors. NACA TN 2599, Technical Note 2599, Lewis Flight Propulsion Laboratory, Cleveland, Ohio (1952).
- [8] C. H. H. A. Kalitinsky, Temperature measurements in high velocity air streams, Trans. ASME 67 (1945) A–25.
- [9] F. S. Simmons, Recovery Corrections for Butt Welded stright wire thermocouples in high velocity, high temperature gas streams, Tech. rep., NACA RM-E54G22a (1954).
- [10] G. Glawe, F. S. Simmons, T. M. Stickney, Radiation and recovery corrections and time constants of several chromel-alumel thermocouple probes in high temperature high velocity gas streams, Tech. rep., NACA TN-3766 (1956).
- [11] R. J. Moffat, Gas temperature measurement.

- [12] A. J. Yule, D. S. Taylor, N. A. Chigier, Thermocouple Signal Processing and On-Line Digital Compensation, *Journal of Energy* 2, No 4 (1978) 223–231.
- [13] R. Dnos, C. Sieverding, Assessment of the cold wire resistance thermometer for high speed turbomachinery applications, *Journal of Turbomachinery* 119, N0 1 (1997) 140–148.
- [14] G. Paniagua, R. Dnos, Digital compensation of pressure sensors in the time domain, *Experiments in Fluids* 32, No 4 (2002) 417–424.





# INFLUENCE OF THERMOCOUPLE THERMAL INERTIA IN IMPINGEMENT HEAT TRANSFER EXPERIMENTS USING TRANSIENT TECHNIQUES

Alexandros Terzis<sup>\*1</sup>, Jens von Wolfersdorf<sup>2</sup>, Guillaume Wagner<sup>3</sup>,  
Bernhard Weigand<sup>2</sup> and Peter Ott<sup>1</sup>

<sup>1</sup>Group of Thermal Turbomachinery (GTT),  
École Polytechnique Fédérale de Lausanne (EPFL) CH-1015, Lausanne, Switzerland

<sup>2</sup>Institute of Aerospace Thermodynamics (ITLR), Universität Stuttgart  
Pfaffenwaldring 31, D-70569, Stuttgart, Germany

<sup>3</sup>Alstom, Baden, Switzerland

\*Contact details: Alexandros Terzis  
Group of Thermal Turbomachinery (GTT), ME A2 475, EPFL SCI-STI-PO Swiss Federal Institute of  
Technology, CH1015, Lausanne, Switzerland  
Tel: +41 (0) 21 693 3539 / E-mail: [alexandros.terzis@epfl.ch](mailto:alexandros.terzis@epfl.ch)

## ABSTRACT

A typical transient heat transfer experiment for an impingement cooling configuration requires usually a temperature step in the flow. A moving isotherm of the liquid crystal surface coating is then monitored using a video camera. However, for small impingement configurations, when only a small number of holes is used, the massflow rates are relatively low, leading to very small plenum velocities. Therefore, a step change in the power settings does not cause a temperature step in the mainstream flow. Many researchers approximated the real hot gas temperature evolution by a number of ideal temperature steps (Duhamel's superposition principle). However, thermocouple acquisition measurements are influenced by the size of the thermocouple due to thermal inertia and therefore direct evaluation of the heat transfer coefficient with these data may be in error. This paper suggests that the hot gas temperature which drives the transient experiment and is measured in the plenum can be corrected according to the time constant of the thermocouples. Several experiments were carried out in order to evaluate the time response of fine thermocouples with exposed junction. For the impingement configuration, a single row of five inline impingement holes is used at in a narrow passage configuration over a range of Reynolds numbers (15000-55000). The liquid crystal signal is evaluated with three different hot gas temperature approaches: (1) *Perfect temperature step*, (2) *Duhamel's principle in the acquired temperature data* and (3) *Correction of hot gas temperature for thermal inertia prior to Duhamel's principle*. The experimental data are analyzed by means of various post-processing procedures and aim to clarify and quantify the effect of thermocouple thermal inertia on the final results.

## INTRODUCTION

Turbine blade impingement cooling finds great applicability in modern gas turbine engines providing enhanced heat transfer capabilities compared to traditional convective cooling passages while the continuously injected coolant flow ensures very high heat fluxes in the stagnation region of the jets. A detailed review for multi-jet impingement configurations can be found e.g. in the review paper of Weigand and Spring (2011) [1].

One of the most famous measurement techniques which is used to evaluate the heat transfer characteristics of impingement cooling systems is the transient liquid crystal technique which finds great applicability in turbomachinery applications over the last 20 years. Detailed reviews of the applied method and its applications can be found e.g. Baughn (1995) [2], Ireland (1999) [3], Ireland and Jones (2000) [4] and Poser and von Wolfersdorf (2011) [5]. The main advantages of this technique are the direct local temperature measurement over

the test surface with high resolution and the non-intrusive measurement. With other words, this technique uses the full surface temperature history derived from the color of the liquid crystals in order to obtain full surface heat transfer coefficient distributions on the examined surfaces.

Van Treuren *et al.* (1994) [6] developed the first test rig capable for a transient liquid crystal experiment measuring both the local adiabatic wall temperature and the local heat transfer coefficient under an array of impinging jets. The idea in this work was to create a sudden temperature step in the flow using a heat exchanger. The temperature step was achieved by switching properly valves and bypass flow so that hot air from an introductory plenum chamber was then introduced inside the impingement array forcing the color change of the liquid crystals. A similar test rig was used by Huang and El-Genk (1994) [7]. They supplied compressed air in an electric heater and a three-way ball diverted valve was used in order to isolate the main flow from the plenum chamber of the test rig. Once the conditions were stabilized, switching off the valve allowed hot gas to enter the plenum chamber and initiated the transient experiment. However, the main disadvantage of fast acting valves is the complexity of the design and that the mainstream temperature rise cannot be represented as a real step. Other approaches include rapidly inserting a model into a wind tunnel of a constant mainstream temperature which is higher than the initial model temperature, as for example in the studies of Falcoz *et al.* (2006) [8] and Wagner *et al.* (2007) [9]. However, the performance of any mechanical injection system is highly dependent on the size of the test rig and hence the inertia forces of the test model. Obviously, the large scale impingement test models which are usually required for higher resolution and increased Reynolds numbers cannot be assumed suitable for pneumatic insertion mechanisms.

The mechanical complexities of fast acting valves or model positioning activators can be avoided using the concept of a heater mesh, originally developed by Gillespie *et al.* (1995) [10]. The heater mesh is used in order to increase the temperature of the mainstream flow taking advantage of *Joule Heating*. Additionally, the temperature step achieved with a heater grid configuration is relatively quick and thus ideal for a transient heat transfer experiment (Esposito *et al.* (2009) [11]). However, in many experiments, and especially for small impingement configurations where the number of holes is low, the massflow rates are relatively small leading to very low plenum velocities ( $<1\text{m/s}$ ). As a result, a step change in the power settings does not cause a step change in the flow temperature. Many researchers used Duhamel's superposition principle assuming a series of step changes in the mainstream temperature, although the accuracy of this method requires a relatively small time step and thus high acquisition rate, as shown by Kwak (2008) [12]. An additional concern at this velocity level is that the thermocouple measurements are influenced by their response time. In such cases, it is quite difficult to determine the hot gas temperature which drives the transient experiment and a correction based on their response time should be applied in order to increase the accuracy of the results. Most of the attempts made to measure experimentally response time of thermocouples involve submersion of the thermocouple inside a liquid bath and the time required to reach 63.2% of the steady state bath temperature was considered as the response time for the given thermocouple (Wormser (1960) [13], Murdock *et al.* (1963) [14]). However, these methods appear to be inappropriate when the thermocouples are subjected to a gas stream. On the other hand, attempts to measure the response time of fine thermocouples in air are limited in the open literature. Farahmand and Kaufman (2001) [15] carried out experiments in order to evaluate thermocouple response time applying velocities above 2m/s and small temperature changes ( $10\text{-}15^\circ\text{C}$ ) which are not consistent with the requirements of many transient heat transfer experiments in impingement cooling applications when the jets are fed from the same plenum chamber.

In this study, the time constant of various K-type thermocouples with exposed junction was experimentally evaluated. Thermocouple thermal inertia characteristics are discussed in details as well as their effect on the calculation of the heat transfer coefficient. For the evaluation of the heat transfer distributions three different scenarios have been considered: (1) Perfect temperature step in the flow (2) Series of step changes (Duhamel's superposition principle) on the acquired thermocouple measurements (3) Series of step changes on the corrected hot gas temperature considering thermocouple thermal inertia characteristics. The results indicate that the calculated heat transfer level is highly affected by the evolution of the hot gas temperature.

**NOMENCLATURE**

- $D$  = impingement hole diameter (m)
- $d$  = thermocouple wire diameter (m)
- $c$  = specific heat [ $J/(kgK)$ ]
- $h$  = heat transfer coefficient [ $W/(m^2K)$ ]
- $k$  = thermal conductivity [ $W/(mK)$ ]
- $L$  = impingement hole length (m)
- $\dot{m}$  = mass flow rate (kg/s)
- $Nu$  = Nusselt number
- $n$  = number of holes
- $Pr$  = Prandtl number
- $Re$  = Reynolds number
- $T$  = temperature ( $^{\circ}C$ )
- $t$  = time (s)
- $U$  = velocity (m/s)
- $V$  = volume ( $m^3$ )
- $x,y,z$  = coordinate system
- $X$  = axial jet-to-jet spacing
- $Y$  = channel width
- $Z$  = separation distance (channel height)

**Greek symbols**

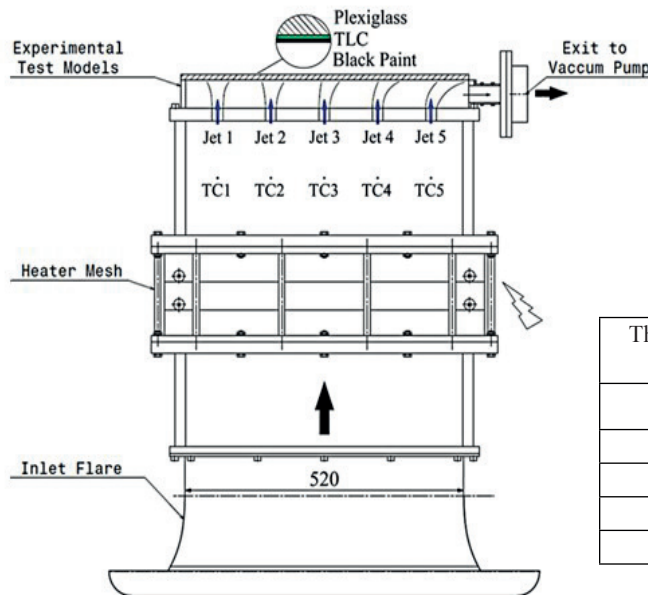
- $\theta$  = temperature ratio =  $(T - T_0)/(T_g - T_0)$
- $\mu$  = dynamic viscosity [ $kg/(ms)$ ]
- $\nu$  = kinematic viscosity ( $m^2/s$ )
- $\rho$  = density ( $kg/m^3$ )
- $\tau_c$  = time constant (sec)

**Subscripts**

- $avg$  = average
- $D$  = hole diameter
- $d$  = junction diameter
- $g$  = gas
- $o$  = initial
- $i$  = time step index
- $j$  = jet
- $p$  = plenum
- $ss$  = steady state
- $TC$  = thermocouple
- $w$  = wall
- $jet$  = thermocouple junction

**EXPERIMENTAL SETUP**

The general arrangement comprises an open circuit wind tunnel operated in suction mode. An overall schematic representation of the wind tunnel is shown in Fig. 1. The low speed wind tunnel consists of the inlet flare, based on McKenzie (1966) [16], a straight section of square ducting that contains the heater grid configuration, the working section which includes the large-scale test models sprayed with liquid crystals, the exhaust pipe and the driving pump. The stainless steel mesh used in this study, is of woven construction, where the wire diameter and the aperture are  $25\mu m$  and  $40\mu m$  respectively, resulting in an open area (mesh porosity) of 38%. The heater mesh covers the whole flow path of the plenum upstream of the impingement plate composing an effective heating area of  $520 \times 150mm^2$  relating to one of the largest mesh heaters (Neely *et al.* (1997) [17]). Power to the mesh is supplied through a  $30 kW$  DC-Power supply whose response time needed to reach steady state conditions has been measured less than 80ms and hence is adequate for the creation of the temperature step in the flow.



**Table 1 Thermocouple characteristics**

Thermocouple Number	Thermocouple Type	Wire diameter [mm]
TC1	K	0.08
TC2	K	0.13
TC3	K	0.25
TC4	K	0.51
TC5	K	0.81

**Fig. 1 Test facility and thermocouple characteristics**

Experiments were carried out using two different narrow impingement channels. Both of them include a single row of five inline impingement holes drilled on the impingement plate of the passage so that  $L/D=1$ , while a single exit mode has been chosen in order to investigate the effect of crossflow generated by the spent air of the jets, representing a realistic situation. All the impingement jets are supplied from the same plenum chamber and therefore have the same total pressure. The axial jet-to-jet spacing and the passage width remained constant at  $X/D=Y/D=5$  at a low separation distance of  $Z/D=1$ . The experimental test models have been manufactured by transparent acrylic material so that the observation of the liquid crystals is performed on the back side of the target plate.

The air exits the impingement channel to a plenum chamber (not shown here) and then to a vacuum pump. The flow rate was adjusted by an inlet vane placed at the suction port of the pump while the mass flow rate was controlled via a laminar flow element mounted in a long duct upstream of the vane pump. This configuration provided the flexibility of very fine regulation of the main stream velocity inside the open circuit wind tunnel. The jet average Reynolds number, based on hole diameter, can be calculated from the total massflow divided by the number of jets used as follows:

$$\frac{4\dot{m}}{nD^2\mu}$$

where,  $n$ , is the number of holes,  $D$  [m], is the jet diameter and  $\mu$  [kg/(ms)] is the dynamic viscosity of the air calculated on the liquid crystal temperature. Several  $Re_D$  were investigated in the range of 15000 and 55000, representing realistic engine flow conditions. The uncertainty in the determination of massflow rate was always below 5%.

## MEASUREMENT TECHNIQUE AND INSTRUMENTATION

The experiments were carried out using the transient liquid crystal technique. In a typical transient heat transfer experiment, the flow temperature is subjected to a sudden temperature step and the optical response of the liquid crystal surface coating is monitored using a digital video camera at the back of the target plate. Liquid crystals are sprayed on the surface of the target plate using an air brush while black paint is applied above them in order to create a black background providing brilliant colors. If the thermal conductivity of the model is sufficiently low, the wall temperature response is limited to a thin layer near the wall surface while the lateral conduction is assumed relatively small and hence negligible (Kingsley-Rowe *et al.* (2005) [18]). Therefore, the heat conduction into the model can be assumed to be one-dimensional and a semi-infinite medium approach is used. Numerical and analytical techniques can be used to solve the 1-D transient conduction equation. The relation between the wall surface (liquid crystal) temperature,  $T_w$ , and the heat transfer coefficient,  $h$ , for the semi-infinite case is then described in many heat transfer textbooks by (Incropera *et al.* (2006) [19]):

$$h = \frac{k}{\sqrt{\pi \alpha \tau}} \left( \frac{T_w - T_\infty}{T_s - T_\infty} \right)$$

However, in a typical impingement experiment the ratio between the total flow areas of the jets to the flow path of the plenum feeding the jets is far below unity resulting in very low plenum velocities, usually less than 1 m/s. According to Ireland and Jones (2000) [4] this is the limit where flow switching needs to be performed for higher heater mesh efficiencies while a step change in the power settings does not cause a step change in the flow. In this case, Duhamel's superposition theorem can be applied to Eq. 1, similar to Poser and von Wolfersdorf (2011) [5], approximating the real temperature evolution by a number of ideal temperature steps as follows:

$$\sum_{i=1}^n [1 - \exp(-\frac{h^2 \tau_i}{\pi \alpha})]$$

The 1-D transient conduction equation is then solved numerically evaluating the heat transfer coefficient. A narrow bandwidth type of TLCs was used for all experiments (38.5°C-39.8°C). Liquid crystals were calibrated *in-situ* using a surface thermocouple glued on the target plate of the channel. Dark green and light blue colors were considered for the post-processing. The evolution of the liquid crystal color was recorded with a high definition RGB camera (AVT Pike F210C) connected with a frame grabber of 800Mbit/s to the tower of an 8GB-RAM PC. The recorded video data were digitized at a frame rate of 25fps. Uniform and strong illumination throughout

the length of the test rig was provided by a pair of two white fluorescent lights (color temperature - 6000K) mounted on both sides of the test rig in order to avoid shadows and reflections.

The hot gas temperature was measured by a set of five K-type thermocouples with exposed junction from OMEGA and equally distributed inside the plenum, as shown in Fig. 1. Each thermocouple had a different wire diameter while the plenum temperature was acquired with a data acquisition system via LabVIEW at a rate of 25Hz in order to minimize the time step effect on Eq.3 (Kwak (2008) [12]). Thermocouple characteristics are indicated in Table 1.

## THERMOCOUPLE TIME CONSTANT AND CORRECTION FOR THERMAL INERTIA

### Thermocouple response time

The ratio between the total flow areas of the jets to the flow path of the plenum feeding the jets is approximately 0.02 in the case of this study. Subsequently, the velocities in the plenum are in the order of 1m/s or even less and therefore the time response of the thermocouples is sufficient for causing an extra delay missing the capture of the real gas temperature evolution.

Fig. 2(a) indicates the evolution of different thermocouples over a range of various temperature steps at a plenum velocity of 0.5m/s. As expected, the smaller the wire diameter, and hence the connection junction, the quicker is the thermocouple response at a given temperature step. Steady state conditions are reached after approximately 10sec for a very fine thermocouple with a wire diameter of 0.08mm, while the indication temperature of a relatively thick thermocouple (0.81mm) does not perfectly reach the asymptotic value even if the time after the initiation of the heating step is 100s. Additionally, the non-dimensional temperature rise ( $\Theta$ ) is independent of the heating step suggesting a negligible effect of temperature level on the response of the thermocouples. The duration of a transient heat transfer experiment may last between 20s and 80s and therefore a relatively fine thermocouple is required in the plenum so that to provide information about the steady state hot gas temperature which drives the transient experiment.

In such a case, the lumped capacitance method can be used where the real hot gas temperature evolution of the plenum can be extracted from the thermocouple acquisition measurements as follows:

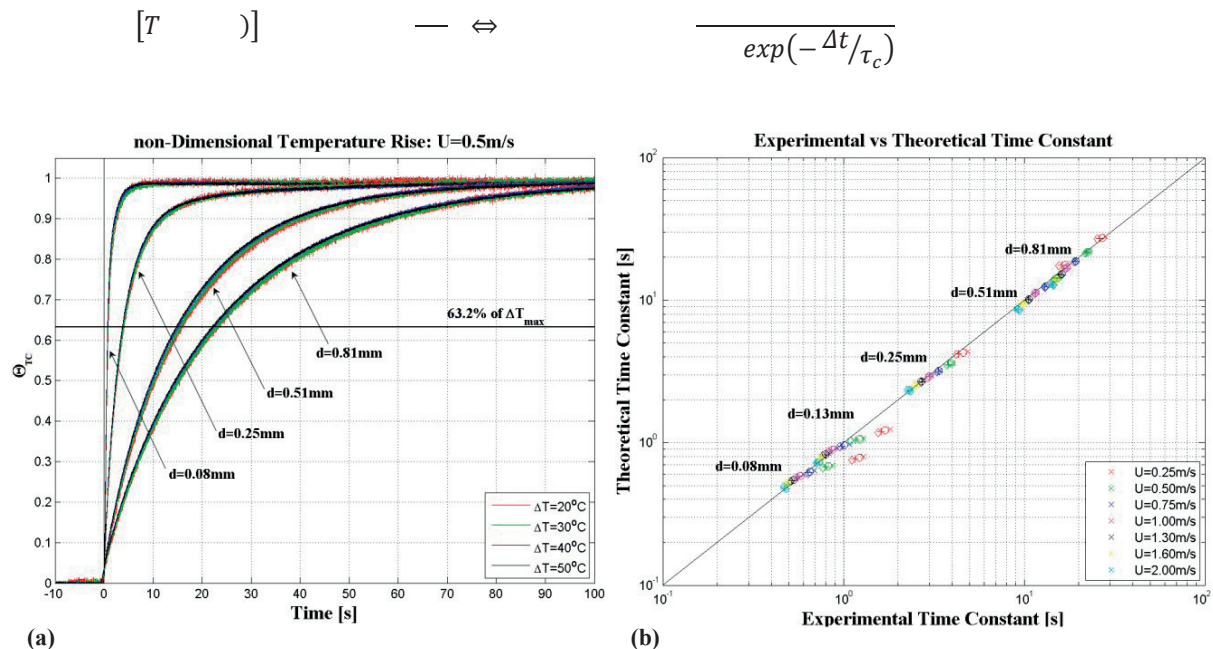


Fig. 2 (a) Temperature steps of various thermocouples. Plenum velocity, 0.5m/s (b) Comparison of  $\tau_{c,th}$  and  $\tau_{c,exp}$  at various temperature steps and plenum velocities ( $\square$  20°C,  $+$  30°C,  $\circ$  40°C,  $\times$  50°C)

where  $\rho_{TC}=8730\text{kg/m}^3$  and  $c_{TC}=550\text{J/(KgK)}$  are the density and the specific heat of the junction material, calculated for a thermocouple wire pair as the average of the thermocouple wire (Chromel-Alumel) properties and  $\tau_{c,th}$  is the theoretical time constant of the thermocouple based on the junction diameter (taken equal to approximately 2.5 times the wire diameter):

$$\tau_{c,th} = \frac{m}{hA} = \frac{\rho_{TC} V}{hA} = \frac{\rho_{TC} \pi d^2 L}{4hA}$$

Finally,  $h_{d,ict}$  is the heat transfer coefficient ( $\text{W/m}^2 \text{K}$ ) calculated by the well-known Whitaker (1972) [20] correlation:

$$Nu_D = \left(0.4 + 0.6 Re_D^{1/4} + 0.5 Pr^{1/4} \right) P \left(\frac{\mu}{\mu_s}\right)$$

Several experiments were carried out evaluating the behavior and the time constant of various thermocouples at different temperature steps and plenum velocities. The theoretical time constant was calculated by Eq. 5 and 6. Physically, this number represents the it time takes for a system's step response to reach 63.2% of its final asymptotic value (Incropera *et al.* (2006) [19]) and therefore the theoretical time constant ( $\tau_{c,th}$ ) was compared with the experimental time constant ( $\tau_{c,exp}$ ) which was assumed to be the time required to reach the 63.2% of the steady state hot gas temperature for a given thermocouple size and temperature step.

Fig. 2(b) shows a comparison of the theoretical thermocouple time constant, calculated from Whitaker's correlation [20] assuming that the thermocouple junction approaches a spherical profile, and the experimental one. Generally, good agreement is observed over the entire range of plenum velocities, wire diameters and different temperature steps. However, at very low plenum velocities ( $U_p=0.25$  and  $0.5\text{m/s}$ ) and very fine thermocouples ( $0.08\text{mm}$  and  $0.13\text{mm}$  wire diameter) a deviation from the  $y=x$  line appears. This could be attributed to the very low  $Re_{d,ict}$ , based on junction diameter, and the inapplicability of Whitaker's equation, which is usually applied for  $Re_d > 3.5$ . At each wire diameter group in the chart, a reduction of time constant with the plenum velocity is observed, however, the impact of thermocouple size is greater than the airstream velocity in the response of each thermocouple. This is better visible in Fig. 3(a) where the time constant is plotted as a function of plenum velocity for various thermocouples and temperature steps. At a given thermocouple size the time constant is reduced by approximately 50% as the plenum velocity is increased from  $0.25\text{m/s}$  to  $2\text{m/s}$ . On the other hand, at a given plenum velocity, the time constant can be reduced by a factor of 25 if the wire diameter of the thermocouple is reduced from  $0.81\text{mm}$  to  $0.08\text{mm}$ . Fig. 3(b) indicates that as the temperature step increases the time constant remains at the same level for all tested thermocouples. This is similar to the results of Farahmand and Kaufman (2006) [21], although a small reduction is observed at small wire diameters.

### Calculation of hot gas temperature

Fig. 4 indicates the hot gas temperature, which drives the transient experiment, extracted from Eq.4. For the calculation of the real plenum temperature, the experimental time constant was used thanks to the good agreement with the theoretical one although it has been proven very little difference on the final results. Fig. 4(a) indicates that the extracted plenum temperature is independent on the size of thermocouple which means that the series of the five thermocouples (TC1 to TC5) experience the same plenum temperature evolution. However, a noisy behavior can be observed where the noise fluctuations depend in a very great extent on the thermocouple size. As shown earlier, for a given type of thermocouple, the diameter of the junction is the most important parameter which affects the time constant. Obviously, the smaller the junction diameter (and hence the time constant), the smaller is the denominator of Eq.4 resulting in a more stable extraction of the plenum temperature. On the other hand, plenum velocity has a smaller impact on the denominator of Eq.4 and therefore the level of fluctuations in the extracted temperature is independent on the freestream velocity as shown in Fig. 4(b).

In all the examined cases, an overshooting of the plenum temperature can be observed directly after the initiation of the heating step. This is attributed to the transient response of the DC-Power supply where an overshooting of the supplied power is observed followed by small oscillations which are however within the experimental uncertainties. Fig. 5(a) shows the power supplied in the heater mesh for the case of  $Z/D=1$  normalized with the power required to heat a flow of  $Re_D=55000$  at  $\Delta T=30^\circ\text{C}$ , approximately  $2.4\text{kW}$ . The duration of power overshoot is relatively small, in the order of  $0.05\text{s}$ , however affects unavoidable the temperature of the

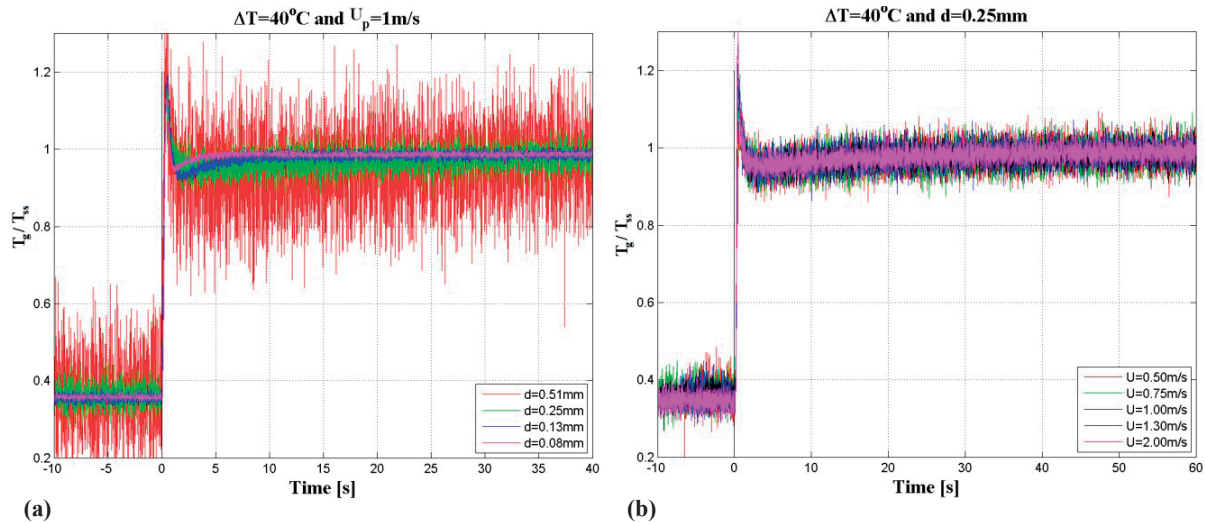


Fig. 4 Unsmoothed hot gas temperature calculated for (a) different thermocouple size and (b) plenum velocities

heater mesh, the only source of resistance in the circuit, and subsequently a thermal shock is generated inside the plenum approaching the impingement plate. Note also that the temperature step is reduced with increasing Reynolds number so that to achieve a relatively constant liquid crystal first appearance time for all the experiments in the order of 1.5-2s.

Fig. 5(b) indicates the evolution of the hot gas temperature,  $T_g(t)$  during the transient experiment. In this figure the three different approaches are presented: (1) the ideal temperature step, (2) the acquired temperature data of a thermocouple ( $d=0.13mm$ ) placed in the middle of the plenum and (3) the hot gas temperature calculated from Eq.4-6. According to the thermocouple measurements, steady state conditions are reached after approximately 8sec, however, the thermal inertia of the thermocouple junction affects the acquisition of the real gas temperature evolution. The blue line in Fig. 5(b) corresponds to the corrected gas temperature smoothed with the *Savitzky-Golay* smoothing method. As expected, the temperature increase is much sharper and the overshooting of  $T_g$  is still observed after the initiation of the heating step due to the overshooting of the achievable power supplied during the adjustment of the desirable electrical energy according to the heater mesh resistance.

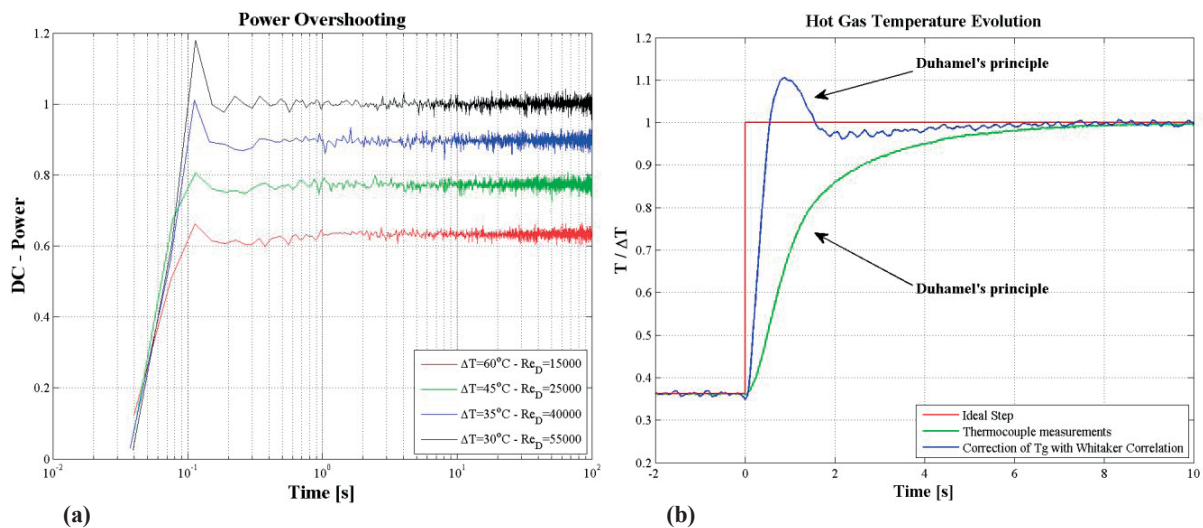


Fig. 5 (a) Power supplied in the heater mesh,  $Z/D=1$  (b) Hot gas temperature evolution,  $\Delta T=35^\circ C$



## EVALUATION OF HEAT TRANSFER COEFFICIENT

## Heat transfer surface contours

Fig. 6 indicates full surface heat transfer coefficient distributions on the target plate of the narrow impingement channel at  $Re_D=25000$  and  $55000$ . These data was calculated with three different hot gas temperature evolution cases: (1) Perfect temperature step in the flow (2) Series of step changes (Duhamel's superposition theorem) on the acquired thermocouple measurements (3) Series of step changes on the corrected hot gas temperature considering thermocouple thermal inertia characteristics. The heat transfer coefficient values are normalized with the maximum value appeared on the data in the case of an ideal temperature step, which were approximately  $205W/(m^2K)$  and  $370W/(m^2K)$  for a  $Re_D$  of  $25000$  and  $55000$  respectively.

The heat transfer rate distribution is symmetrical along the  $x$ -centerline. As the flow accelerates to the exit of the channel the effect of crossflow generated by the spent air of the upstream jet(s) becomes visible. The pattern of the heat transfer coefficient is progressively converted from a circular distribution (Jet 1) to a horseshoe vortex shape distribution (Jet 5). Secondary peaks around the stagnation region of the upstream jets appear similar to single impingement patterns (Baughn and Shimizu (1989) [22]). At Jets 2 and 3 the formation of the horseshoe vortex due to the continuously increased crossflow momentum destroys the circular pattern of the ring. However, the secondary peak is always visible in the wake region downstream of each jet since it is protected somehow from the fluid of the jet. At the last hole (Jet 5) the momentum of the jet is still relatively high compared to the momentum of the crossflow and therefore a similarity with a flow over a cylinder can be observed. Note also that the stagnation point heat transfer coefficient increases for the downstream jets due to the lower static pressure and hence higher local Reynolds numbers.

Although the general flow patterns is similar for the three different cases of hot gas temperature history, the level of heat transfer coefficient is different especially in the stagnation region of the jets where the appearance of liquid crystals is rather quick (1.5-2s). This time of appearance is shorter than the time the thermocouple needs to reach steady state conditions due to its thermal inertia and therefore a relatively lower  $T_g$  is considered in the solution of Eq.4. At  $Re_D=25000$ , where the plenum velocity is  $0.39m/s$ , the overestimation of the heat transfer coefficient is far above 50% if Duhamel's superposition principle is applied directly on the thermocouple

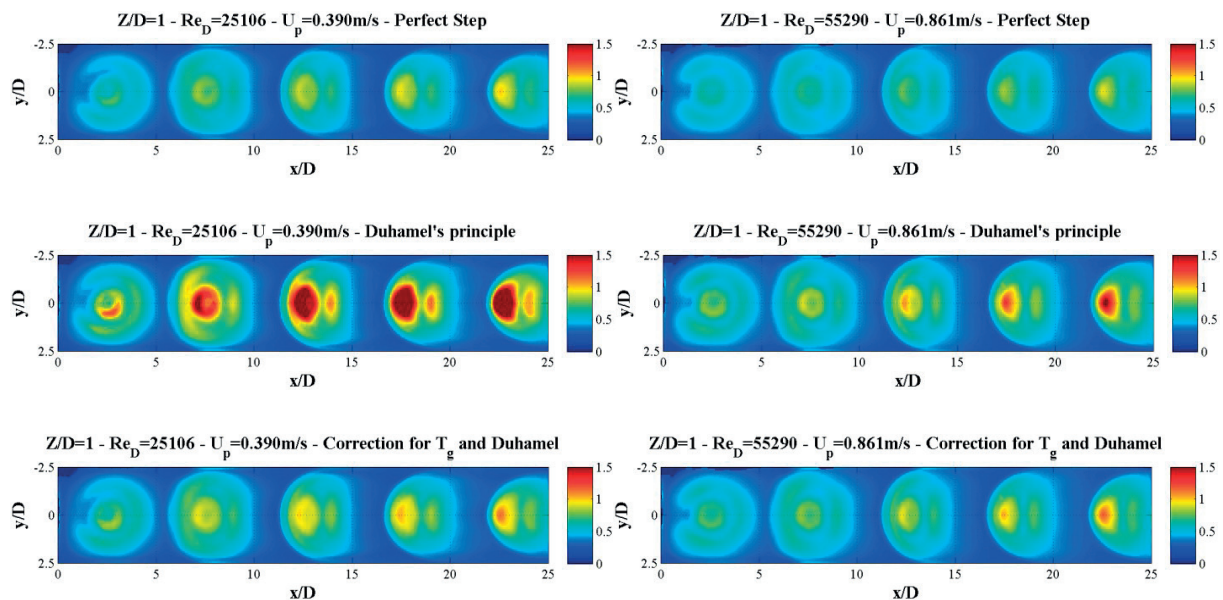


Fig. 6 Heat transfer coefficient surface contours for various hot gas temperatures (a)  $Re_D=25000$  (b)  $Re_D=55000$

measurements. On the other hand, a perfect temperature step may result in an underestimation of the heat transfer coefficient since the plenum velocity is low and a step change in the power settings do not cause a step change in the mainstream temperature as well as the temperature overshooting due to the transient response of the DC-Power supply is not considered. For these reasons, Eq.4 5 and 6 was used to calculate the real plenum temperature evolution based on the thermocouple measurements. The level of heat transfer coefficient lies between the aforementioned cases but it is closer to the ideal temperature step assumption. The authors believe that this is not very far from reality since the time needed for DC-Power supply to reach steady state conditions is in the order of *60-100m* which is still rather quick. At  $Re_D=55000$  similar trends are observed, however the plenum velocity is higher (*0.86m/s*) resulting to lower thermocouple time constant. Therefore, the green line in Fig. 5(b) approaches more the ideal step situation and subsequently the differences in the heat transfer level between the three cases are smaller compared to  $Re_D=25000$ .

### Local $Nu_D$ distributions

Fig. 7 indicates the local  $Nu_D$  distributions in the centerline of the channel at the same flow conditions from Fig. 6. For both  $Re_D$  and a given hot gas temperature evolution approach, at the upstream jets of the channel, a donut shape distribution of  $Nu_D$  is observed. However, as the crossflow generated from the spent air of Jets 1 and 2 is developed, the distribution of the heat transfer coefficient is rearranged and slightly shifted in the direction of the flow due to the deflection of the jets. Additionally, the stagnation point heat transfer coefficient increases along the length of the channel due to the decreasing static pressure and hence increasing local  $Re_D$ . Regarding the heat transfer level similar trends are observed. An overestimation of the heat transfer coefficient in the stagnation point regions is obtained when Duhamel's superposition principle is applied directly on the thermocouple data. In this case the level of heat transfer can be more than double compared to the ideal temperature step situation, as for example in the stagnation point of Jet 5 at  $Re_D=25000$  which lies at the same level of  $Re_D=55000$  and of course represent a non-realistic situation. As discussed earlier, the difference with the ideal temperature step situation is reduced with increasing  $Re_D$  (and hence plenum velocity). This is visible at the high Reynolds number of Fig. 7 where the local heat transfer coefficients are apparently closer compared to  $Re_D=25000$ . However, the  $Nu_D$  overestimation compared to the data for the heat transfer rate for the ideal temperature step is 25% for the stagnation region of Jet 1 and approximately 38% for Jet 5. When  $T_g$  is corrected prior to Duhamel's superposition principle, the evaluation of heat transfer coefficient results in values in between the above cases. Lower Nusselt numbers agree better as TLC indications appear later in time and therefore the fluid temperature history has a smaller influence on the evaluated data.

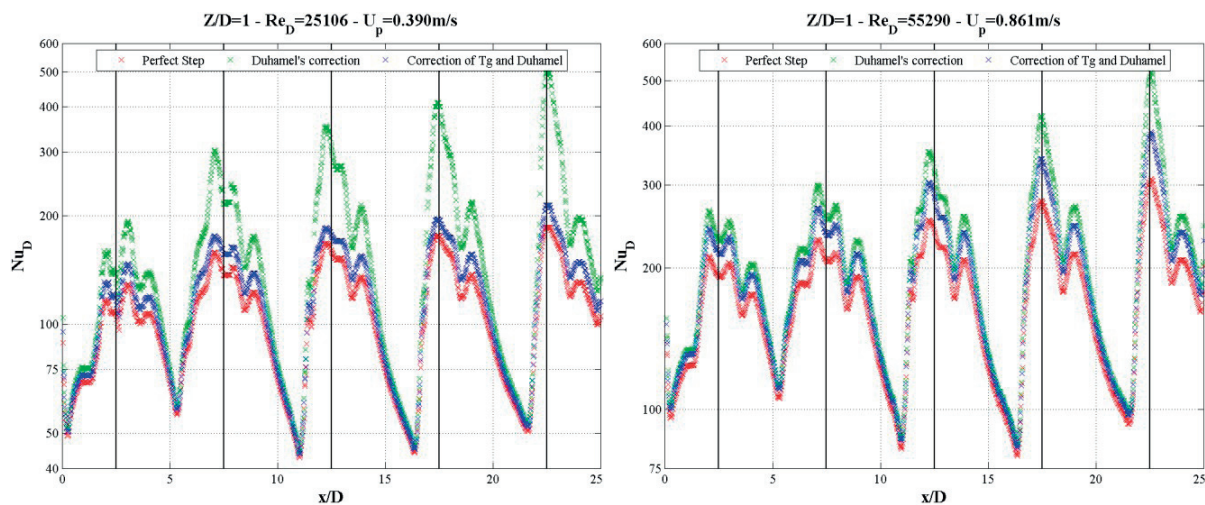


Fig. 7 Local  $Nu_D$  distributions for various hot gas temperatures at  $Re_D=25000$  and  $55000$ ,  $y=0$

### Spanwise averaged $Nu_D$ distributions

Fig. 8 indicates the spanwise averaged  $Nu_D$  at the target plate of the narrow impingement passage. The increase of stagnation heat transfer from Jet 1 to Jet 5 observed in Fig. 7 is somewhat smoothed out in the spanwise averaged results. The lower stagnation heat transfer of the first jets is compensated by a better lateral coverage of the wall jet due to lower interaction with the crossflow. For the downstream jets, the displacement of the peak heat transfer coefficient values compared to the jet exit positions (black lines) observed in Fig. 7 are also visible in the spanwise averaged results. This was also observed by Bouchez and Goldstein (1975) [23] in a single impingement jet experiment.

Contrary to the local heat transfer distribution of Fig. 7, the  $Nu_D$  evaluated with the three different approaches for  $T_g$  lie at the same level in the case of spanwise averaged data. This is because the spanwise averaged appearance time of the liquid crystal is larger than the appearance time at the stagnation regions and hence the effect of thermocouple thermal inertia is less intense. In particular, the  $Nu_D$  values coincidence at the wall jet regions indicating that the results are nearly independent from the hot gas temperature approach. Maximum difference is in the order of 50% for the stagnation point of Jet 5 and  $Re_D=25000$  which is still below the differences observed in the local heat transfer data of Fig. 7. At the higher plenum velocity of  $0.86\text{m/s}$  the differences are much less and the data seem to agree relatively well also for the stagnation regions of the jets. However, there are still some differences in the order of 10% and 20% from the ideal step for the corrected  $T_g$  considering thermocouple thermal inertia and the direct application of Duhamel's superposition principle to the thermocouple measurements.

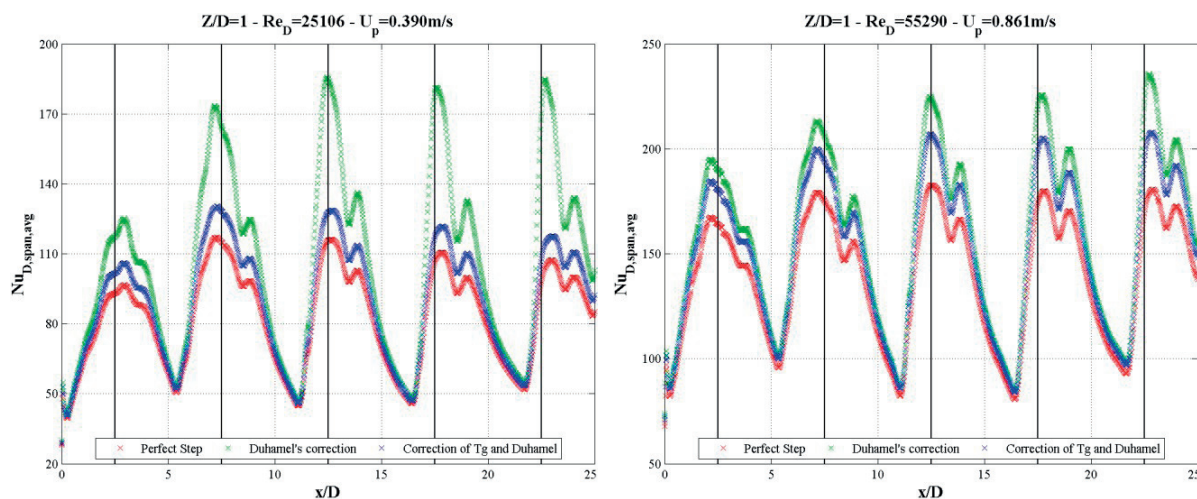


Fig. 8 Spanwise averaged  $Nu_D$  distributions for various hot gas temperatures at  $Re_D=25000$  and  $55000$ ,  $y=0$

### Area averaged heat transfer data

This section discusses the average heat transfer coefficient obtained on the target plate of the examined test models. In the majority of experiments, a liquid crystal signal could be recorded over 95% or more of the target plate area and therefore, the data are assumed adequate for statistical analysis providing a fairly good representation of the average heat transfer rate. The experimental results of this study have been compared also with various literature data obtained from multi-jet configurations with maximum crossflow orientation and similar geometrical factors ( $X/D$ ,  $Y/D$  and  $Z/D$ ) and hence open area (Metzger *et al.* (1979) [24], Florschuetz *et al.* (1980) [25], El-Gabry and Kaminski (2005) [26], Xing *et al.* (2010) [27]), Son *et al.* (2001) [28], Ricklick *et al.* (2010) [29]). As expected, Fig. 9 indicates that  $Nu_D$  is increased with Reynolds number following a power law of

$Nu_D \sim Re^\alpha$ . Exponent,  $\alpha$ , was estimated to be 0.72 which is a typical value for turbulent boundary layers as expected. More details about the exponent,  $\alpha$ , can be found in the study of Terzis *et al.* (2012) [30]. The large

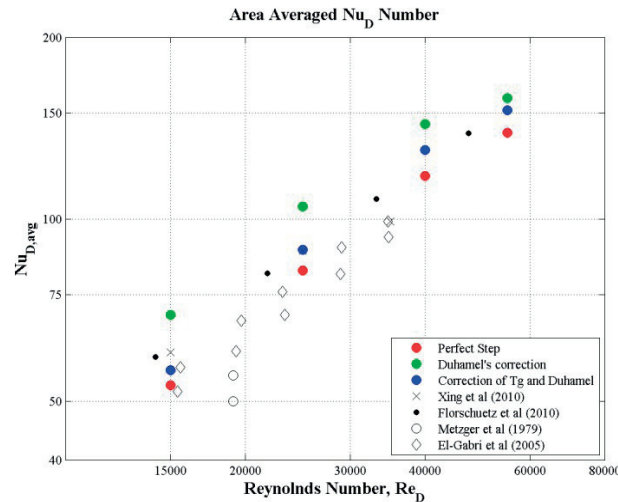


Fig. 9 Area averaged Nusselt number on the target plate

scatter in the chart can be attributed to the different geometrical details of the above studies including also nozzle shapes and design, jet turbulence, region of averaging area, mass flow rate determination or even differences of the applied measurement techniques. Nevertheless, good agreement with previous researchers can be observed indicating that the cooling performance of narrow impingement channels in terms of average heat transfer rate on the target plate is comparable with multi-array configurations.

Regarding the optimum hot gas temperature evolution, direct application of Duhamel's principle on the thermocouple measurements without any correction overestimates the heat transfer coefficient as expected; however, the differences in this chart are relatively small compared to the local and spanwise averaged data of Fig. 7 and Fig. 8, due to the fact that the target plate includes also the wall jets regions apart from the stagnation zones where the final results are relatively independent from the hot gas temperature approach, as shown also by the surface contours of Fig. 6. Correction of  $T_g$  prior to Duhamel's principle as well as an ideal temperature step are closer to the literature data indicating possibly a more realistic approach to the distribution of the heat transfer coefficient in the stagnation regions and hence have a better approach in the calculation of the average heat transfer rate. In particular, the corrected hot gas temperature data seem to agree relatively well with the results of Florschuetz *et al.* (1980) [21] for  $Z/D=1$  over the entire range of Reynolds number.

## UNCERTAINTY ANALYSIS

The estimation of the uncertainties associated with the heat transfer results of the current investigation is based on the method of small perturbations, outlined by Moffat (1998) [31], which has been applied in transient heat transfer experiments by Terzis *et al.* (2012) [30] and Chambers *et al.* (2010) [32]. For the calculation of heat transfer coefficient the temperature in the plenum was measured at a sampling rate of 25Hz in order to minimize the effect of time step level in Eq.3, as discussed by Kwak (2008) [12]. The flow temperature measurements indicate a slight increased uncertainty level of thermocouples for the heated flow, which is in agreement with the data of Schueren *et al.* (2011) [33]. The time required for the liquid crystals to reach their calibrated temperature level was evaluated from the recorded video with a frame rate of 25Hz. An extra error, that for the determination of the initiation of the heating step and hence the transient test was estimated in the order of 0.02s while the uncertainty in the thermal properties of Perspex ( $\rho_w c_w k_w$ )<sup>1/2</sup> has been assumed to be 5% according to Ireland (1987) [34]. The effect of each type of measurement error on the heat transfer coefficient is considered alone while the error analysis is performed by applying small perturbations in the test case of  $Z/D=1$  and  $Re_D=40000$ . Table 2 indicates typical values and the uncertainty levels for the heat transfer results and their effect when propagated, in the calculation of the average heat transfer coefficient (typical value  $166W/m^2 K$ ). The maximum error can be estimated in the order of 12.6% which is a fairly good value for a transient heat transfer experiment.

**Table 2 Experimental uncertainties for the heat transfer results**

Parameters	Units	Values	Error	Error in HTC [%]
$T_i$	[°C]	22.9	±0.12	0.99
$T_g$	[°C]	68.6	±0.25	1.51
$T_w$	[°C]	39.3	±0.2	3.18
$\sqrt{\rho c k}$	[W√s/(m <sup>2</sup> K)]	569	±29	5.35
$t$	[sec]	8.84	±0.1	1.61
<b>HTCavg</b>	<b>[W/(m<sup>2</sup>K)]</b>	<b>166</b>	<b>max error</b>	<b>~12.6</b>

## SUMMARY AND CONCLUSIONS

In this study, the distribution of the heat transfer coefficients on the target plate of a narrow impingement passage was experimentally measured using the transient liquid crystal technique. The results were evaluated using three different approaches for the hot gas temperature evolution which drives the transient experiment: (1) Perfect temperature step, (2) Duhamel's superposition theorem in the acquired temperature data and (3) Correction of hot gas temperature for thermocouple thermal inertia prior to superposition principle. For the correction of  $T_g$  the time constant of thermocouples, which was experimentally measured using various wire diameters and flow conditions, was considered. An uncertainty analysis showed a fairly good repeatability of the measurement technique. The findings of this investigation can be summarized as follows:

1. Thermocouple time constant decreases with reducing the wire diameter and increasing the freestream (plenum) velocity. A negligible effect of the temperature level was observed on the response of thermocouples.
2. Direct application of Duhamel's superposition principle overestimates the local heat transfer coefficients. The faster the appearance time the bigger is the overestimation in the final results which can be more than double, as for example in the local distribution of the stagnation regions of the jets and low Reynolds numbers.
3. Direct application of Duhamel's superposition principle overestimates the area averaged heat transfer coefficient values. The difference from the ideal temperature is 30% and 13% for a  $Re_D=15000$  and 55000 respectively. The higher the  $Re_D$  the smaller difference between the two assumptions since the plenum velocity is higher and therefore the thermocouple time constant as well.
4. The effect of thermocouple thermal inertia is less intense as the results are averaged in spanwise direction or in the whole target plate area.
5. Lower Nusselt numbers agree better as TLC indications appear later in time and therefore the fluid temperature history has a smaller influence on the evaluated data.

In transient liquid crystal experiments where the thermocouples measuring the driving fluid temperature are located in a low velocity region, it is therefore recommended to correct  $T_g$  with the thermocouple thermal inertia prior to Duhamel's superposition principle. This is the case in an impingement configuration where the jets are fed from a common plenum.

## ACKNOWLEDGMENTS

This study was performed in the framework of KW2020 (KraftWerke 2020) project funded by the Swiss Federal Office of Energy (SFOE/BFE, Bern, Switzerland) and Alstom (Baden, Switzerland). All the pieces of this test facility have been manufactured in-house in Atelier de l'Institut de génie Mécanique (ATME) of EPFL.

The authors are grateful to Theodoros Kyriakidis (EPFL, Switzerland) and Serafeim Perdakis (EPFL, Switzerland) for their valuable support during the setup of electronic equipment. Special thanks to Prof. Anesits I. Kalfas (Aristotle University, Greece) for the discussions during the construction of the test facility.

## REFERENCES

- Weigand B. and Spring S. (2011) "Multiple Jet Impingement - A Review" *Heat Transfer Research*, Vol. **42**(2), pp. 101-142.
- Baughn J. W. (1995) "Liquid Crystal Methods for Studying Turbulent Heat Transfer" *International Journal of Heat and Fluid Flow*, Vol. **16**, pp. 365-375.
- Ireland P. T., Neely, A.J., Gillespie, D.H.R., Robertson, A.J. (1999) "Turbulent Heat Transfer Measurements Using Liquid Crystals" *International Journal of Heat and Fluid Flow*, Vol. **20**, pp. 355-367.
- Ireland P. T. and Jones T. V. (2000) "Liquid Crystal Measurements of Heat Transfer and Surface Shear Stress" *Measurement Science and Technology*, Vol. **11**, pp. 969-986.
- Poser R. and von Wolfersdorf J. (2011) "Liquid Crystal Thermography for Transient Heat Transfer Measurements in Complex Internal Cooling Systems" *Heat Transfer Research*, Vol. **42**(2), pp. 181-197.
- Van Treuren K. W., Wang Z., Ireland P. T. and Jones T. V. (1994) "Detailed Measurements of Local Heat Transfer Coefficient and Adiabatic Wall Temperature Beneath an Array of Impinging Jets" *Journal of Turbomachinery, ASME*, Vol. **116**(3), pp. 336-374.
- Huang L. and El-Genk M. S. (1994) "Heat Transfer of an Impinging Jet on a Flat Surface" *International Journal of Heat and Mass Transfer*, Vol. **37**(13), pp. 1915-1923.
- Falcoz C., Weigand B. and Ott P. (2006) "Experimental Investigations on Showerhead Cooling on a Blunt Body" *International Journal of Heat and Mass Transfer*, Vol. **49**, pp. 1287-1298.
- Wagner G., Schneider E., von Wolfersdorf J., Ott P., et al. (2007) "Method for Analysis of Showerhead Film Cooling Experiments on Highly Curved Surfaces" *Experimental Thermal and Fluid Science*, Vol. **31**, pp. 381-389.
- Gillespie D. R. H., Wang Z. and Ireland P. T. (1995). Heating Element. PCT/G96/2017. Application, B. P. Esposito E. I., Ekkad S. V., Kim Y. and Dutta P. (2009) "Novel Jet Impingement Cooling Geometry for Combustor Liner Backside Cooling" *Journal of Thermal Science and Engineering Applications*, Vol. **1**(2), pp. 021001-021008.
- Kwak J. S. (2008) "Comparison of Analytical and Superposition Solutions of the Transient Liquid Crystal Technique" *Journal of Thermophysics and Heat Transfer*, Vol. **22**(290-295).
- Wormser A. F. (1960) "Experimental Determination of Thermocouple Time Constants with Use of a Variable Turbulence, Variable Density Wind Tunnel, and the Analytic Evaluation of Conduction, Radiation, and Other Secondary Effects" *SAE Trans., April 5-8, 1960*, Vol. Murdock J. W., Foltz C. J. and Gregory C. (1963) "A Practical Method of Determining Response Time of Thermometers in Liquid Baths" *Journal of Engineering for Power, ASME*, Vol., pp. 27-32.
- Farahmand K. and Kaufman J. W. (2001) "Experimental Measurement of Fine Thermocouple Response Time in Air" *Experimental Heat Transfer*, Vol. **14**, pp. 104-118.
- McKenzie A. B. (1966). An Investigation of Flare Dimensions for Standard and Annular Air Meters. Report, C. D. Derby, UK, Rolls-Royce Plc.
- Neely A. J., Ireland P. T. and Harper L. R. (1997) "Extended Surface Convective Cooling of Engine Components Using the Transient Liquid Crystal Technique" *Journal of Power and Energy A*, Vol. **211**, pp. 273-287.
- Kingsley-Rowe J. R., Lock G. D. and Owen J. M. (2005) "Transient Heat Transfer Measurements Using Thermochromic Liquid Crystals: Lateral-Conduction Error" *International Journal of Heat and Fluid Flow*, Vol. **26**(2), pp. 256-263.
- Incropera F. P., Dewitt D. P., Bergman T. L. and Lavine A. S. (2006). Fundamentals of Heat and Mass Transfer. 6th Edition, John Wiley & Sons.
- Whitaker S. (1972) "Forced convection heat transfer correlations for flow in pipes, past flat plates, single cylinders, single spheres, and for flow in packed beds and tube bundles" *AIChE Journal*, Vol. **18**(2), pp. 361-371.
- Farahmand K. and Kaufman J. W. (2006) "Measurement of Time Constant of Wet-Bulb Thermocouple in Air" *Experimental Heat Transfer*, Vol. **19**, pp. 165-180.
- Baughn J. W. and Shimizu S. (1989) "Heat Transfer Measurements From a Surface With Uniform Heat Flux and an Impinging Jet" *Journal of Heat Transfer, ASME*, Vol. **111**, pp. 1096-1098.

- Bouchez J.-P. and Goldstein J. (1975) "Impingement Cooling From a Circular Jet in a Crossflow" *International Journal of Heat and Fluid Flow*, Vol. **18**, pp. 719-730.
- Metzger D. E., Florschuetz L. W., Takeuchi D. I., Behee R. D., et al. (1979) "Heat Transfer Characteristics For Inline and Staggered Arrays of Circular Jets With Crossflow of Spent Air" *Journal of Heat Transfer, ASME*, Vol. **101**, pp. 526-531.
- Florschuetz L. W., Berry R. A. and Metzger D. E. (1980) "Periodic Streamwise Variations of Heat Transfer Coefficients For Inline and Staggered Arrays of Circular Jets With Crossflow of Spent Air" *Journal of Heat Transfer, ASME*, Vol. **102**(1), pp. 132-137.
- El-Gabry L. A. and Kaminski D. A. (2005) "Experimental Investigation of Local Heat Transfer Distribution on Smooth and Roughened Surfaces Under an Array of Angled Jets" *Journal of Turbomachinery, ASME*, Vol. **127**(3), pp. 532-544.
- Xing Y., Spring S. and Weigand B. (2010) "Experimental and Numerical Investigation of Heat Transfer Characteristics of Inline and Staggered Arrays of Impinging Jets" *Journal of Heat Transfer, ASME*, Vol. **132**, pp. 092201-092211.
- Son C. M., Gillespie D. R. H., Ireland P. T. and Dailey G. M. (2001) "Heat Transfer and Flow Characteristics of an Engine Representative Impingement Cooling System" *Journal of Turbomachinery*, Vol. **123**, pp. 154-160.
- Ricklick M., Kapat J. S. and Heidmann J. (2010) "Sidewall Effects on Heat Transfer Coefficient" *Journal of Thermophysics and Heat Transfer*, Vol. **24**(1), pp. 123-132.
- Terzis A., Wagner G. and Ott P. (2012). Hole Staggering Effect on the Cooling Performance of Narrow Impingement Channels. ASME, TurboExpo 2012, 11-15 June 2012, Copenhagen.
- Moffat R. J. (1998) "Describing the Uncertainties in Experimental Results" *Experimental Thermal and Fluid Science*, Vol. **1**(1), pp. 3-17.
- Chambers C. A., Gillespie D. R. H., Ireland P. T. and Kingston R. (2010) "Enhancement of Impingement Cooling in a High Crossflow Channel Using Shaped Impingement Cooling Holes" *Journal of Turbomachinery, ASME*, Vol. **132**, pp. 021-021 - 021-028.
- Schueren S., Hoefler F., von Wolfersdorf J. and Naik S. (2011). Heat Transfer in an Oblique Jet Impingement Configuration With Varying Jet Geometries. ASME TurboExpo - GT2011-45169.
- Ireland P. T. (1987). Internal Cooling of Turbine Blades. D. Phil. Oxford University, United Kingdom.

## TOTAL TEMPERATURE PROBES FOR TURBINE EFFICIENCY MEASUREMENTS IN TRANSONIC ROTATING RIGS

**Victor Pinilla, Raúl Vázquez**  
Industria de Turbo Propulsores,  
San Fernando de Henares, 28830, Spain

**Andoni Puente**  
Centro de Tecnologías Aeronáuticas  
Zamudio, 48170, Bizcaia, Spain

### ABSTRACT

Modern Low Pressure Turbines (LPT) shown very high efficiencies, therefore future improvements are expected to be low enough to produce a small exit temperature variation. This trend requires a continuous precision increase of the total gas temperature measurement system if a good global descriptor of the turbine efficiency is sought.

Traditionally gas turbine temperatures have been measured using thermocouples. However, several total temperature probes are available nowadays like dual hot wire aspirating probe, cold wire thermo resistor or the dual thin film total probe. Due to the high reliability, robustness, low cost and simplicity the thermocouples are the most used device to measure of time average total temperature.

In this paper, a detailed experimental study of total temperature probe composed by a Kiel Head instrumented with thermocouples is presented, throwing some light onto the physics of the probe. This study yields the systematic error of the total temperature probe measurements and its relationship with probe geometry and fluid characteristics. In order to quantify the source of errors, an analytical model has been developed to simulate the behavior of the total temperature probe.

### INTRODUCTION

Over the last 20 years the efficiencies of Low Pressure Turbines (LPT) have increased continuously. They have achieved very high efficiencies that are progressively closer to the ultimate physical limit. As the room for improvement is getting narrow, benefits from novel technologies are expected to be smaller in such a way that the efficiency will trend asymptotically to the maximum achievable.

The new improvements will be validated in turbine cold flow rigs that consequently will need a more sophisticated and accurate methods to measure the efficiency. Two methods have been pursued in the past: “mechanical efficiency” and “thermal efficiency” [1]. Mechanical efficiency has been obtained from the torque, mass flow and pressure ratio while the thermal efficiency has been obtained from pressure ratio and temperature rakes placed at the inlet and outlet of the turbine.

To get experimentally the absolute efficiency with a precision better than 0.5% is challenging. However, this precision is achievable by any of the previous methods for getting variations of efficiency from a proper back-to-back test. To improve the precision further, up to 0.1 or 0.2%, it is needed to be capable to repeat the reading within 0.1/0.2% of the mass flow, temperature ratio, torque and pressure ratio along the turbine. The first two are the hardest to reach. In a characteristic cold flow rig, 0.1% of temperature ratio can be 0.02°K per stage and in terms of mass flow can be 0.01 Kg/s.

The standard temperature probes on those experiments use to be “shielded thermocouples”. The errors of these probes are very small and they are very well known since long time. Nevertheless, due to the so high precision requested makes convenient to revisit the source of those errors to assure their magnitude and to try to reduce them as much as possible. Therefore, this is the motivation and objective of the present paper.



**NOMENCLATURE****Roman**

$A_r$	area ratio (inlet to bleed hole area)
Cu	copper wire
$C_p$	specific heat at constant pressure [ $J\ kg^{-1}\ K^{-1}$ ]
D	thermocouple wire diameter [m]
g	Acceleration due to the gravity [ $m\ s^{-2}$ ]
$h_c$	convective heat transfer coefficient [ $W\ m^{-2}\ K^{-1}$ ]
k	thermal conductivity [ $W\ m^{-1}\ K^{-1}$ ]
L	thermocouple wire length [m]
M	mach number
Ni	nickel wire
Nu	Nusselt number [ $h_c D/k_{air}$ base on wire diameter]
P	pressure [bar]
Pr	Prandtl number
r	recovery factor
R	gas constant ( $287.05\ m^2\ s^2 /K$ for air)
Re	Reynolds number, [ $\rho U D/\mu$ ]
T	temperature [K]
$T_0$	Total or stagnation temperature [K]
U	air velocity [m/s]
V	thermocouple voltage [Volt]

**Greek**

$\gamma$	specific heat ratio (1.4 for air)
$\varepsilon$	Emissivity
$\eta$	recovery ratio
$\mu$	viscosity [Pa s]
$\rho$	density [ $Kg/m^3$ ]
$\sigma$	Boltzmann constant

**EXPERIMENTAL APPARATUS****Total temperature probes**

The total temperature probes studied in this paper are composed of a thermocouple placed inside a stagnation tube called Kiel Head.

A thermocouple is an active transducer based on the Seebeck effect. When two different metal wires are in contact in a junction, a net voltage is generated between the two wires extremities. The voltage is proportional to the temperature difference between the junction and these extremities. The current research is performed using special T thermocouples due to the high uniformity of the metal wires, which yields almost the same calibration law for all the thermocouples.

An adiabatic thermocouple placed on a stagnation flow reaches in stationary conditions the temperature of the flow. However, when the flow is in motion, the thermocouple will achieve a temperature, called adiabatic recovery temperature that will be slightly smaller than the total temperature of the flow. The difference between both temperatures will increase as the Mach number of the flow increases and it is also higher for fluids with higher Prandtl numbers. That difference is referred as velocity error in the literature. One way to reduce the velocity error is to hold the thermocouple inside a small stagnation tube called "kiel head". Ideally the stagnation tube would allow the elimination of the velocity error and it also will help to align the flow in those cases when the flow is not axial. Unfortunately, the flow stagnation in the tube amplifies other errors that are caused by thermal conductivity between the thermocouple and the other parts of the probe. Therefore, a compromise solution is adopted which consists in a tube with a pair of side holes called bleed holes that are drilled on the tube, see figure 1. The area of those holes is optimized in each probe to reduce the velocity errors

together with the impact of the thermal conductivity. The bleed holes also help to improve the time response of the probe, although for stationary measurements this is not relevant.

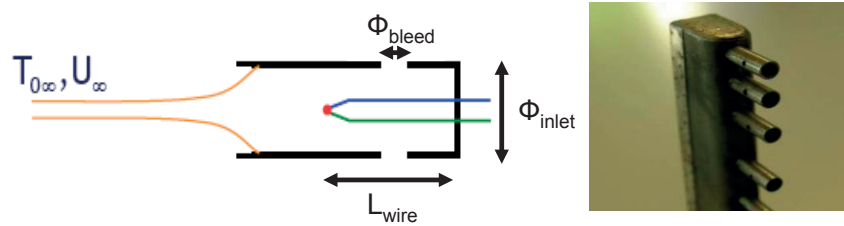


Fig. 1: Tested Kiel Head.

### Wind tunnel

Experiments have been run in the high speed calibration facility at CTA Zamudio. This facility provides a high Mach number horizontal jet (up to 0.8). The air coming from a 90kW compressor goes through a heat exchanger, where the air temperature is conditioned at constant temperature. Several grids and honey comb are installed just after the heat exchanger to ensure flow uniformity and low turbulence level. Finally, a 23:1 contraction nozzle with a 50mm outlet diameter accelerates the flow up to the required velocity, discharging to the atmosphere.

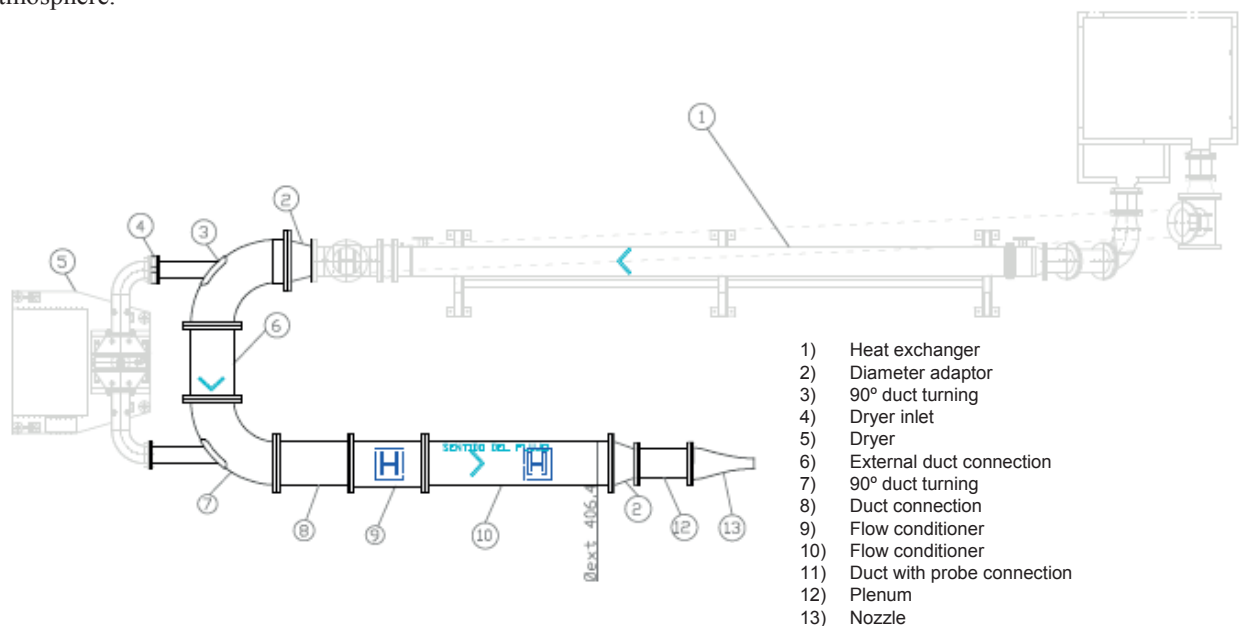


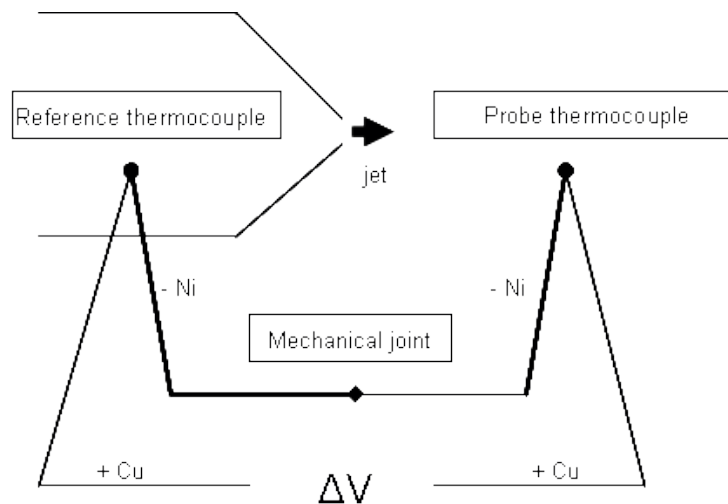
Fig. 2: Calibration facility

This facility is able to give a high quality jet with variations in velocity in the potential core less than 0.4% and variations in total pressure less than 0.02%. The total temperature variations inside the potential core are less than 0.04K.

### Measurement Chain

As part of the probe calibration, the temperature obtained from the sensor must be compared with the total temperature of the flow. The difference between these temperatures will be named as a temperature error, of course, the lower the temperature error the higher the measurement precision. Two strategies can be adopted to get the difference between those temperatures. The first approach consists in getting the “true” total temperature of the flow from a thermocouple placed at the plenum of the facility where the velocity of the flow is negligible

and the sensor temperature will be obtained from the thermocouple of the probe itself. The temperature error then will be externally calculated as the difference between both readings. In the second approach, the thermocouple placed inside the probe is connected directly with the thermocouple placed at the facility plenum as it is shown in figure 3. In this configuration the total temperature error  $\Delta T$  is directly proportional to the voltage difference between the wire extremities and no uniform temperature reference (UTR) is needed, reducing the uncertainty sources from the measurement chain. This latter approach will be the one selected for this paper.



**Fig. 3: Thermocouple connection**

Both wire extremities were directly connected to a VXI electronic system based on HP cards E1509. This system was placed in a closed room equipped with an ambient temperature control mechanism, designed to keep constant the working temperature of the electronic cards. Variations of this temperature can cause signal drifts in the readings that yield to systematics errors in the measured temperature.

### ANALISIS OF HEAT TRANSFER IN A KIEL HEAD PROBE

In the thermocouple configuration shown in figure 3, the generated voltage will be proportional to the difference between the temperatures of the two junctions. Hereinafter the junction placed in the probe will be called sensor and the junction placed at the plenum, 'reference junction'. Both junctions have approximately spherical shape and they have been made by welding.

Both junctions are surrounded by air and by metal bodies, like the pipe that constitutes the plenum for the reference junction and the Kiel for the sensor. The presence of the air will produce a heat transfer between the gas and the junction governed by a forced convection mechanism, while the presence of the metal bodies will produce a heat transfer between the junctions and those bodies by thermal radiation.

If the sphere was hold in the air without any support, the energy conservation equation applied to the sphere would establish a balance between the former overall heat fluxes in stationary conditions, in such a way that:

$$\dot{Q}_{conv} + \dot{Q}_{rad} = 0 \quad (\text{Eq. 1})$$

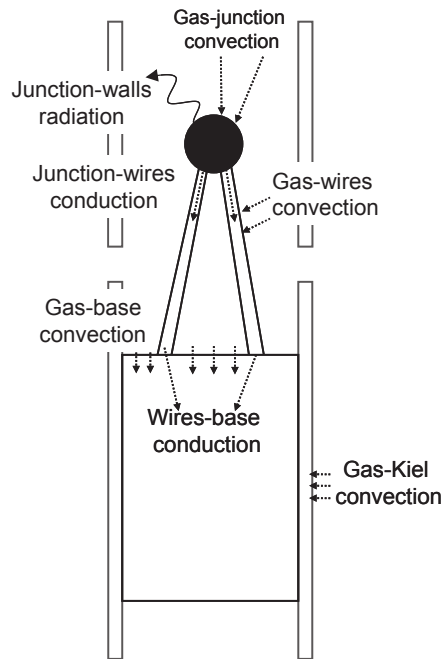
As this is not possible, the sphere or junction is hold in the air by means of the thermocouple wires. These two wires are very thin and therefore their cantilever length cannot be very long to avoid the wire bending. The order of magnitude of the ratio between the length and the diameter is usually 10. After this cantilever length, the two wires are hold by a stem, referred as base in figure 4. The two wires, like the junctions, will also transfer heat with the surrounded air by convention and with the metal bodies by radiation. Hence, the equation 1 is still valid for the system constituted by the junctions and the wires, reaching ideally the same temperature than the junctions alone.

The balance expressed in equation 1, will only vary by thermal conduction between the base and the wires. Unless, either the conductivity of the base material will be null or the boundaries of the base are at the same

temperature than the junction, a new heat flux will be appear in equation 1 that can modify the temperature of the junction and then the temperature error. The modified equation will be:

$$\dot{Q}_{conv} + \dot{Q}_{rad} + \dot{Q}_{cond} = 0 \quad (\text{Eq. 2})$$

These heat fluxes have been reproduced in the sketch of figure 4 for the probe junction. The rest of this section will explain how those fluxes are responsible of the three source of error in the temperature measurement.



**Fig. 4: Heat flux inside the probe**

**Velocity error**

The velocity inside the Kiel Head depends mostly on the free stream velocity and the ratio between inlet and exit area (bleed holes). In an adiabatic process, the temperature measured by the thermocouple would be the total temperature if the inner velocity was zero. But in real instruments the inner velocity is higher and the temperature of the thermocouple junction is less than the total temperature due to heat transfer within the boundary layer and viscous stresses. Then the conversion from kinetic energy to thermal enthalpy is not perfect and the measured temperature is less than the total temperature. Usually this error has been characterized using the recovery factor, an efficiency factor which summarized the energy conversion losses. A recovery factor of 1 says that the conversion is perfect and no losses are achieved.

$$r = \frac{T_{junction} - T_{static}}{T_{total} - T_{static}} \quad (\text{Eq. 3})$$

Several studies of this topic have been performed in numerous geometries and a great variety of correlations have been revealed to model the recovery factors with dimensionless numbers. For a laminar boundary layer over a flat plate the value of r is normally  $Pr^{1/2}$  and for a turbulent laminar layer r is  $Pr^{1/3}$ .

**Radiation Error**

Due to the flow deceleration the junction temperature is higher than the surrounding parts and a radiation process between this junction and the walls takes place. In the transonic rotating rig at CTA, as many others

facilities, the flow is relatively cold, so the radiation processes are an order of magnitude weaker than other heat flows inside the probe. This is not the case for real engine temperature probes. In this case some engine parts in front of the sensor might have a higher or lower temperature due to flame radiation or excessive air cooling. When the sensor is used in these high temperature applications the radiation heat transfer can be of prime importance, being the most important source of error. The radiation error  $\Delta T_{radiation}$  can be modeled by the equation:

$$\Delta T_{radiation} = T_{total} - T_{junction} = \frac{\sigma \cdot \varepsilon}{h_c} (T_{junction}^4 - T_{wall}^4) \quad (\text{Eq. 4})$$

The emissivity  $\varepsilon$  is basically fixed by the thermocouple material and  $T_{wall}$  is the temperature of the surrounding walls.

### Conduction error

Due to the temperature difference between the junction, which is close to the total temperature, and the probe base, which can be higher/lower than the total temperature, a heat conduction phenomena gets increase/reduce the temperature of the sensing element. The thermocouple can be modeled as one dimensional wire with average properties in order to obtain an expression for the conduction error:

$$\Delta T_{conduction} = T_{total} - T_{junction} = \frac{T_{total} - T_{base}}{\cosh \left[ L \left( \frac{4 \cdot h_c}{D \cdot k_s} \right) \right]^{1/2}} \quad (\text{Eq. 5})$$

As this equation shows, if the convective heat transfer coefficient  $h_c$  is increased, the conduction error gets reduce because the boundary layer around the wire acts like a thermal isolator between the junction and the probe stem. “ $h_c$ ” could be increased if the velocity inside the Kiel Head is augmented, but it means that the velocity error is also augmented as it has been shown before. Then, an optimum balance between these both errors can be found to reduce the total temperature error. Some correlation for Nusselt numbers were proposed by Moffat [5] based on experimental data gathered from many thermocouples. For wire normal to the flow:  $Nu = (0.44 \pm 0.06) Re^{0.5}$  and for wires parallel to the flow:  $Nu = (0.085 \pm 0.009) Re^{0.674}$ , where the Reynolds number is based on the wire diameter.

The wire length to diameter ratio plays also a fundamental role in the conduction error. Increasing  $L_{wire}/D_{wire}$  leads to lower values of the conductive error, but the mechanical integrity of the thermocouple wires can be affected, and bending problems arise because the momentum of the flow forces on the wires increases with the relative length.

### Errors influence on the total temperature measurements

The three errors stated above have different influence on the total temperature error measurements depending on the operating conditions. As it will show later, for low temperature applications as the calibration tests presented in this paper, the radiation error is two orders of magnitude lower than the total temperature error, so it can be neglected from the next analysis.

Then, the total temperature error should be a function of the aero-thermodynamic of the flow ( $P_{total}$ ,  $T_{total}$  and  $U$ ), the viscosity, the main geometric characteristics of the temperature probe as  $L$ ,  $D$  and area ratio, and a function of the air and wire thermal conductivity. Finally, the conduction error is controlled by the base temperature  $T_{base}$  (equation 5), and this error plays a primary role in the thermal problem. This base temperature is fixed by the aero-thermodynamic around the whole temperature probe, the air conductivity and base material conductivity. In order to derive  $T_{base}$  a simplified one dimensional model of the heat transfer between the external face of the kiel head and the junction is presented. This model takes into account the next heat fluxes over the Kiel base (figure 4):

- Heat transfer from thermocouple wires to base.
- Heat transfer from the stagnation air inside the kiel to base.
- Heat transfer from the surrounding metallic Kiel case to base.

The air in contact with the base has no velocity because the bleed holes are placed upstream of them. Then a process of natural convection takes place between air and the base which can be obviated because the heat transfer is one order of magnitude lower than the one given by the conduction between wires and base. That means the heat conduction from the surrounding metallic Kiel case to ceramic is equal to the heat transfer from wires to base in a stationary case. The heat flow from the thermocouple wires to base is the same heat flow the wires takes from the surrounding air so the energy equation can be simplified up to the next form:

$$\dot{Q}_{cond} = \dot{Q}_{conv} \quad (\text{Eq. 6})$$

Where  $\dot{Q}_{cond}$  is the conduction heat flux from the metallic case to ceramic and  $\dot{Q}_{conv}$  is the heat flux from the air to the thermocouple wires. These both terms can be calculated as follows:

$$\dot{Q}_{cond} = k_{cer} \frac{(T_{Kiel} - T_{base})}{D_{cer}} \cdot A_{cer} \quad \text{where } A_{cer} \text{ is the ceramic area in contact with the Kiel case.}$$

$\dot{Q}_{conv} = h_{conv} \cdot (T_{total} - T_{base}) \cdot A_{wires}$  where  $A_{wires}$  is the thermocouples wires area exposed to convection.

A relationship for  $T_{base}$ ,  $T_{total}$  and  $T_{kiel}$  can be yielded from equation 6:

$$\frac{T_{base} - T_{total}}{T_{Kiel} - T_{total}} = \frac{\beta}{1 + \beta} \quad (\text{Eq. 7})$$

Where  $\beta$  is a parameter which takes into account the thermal conductivity ratio between ceramic base and air:

$$\beta = \frac{1}{Nu} \cdot \frac{k_{cer}}{k_{air}} \cdot \frac{L_{cer}}{D_{cer}} \cdot \frac{D_{wire}}{L_{wire}} \quad (\text{Eq. 8})$$

The lower the value the  $\beta$ , the lower the conductivity error is. So the thermal conductivity ratio should keep as low as possible. For high  $\beta$  values (order of 1000)  $T_{base}$  would be close to  $T_{kiel}$ , which means the base material thermal insulation is inefficient and the conductivity error plays the major role. For low  $\beta$  values (order of 1),  $T_{base}$  would be close to  $T_{total}$  and the total temperature error would be independent from the Kiel external flow conditions. In this case the conductivity error is reduced and the main temperature error comes from the velocity error. Then, the junction temperature  $T_{junction}$  would be close to the recovery temperature of the air inside the Kiel, which would be at low Mach number if the bleed holes area is selected properly.

$T_{kiel}$ , can be modeled as a recovery temperature of the external flow with a recovery factor of  $r=Pr^{1/2}$ . This assumption has been validated experimentally from the measurements of a thermocouple that has been glued on the Kiel metallic casing. Due to that, the  $T_{base}$  depends strongly on the thermal conductivity ratio and the base material of any temperature probe must be carefully selected in function of the application for reducing the conductivity error as much as possible.

In the present analysis there are no effects of water condensation and later on it will show how geometry details as junction position inside the Kiel and roughness do not play an important role in the thermal problem inside the probe. Then the total temperature error can be expressed as:

$$\frac{\Delta T_{total}}{T_{total}} = f\left(\beta, \frac{L_{wire}}{D_{wire}}, \frac{k_{wire}}{k_{air}}, A_r, Re, M_\infty^2, Pr, \gamma, \frac{\mu_v}{\mu}\right) \quad (\text{Eq. 9})$$

Considering that the working fluid is low temperature air, this expression can be simplified up to the next form:

$$\frac{\Delta T_{total}}{T_{total}} = f\left(\beta, \frac{L_{wire}}{D_{wire}}, \frac{k_{wire}}{k_{air}}, A_r, Re, M_\infty^2\right) \quad (\text{Eq. 10})$$

Instead using the non-dimensional value of the total temperature error, the measurements will be plotted using the recovery ratio  $\eta$  defined as follows:

$$\eta = \frac{T_{junction}}{T_{total}} = 1 - \frac{\Delta T_{total}}{T_{total}} \quad (\text{Eq. 11})$$

The rest of the paper will explore the sensitivity to the parameters of expression 10.

## SIMULATION TOOL

A simulation tool has been developed to calculate an estimated total temperature error for given geometrical, thermocouple wires and flow parameters. The tool incorporates the one-dimensional equations presented above and considers the following hypothesis:

- Internal flow velocity fixed by the area ratio between inlet and bleed holes, and discharge coefficient of 0.5.
- Velocity error based on a recovery factor of  $r=Pr^{1/2}$
- Heat conduction from junction to base stem based on equation 5. The base temperature is measured using a thermocouple glue on the surface.
- Heat radiation between the junction and the enclosure (equation 4).
- Heat conduction between wires, base and Kiel casing.

As a result not only the temperature of the tip of the thermocouple is given but the complete temperature profiles and heat fluxes in the thermocouple are calculated.

## RESULTS AND DISCUSSION

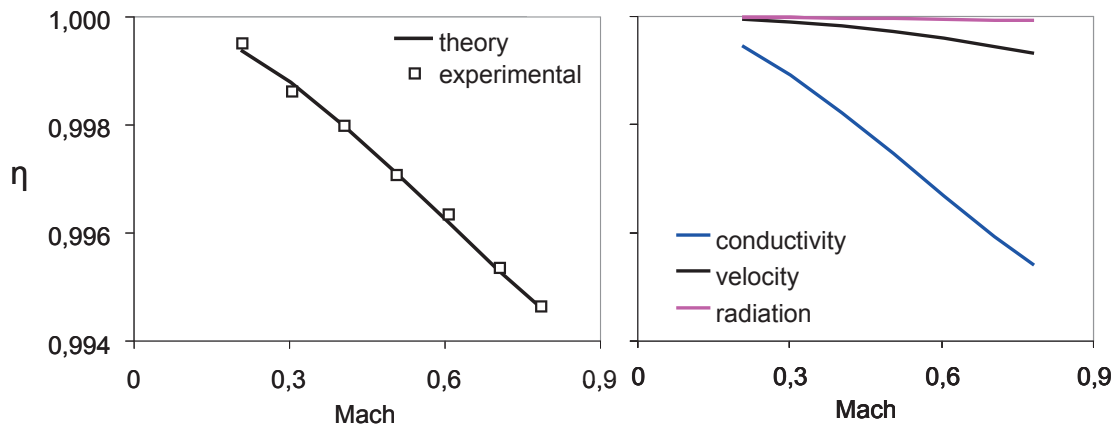
### Nominal Kiel Head results

The tested temperature probe, with exception of the thermocouple type, has been designed for engine applications (hot environment). It is a common practice in the industry to calibrate this kind of probes in low temperature facilities, which can sometimes yield big errors. The main parameters of the tested probe (called nominal Kiel Head geometry) are summarized in the next table:

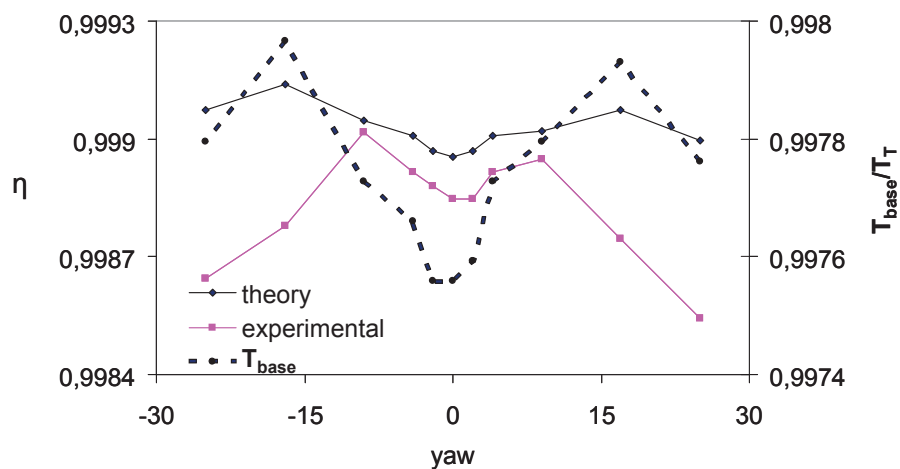
Base Type	Al <sub>2</sub> O <sub>3</sub> based
TC Type	T
Area ratio	0,37
L <sub>wire</sub> /D <sub>wire</sub>	10

**Table 1: Nominal Kiel Head geometry. Main parameters**

Figure 5 compares the measured total temperature error and the calculated one for this Kiel head geometry. The calculated results represent the experimental values and the analysis of the different heat fluxes gives an insight of the total temperature error sources.



**Fig. 5: Mach number influence**



**Fig. 6: Yaw angle influence for M=0.3**

Despite all simplifications of this analytical tool it seems to give good results and it can be used to analyse the thermal problem. These results show low radiation error due to the almost isothermal condition between junction and surrounding walls. The radiation error is two orders of magnitude lower than the total temperature error and it can be obviated from the calculations. The biggest error is the conductivity one, which represents the 80% of the total temperature error meanwhile the velocity error is just the 20%. This fact means the best way to improve the total temperature measurements for the tested probe goes through reducing the conductivity error.

Figure 6 shows the variation of the total temperature error in function of the flow incidence angle. The blue discontinuous line shows the base temperature in function of this incidence angle. This temperature has a great influence in the conduction error and the total temperature error behaves like the base temperature. Between angles 0° and ± 10° the base temperature goes up and gets closer to the total temperature because the heat



transfer is more efficient for perpendicular cylinders ( $Nu=0.44Re^{0.5}$ ) than parallel cylinders ( $Nu=0.085Re^{0.674}$ ). Then the conduction error gets reduce and the total temperature error improves. For angles higher than  $\pm 10^\circ$  two different effects take place. Up to  $\pm 15^\circ$  the base temperature increases and then the theory says that the temperature error goes down. From  $\pm 15^\circ$  the probe gets out of the potential core and the base temperature decreases, enhancing the conduction losses. However, the experimental total temperature error increases from  $\pm 10^\circ$  onwards. For this angle the Kiel can be unable to straighten the flow, so a big flow separation area appears that causes a lower measured temperature by the thermocouple. The measurement range of this probe is  $\pm 10^\circ$ , so the total temperature error in this case is about 0.1K.

Therefore, the total temperature error is dominated by the conduction error. This fact is a consequence of two selections: the thermocouple and the base material. Thermocouple T type is based on copper wire with high thermal conductivity and the heat flux from junction to base is enhanced. The base material is made of aluminum oxide. This oxide has a thermal conductivity of order 1W/mK for 1000°C which makes it suitable for engine applications. However for low temperature the thermal conductivity increases up to 30 W/mK and the base material does not work as it should. Then  $T_{base}$  is practically equal to  $T_{kiel}$ .

### Kiel Head geometry influence

Once the nominal Kiel Head geometry had been tested some variations of the Kiel geometry were tested in order to understand the physics of the probe and validate the theoretical tool. Three main parameters were varied: the bleed hole area, which modifies the inlet-outlet flow area ratio, the axial position of the junction inside the Kiel and the bleed holes position. Other second influence parameters had been tested as Kiel ruggedness and axial junction deviations.

Figure 7 compares the total temperature error for the nominal Kiel Heat (K1), a Kiel Head with  $A_r = 0.94$  (K3) and a bare thermocouple (no Kiel). For low Mach number the model does not fit the experimental results for bare thermocouple, which is probably a conduction underestimation effect. However the theoretical results correlate with the experiments for K1 and K3 geometries and in the bare thermocouple case, the theory also fits the experiments for high Mach number. The lowest error is the one yielded by the K1 geometry but it is close to the K3 geometry error, meanwhile the bare thermocouple yields temperature error three times bigger. The different source errors explain this behaviour.

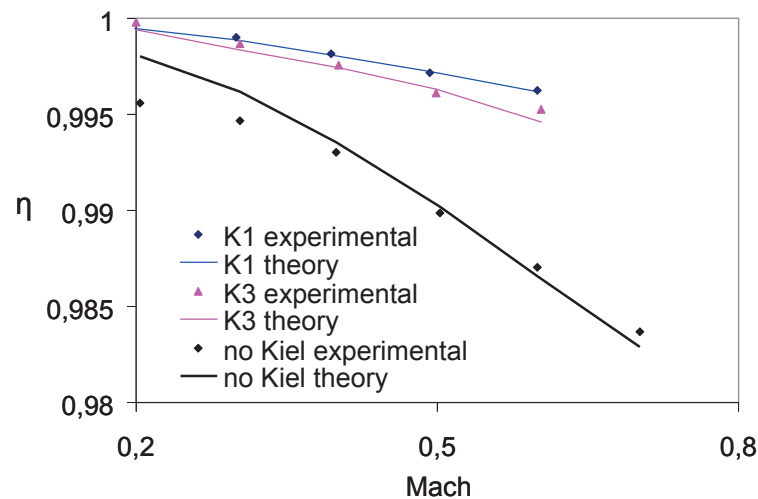


Fig. 7: Total Temperature error for three different Kiel Geometries.

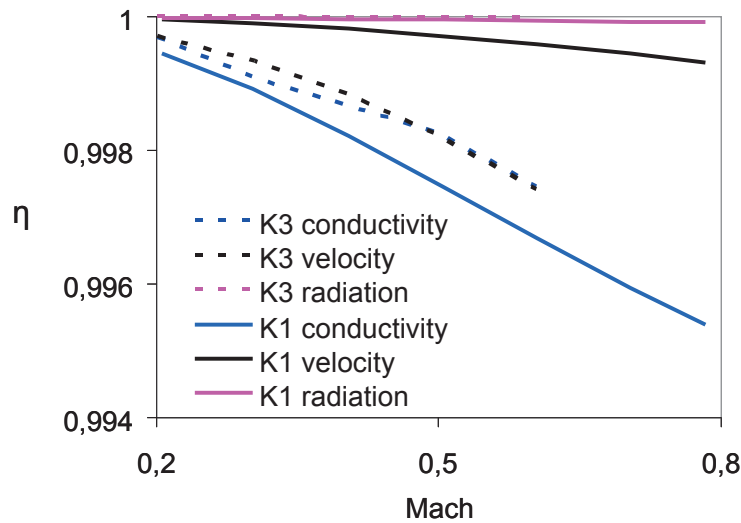


Fig. 8: Temperature errors for K1 and K3 geometries.

Figure 8 shows the temperature errors for K1 and K3 geometries. K3 geometry has the biggest area ratio which means the inner velocity is the highest one. Then the K3 velocity error is higher than the one given by K1. In contrast, the conduction error behaves in opposite direction. Due to the high inner velocity, the conduction error goes down because this high velocity enhances the convective heat transfer over the thermocouple wires and the conduction through them is reduced. There are two different effects with different trends and the theoretical model developed in this work takes them in account. An optimal area ratio can be derived, which optimized the thermal fluxes inside the probe and the total temperature error is reduced at its minimum. The value of the area ratio for minimum temperature error ranges between 0.3 and 0.4, depending on the Mach number.

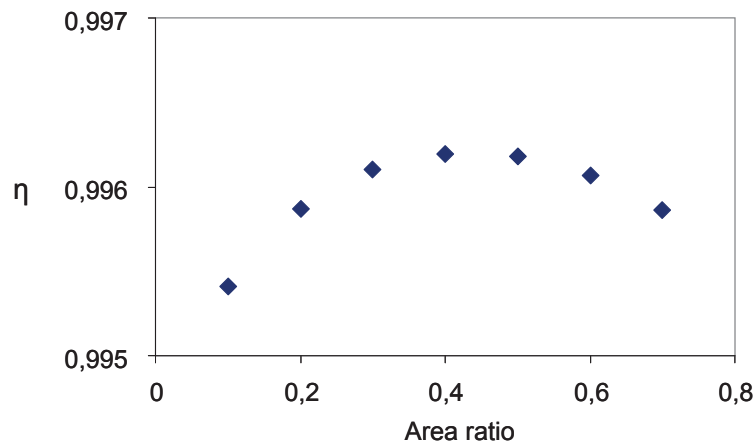


Fig. 9: Recovery ratio for M=0.6 as a function of area ratio.

Figure 9 shows the area ratio influence on the recovery ratio. For an area ratio close to 0.3 or 0.4 the recovery ratio sensitivity  $\partial\eta/\partial A_r$  is less than 0.02% and then manufacturing errors of the probe (diameter tolerance) of 1% means a variation on recovery ratio of 0.3%.

The bleed hole position on the stagnation tube has been studied and it has an influence on the angle behaviour of the probe. Two different configurations has been tested, configuration C-1 which is the nominal configuration and configuration C-2, which is the C-1 configuration but with the two holes turned 90 degrees around the probe axis (figure 10)

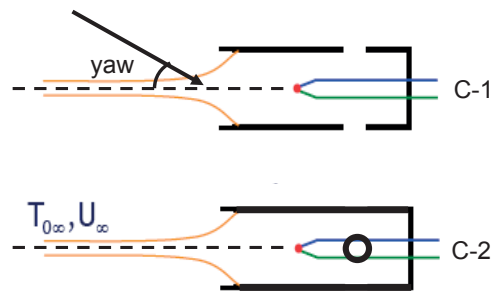


Fig. 10: C-1 and C-2 configurations

Between  $-5^\circ$  to  $5^\circ$  configuration C-2 behaves much better than configuration C-1 (figure 11), yielding an almost invariant temperature error., meanwhile C-1 has a reduce yaw range where the total temperature does not change. The maximum value is reached for both configurations at  $\pm 10^\circ$ . At this yaw angle the flow starts to separate inside the Kiel and the thermal losses increases the total temperature error. From the 'measurement range' point of view ( $\pm 10^\circ$ ), both configurations have the same total temperature error, which is of the order of 0.1K.

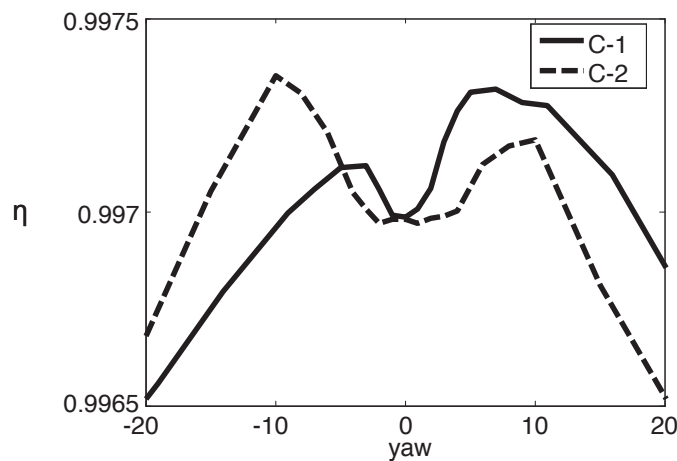


Fig. 11: C-1 and C-2 configurations influence on the yaw behaviour

The position of the junction inside the Kiel (figure 12) and the ruggedness have been also studied experimentally, keeping the inlet-outlet area ratio and the wire length constant and equal to the nominal configuration. Figure 13 compares the total temperature error for two different axial junction positions: P1 (nominal geometry) and P2 (figure 12), separated 20% Kiel diameter (the value  $L_{\text{wire}}/D_{\text{wire}}$  has been kept constant). Both geometries yield the same results. This figure includes also the effect of the Kiel surface roughness (figure 14) and axial deviation of the junction (figure 15)

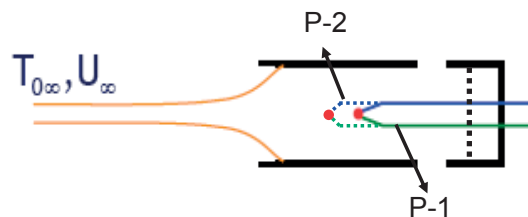


Fig. 12: P-1 and P-2 configurations

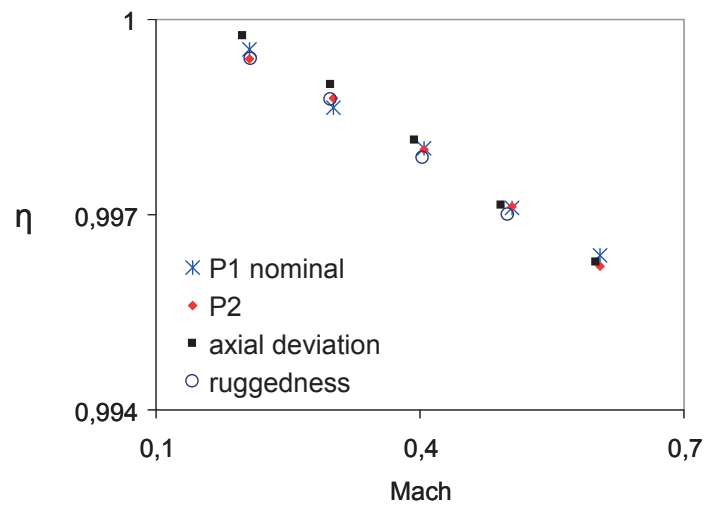


Fig. 13: Temperature errors for two junction axial positions

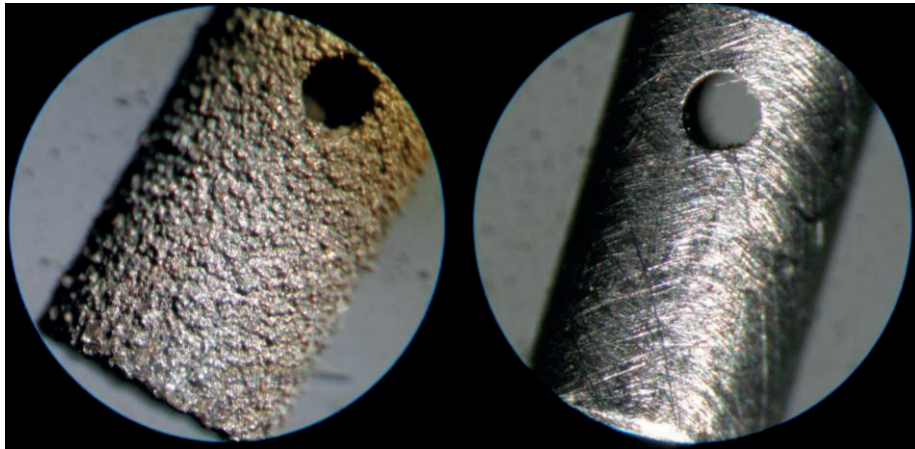


Fig. 14: Different surface roughness tested

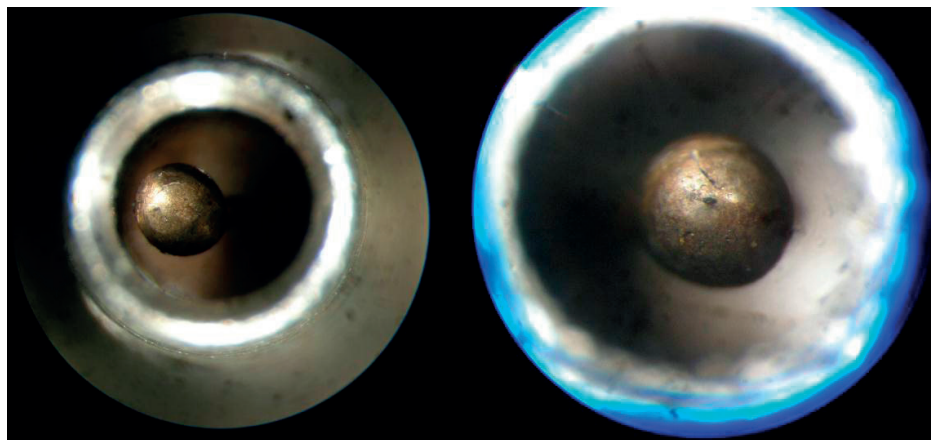


Fig. 15: Axial deviation of the junction

### Sensor optimization

Results have shown the biggest influence on the total temperature error comes from the  $L_{\text{wire}}/D_{\text{wire}}$  ratio, thermocouple type and base material, meanwhile another effects as roughness or variations in junction location inside the Kiel have low incidence in the thermal behaviour of the temperature probe. The theoretical model has shown itself robust and precise and it can be used to estimate the total temperature error when other parameters are changed.

As figure 5 shows, the biggest thermal error comes from the conductivity error. Then the main efforts to reduce the total temperature error should be focus on the reduction of the heat transfer from the junction to the probe base.

The thermocouple type used in this set of experiments was special T-type. This selection was performed in order to avoid any aging problem and to have a uniform static calibration law for all thermocouples. However, the material the thermocouple is made of should be of primary importance for reducing the conduction error as far as possible. The next table shows the wire conductivities for the most used thermocouples:

	Conductivity W/mK
K Type	
Chromel	19
Alumel	29,6
E Type	
Chromel	19
Constantan	21,1
J Type	
Iron	67,5
Constantan	21,1
N Type	
Nicrosil	14,9
Nisil	27,7
T Type	
Copper	375
Constantan	21,1

**Table 2: Thermal conductivities**

Type T thermocouple has the biggest conductivity and it would yield the biggest conduction error. Due to the high reliability and low thermal conductivity, type-K thermocouple seems the most suitable sensing element for low temperature sensors based on Kiel Head.

The parameter  $L_{\text{wire}}/D_{\text{wire}}$  also can be also modified to reduce the conduction error. The bigger this parameter is, the lower the conduction error. This value has a limit due to the mechanical integrity of the wires. According to Moffat [5],  $L_{\text{wire}}/D_{\text{wire}} = 20$  is a good compromise between mechanical integrity and conduction error.

A special attention must be paid on the selection of the base material. The thermal conductivity should be as low as possible taking into account others material properties as operating temperature limit.

Figure 16 compares the total temperature error from the nominal probe (table 1) and a similar temperature probe instrumented with type-K thermocouple and  $L_{\text{wire}}/D_{\text{wire}} = 20$ .

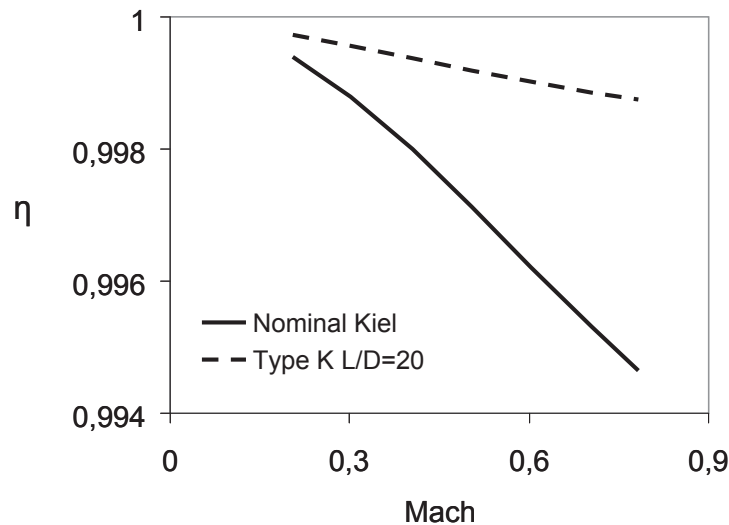


Fig. 16: Temperature errors

The improvement is obvious, but changing the thermocouple type should be a careful process due to aging and reliability problems.

## CONCLUSION

The efficiency measurements error is closely related to the total temperature error, and this one is finally strongly linked with the recovery ratio. Turbine efficiency measurements precision can be strongly improved if the total temperature error is reduced as far as possible and calibrated in a well-controlled calibration facility.

This work has thrown some light onto the physics and heat flows of a total temperature probe based on a thermocouple placed inside a Kiel Head. It has been discussed the principal thermal errors of the measurements and the main influence factors have been revealed. Conductivity and velocity errors are the main source of total temperature error for low temperature application; meanwhile for high temperature applications the radiation error plays an important role. The velocity error depends mainly on the Mach number inside the Kiel and the conductivity error depends on this Mach number and the probe base temperature, which relies on the external air velocity and temperature.

Therefore, the Mach number inside the Kiel plays a major role, so this parameter controls both the conductivity and the velocity error. This Mach number is fixed by the bleed holes to inlet area ratio and the optimum area ratio moves between 0.3 and 0.4 depending on the inlet Mach number. The nominal probe tested in this work, showed an area ratio of 0.37 that was proven to be close to the optimal value. The thermocouple wire ratio  $L_{\text{wire}}/D_{\text{wire}}$  is another parameter with a great influence on the total temperature error through the conductivity error. The bigger this value, the lower the conductivity error is. However,  $L_{\text{wire}}/D_{\text{wire}}$  has an upper limit depending on wire material due to bending problems. An optimal value for T and K thermocouples is around 20. Thermocouple Type is of prime importance due to its impact on the conductivity error. The selection process of the thermocouple type should take into account aspects as sensor aging, reliability or stability, which could have a big impact on the measurements. On the other hand, a proper selection of the base material leads to a low temperature difference between Kiel base and total temperature, reducing the conductivity error.

Yaw angle also has a great influence on the recovery ratio. For angles between  $\pm 10$  degrees the recovery ratio goes up because the base temperature gets closer to the total temperature. Anyway, low conductivity errors would yield low variation of recovery ratio for different yaw angles in this range. For this angle onwards the thermal effectiveness of the probe is reduced. Configuration C-2 yields the best option so the recovery ratio variations are almost zero for  $\pm 5$  degrees. However in the  $\pm 10$  degrees range, both configurations C-1 and C-2 yields the same error, 0.1K.

Tests also have shown the influence of minor variations in geometry as junction position deviations inside the Kiel and roughness. This geometrical variations are similar than the ones found on Kiel Head manufacturing processes and not measurably variations in recovery ratio have been yielded

Finally, the one dimensional tool developed for this work has shown itself robust for this kind of Kiel probe and fluid conditions. It is based on the inlet Mach number, base temperature, L/D wire ratio and inlet to bleed hole area ratio, and yields accurate total temperature errors, which match reasonably well with the experimental results. This analytical can be used for designing the Kiel Head total temperature probe at the early stages of the design process.

## ACKNOWLEDGMENTS

The authors wish to thank ITP for their support of the project and their permission to publish this paper. Also J. Pradera for his successful realization of the probes and his technical support.

## REFERENCES

1. Vázquez R., Sánchez J.M. 2003: "Temperature Measurements System for Low Pressure Ratio Turbine Testing". ASME TURBO EXPO, GT-2003-38685.
2. Eckert, E. R. G. and Drake, R. M., 1972, "Analysis of Heat Transfer and Mass Transfer," McGraw-Hill, New York.
3. Zeisberger A., 2007: "Total Temperature Probes for Turbine and Combustor Applications". ISABE-2007-1108.
4. Saravanamuttoo H.I.H, 1990: "Recommended practices for measurement of gas path pressures and temperatures for performance assessment of aircraft turbine engines and components". AGARD Advisory Report No. 245.
5. Moffat R.J., 1961: "Gas Temperature Measurement". Proceeding of temperature – its Measurement and Control in Science and Industry. Applied Methods and Instruments. 3 (part2), pp 553-571. Reynolds Publ. New York.
6. Moffat R.J., 1986: "Advance Experimental Techniques in Turbomachinery". Chapter 3: "Thermocouple Theory and Practice". Principal Lecture series No. 1. Concepts ETI, Vermont 05055.
7. Paniagua G., Dénos R., Oropesa M., 2002: "Thermocouple Probes for Accurate Temperature Measurements in Short Duration Facilities". ASME TURBO EXPO, GT-2002-30043.
8. Behrens W., 1971: "Total Temperature Thermocouple Probe Based on Recovery Temperature of Circular Cylinder". Int. J. Heat Mas Transfer, Vol. 14, pp. 1621-1630.
9. Ballantyne A., 1977: "Fine Wire Thermocouple Measurements of Fluctuating Temperature". Combustion Science and Technology, Vol. 17, pp. 63-72.
10. Toenshoff D. A. 1969: " A Discussion on Common Thermocouple Calibration Problems". SAE 690429. Society of Automotive Engineers.
11. Forbes Dewey JR. C. 1964: " A Correlation of Convective Heat Transfer and Recovery Temperature Data for Cylinders in Compressible Flow". Int. J. Heat Mass Transfer. Vol. 8 pp. 245-252.
12. Gostelow J.P. and Watson P.J 1976: "A Closed Circuit Variable Density Air Supply for Turbomachinery Research". ASME paper 76-GT-62.
13. Rom J. Kronzon Y. 1967: "Small Shielde Thermocouple Total Probes" TAE Report No. 79. Institute of Technology, Israel.
14. Nozicka J., 1994: "Unconvencional Combined Probe for Flow Speed and Temperature Measurement". Proceedings FLUCOME 94. Edited by ONERA CERT. 1, pp. 11-16. Toulouse. ISBN 2-84088-010-5.
15. Nozicka J., 2001: "The Calibration of Probe for Measurement of the Total Temperature of Compressible Fluid Flos". Proceedings of the 4<sup>th</sup> European Conference on Turbomachinery, pp 57-66. Firenze.
16. Collis D.C. Williams M.J., 1959: "Two Dimensional Convection From Heated Wires at Low Reynolds Number". J. of Fluid Mechanics. 6 pp 357-384.
17. Fleeger D.W. and Seyb N.J., 1975: "Aerodynamic Measurements in Turbomachines". AGARD Report No. 207. pp 79-120.

## EXPERIMENTAL ANALYSIS MEANS OF THE TURBINE PARTS THERMAL STATE

D.V. Karelin, NPO Saturn, Russia  
dmitry.karelin@npo-saturn.ru

S.D. Mukhina, NPO Satum, Russia  
lanamuchina@rambler.ru

### ABSTRACT

The present paper reports experimental data acquisition and processing with application of different temperature measuring instruments, stating their advantages and disadvantages.

### INTRODUCTION

For the purposes of experimental analysis of the turbine parts thermal state, NPO Saturn applies thermometry during the tests within the engine and at component test benches. Thermocouples (for stator parts) and IMTK probes (for rotor parts) are used for thermometry.

### RESULTS AND DISCUSSION

#### *Peculiarities of thermometry with the help of the IMTK probes*

The IMTK probe (crystal-type maximum temperature meter) is an irradiated silicon carbide of cubic modification. Point defects are accumulated in it during the neutron irradiation. The defects presence results in the change of its crystal lattice. When heating the irradiated crystal to the temperature exceeding the irradiation temperature, the defects start to anneal. As a consequence, gradual crystal lattice recovery is taking place. The IMTK performance is based upon the dependence of the rate of irradiated crystal angle on the temperature and the anneal time. The scheme of IMTK mounting on the part under examination is given in Figure 1. The IMTK probe is mounted into the hole at a depth of 0,45...0,6 mm.

The IMTK probe measuring range is 100 to 1200°C. Absolute error of measurement is ~12°C.

The advantages of IMTK probes are absence of necessity to use the slip ring when measuring the temperature on the rotating parts, as well as reliability of mounting on the part. Another important advantage of IMTK probes is minimum protrusion of instrumentation above the part surface (because it is very important to keep the expected profile flow and the air curtain structure during the blade airfoil thermometry).

The IMTK probe disadvantages can be as follows:

1) As the IMTK probe annealing for the temperature test can be done only once, the new assembly of the part under examination with the new set of IMTK probes is required for each test condition. This increases the time and financial expenses of the experiment.

2) The IMTK probe is mounted at a depth of 0,45...0,6 mm. That is why in case of considerable temperature gradient inside the part body, the probe readings can differ from the real temperature on the part body. The calculations testified to the fact that during the blade tests, the temperature at the depth of the IMTK mounting was 20 °C lower than the temperature on the blade surface on the average. It is necessary to take this feature into account during the experimental data processing.

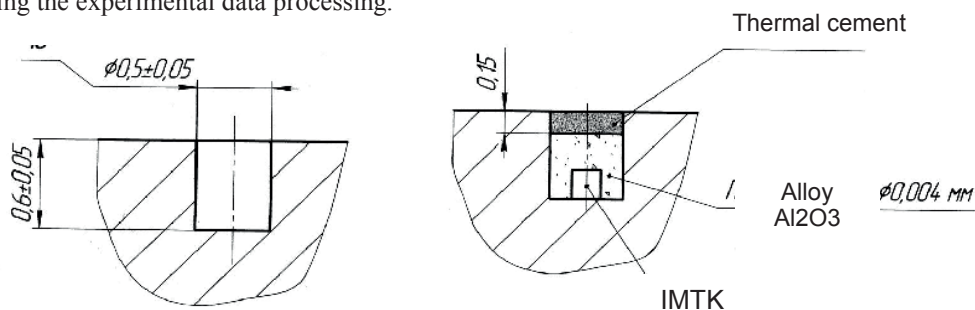


Fig. 1. Scheme of IMTK probe mounting into the examined part.



Peculiarities of thermomentering with the help of thermocouple probes

The main advantage of the thermocouple application (as compared to the IMTK probe) is the possibility to examine the part temperature at one assembly at all required modes without reassembling the part under examination.

The characteristic feature of traditional method of blade airfoil temperature measurement with the help of thermocouples is their location outside the airfoil.

One of the disadvantages of this location is the influence of instrumentation protrusion on the downstream flow parameters and structure. The performed calculations of instrumentation influence on the flow parameters in the blade passage (Figure 2), revealed significant influence of the instrumentation protrusion on the profile flow.

The second disadvantage of the thermocouple outer location is urgent for examination of blades with convective-film cooling system. The instrumentation protrusion has major effect on the cooling film structure, by degrading it. Figure 3 shows testing the blade with convective-film cooling system.

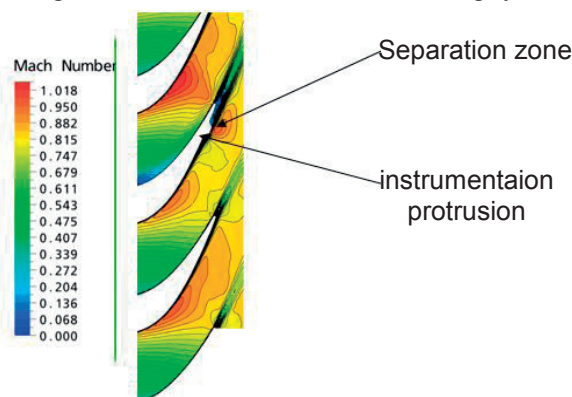


Fig. 2. Instrumentation influence on the flow structure in the blade passage

## ANALYSIS OF THERMOCOUPLES AND IMTK PROBES READINGS

Actual experience of thermocouples and IMTK probes application was get on the test benches during the tests of the blade thermal state under the external flow with hot gas. The blades with different cooling systems were tested within a wide range of  $M_2$  (0,7...1) and  $Re_1$  ( $10^5$  ...  $10^6$ ) numbers. Typical size for  $Re_1$  number is the blade chord.

Film cooling of the blades under examination was provided by multiple perforation holes on the pressure and suction surface walls. Based on the IMTK readings it is seen that the experimental cooling effectiveness is 5-10% more, as compared to the thermocouples readings. Probably this is connected to the fact that the thermocouples were mounted in the same blade section. The film was gradually broken while flowing successively located thermocouple protrusions downstream. It is seen that in the leading edge area in the zone of film formation, the difference between the thermocouple and IMTK readings is not large. But on the trailing edge, in the zone of a developed film, this difference is much greater. In case, when the film is not provided by the design (Figure 4), the cooling effectiveness determined with the help of thermocouples and the IMTK probes practically coincide.

To maintain the flow structure in the blade passage and the cooling film configuration, minimum protrusion of measuring instruments in the blade passage shall be provided. To this effect, the thermocouples are mounted into the slots (Figure 5). When examining the thermal state of modern thin-walled blades, the cable thermocouples with the working section diameter of 0,5 mm are used to minimize the slot depth.

## CONCLUSION

To examine the thermal state of blades with convective-film cooling system under the conditions of external flow, it is necessary to use the measuring means with minimum flow distortion in the blade passage, allowing performing tests within large range of the parameters without dismounting the part under examination. The IMTK probes meet the first requirement, but they fail to meet the second one. The thermocouples fixed on the blade surface allow performing the tests within the wide range of parameters, but depending on their fastening technique, introduce different distortions in the leaked-in flow structure. To correct the measurement errors caused by different methods of the thermocouples fastening on the blade, works on assessment of measuring error are going on with the purpose to take this information into account when analyzing the thermomentering results.

Application of noncontact optical measuring instruments for the turbine parts thermomentering is more expensive as compared with the application of touch trigger probing technique, and requires more complex

secondary processing, but it meets the requirements stated above and besides, increases the information content of the experiment.

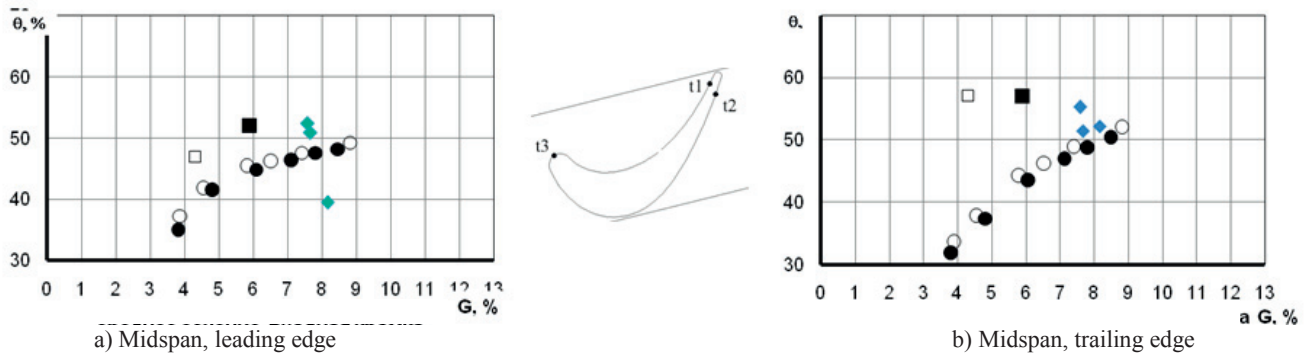


Fig. 3. Difference between the thermocouple and IMTK probe readings when measured on the blade leading edge (a) and trailing edge (b)

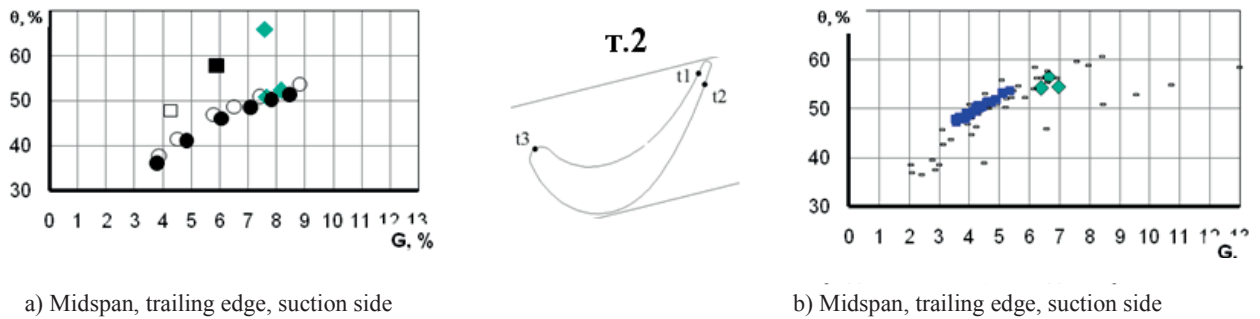


Fig. 4. Difference between the thermocouple and IMTK probe readings when measured on the blade trailing edge in case of the developed film (a) and without the film (b).



## ON MEASUREMENT AND EVALUATION OF FLOW CONDITIONS AT LIMIT LOAD OF TURBINE BLADE CASCADES

Pavel Šafařík  
Czech Technical University in Prague  
Department of Mechanical Engineering  
Prague, Czech Republic  
e-mail: pavel.safarik@fs.cvut.cz

Martin Luxa, Helena Picmausova, David Šimurda  
Institute of Thermomechanics  
Academy of Sciences, v.v.i.  
Prague, Czech Republic

### ABSTRACT

This paper deals with methods of experimental research on flow past turbine blade cascades under conditions of limit load. Measurements are performed by both optical and pneumatic methods (probe traversing). Obtained experimental data – pictures of flow fields and distributions of total pressure, static pressure, and exit velocity argument – are utilized for evaluation of forces and parameters to show limit load regimes. Subject of the investigation are blade cascades representing tip section and root section of rotor blading with relatively long blades.

### INTRODUCTION

There are four significant regimes at operation of high-speed turbine blade cascades. The first regime, called critical Mach number, determines (and is determined by) first occurrence of maximum local flow velocity equal to sound speed of the flowing medium. The second regime concerns transonic flow conditions when aerodynamic choking takes place, i.e. when sonic line first time fully crosses the interblade channel. At aerodynamic choking, maximum nominal flow flux is achieved. The third significant regime can be characterized by flow conditions when regular interaction of internal branch of exit shock waves at the suction side of adjacent blade occurs. This regime determines supersonic flow regimes in exit part of turbine blade cascades. The fourth regime, called limit load, determines conditions at which the back pressure cannot affect flow development in exit part of the blade cascade. In this paper methods enabling to measure flow conditions at limit load of turbine blade cascade are presented and discussed. Remaining three regimes, critical Mach number, aerodynamic choking and regular interaction of internal branch of exit shock waves, are possible to study according to experimental data from optical measurements described in [1].

Parameters of blade cascade limit load are important for designers of those turbomachine blades where working medium exits blading at supersonic velocities. Collocation limit load means no possibility to increase aerodynamic force acting on blade cascade profiles by decreasing exit static pressure under constant inlet flow conditions [2]. Experimental research confirms that with decreasing back pressure flow develops to limit load regime for transonic blade cascades where aerodynamic choking takes place. Pictures of flow fields prove that limit load occurs when the internal branch of exit shock waves touches trailing edge of adjacent blade. Further increase of exit Mach number leads to flow structure at which inner branch of exit shock waves completely misses adjacent blade.

Optical methods provide pictures and data on flow conditions at turbine blade cascade limit load. The authors applied interferometric measurement method and aerodynamic forces are evaluated from interferograms [3]. Obtained data can determine limit load conditions.

Traversing probe method gives also possibility to obtain data on limit load of turbine blade cascade. Parameters from data reduction method – namely exit Mach number  $M_2$  and exit angle  $\alpha_2$  (oriented to machine rotor axial direction) – can determine conditions of limit load according to following condition:

$$|M_2 \sin \alpha_2| \geq 1 \quad (1)$$

The authors have at their disposal extensive archive of results from aerodynamic investigations of different blade cascades. Specific regimes can be studied. For purpose of this paper results of investigations of two blade cascades – tip sections and root sections of rotor blading with relatively long blades – are presented and discussed [4].

## RESULTS AND DISCUSSION

Application of optical methods for observation of limit load regime of a turbine blade cascade is very convenient. These methods give pictures of flow structures namely configurations of shock waves. Visual information offers evidence of flow development at decreasing back pressure. At supersonic exit velocities exit shock waves arise downstream of trailing edges. Their internal branch determines region which cannot be affected by downstream flow parameters. If the internal branch of exit shock waves interacts with external branch of exit shock waves arising downstream of trailing edge of adjacent blade limit load regime is exceeded.

Figure 1 shows interferogram of flow field at the root section of rotor blading at isentropic exit Mach number  $M_{2is} = 1.828$  and incidence angle  $i = 0^\circ$ . Exit shock waves arise behind trailing edges and do not interact with adjacent blades. Namely the internal branch of exit shock waves misses the trailing edge of the adjacent blade i.e. blade loading is at its limit.



**Fig. 1: Interferogram taken at isentropic exit Mach number  $M_{2is} = 1.828$  and angle of incidence  $i = 0^\circ$**

Figure 2 shows dependencies of non-dimensional aerodynamic forces  $F/(A \cdot p_{01})$  on isentropic exit Mach number  $M_{2is}$  for constant incidences  $i$  [°]. Forces are evaluated from interferograms for the profile of the root section. Aerodynamic force is denoted  $F$  [N],  $A$  is defined area (pitch x length of the blade) [m<sup>2</sup>], and  $p_{01}$  [Pa] is the total pressure of the inlet flow. The evaluation is based on the principle of the interferometric method [1] – fringes in the flow field represent lines of constant index of refraction – and on the assumption of isentropic changes in the main flow and constant static pressure across the boundary layer. Aerodynamic force is solved by integration of a distribution of static pressure along pressure and suction sides in peripheral direction. Constant value of aerodynamic force shows limit load regimes of the blade cascade.

Application of traversing probe method for observation of limit load regime of a turbine blade cascade is not so convenient and objective in comparison with optical methods. Measurements of distributions of static pressure, total pressure and argument of velocity vector along pitch in traversing plane give basic data for evaluation of representative data of exit flow. Data reduction method [5] evaluates exit Mach number  $M_2$  and exit angle  $\alpha_2$  (total temperature is assumed to be constant,  $T_{01} = T_{02} = T_0$ ). From the values of  $M_2$  and  $\alpha_2$  it is possible to determine whether limit load regime of the blade cascade is achieved, Eq.(1).

Figure 3 depicts dependencies of kinetic energy loss coefficient  $\zeta$  on isentropic exit Mach number  $M_{2is}$  for constant incidences  $i$ . These dependencies were evaluated from traversing probe measurements behind the root section blade cascade. For higher Mach numbers it is possible to observe almost constant values of kinetic

energy loss coefficients. It can be significant for achievement of limit load regime. Kinetic energy loss coefficient is defined by relation

$$\zeta = 1 - \frac{M_2^*}{M_{2is}^*} \quad (2)$$

where  $M_2^*$  is non-dimensional exit velocity and  $M_{2is}^*$  isentropic non-dimensional exit velocity.

Figure 4 shows dependencies of exit angle oriented to axial direction for the same blade cascade on isentropic exit Mach number  $M_{2is}$  for constant incidences  $i$ . Experimental data prove obvious changes in the region of high values of isentropic exit Mach numbers. Limit load regimes can be indicated.

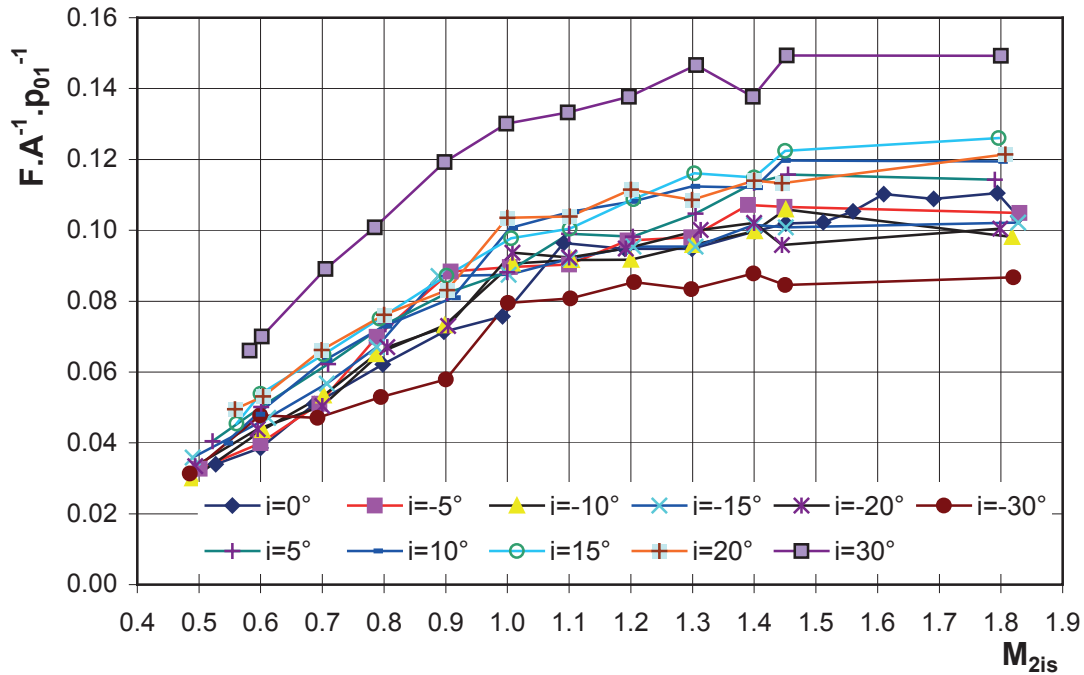


Fig. 2: Dependence of root blade cascade nondimensional peripheral loading on isentropic exit Mach number  $M_{2is}$  and angle of incidence  $i$ .

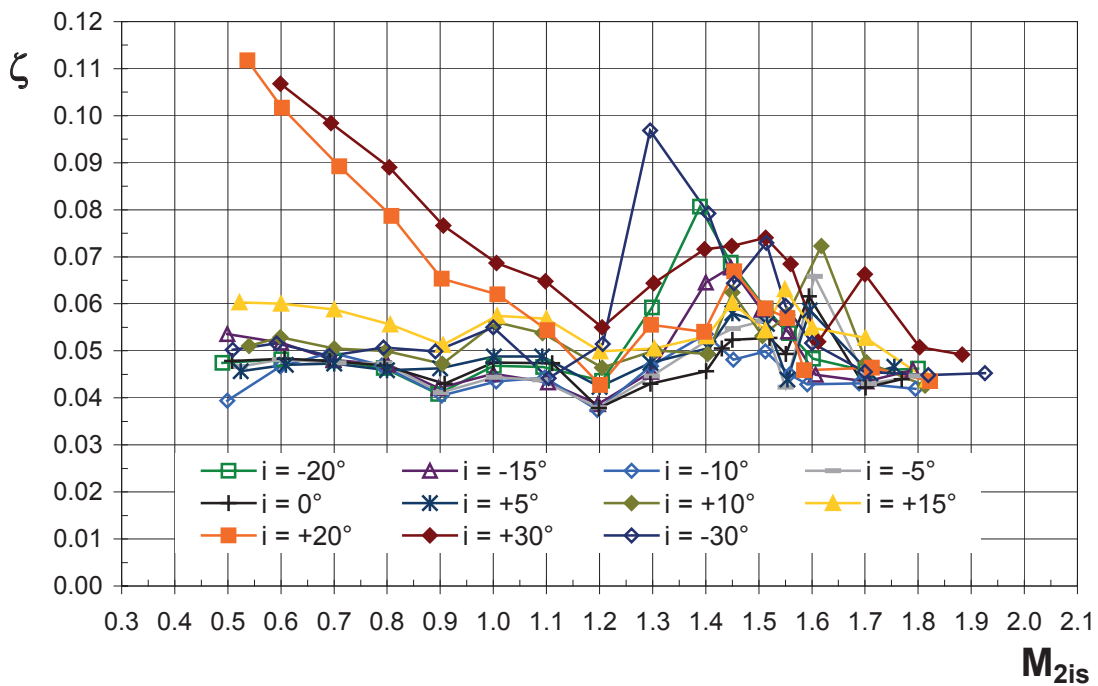


Fig. 3: Dependence of kinetic energy loss coefficient  $\zeta$  on isentropic exit Mach number  $M_{2is}$  and angle of incidence  $i$ .

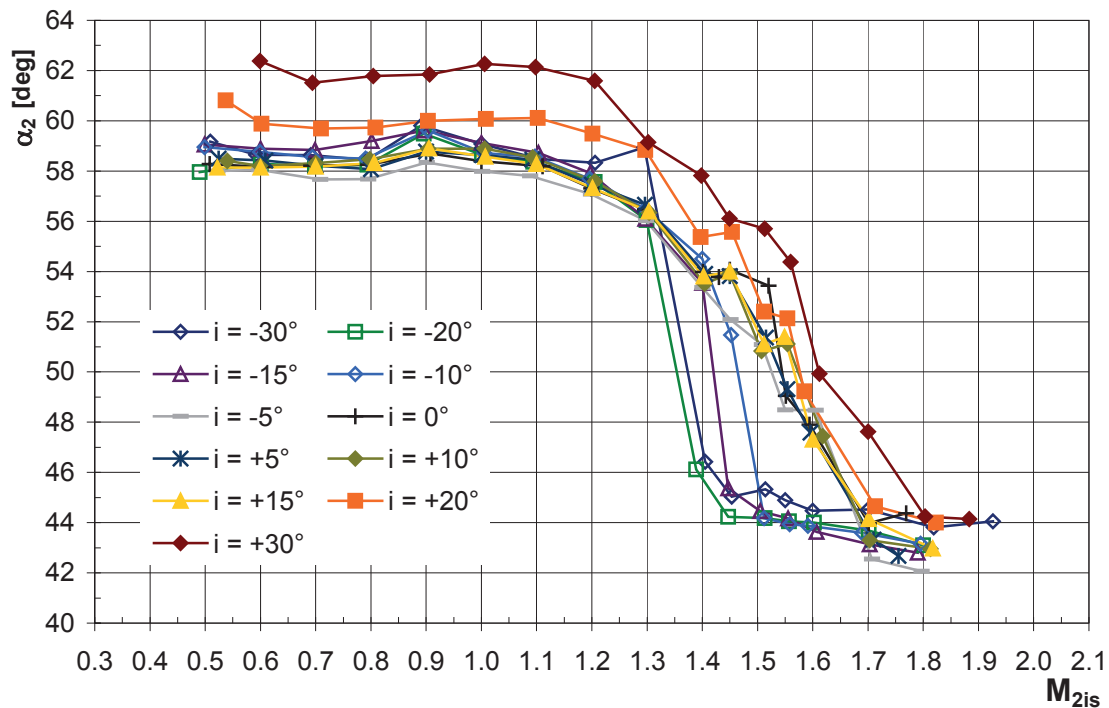


Fig. 4: Dependence of exit flow angle  $\alpha_2$  on isentropic exit Mach number  $M_{2is}$  and angle of incidence  $i$ .

Detail analysis of traversing probe measurement results can show new approaches to identify limit load regimes. Figure 5 shows results following from analysis by reduction data method [5]. In the diagram, values of modified quadratic expressions  $(I_C/I_M)^2$  and  $(I_A/I_M)^2$  are plotted.  $I_M$  is the integral of mass flux,  $I_A$  is the integral of momentum flux normal to the cascade plane and  $I_C$  is the integral of momentum flux parallel to the cascade plane. Values of these integrals are solved from traversing probe data. In the detail in Fig. 5, triangles represent measurement points obtained at subsonic flow regimes, transonic regimes, supersonic regimes and limit load regimes defined by  $D = 0$ .  $D$  is a discriminant defined in data reduction method [5]. Maximum non-dimensional velocity  $M_{max}^*$  is given by

$$M_{max}^* = \sqrt{\frac{\kappa + 1}{\kappa - 1}} \quad (3)$$

where  $\kappa$  is the isentropic exponent (ratio of specific heats). Experimental data on aerodynamic parameters of the blade cascade representing the root section is presented in the reports [6], [7].

Investigations of supersonic flows in exit part of turbine blade cascades enables to understand complex flow processes. Conditions for limit load regimes in turbine blade cascades are studied in [6] where distribution of velocity in trailing edge plane is compared for cases of different shapes of suction side in exit part of blade cascade. Parameters and configurations of shock waves should be solved more in detail. A contribution to both regular and Mach interaction of shock waves is presented in [7].

Topical problem of investigations of supersonic flows in blade cascades is still to ensure periodical conditions downstream of the blade cascade. Occurrence of parasite shock waves downstream of the blade cascade is a serious problem namely when the parasite shock wave crosses traversing plane and interacts with suction side of the blade. In Fig. 6 interferogram shows flow field regime close to design parameters of the blade cascade representing middle section of rotor blading of the last stage of large output steam turbine. Parameters upstream of the parasite shock wave are evidently in limit load regime. Parameters downstream of the parasite shock wave show that limit load is not achieved.

## CONCLUSIONS

Optical and pneumatic methods enable to determine aerodynamic conditions of blade cascade limit load. Under these conditions working medium flows at supersonic exit velocities. Aerodynamic data on limit load provide important information for designers of turbomachine blades. Supersonic flow in turbine blade cascades is still topical problem for basic research and for its application in turbomachinery.

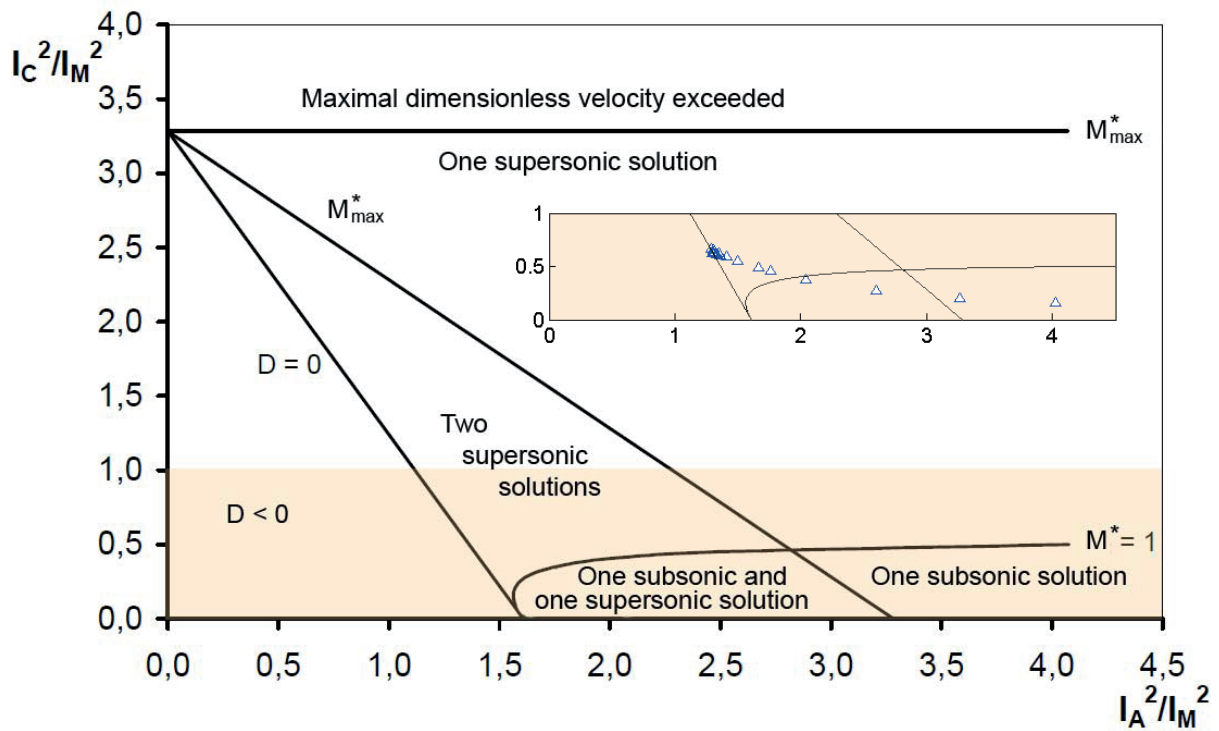


Fig. 5: Diagram of arguments for solution of the conservation equations of data reduction method

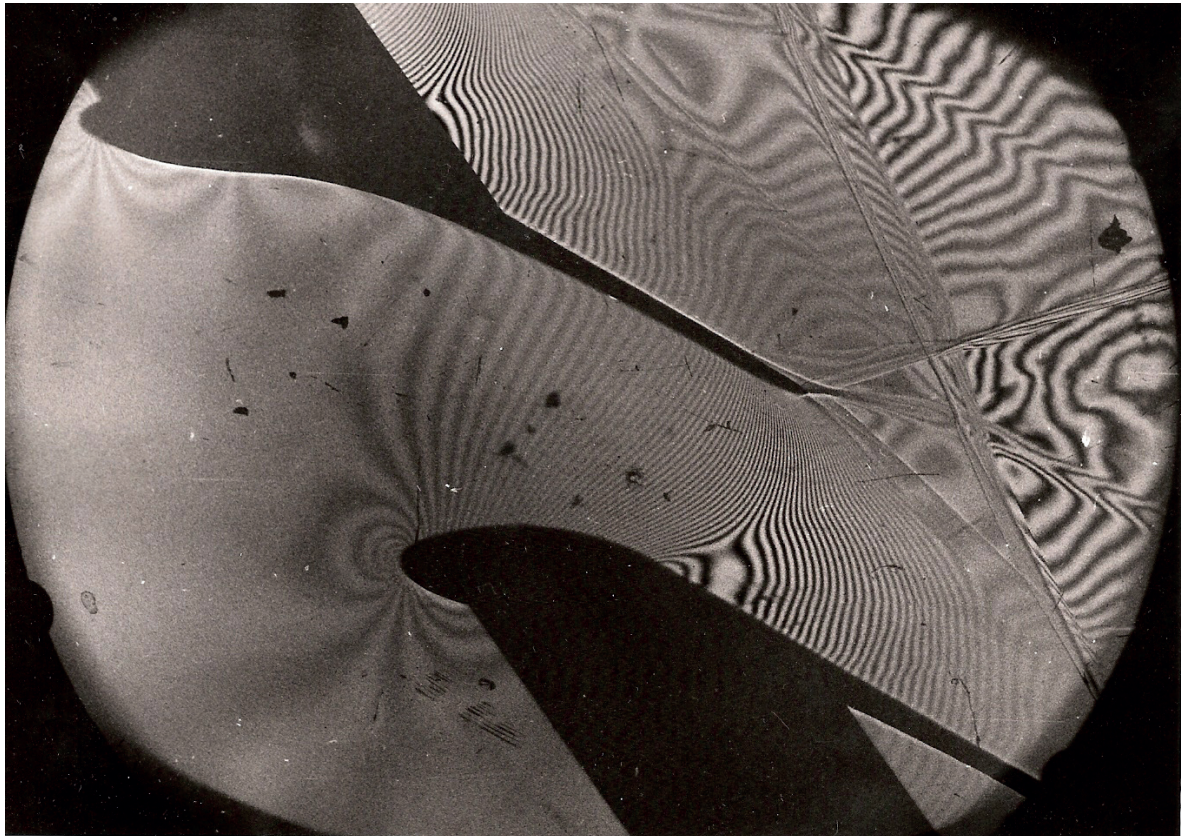


Fig. 6: Interferogram taken at isentropic exit Mach number  $M_{2is} = 1.353$  and angle of incidence  $i = 0^\circ$



## REFERENCES

- [1] P.Šafařík : Experimental Data from Optical Measurement Tests on a Transonic Turbine Blade Cascade, pp.20(0-14). In : Measuring Techniques for Transonic and Supersonic Flow in Cascades and Turbomachines (editors : C.Gossweiler, G.Gyarmathy), Proceedings of 13<sup>th</sup> Symposium, ETH Zürich, 1997
- [2] S.L.Dixon, C.A.Hall : Fluid Mechanics and Thermodynamics of Turbomachinery, Elsevier, Burlington, 2010
- [3] P.Šafařík, V.Vlček : Using Interferometric Measurements in Calculation of Aerodynamic Forces, pp.301-305. In : Optical Methods in Dynamics of Fluid and Solids (editor M.Píchal), Springer Verlag, Berlin, 1985
- [4] M.Luxa : On Selected Experimental Methods in High Speed Aerodynamics, Invited lecture VM 2011, Pilsen, 2011
- [5] J.Amecke, P.Šafařík : Data Reduction of Wake Flow Measurements with Injection of an Other Gas, Forschungsbericht No.95-32, DLR, Göttingen, 1995
- [6] M.Luxa, D.Šimurda : Optical Measurements of the TR-P-2 Cascade, Report Z-1472/11, Institute of Thermomechanics ASCR, Prague, 2011 (in Czech)
- [7] D.Šimurda, M.Luxa : Pneumatic Measurements of the TR-P-2 Cascade, Report Z-1473/11, Institute of Thermomechanics ASCR, Prague, 2011 (in Czech)
- [8] C.H.Sieverding : Aerodynamic Characteristics of Last Stage Blade Profiles, pp.144-165. In : Aerothermodynamics of Low Pressure Steam Turbines and Condensers (editors : M.J.Moore, .H.Sieverding), Hemisphere Publishing Corporation, Washington, 1986
- [9] D.Šimurda : Transonic and Supersonic Flow past Turbine Profile Cascades, PhD. Thesis, Czech Technical University in Prague, Prague, 2011 (in Czech)

## ACKNOWLEDGEMENT

The support of GA ASCR (IAA 200760801) is gratefully acknowledged.

## COMPARISON OF TWO OPTICAL TECHNIQUES TO OBSERVE TURBOCHARGER SHAFT MOTION

J.V. Pastor<sup>1</sup>, J.R. Serrano<sup>1</sup>, V. Dolz<sup>1,\*</sup>, M.A. López<sup>1</sup>, F. Bouffaud<sup>2</sup>

<sup>1</sup>CMT – Motores Térmicos, Universitat Politècnica de València, Spain

<sup>2</sup>RSA – Renault SA, France

\* Corresponding author. Tel.: +34 963877650; Fax: +34 963877659.

Camino de Vera s/n, 46022 Valencia, Spain  
E-mail address: vidolrui@mot.upv.es (V. Dolz).

### ABSTRACT

This paper presents two techniques to estimate the turbocharger shaft whirl motion. The aim of this article is to present these systems for monitoring the shaft motion of a turbocharger, in order to compare these two techniques for different purposes. The first technique is based in the image processing of the shaft tip, which is obtained using a digital camera. To achieve this, a camera and a light source were installed in a turbocharger test bench. An image recording methodology and a process algorithm have been developed, in order to estimate the shaft motion. This processing consists on differentiating specific zones of the image, in order to obtain their coordinates. A luminosity study has been also done, in order to improve the process and to obtain locus of shaft position in a picture exposition time period. The second technique involves the installation of two infrared sensors which measure the radial displacement of the shaft at two different angles. The two signals obtained by the sensors must be processed to remove the sources of error and obtain a filtered signal with the basic movement of the shaft.

**Keywords:** Turbocharger, Lubrication, Bearing, Shaft motion.

### 1 INTRODUCTION

Nowadays, the tendency to reduce the cylinder capacity -downsizing- in reciprocating internal combustion (IC) engines requires the use of turbochargers. The final objective of this boost is to maintain or increase the engine air mass flow, thereby increasing engine power. The performance and reliability of these turbochargers is related with many factors like mechanical losses, heat transfer, shaft motion, lubrication, etc.

The dynamic model of the shaft has been studied extensively since the early twentieth century until nowadays [1] [2] [3] [4]. The focus of these models has changed with technological developments, from the purely theoretical until their validation by experimental techniques. These types of models have been used to study the operative problems of turbomachinery [5]. Nowadays, some experimental measurement techniques with accelerometers [6] and laser [7], feedback these models, and both models and experimental techniques contribute to improve the knowledge about the functioning of these shafts.

The lubrication problems in these turbochargers have been extensively studied both experimentally, by measuring the thermodynamic variables in turbocharger test benches [8], and theoretical, by means of CFD models [9] [10]. In this paper, the whirl movement of the shaft of an IC engine turbocharger, during normal and abnormal operation, is estimated using two different techniques: by the digital processing of high magnification images of the rotor axis and by the shaft tip position measurement using infrared sensors. The objective is to obtain information about the whirl shaft movement and compare these two techniques.

The first technique, with the digital camera, provides information from the movement of the shaft to another type of visual information, as the apparition of oil on the compressor side, or the deformation of the shaft

tip. Furthermore, this technique is not intrusive and robust enough to avoid the destruction of the measurement components if a catastrophic failure of the turbocharger happens. To accomplish these objectives, a window in the compressor inlet duct with a camera focused on the shaft tip has been used [11]. To obtain the expected results some difficulties presented by the test bench Diesel engines used in turbocharging [12] [13] should be considered such as structural vibration and space to install the equipment. During these tests, turbocharger thermodynamic variables have been also recorded to obtain complete information on the evolution of the turbocharger when it has lubrication problems [14].

The second technique, with the infrared sensors, is more intrusive, because it needs shaft modifications and consequently the re-equilibration of the shaft to obtain satisfactory results. However, this technique provides additional information regarding the technique of digital images, such as: high frequency acquisition data (transient conditions), whirl frequencies and movement decomposition.

This paper describes the test bench configuration and the different processing techniques to obtain information about these shaft motion techniques.

## 2 TEST BENCH LAYOUTS

### 2.1 Digital camera technique

The turbine feeding gas is provided by a 6 cylinders heavy duty diesel engine (Table 1). More details about test bench components and configuration can be found in reference [11]. The flow intake is controlled by means of a guillotine valve, allowing accelerating, decelerating and fixing the working point of the turbocharger. A 3-way valve controls the lubrication oil circuit and it allows the turbo lubrication or cutting the oil flow to the turbo. Additionally, transducers were employed in the oil circuit, turbine gas circuit and compressor air circuit to measure thermodynamic variables, such as pressure, temperature and mass flow (Figure 1).

Number of cylinders	6
Piston Bore	150mm
Stroke	125mm
Compression ratio	17:1
Max. speed	1800rpm

Table 1. Characteristics of the engine used in the turbocharger test bench

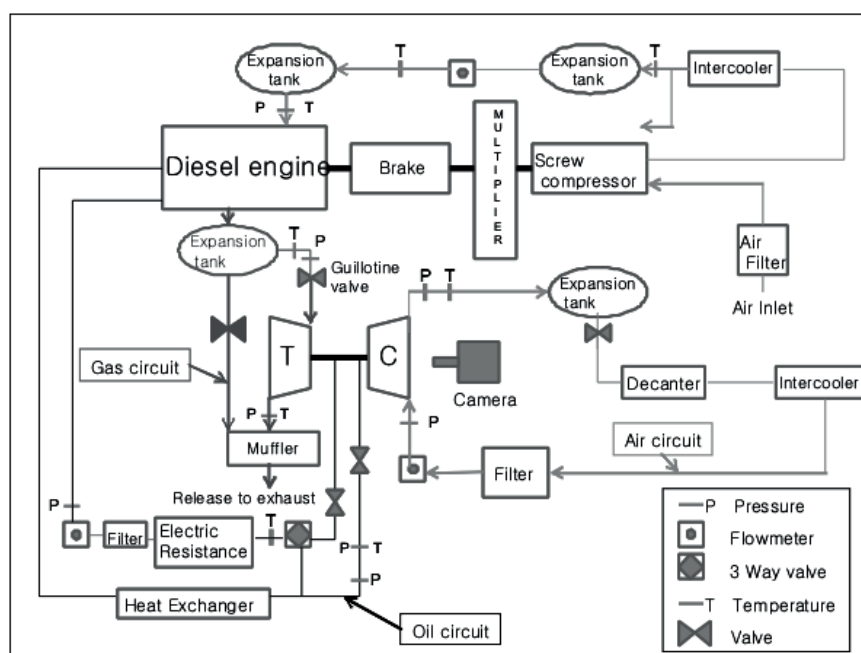
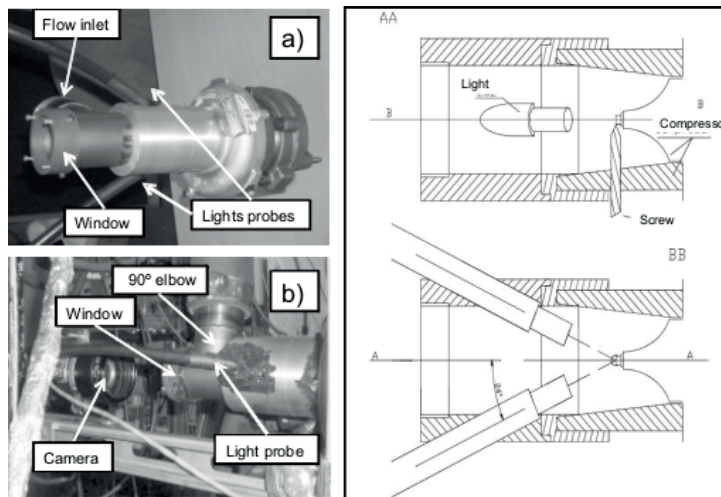


Figure 1. General sketch of the Test Bench

The camera is placed in front of the turbocharger on the compressor side, positioning it as coaxial as possible to the turbocharger shaft and focused to the shaft tip. A 90° elbow is attached at the inlet of the compressor housing with a glass window to allow the proper display of the shaft through the camera (*Figure 2*). Light provided by a 250W halogen lamp is driven to the test section through two liquid light guides, which have 8 mm in diameter. These probes are arranged in a horizontal plane and are coupled into the duct, pointing to the tip of the compressor shaft (*Figure 2*). The function of these probes is properly enlighten the shaft to get photographs with enough quality for further processing.



**Figure 2. Camera layout and lights probes sketch**

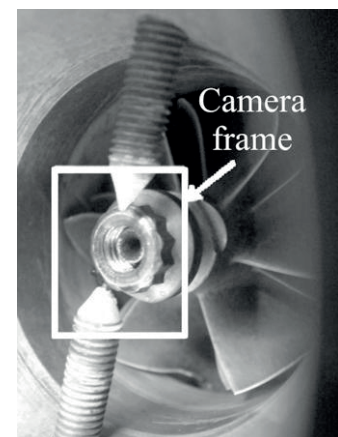
Images are taken with a PCO Pixelfly 12-bit CCD Camera with spatial resolution of 1280x1024 pixels. The distance between the compressor and the camera is approximately 300 mm.

The resolution obtained with this layout is approximately 5  $\mu\text{m}$  per pixel. This resolution allows us to observe the shaft movements, which have similar order of magnitude.

A major problem of this measurement technique is the relative motion between the camera and the turbocharger while the shaft motion is being measured. Structural vibrations in the reciprocating engines or in the turbocharger test benches are quite common and they introduce uncontrolled displacement between camera and turbo, which can introduce a significant error in the measurements. To avoid this, two screws, whose tips are located a few millimetres from the compressor shaft tip, are placed in the compressor housing. These screws are used to facilitate the processing of the images, offering two clear references fixed with the turbo housing. The previously stated error sources can be avoided using these fixed references.

It is necessary to distinguish clearly the objects in the image, in order to find the shaft position through the recorded pictures. So, the screws have been painted white and the compressor wheel has been painted black, leaving the shaft tip shining. These colors are used in order to improve the image processing. This processing involves identifying the position of the important objects (screws and shaft tip) and distinguishing luminosity of the pixels in the image (this technique is explained in the next paragraphs). *Figure 3* shows the compressor side of the turbocharger with the focused camera frame and the 2 reference screws.

The turbochargers shaft tips have several shapes; they depend on the compressor nut configuration. Two kinds of turbochargers have been used for this work, the first one is a Borg Warner turbocharger (BWTS) (with the shape of the shaft tip like a circle) and the second one is a Honeywell turbocharger (HTT) (with the shape of the shaft tip like a ring). An example of captured images by the camera with stopped shaft and rotating shaft can be observed in *Figure 4*. As the exposure time of the photograph has the



**Figure 3. Photograph of screws and tip shaft**

same order of magnitude as the time per revolution of the turbocharger shaft, the image obtained from the rotating shaft has a smoother contour than the stationary shaft. This has implications for the accuracy of the method and the image processing, as it will be described in the following sections.

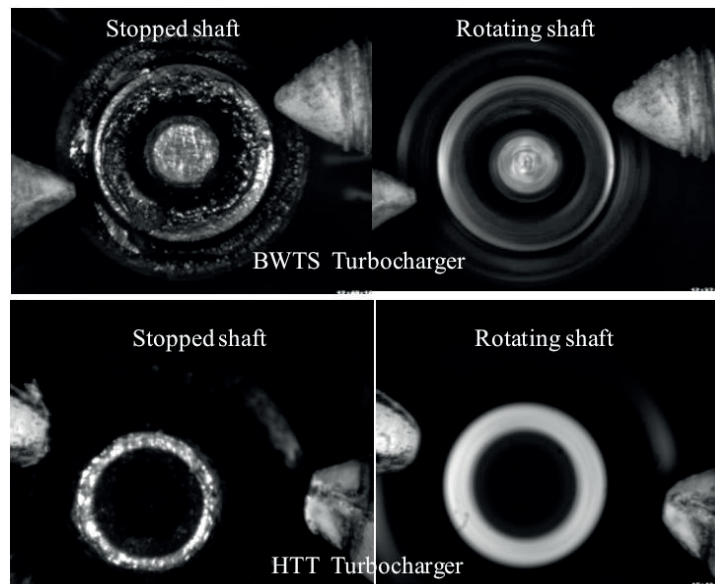


Figure 4 Photographs of the compressor shaft tip

## 2.2 Infrared sensors technique

To perform this measurement technique, two infrared sensors to measure the distance to the shaft are placed radially to it, pointing to the tip of the shaft at the compressor side and forming together an angle of  $90^\circ$ . To minimize the opening of the light beam after reflection, a cylinder with a large diameter of about 12mm is placed in the tip of the compressor shaft. Furthermore, the surface finish of the cylinder has color with an albedo that maximizes the reflection of infrared light to increase the sensitivity of the sensors. The Figure 5 shows a scheme of the described system.

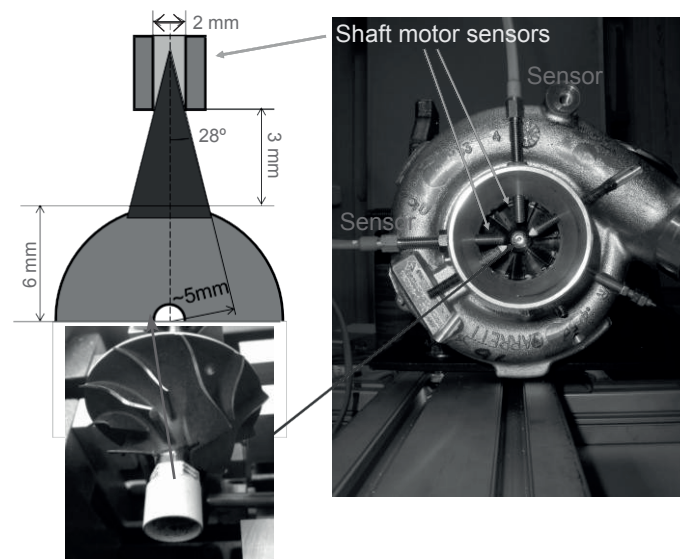
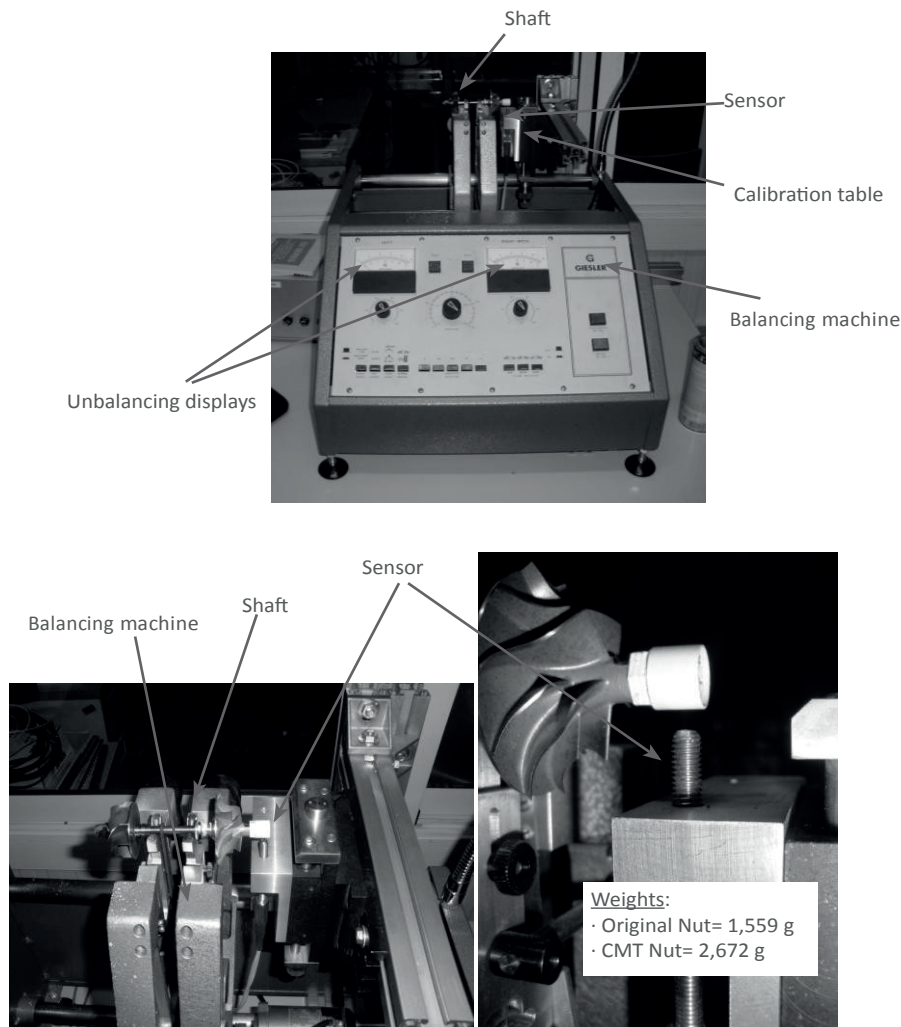


Figure 5 Scheme of the infrared sensors setup

The sensors used are placed approximately 3mm to the surface of the cylinder assembled to the shaft, which has been described above. These sensors have operative ranges between 0.5mm and 10mm and are able to record data at frequencies of 1MHz. However, to avoid memory problems in the recording of the data, the acquisition frequency of the sensors has been limited to 100kHz.

The Figure 6 shows the equipment for balancing the shaft with the assembled cylinder and the device to calibrate the sensors. The modified shaft is balanced in a device with two Y-shaped supports with two strain gauges which estimate the unbalancing of the shaft. A belt and an electric motor produce the shaft rotation movement to determine the unbalancing of it. Furthermore, in this work table, the equipment to calibrate the sensors is mounted. This equipment consists of a position table which allows the sensor movement radially to the axis of the modified turbocharger shaft. Thus, the sensor can be positioned at different distances to the cylinder, in order to determine the relationship between the voltage obtained by the electronic device of the sensor and the distance from the sensor tip to the surface of the cylinder.



**Figure 6. Installation to balancing the shaft and calibrate the sensors**

When the shaft has been balanced and the sensors have been calibrated, the modified shaft and the sensors are assembled on the turbogroup and it is installed in an engine test bench. This setup on the engine test bench allows testing the turbocharger in both normal and abnormal operative conditions, in order to reproduce, failures of lubrication, pumping conditions, overspeed,...

### 3 METHODOLOGIES

#### 3.1 Digital camera methodology

Different image processing codes have been programmed in Matlab, in order to obtain the relative position of the shaft centre from the photographs.

The shaft motion analysis process consists of four steps that are detailed below. The first step includes as well: the positioning of reference points (reference screws) and shaft centre in the picture, the determination of the scales in mm per pixel and the correction of the absence of perpendicularity between the camera and the turbocharger housing. The second step is to determine maximum eccentricity of the shaft in the turbocharger before the test. The third step is to determine the position of the shaft when it is spinning and its position relative to the maximum eccentricity determined in the previous step. The fourth step is the analysis of shaft luminosity to determine if sudden movements have been done during the exposure time of the camera.

##### 3.1.1 Reference points and shaft position calculation

The shape of the compressor shaft tip is considered a perfect circle or a perfect ring in the used code (Matlab). To improve the precision of the method, it has been assumed that the camera could not be located coaxially to the turbocharger shaft. Thus, this circle or ring has become an ellipse in the image process in order to consider the error due to the lack of coaxiality between camera and shaft tip.

As mentioned above reference screws are used to avoid errors in processing images from structural vibrations. A set of pictures is recorded from a given experiment at which the shaft motion wishes to be known. The steps to estimate the positions of the reference points (screws) and the centre of the shaft in these pictures are following depicted:

- a. **The processing of the pictures.** The pictures obtained are processed into a binary image with black and white pixels. An example of a photograph before and after processing can be seen in the figure below.

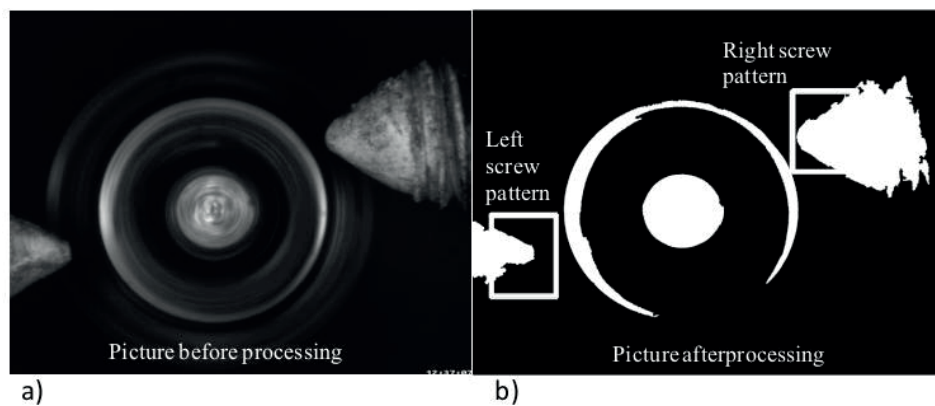
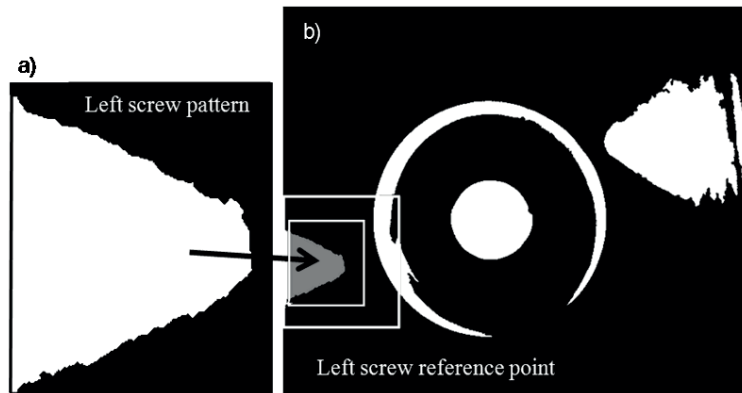


Figure 7. Pictures before (a) and after (b) processing

- b. **Obtaining the screws patterns.** The picture with the best quality (this is the photo whose brightness and focus have the highest quality) is chosen to be used as a standard for the reference screws. This photo is processed as in previous step and a binary image is obtained. The pictures of screws tips in these binary images are cut to use them as a pattern in the process of locating the screws in other photographs. Figure 8 a) shows an example of these patterns.
- c. **Reference point position.** The program code used to determine the reference benchmarks compares these screws patterns with each one of the processed images in binary (black and white) format. This comparison is made in a range of coordinates where the program searches for the closest match between the shape of the processed image and the screw pattern. This convolution is performed by comparing the pixels of the two binary images using the logical operator “exclusive or” (XOR), seeking to minimize the number of pixels different between the two images. This range is represented with the

large rectangle in Figure 8 b). The figure also shows the left screw pattern in gray colour, at the point where the maximum coincidence has been found between the screw pattern and the processed image. The program establishes the centre of coordinates (0, 0) in the upper left position of the image, as *Figure 10* shows. When the code of the program has found the best match between the reference screw and the screw of the image, it sets the coordinate of the pixel at the tip of the left screw ( $x_{i\_ref}$ ,  $y_{i\_ref}$ ) as a reference pixel. The process to find the position of the right screw ( $x_{d\_ref}$ ,  $y_{d\_ref}$ ) is similar to the process described previously for the left screw.



**Figure 8. Position of the left screw reference point**

- d. **Shaft tip centre position.** The code programmed in Matlab searches a white circular shape which is at the centre of the processed image. Once the program finds this region, continues around the edge of this zone with white pixels, in order to complete the circular shape. This circular shape can be seen in *Figure 9* with gray pixels. Using these gray pixel coordinates, the program approximates an ellipse and calculates its centre, its main angle and its semi-axes. The centre of this ellipse is shown in the *Figure 9* by a small black dot. Then, the program sets the coordinate of the pixel at the ellipse centre ( $X_c$ ,  $Y_c$ ) as the reference centre pixel, as *Figure 10* shows.



**Figure 9. Position of the shaft tip centre**

- e. **Coordinates and scales.** A pre-processing methodology, previous to processing the results from the experiments with the shaft in motion, is done, in order to determine the scales of the images. In this pre-processing phase, it is necessary to take pictures from the turbocharger stopped. This pre-process involves a study of the shaft tip position and shape, to estimate the scales using these images where the shaft is stopped. It is possible to obtain the distances in pixels  $\Delta x_{ref}$  and  $\Delta y_{ref}$  shown in the *Figure 10* using the parametric equation of the ellipse, on these images. These distances can be scaled from pixels to millimetres, knowing the radius of the shaft tip ( $R$ ):

$$\text{Scale}_X [\text{mm/pix}] = \frac{R[\text{mm}]}{\Delta x_{ref} [\text{pix}]} \quad \text{and} \quad \text{Scale}_Y [\text{mm/pix}] = \frac{R[\text{mm}]}{\Delta y_{ref} [\text{pix}]} \quad (1)$$



This double scale permits to correct the possible errors, due to faults in the placement of the camera and the lack of coaxiality between the axis of the turbo and the camera. Knowing these scales, it can be obtained the distance in millimetres between the screws ( $\Delta d_{ref}$  [mm]) from their distance in pixels ( $\Delta d_{ref}$  [pix]). This distance is the distance between the two fixed points and therefore should be always the same, although the shaft is in motion or there is a relative motion between the camera and the turbocharger due to engine vibrations. Finally, this distance ( $\Delta d_{ref}$ ) and the positions of screws ( $x_{i\_ref}$ ,  $y_{i\_ref}$ ,  $x_{d\_ref}$  and  $y_{d\_ref}$ ) and shaft centre ( $x_c$  and  $y_c$ ) are the parameters to be used for the processing of all the photos of the experiment performed with the turbocharger for which these parameters were obtained, with the objective of determining the relative motion of the shaft.

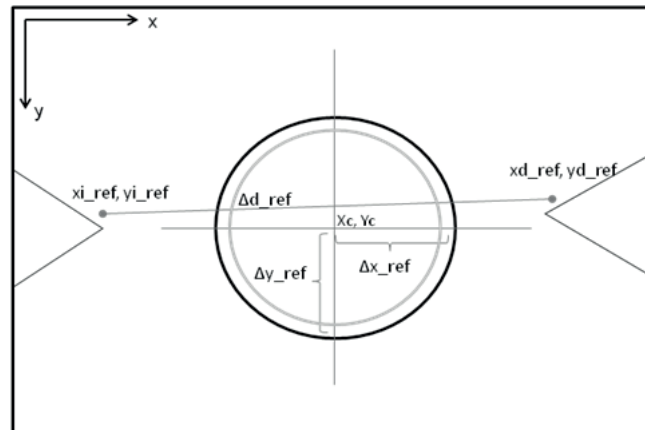


Figure 10. Scheme of shaft and screws

### 3.1.2 Maximum eccentricity

The maximum eccentricity is determined when the turbocharger is stopped, pressing radially the shaft from the turbine side in different directions (maximum eccentricity allowed by the components of the turbocompressor in order that it is kept in a normal functioning). After, these images with the shaft pressed are processed, in order to obtain each relative position of the shaft centre with respect to the positions of the reference screws. Processing of the images consists of locating the position in pixels of both screws and the centre of the shaft, as it has been described in the preceding paragraphs. Normally, the positions of the screws ( $x_{i\_ref}$ ,  $y_{i\_ref}$ ,  $x_{d\_ref}$  and  $y_{d\_ref}$ ) in these pictures have changed with respect to the screws positions of the reference picture, this is due to possible relative movements between the camera and the turbocharger, they are normalized in order to become the fixed points of the experiment, since they are fixed to the compressor case and the important movement is that of the shaft centre with respect to them. Therefore, the relative position between both screws is used to determine the particular scale (scale X and it climbs Y) of every image. These particular scales allow to relate the distance in millimeters and in pixels of each image. These scales are used to determine the position of both screws and the shaft centre in millimeters with respect to the fixed reference system determined by the screws.

Finally, the obtained shaft centre positions in millimetres relative to the screws position can be seen in *Figure 1* with a correlated ellipse. This region of maximum eccentricity (ellipse) will be compared with the shaft motion when shaft is spinning.

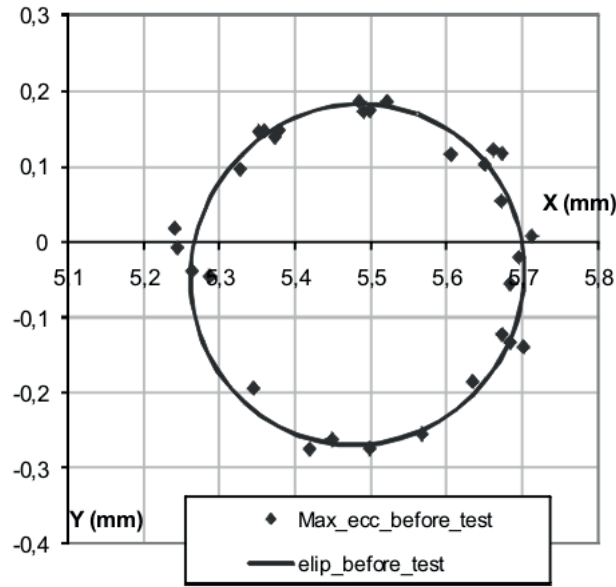


Figure 11. Maximum eccentricity points measured with the camera

### 3.1.3 Shaft motion

The next step, after the shaft maximum eccentricity has been processed, is to process the images with the shaft spinning. The image processing procedure is similar to the previous case; again the relative distance between the screws is used as a reference distance to determine the scale and shaft position when shaft is spinning. Figure 12 shows an example of this shaft motion. The big dots determine the maximum eccentricity and the small dots are the different positions of the shaft during a test at 150.000rpm and with an exposure time of 1ms.

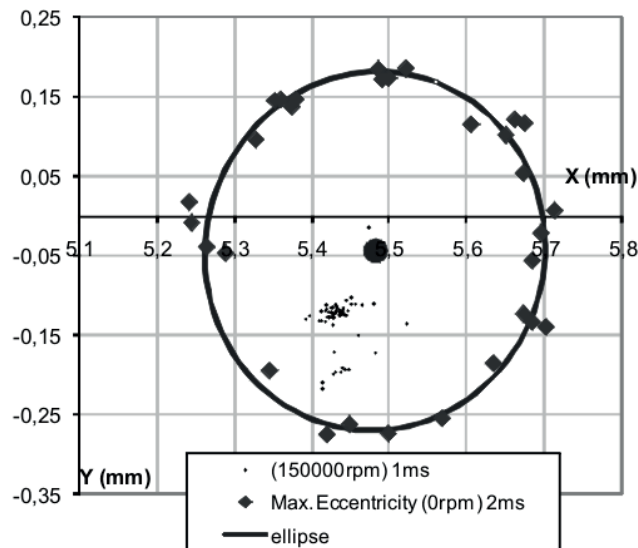


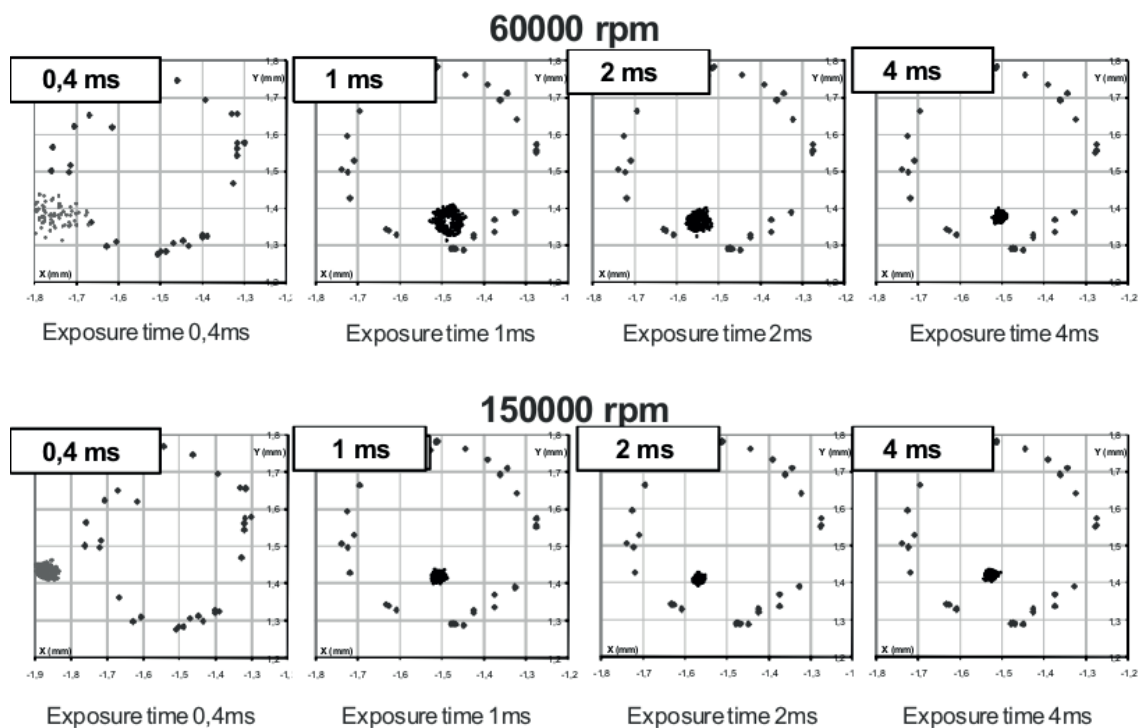
Figure 12. Maximum eccentricity and shaft motion points measured with the camera

A parametric study was conducted in order to determine the optimal exposure time of the camera, for getting images. This study was done with the turbocharger spinning at 150000rpm and 60000rpm and with different camera's exposure times (0.4, 1, 2 and 4 ms). The camera's exposure time was the parameter to optimize. The results are shown in *Figure 13*.

The results obtained indicate that if the exposure time of the camera is increased, the zone where the shaft is moving becomes more concentrated (*Figure 13*). This happens because the shaft spins and whirls more times within the time of a picture if the exposure time is increased. Consequently, all these whirls are captured in the obtained photograph. Thus, the theoretical centre of the shaft in the obtained picture is an average of the real shaft position during the exposure time that has been chosen.

On the other hand, greatly reducing the exposure time could cause that the zone where the shaft is moving cannot be processed with enough precision, because of poor image quality. This poor quality is due to a poor illumination of the shaft tip when the exposure time is too short and it causes that the obtained results, when the image is processed, do not have the necessary precision. So, the optimal result depends also on illumination power, in this study it was used a 250W lamp. If a higher power lamp is available, the exposure time could be reduced. *Figure 13* shows that when the exposure time is too short, the final result can be illogical (0.4 ms), i.e. the axis is moving outside the logical limits set by the maximum eccentricity.

Summarizing, as it was remarked previously, the pictures with short exposure times do not capture enough light and consequently, saturation points in black prevent proper processing of the images. However, long exposure times can cause that the shaft has moved in many positions and consequently the information processing of the shaft motion does not transmit the exact position of the shaft, but a kind of average. Thus, the main purpose of this parametric study was that the camera works with exposure times as small as possible, without reducing the accuracy in calculations of shaft position. Thus, the optimal resolution in this parametric study was to work with an exposure time of 1ms (*Figure 13*). During this period of 1ms, if the shaft is spinning at 150000 rpm, the shaft will be rotated 2.5 times. Such study to optimize the exposure time should be performed before any new turbocharger model would be tested with this proposed technique. If these results with exposure times of 1 ms are compared, it can be observed that the position in which the shaft is moving changes depending on the engine speed. The smaller the engine speed, the greater is the variation of the eccentricity of the shaft movement (the zone in which the shaft is moving is larger). These results are consistent with theoretical lubrication models for bearings.



**Figure 13. Shaft motion (exposure time study)**

### 3.1.4 Luminosity analysis

A preliminary study about the shaft illumination must be done, before the shaft motion study. The study consists of observing the image quality of photos with different exposure times. As it was remarked previously, the pictures with short exposure times do not capture enough light and saturation points in black prevent proper processing of the images. However, long exposure times can cause that the shaft had moved through many positions and consequently the information processing of the shaft motion does not transmit the exact position of the centre, but a kind of average.

An analysis of the radial light gradients and patterns, between a processed picture and a reference picture, may be used to determine the relative displacement during the exposure time between this processed photography and the reference; i.e. during the 2.5 turns at 150krpm claimed in previous section. It is necessary to follow several steps to perform the analysis of the radial brightness at a certain radial angle ( $\alpha$ ):

1. **To get the lighting pattern for the studied radial shaft angle ( $\alpha$ ). This pattern is obtained from a grey scaled reference picture.** This reference picture is a photo taken where the shaft is moving in its “normal” operation, it means stable and lubricated by oil. It is considered the reference movement. This picture should have a very small “halo” around the shaft tip. *Figure 14 a)* shows a sketch of this radial luminosity pattern on a radial angle ( $\alpha$ ) with a shaft tip of ring shape (*Figure 15*). A point to consider is that the radial luminosity gradient in the metallic surface of the shaft tip depends on the angle observed. A radial angle of the shaft tip can receive more light than other due to the direction of the light to the turbocharger shaft tip.
2. **To compare the reference pattern obtained in the previous step with the processed photo for a studied angle ( $\alpha$ ).** If the turbocharger is tested with different conditions than the reference condition, i.e. with abnormal lubrication, the shaft could be moving with a different pattern when the photo is taken. When this photo is processed it will have a different “halo” around the shaft tip, due to the whirl motion of the shaft during the exposure time of the picture. *Figure 14 b)*
3. **To determine the shaft shape differences (halo difference between the reference and the processed photo).** This halo difference is related with the distance that the shaft has moved during the exposure time of the photo. It is because the halo represents the zones where the shaft has been present during this exposure time. Then, an increment in the halo represents higher displacements of the shaft during the exposure time. Thus, comparing the difference between the reference radial pattern and the processed radial pattern of their halos, it is possible estimate the shaft displacement as *Figure 14 c)* shows.

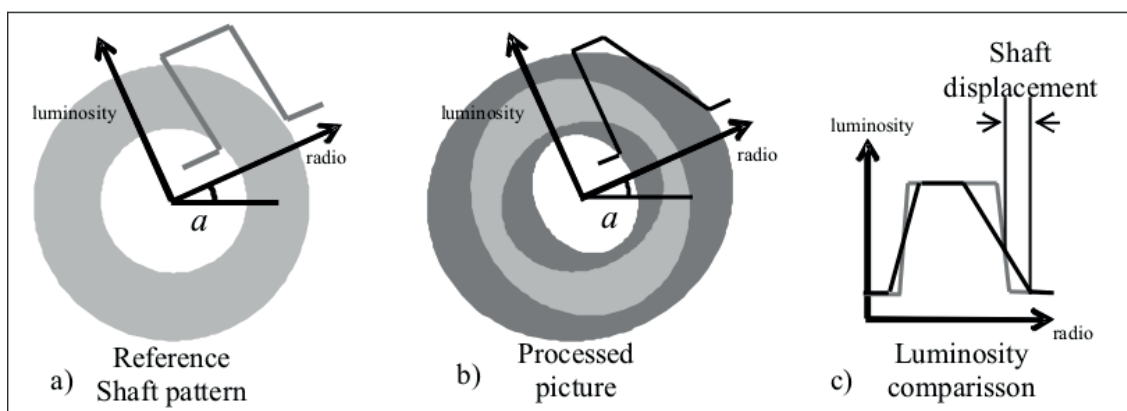


Figure 14. Luminosity comparison process

Several images obtained during the test with abnormal lubrication conditions (no-oil pressure) showed sudden movements of the shaft during their exposure time. In order to illustrate this technique, two of these photographs were processed by the luminosity analysis technique described previously. The Figure 15 a) photograph was taken in the second 57th and the Figure 15 b) photograph was taken in the second 274th of the test. Figure 15 shows these images.

The shaft motion was studied in different radial directions ( $0^\circ$ ,  $45^\circ$  and  $90^\circ$ ) by means of the luminosity analysis. Figure 15 Reference shows these directions on the reference picture of the shaft tip.

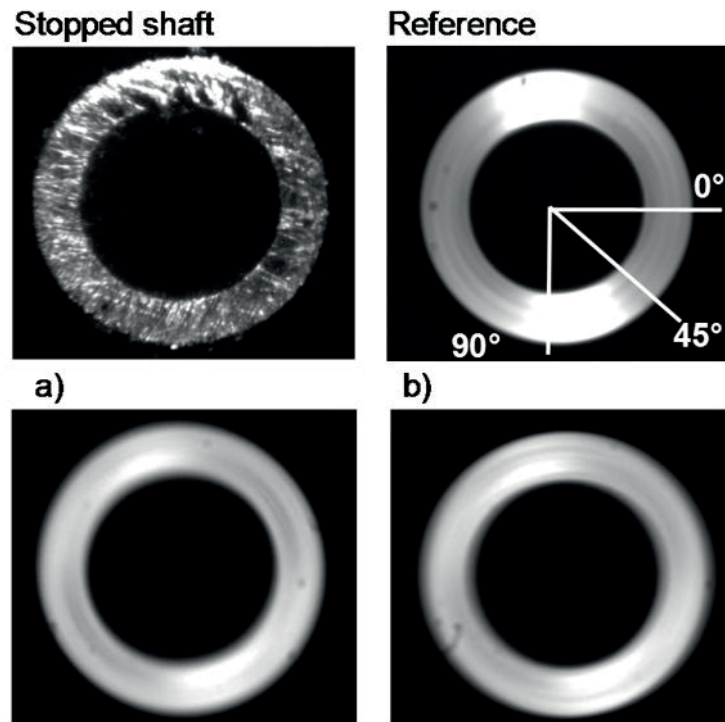


Figure 15. Studied angles on the reference picture and processed pictures

As an example, *Figure 16* shows the luminosity analysis of these studied images for the  $0^\circ$  angle. The relative displacement of the shaft during the exposure time of the photograph is obtained from these graphs. To analyze this luminosity, the grey colors of the image in the studied angle have been scaled using 0 with the darkest pixel and 1 with the brightest one. *Figure 16* shows this scaled luminosity versus radial position in microns. This plot shows that the most luminous area is located between the 1000 microns and the 1750 microns (the shaft has a radius of 1750 microns). The shape of this area depends on the reflections of the light on the shaft tip. The slope of the two light gradients located from 1000 to 1250 microns and from 1500 to 1750 microns, depends on the radial movement of the shaft in the studied direction during the exposure time of the photography. To estimate this radial movement, the variation of the slope inclination is evaluated at a reference point placed at 0.1 non-dimensional luminosity, as can be observed in *Figure 16*.

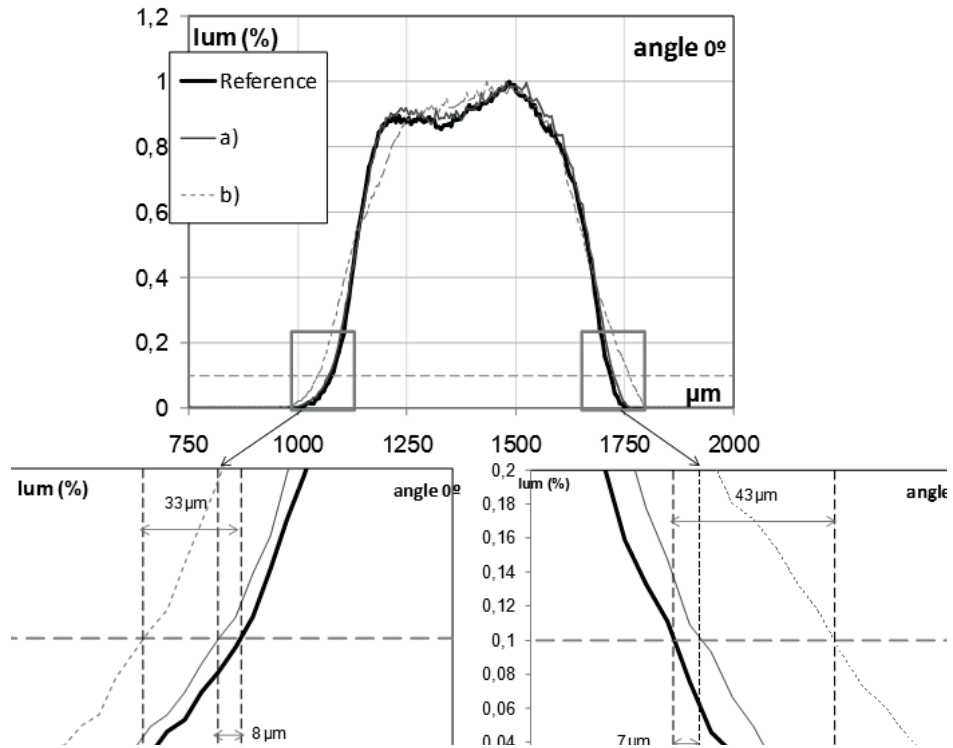


Figure 16. Luminosity analysis for 0° direction

Figure 17 shows the spatial representation of the estimated positions of the shaft for each of the photographs taken during the test. The two pictures shown in Figure 15 a) and in Figure 15 b) are those in which it has been detected a greater movement of the shaft during the exposure time of the respective photographs. Figure 15 shows the relative movement of these two points on the studied directions (0°, 45° and 90°). Figure 15 shows that this relative movement of the shaft in some cases becomes approximately 80μm during the exposure time of photography. It is a sharp movement during the short period of the photograph exposure time as (2.5 turns) can be observed in the segments drawn in the two studied points at Figure 17.

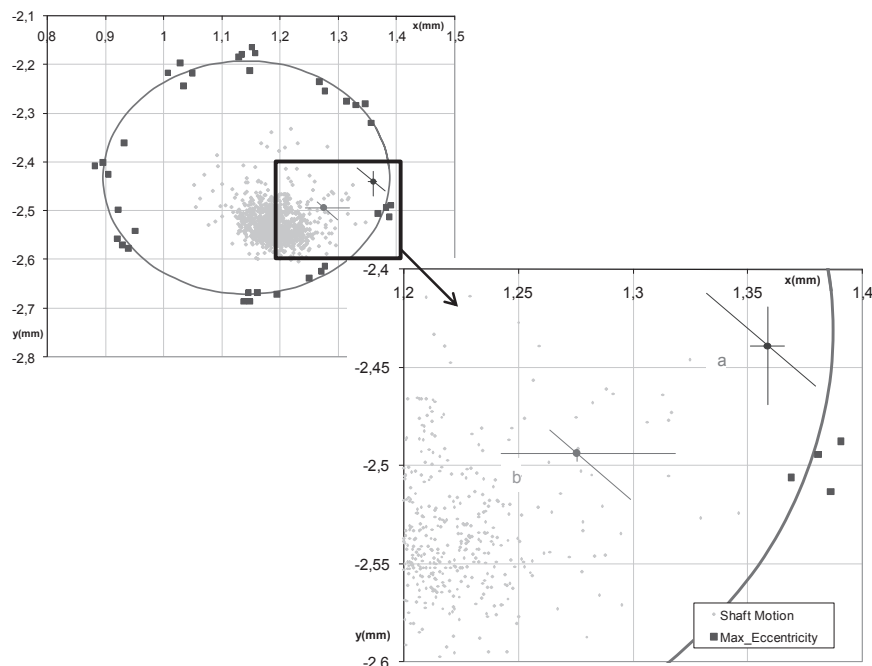
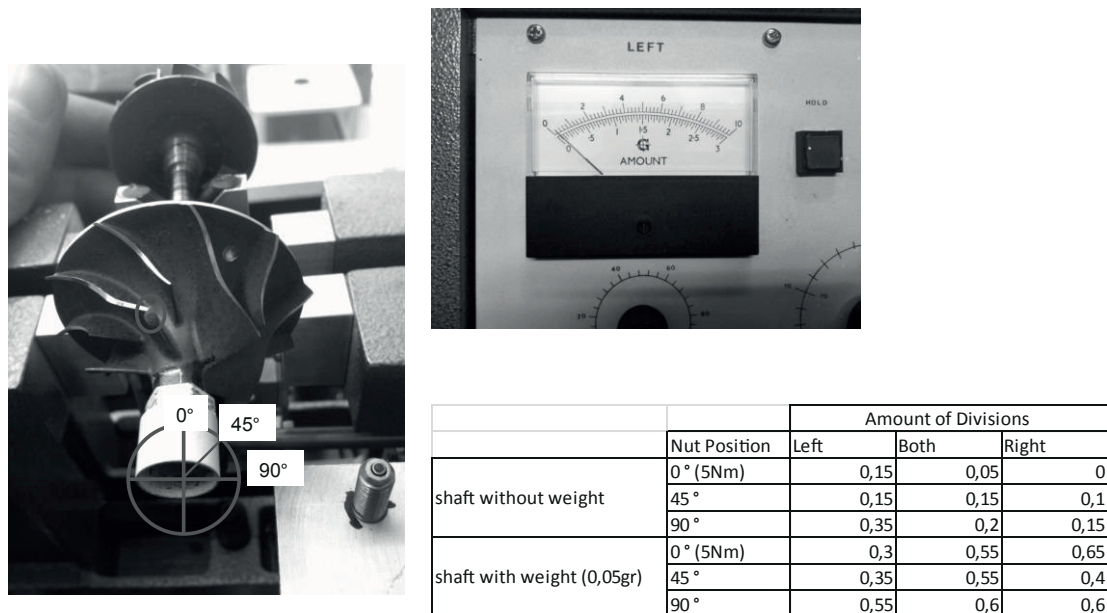


Figure 17. Shaft motion measured with the camera

## 3.2 INFRARED SENSORS METHODOLOGY

### 3.2.1 Balancing shaft and sensor calibration

To measure with the infrared sensors, the original shaft of the turbocharger must be modified by mounting a cylinder with a diameter of 12mm at the shaft tip on the compressor side. So, the first step to measure with the infrared sensors is study the balance of this modified shaft. The Figure 18 shows a sensitivity study of the balancing device to the changes produced in the shaft. To do this study, the cylinder nut is placed in three different positions (angle  $0^\circ$ ,  $45^\circ$  and  $90^\circ$ ) and a weighing of 0.05gr at the tip of one of the blades. The table of the figure shows the stress of the strain gauges in each of the shaft supports (right and left) and a combination of both (both). This study presents a good balanced shaft in the case of  $0^\circ$  with no additional weight on the blade, lower even than the original shaft.



Standard shaft, amount of division (L=0 B=0.15 R=0.25)

**Figure 18. Study results of the balancing machine sensibility with the modified shaft**

The Figure 19 shows the results of the frequency spectrum of the signal captured by the infrared sensor in five measurements with the modified shaft balanced. These measurements show the repeatability of the measurements using the sensor. The peak situated at 45Hz frequency corresponds to the rotational speed of the shaft placed in the balancing machine (2700rpm). Considering that the whirl movement of the shaft is negligible when the modified shaft is balanced, we can conclude that this peak and its multiples are due to imperfections in the surface of the cylinder mounted on the shaft. This result is important because it represents an error in the measurement of the shaft position and it must be subtracted in the raw signal captured by the sensors. As can be observed in the figure, the synchronous peak is approximately 0.02V. This is the voltage that will be subtracted from the raw signal captured by the sensors.

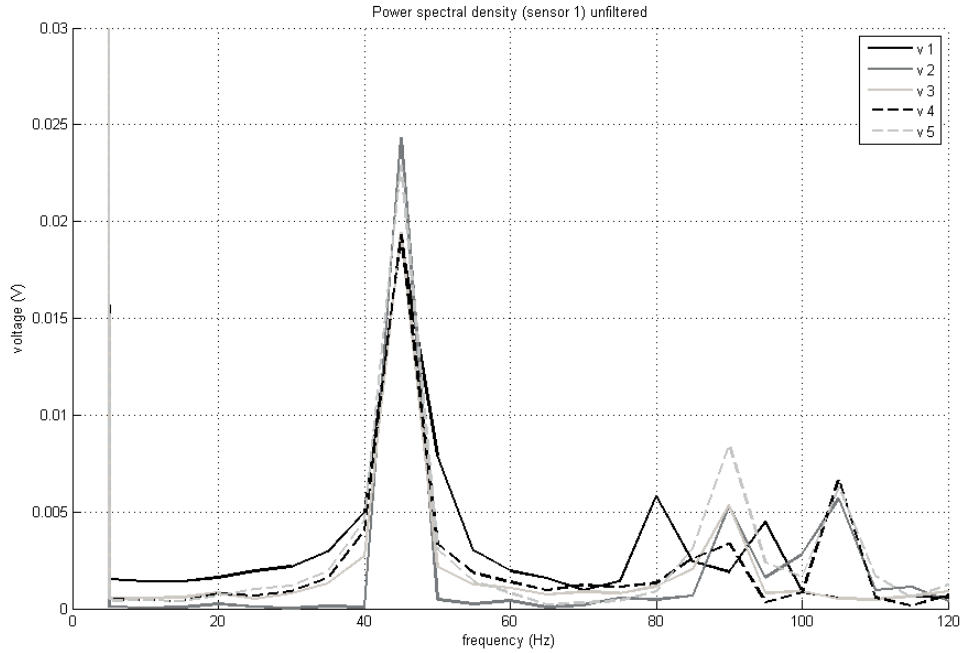


Figure 19. Repeatability study of the modified balanced shaft

Finally, the calibration curves of the sensors are determined using the calibration table. This table allows radial movement of the sensor with respect to the modified shaft. The sensor is placed at different distances to the surface of the cylinder mounted on the shaft, in order to determine the sensor calibration curve. The Figure 20 shows the result of such calibrations for distances close to 3mm, which is the distance at which they are placed to perform the measurements. The two curves show a good correlation between the measured voltage by the sensors and the distance to the cylinder surface.

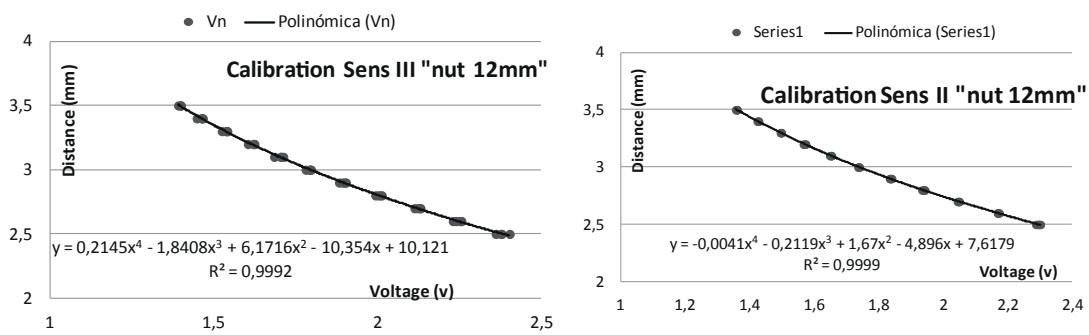


Figure 20. Calibration curves of the infrared sensors



### 3.2.2 Maximum eccentricity

As in the case of the methodology applied to the digital camera, in this case with the infrared sensors, the maximum eccentricity of the shaft is also estimated, in order to compare it with the measurements of the shaft motion. To estimate the maximum eccentricity using infrared sensors, the shaft is also forced by hand in radial directions on the turbine side. Then, the shaft is forced by hand to move in a maximum precess movement without any rotational movement, while the sensors register the position of the shaft. As the shaft doesn't have rotational movement, the sensor is always aiming to the same cylinder surface. Thus, different angular positions of the shaft imply different results, due to the small imperfections in the cylinder surface. All of these inaccuracies are taken into account in the processing of raw signals. The Figure 21 shows the results of this maximum eccentricity test.

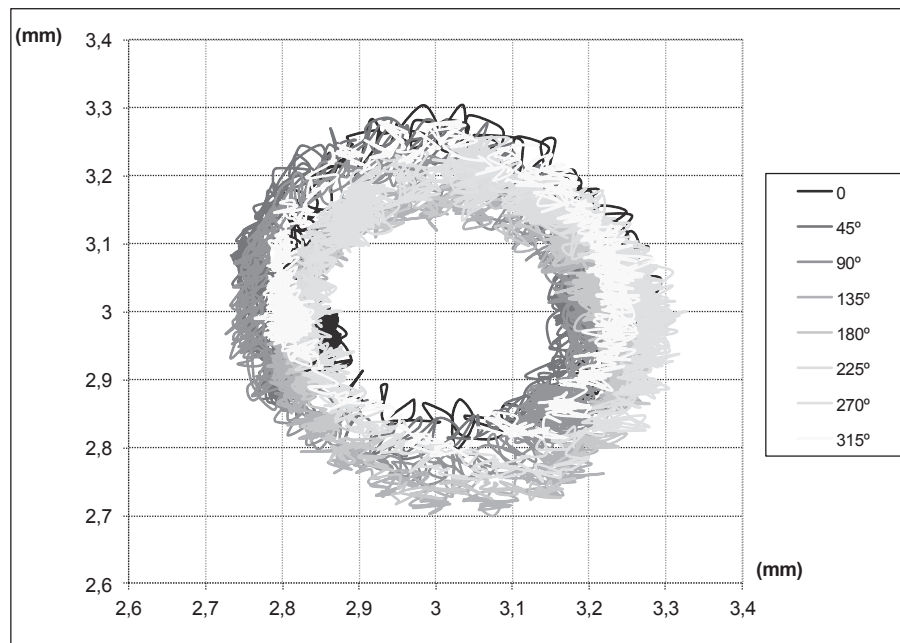


Figure 21. Maximum eccentricity measured with the infrared sensors

### 3.2.3 Shaft motion

To illustrate the signal processing to determine the shaft motion, a transient test with the modified turbocharger has been done. The top left graph of the Figure 22 shows the variation of the turbocharger speed during the test.

The other graphs of this figure show the processing of the infrared sensors signals during a tenth of a second of the test. The top right graph shows the frequency spectra of the raw signals from both sensors. The peaks in the frequency of 570Hz correspond to the synchronous rotation frequency of the shaft (34200rpm). The subsynchronous peaks situated at 300Hz correspond to the main mode of precession movement of the shaft. The other peaks are of lower order of magnitude and in some cases they are due to noise from electromagnetic fields in the electronic components of the sensors, as the peak located at 620Hz frequency or they are multiples of the synchronous frequency, as the case of the peaks located in 1140Hz and 1710Hz. To remove any noise sources received by sensors, which does not correspond with the precession movement of the shaft, the raw signals are filtered.

The bottom right graph shows the frequency spectrum of these filtered signals. The filtered signal is the continuous signal (0 Hz) and the peaks of the main subsynchronous frequency (300Hz) and the synchronous frequency (570Hz) after subtracting from this frequency the magnitude of 0.02V, which is due to errors in the shaft cylindricity. This error due to the lack of cylindricity was determined when the calibration tests of the sensors were done.

Finally, the bottom left graph shows the shaft movement during this tenth of second (the central ellipse with approximately 0.1mm in diameter), the raw signal measured with the sensors (the gray dots with approximately 0.3mm in diameter) and the points of maximum eccentricity (the black dots with approximately 0.5mm in diameter).

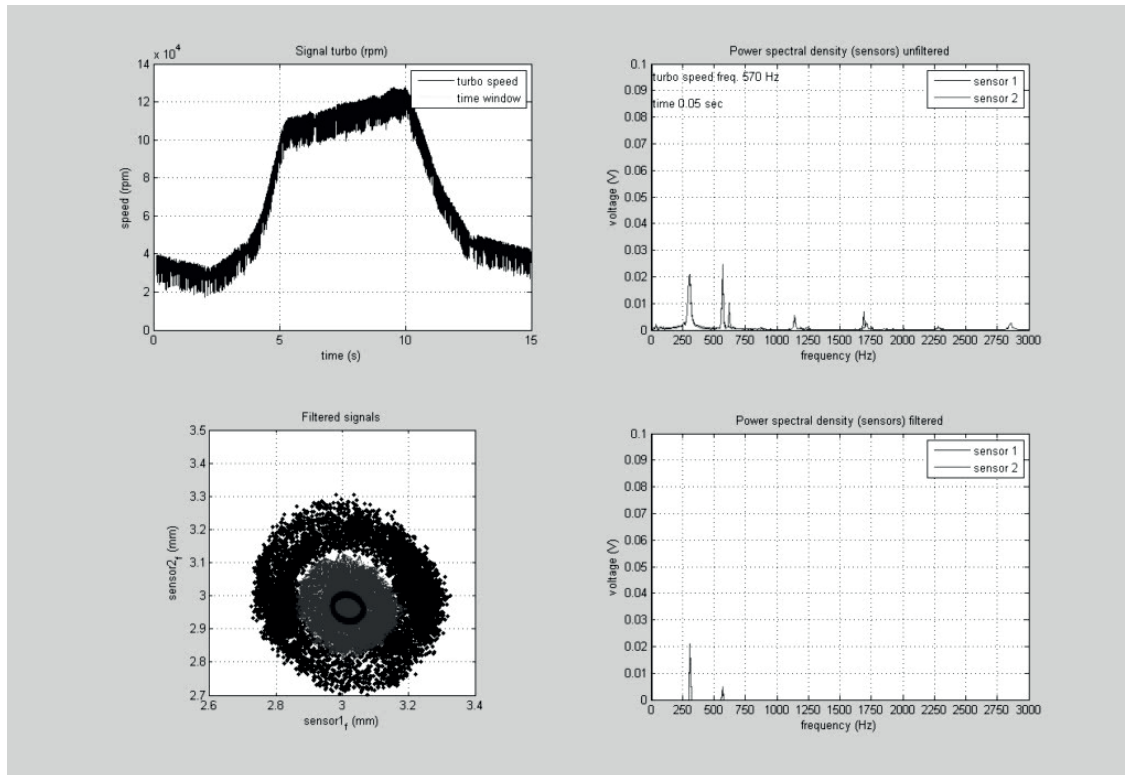


Figure 22. Frame of the shaft motion video measured with the infrared sensors

## 4 CONCLUSIONS

This article describes two alternative methodologies to observe the whirl movement of a turbocharger shaft when it is spinning: the first technique with a digital camera and the second technique with two infrared sensors.

The first technique, with the digital camera, is simple and relatively easy to implement in a test bench room, because it is not excessively intrusive. However, the second technique, with the infrared sensors, is very intrusive compared with the digital camera technique, which has a wide field of improvement through the use of higher quality cameras and light sources with more power. In addition, the digital camera technique, as it is a photographic technique, allows extracting visual information from the test, like the appearance of oil on the compressor side, sudden movements of the shaft or possible deformations of the area focused by the camera. Another highlight in the digital camera methodology is that the measuring elements can resist any destructive failure of the turbocharger, because the camera is out of the turbocharger, and the reference screws, which are placed in the turbocharger, are easily replaceable.

The accuracy obtained with the camera and with the light source used in this work is 5 $\mu$ m per pixel during an exposure time of 1ms. This accuracy allows observing with enough precision the movement of the shaft on the side of the compressor when it is spinning. Although, this information is not enough to determine the three-dimensional position of the shaft at every time instant, whether it provides important information when the photographed shaft position is compared with the maximum eccentricity zone permitted by the turbocharger bearings system. Thus, when the shaft is closest to the maximum eccentricity zone, the possibilities of the turbocharger to suffer a critical damage increases. However, the infrared sensors technique doesn't need external lighting sources and can record high frequency data, in order to determine the transient behaviour of the shaft movement.

Finally, the space requirements of the digital camera technique are higher than the infrared sensors technique, due to the digital camera placement and the lighting source devices.

This comparison between the two techniques is summarized in the next paragraphs.

#### **Digital camera technique:**

- Mounting non-intrusive. It is not necessary disassembling the rotating parts of the turbocharger (avoid risk of unbalancing).
- It provides a direct observation of the phenomena (images of the shaft tip that can help to explain anomalous behaviors).
- This technique can resist destructive failures of the turbocharger.
- Shaft position is not continuously recorded but from shot to shot. It means a bad time resolution (bad transient measurements).
- It is necessary a good lighting (lighting power higher than 1000 W).

Otherwise, the shaft motion is averaged with a degree of averaging that depends on turbo speed and the exposure time of the camera.

- Extra space is required to install the accessories, like the camera, the optical access and the light devices.

#### **Infrared sensor technique:**

- Intrusive mounting (big diameter nut is necessary to avoid scattering in light reflection). It is necessary to balance the rotating components.
- It does not provide direct observation of the phenomena (poorer understanding).
- This technique can't resist destructive failures of the turbocharger.
- Shaft position is instantaneously recorded with a high frequency acquisition data (good transient measurements).
- It is not necessary an extra light source. External infrared sources can cause measurement errors.
- The room space availability is lower, because only the sensors space is required.

## **REFERENCES**

- [1] Jeffcott H.H. The Lateral Vibration Loaded Shafts in the Neighborhood of a Whirling Speed. - The Effect of Want of Balance. *Philosophical Magazine* 1919; 6 37.
- [2] Nelson F.C. Rotor Dynamics without Equations. *International Journal of COMADEM* 2007; 10(3): 2-10.

- [3] Tian L., Wang W.J. and Peng Z.J. Dynamics behaviours of a full floating bearing supported turbocharger rotor with engine excitation. *Journal of Sound and Vibration* 330; 2011: 4851-4874.
- [4] Flores P., Pimenta Claro J.C. and Ambrósio J. Journal Bearings Subjected to dynamic loads: The analytical mobility Method. *Revista da Associação Portuguesa de Análise Experimental de Tensões* ISN -122 922.
- [5] Green I. and Casey C. Crack Detection in a Rotor Dynamic System by Vibration Monitoring—Part I: Analysis. *Journal of Engineering for Gas Turbines and Power* 2005; 127: 425-436.
- [6] Schweizer B. Dynamics and stability of turbocharger rotors. *Arch Appl Mech* 2010; 80: 1017–1043.
- [7] Günther P., Dreier F., Pfister T., Czarske J., Haupt T. and Hufenbach W. Measurement of radial expansion and tumbling motion of a high-speed rotor using an optical sensor system. *Mechanical Systems and Signal Processing* 2010; 25: 319-330.
- [8] Podevin P., Clenci A. and Descombes G. Influence of the lubricating oil pressure and temperature on the performance at low speeds of a centrifugal compressor for an automotive engine. *Applied Thermal Engineering* 2011; 31: 194-201.
- [9] Deligant M., Podevin P. and Descombes G. CFD model for turbocharger journal bearing performances. *Applied Thermal Engineering* 2011; 31: 811-819.
- [10] Gertzos K.P., Nikolakopoulos P.G., Chasalevris A.C., Papadopoulos C.A. Wear identification in rotor-bearing systems by measurements of dynamic bearing characteristics. *Computers and Structures*. 89 (2011) 55-56.
- [11] Serrano J.R., Tormos B., Gargar K.L. and Bouffaud F. Study of the effects on turbocharger performance generated by the presence of foreign objects at the compressor intake. *Experimental Techniques* (2011) Society for experimental Mechanics.
- [12] Galindo J., Serrano J.R., Guardiola C. and Cervelló C. Surge limit definition in a specific test bench for the characterization of automotive turbochargers. *Experimental Thermal and Fluid Science*. 2006;30: 449-462.
- [13] Chauvin J., Moulin P., Corde G., Petit N. and Rouchon P. Real-Time nonlinear individual cylinder air fuel ratio observer on a Diesel engine test bench. In *Proc. of the IFAC World Congress*, 2005.
- [14] Payri F., Galindo J., Climent H. and Guardiola C. Measurement of the oil consumption of an automotive turbocharger. *Experimental Techniques*. September/October 2005.



# APPLICATION OF SPECTROSCOPY FOR ANALYSIS OF ADVANCED COMBUSTION MODES IN COMPRESSION IGNITION ENGINES

J.V. Pastor, J. M. García-Oliver, A. García and C. Micó

CMT- Motores Térmicos - Universidad Politécnica de Valencia,  
Camino de Vera s/n 46022 Valencia - SPAIN

## ABSTRACT

Nowadays many research efforts are focused on the study and development of new combustion modes, looking for higher efficiencies and lower pollutant formation. The aim of this paper is to present the UV-Visible spectrometry as a valuable tool for experimental research on hydrocarbon combustion reactions. The method is based on the analysis of emission spectra of the reaction, identifying the formation and evolution of different characteristic chemical species like OH and CH radicals or soot luminosity. An experimental application is shown, where the combustion process on a compression ignition engine is analyzed by means of this technique..

## 1 INTRODUCTION

One of the main benefits of the compression ignition combustion is the high efficiency it achieves, specially compared with other conventional systems like the spark ignition, employed in automotive engines. However it has some important drawbacks that must be overcome like the formation of pollutant species, such as soot particles or NO<sub>x</sub>. A remarkable example is the automotive industry, where new and more restrictive legislations make it compulsory to focus part of the research efforts on the investigation of new combustion modes [1] with the aim of reducing fuel consumption and emissions. Within this framework, new concepts appeared based on promoting leaner air-fuel mixtures and lower combustion temperatures [2, 3] (PCCI, HCCI, etc.), leading to a reduction of pollutant formation. However, despite the benefits, application still presents some challenges that must be overcome before their practical implementation in ICEs. The main limitation is obtaining a proper combustion phasing and control over a wide range of engine load and speed.

Different strategies are proposed on the literature [4-6], based on controlling more precisely the thermodynamic conditions inside the cylinder or modifying the reactivity of the fuel employed. Nowadays, research work is centered on combining some of these different solutions to take advantage of the main benefits, but also solving the most important drawbacks.

At this point, the development of new ways of analysis becomes relevant, offering new possibilities of improving insight into these new combustion concepts. During last years optical techniques are becoming popular due to the evolution of optical equipment and electronics, which increase their potential and make it possible to study phenomena that are not resolved by other techniques. Thereby, the main objective of this paper is to present and evaluate the performance of UV-Visible spectrometry as a tool for the analysis of a novel combustion mode, where a low reactivity fuel is employed on a compression ignition engine under partially premixed combustion conditions, combined with a spark assisted combustion phasing system.

Experiments have been performed in an optical engine, with a diesel-like compression ratio and equipped with a common rail injection system enabling high-pressure injection. Moreover, the experimental work was carried out using gasoline, as a low reactivity fuel.. The main aspects of the experimental methodology are going to be presented and discussed, along with results obtained from the application of UV-Visible spectrometry.

## 2 EXPERIMENTAL TOOLS AND MEASUREMENT PROCEDURE

The experimental work was performed on a 4-stroke DI diesel single cylinder optical engine. It is equipped with an elongated piston and a cylindrical bowl, allowing optical access to the combustion chamber through a sapphire window located at its bottom. Below the piston bowl an elliptical UV mirror is placed at 45°, aligned with the piston axis.

A Jovin Yvon Horiba Triax 180 spectrograph was used to decompose the light emitted by combustion in the UV-Visible range, which was coupled with a LaVision Dynamight intensified CCD camera. A grating with 300 groove/mm was used which, combined with the 512 x 512 pixels of the ICCD camera, allows detecting a wavelength bandwidth of 170 nm. The grating was centered at 350 nm (260-440 nm) and the entrance slit width was set to 0.3 mm. The exposure time of the ICCD camera was 500  $\mu$ s (approx. 2.25 CAD). A UV-Lens ( $\varnothing$ 25.4 - 100 mm focal length) was used to focus the light inside the spectrograph.

The ICCD records spectrum as raw images, with both wavelength and 1-D spatial resolution. Fig. 1A shows a raw recorded spectrum, where the X-axis corresponds to wavelength while Y-axis contains the spatial coordinate. A calibration process enables establishing a correlation between wavelength and x-pixels ( $\pm$  2nm precision). A second processing step is based on intensity correction, due to the different efficiency of the optical elements present on the arrangement. Finally a wavelength-resolved spectrum (Fig. 1B) is obtained.

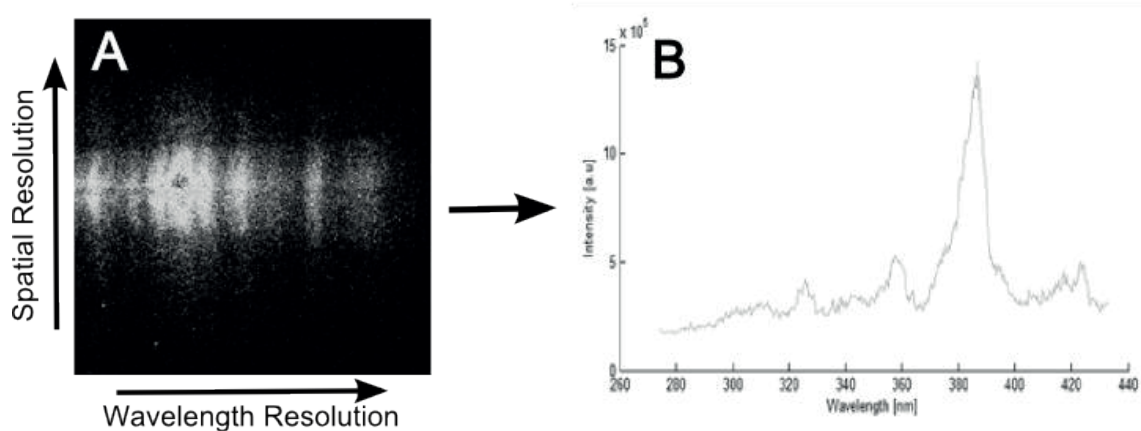


Figure 1. A: Raw spectrum recorded by ICCD camera; B: Final light spectrum

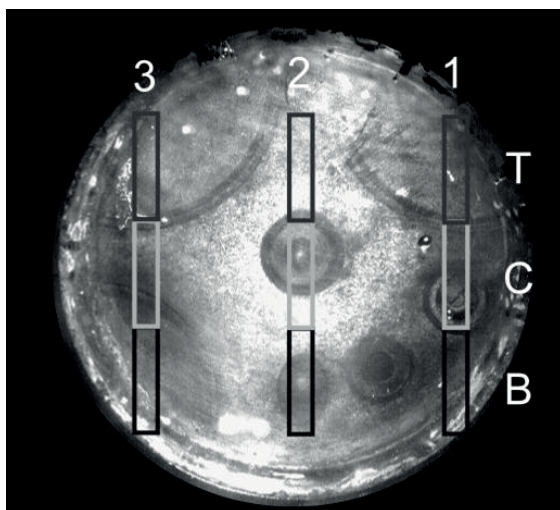
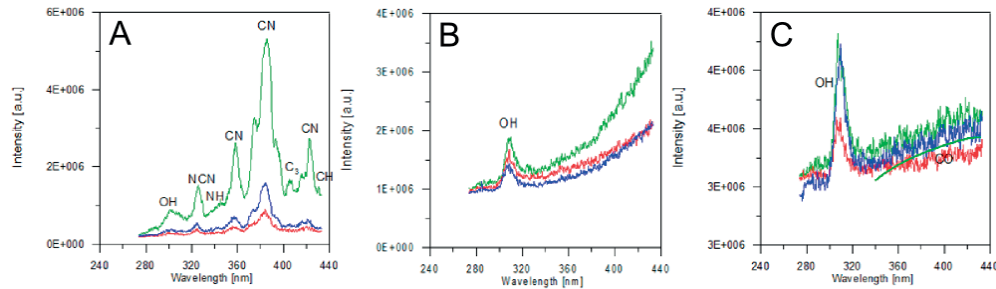


Figure 2. Combustion chamber division for UV-Spectrometry measurements

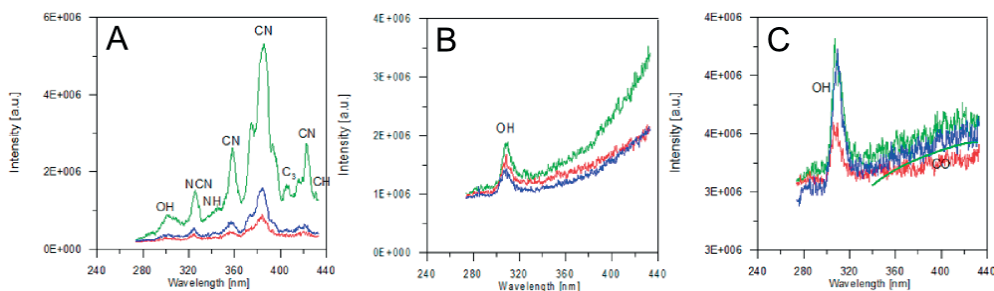
Due to the reduced size of the entrance slit, the spatial resolution of the spectrometer is reduced. In order to improve it, three different test positions were defined: centered at the spark plug (1), at the injector (2) and at a diametrically opposed position to the spark plug (3). Moreover, the combustion chamber was divided in three areas: top (T), center (C) and bottom (B). Thereby, a matrix of nine different regions of interest was defined (Fig. 2). By averaging the corresponding pixels of a raw recorded spectrum, at each test position, it was possible to obtain a spectra for the nine defined areas.

### 3 RESULTS AND DISCUSSION

Spectral analysis is useful to better understand the combustion process. In the literature, different chemical species and radicals are identified as good tracers of the stages of a hydrocarbon combustion reaction. Thus their presence characterizes the emission spectra and helps describing the evolution of the reaction.



**Figure 3. Spectra at spark plug for different CAD: -10.8 to -8.5 CAD (A), -5.5 to -3.2 CAD (B) and 2 to 4.3 CAD (C)**



**Figure 4 - Spectra at the position opposite to the spark plug for different CAD: -5.5 to -3.2 CAD (A), 2 to 4.3 CAD (B) and 5.8 to 8.1 CAD (C)**

The most relevant spectra of the combustion process are presented in Fig. 3 and Fig. 4. At Fig. 3, the evolution of the spectra around the spark plug can be observed. It is possible to see that at the first stage (Fig 3A, -10.8 to -8.5 CAD), the spectra is characteristic of the plasma generated by the spark discharge [13]. However, two weak peaks at 310nm and 430 nm can be observed. They correspond to OH and CH radicals, respectively, and are related to the formation of a first flame kernel. As combustion progresses (Fig 3B, -5.5 to -2.3 CAD), the spectra evolve showing a remarkable peak of OH and continuous soot luminosity, which is characteristic of premixed combustion.

On the other hand, at the diametrically opposed position (Fig. 4), the spectra observed are different. During the first stages, when reaction is taking place around the spark, the recorded signal is weak and near background noise. However, coinciding with the stage of autoignition (Fig 4B, 2 to 4.3 CAD) spectra starts showing chemiluminescence. Both peaks of OH and CH and also continuous radiation from other radicals like HCO and HCHO [14] can be observed. The most important observation at this position is that the relative intensity of the OH peak is weaker than others, according to the idea that the reaction takes place as an autoignition process, instead of as a premixed flame propagation. At final stages of combustion (Fig. 3C and Fig. 4C), the spectra are characterized by the presence of CO continuous emission [13,14].



## 4 CONCLUSIONS

UV-Visible spectrometry has been evaluated as a tool for the study of different modes of hydrocarbon combustion. It has provided information about radical formation during combustion, useful for a qualitative analysis of new combustion modes like the one described on this paper. The main advantage is the high wavelength resolution it offers, allowing to track emission at different wavelengths at the same time. On the other hand, the main limitation is the spatial and time resolution of the technique.

According to the results from UV-Visible spectrometry and the evolution of different characteristic chemical species, three different stages of combustion have been identified. The process starts with the spark discharge, which produces a flame kernel around the spark plug that later evolves to a premixed flame front. This premixed flame front heats unburned mixture and progresses into an auto-ignition combustion. The evolution of the combustion process has been followed, based on the recorded spectra.

## ACKNOWLEDGEMENTS

The authors acknowledge that part of this work was performed in the frame of project DUFUEL TRA2011-26359, funded by the Spanish Government.

## REFERENCES

- [1] H. Yanagihara, Y. Sato, J. Minuta, 17th International Vienna Motor Symposium (1996) 303-314.
- [2] S. Kimura, O. Aoki, H. Ogawa, S. Muranaka et al., SAE Technical Paper 1999-01-3681 (1999).
- [3] H. Akagawa, T. Miyamoto, A. Harada, S. Sasaki et al., SAE Technical Paper 1999-01-0183 (1999).
- [4] Mingfa Yao, Zhaolei Zheng, Haifeng Liu, Progress in Energy and Combustion Science 35 (5)(2009) 398-437.
- [5] R. M. Hanson, S. L. Kokjohn, D. A. Splitter, R. D. Reitz, SAE international journal of engines 3 (1)(2010) 700-716.
- [6] B. Keeler, P. J. Shayler, SAE 2008-01-1327 (2008).
- [7] J. Benajes, J.J. López, R. Novella, A. Garcia, Experimental Techniques 32 (2008)41-47.
- [8] J. Benajes, R. Novella, A. Garcia, V. Domenech, SAE Int. J. Engines doi:10.42712011-37-0008 4:2590-2602 (2011).
- [9] M. Lapuerta, O. Armas, J.J. Hernández, Applied Thermal Engineering 19 (5)(1999) 513–529.
- [10] J.V.Pastor, J.M. Garcia-Oliver, J.M. Pastor, J.G. Ramirez-Hernandez, Fuel doi:10.1016/j.fuel.2011.01.008 (2011).
- [11] F. Payri, S. Molina, J. Martín, O. Armas, Applied Thermal Engineering 26 (2-3)(2006) 226–236.
- [12] C. Tornatore, P. Sementa, S.S. Merola, Proceedings of the Institution of Mechanical Engineers, Part D: Journal of Automobile Engineering, 225 (2011).
- [13] Gaydon A.G., The spectroscopy of flame, Chapman and Hall, London, UK, 1957.
- [14] E. Mancaruso, B.M. Vaglieco, Fuel 90 (2011) 511-520.

## A DECISION MAKING ALGORITHM FOR AUTOMATIC SHOCK WAVES DETECTION IN SCHLIEREN IMAGING

Flora Tomasoni, Bayindir H. Saracoglu, Guillermo Paniagua  
 von Karman Institute for Fluid Dynamics,  
 Chaussée de Waterloo 72,  
 B-1640, Rhode-Saint-Genèse, Belgium  
[tomasoni@vki.ac.be](mailto:tomasoni@vki.ac.be)

### ABSTRACT

High frequency Schlieren was used to investigate the effect of cooling on the fish tail shock waves that appear at the trailing edge in transonic and supersonic turbomachinery. Both continuous and pulsating coolant blowing were tested at various rates. An original digital image processing algorithm was developed to gain a deeper understanding on the shock waves behaviour, allowing to quantify flow features in an unsteady and non intrusive way. The software is based on image binarization and object identification. The geometrical properties of the detected elements are obtained by measuring the characteristics of each connected components. In case of multiple waves or shock bifurcations, a "decision-making" algorithm is called that chooses the best wave path, based on the original image intensity and local orientation. The centre and the inclination of the waves are stored for further investigation. The measured shock wave angle fluctuation showed to be in phase with the coolant pulsation.

### INTRODUCTION

Improving the turbine durability while preserving a high efficiency is a challenging task. Trailing edge shock interactions are a major source of loss for supersonic airfoils. Additionally vane shocks cause large pressure fluctuations that may result in low and high cycle fatigue problems.

The downstream flow field of nozzle guide waves contained in modern high-pressure turbines suffers from fish tail shock structures at the trailing edge [1]. The impingement of those compression waves on the downstream rotor row and rear suction side of adjacent vane results in unsteady entropy generation. Quantification of unsteady loss and pressure variation in a transonic turbine was studied numerically and experimentally in the literature [2]. Possible improvements on attenuation of the shock waves in transonic turbines are well appreciated by adjudging tabulated efficiency deductions and unsteady forcing due to compression waves. Published research has demonstrated that cooling ejection has significant effects on the base region and trailing edge shock patterns. The applicability of pulsating coolant on turbine bladings was considered to prevent boundary layer separation through film cooling holes [3]. Separation control was achieved by various duty cycles.

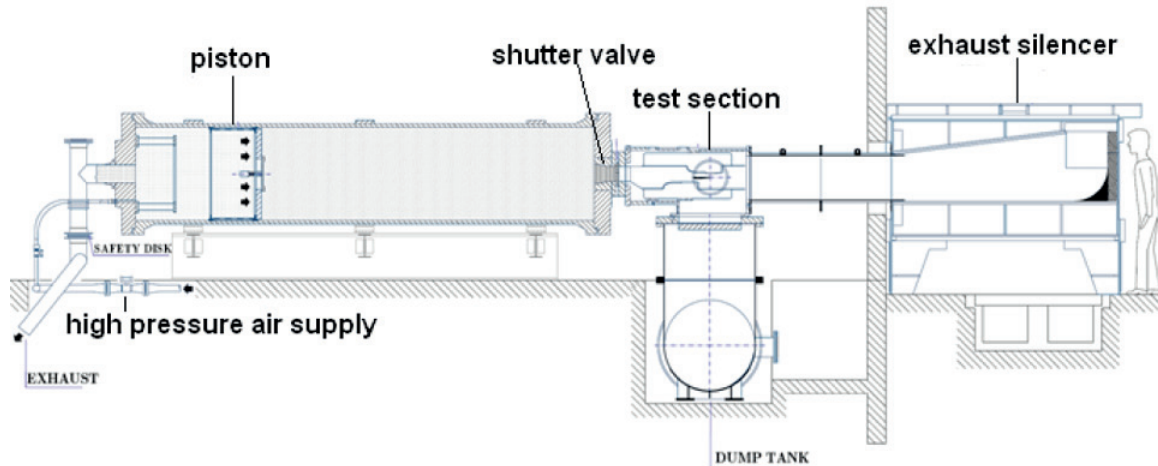
Pulsating coolant was proposed to control shocks by the authors for the first time in the literature [4]. Experimental and numerical work was performed to understand the base region flow topology depending on cooling ejection rates. Both unsteady temperature and pressure measurements were performed, together with high-speed Schlieren imaging. In order to move from a qualitative/topological use of the images to a quantitative assessment of flow features, i.e. shock waves inclination and fluctuations frequency, an algorithm able to automatically read and analyse the images was needed to be designed.

In the following sections, the original decision-making algorithm developed is described and applied to the high frequency Schlieren images. This program proved to be successful in driving toward a deeper understanding of the phenomena under investigation.

### EXPERIMENTAL APPROACH

In order to investigate the effect of cooling on the fish tail shock waves that appear at the airfoil trailing edge, tests are made for a range of high subsonic to low supersonic Mach numbers ( $M_{2,is}=0.8-1.2$ ). Two Reynolds numbers representative of aero-engine conditions are selected ( $Re=4 \times 10^6$  &  $6 \times 10^6$ ). All conditions are tested for no blowing and continuous blowing at 1.1, 1.5 and 1.9 bars of coolant total pressures ( $P_{0,cool}$ ). Pulsating coolant stream is introduced for transonic and supersonic test cases at average coolant total pressure of 1.9 bars with a frequency of 200 Hz.

An isentropic compression tube facility was used to perform all experiments at the von Karman Institute (Fig. 1). Optical access permits Schlieren and oil flow visualizations. The air inside the cylindrical vessel is compressed by a free piston driven by high-pressure dry air (300 bars) until the desired upstream conditions are attained. Subsequently, the fast acting shutter downstream of the cylinder is opened and air is released into the test section, providing 100 to 800 ms of testing time ([5],[6]). The flow is vented axially to the atmosphere.



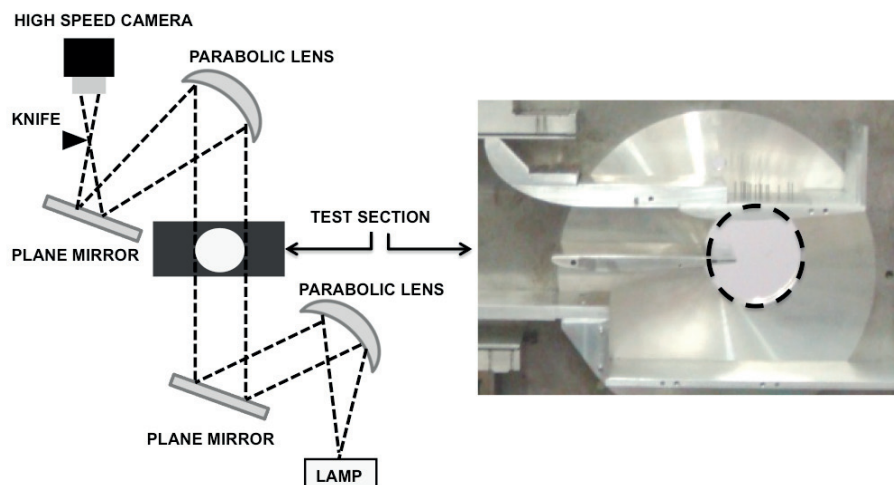
**Fig. 1: The schematic of the experimental facility**

A linear cascade test section was designed in order to understand the effect of pulsating trailing edge cooling on the turbomachinery trailing edge shock formation and strength [7]. The airfoil tested was derived from existing vane geometry to reproduce the velocity distribution encountered in a modern cooled NGV. The model was staggered at 66 degrees in the test section.

Pulsation in the coolant stream was provided by a valve [8] with a perforated rotating disc inside and measured at 1.5 kHz with a SENSYM pressure transducer.

High-speed Schlieren flow visualizations were performed with the Z-type Schlieren setup [9] sketched in Fig. 2. The 800 by 600 pixel resolution pictures were acquired at a rate of 3.2 kHz by a Phantom V9 high-speed camera.

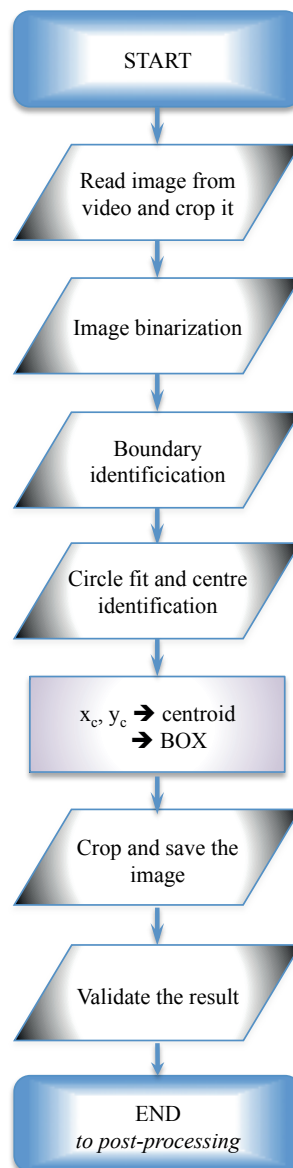
In such critical experimental conditions the facility, Schlieren mirrors and the surrounding typically suffer from vibrations. This phenomenon causes the picture illumination to be inhomogeneous and the target to be in different position inside the image itself, seriously compromising the possibility of automating the analysis of the results.



**Fig. 2: Schematic of Schlieren setup and test section**

**ALGORITHMS DEVELOPMENT***Vibration suppression algorithm*

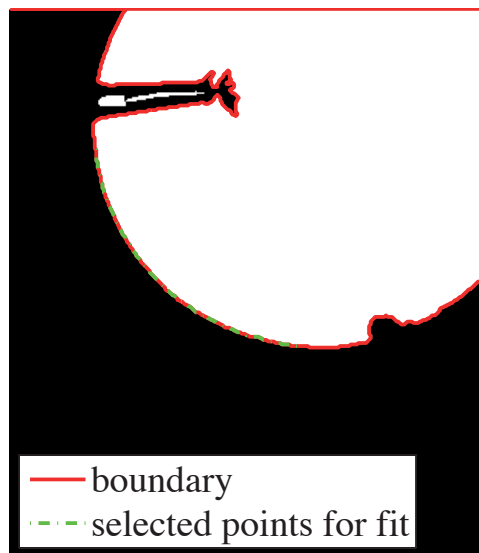
In order to correctly analyse Schlieren images, it is necessary to suppress the vibration-induced image shift by re-centring them. A devoted algorithm named *Vibration-Suppression-Algorithm* (VSA) has been developed (Fig. 3) and it is described hereafter.



**Fig. 3: Vibration suppression algorithm flowchart**

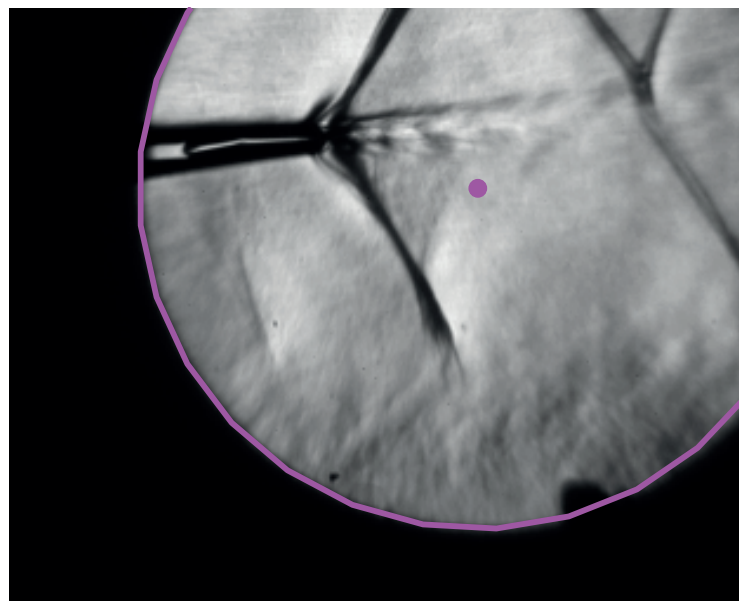
- Each image is read from the Schlieren video. In order to re-centre the images, an object that preserves its shape and size despite vibrations and illumination inhomogeneity needs to be chosen and used as reference target. In this case two objects were suitable: the trailing edge cooling channel and the set-up optical window. The latter was selected since its results were found to be more reliable and stable. The image is cropped around the bottom left optical window quadrant, that is the less sensitive image portion to light variation.
- The image is binarized with a modified global image threshold based on Otsu's method [10]. The threshold is in fact halved respect to the default value, so that the optical window is emphasized. The holes inside the binary image are filled, in order to obtain a unique continuous circle corresponding to the window itself.

- The exterior boundary (Fig. 4) of the window is traced via the *bwboundaries* function in the binary image. A subset of points is selected for the fitting. Those points correspond to the bottom left quadrant of the circle and are automatically found by the program.



**Fig. 4: Binary image boundary selection**

- The points belonging to the circle boundary are fitted with Bucher's circle-fit function [11], which is based on the minimization of the sum of squared radial deviations. The method provides the centre coordinate and the radius of the circle (Fig. 5).



**Fig. 5: Circle fit and centre identification**

- The program stores both the centre  $(x_c, y_c)$  and the radius of the circle for further analysis. A crop-rectangle *BOX* is then built starting from the circle centre. *BOX* is a four-element position vector  $[x_{\min}, y_{\min}, \text{width}, \text{height}]$  that specifies the size and position of the crop rectangle. The box width and height are set at about 1.5 times the mean optical window diameter.
- The original image is cropped according to *BOX*, i.e. the new image is centred in  $(x_c, y_c)$ , and saved.
- The vibration suppression algorithm is validated by re-running the program on the new re-centred images (no initial crop applied) and comparing the centre dispersions  $(x_c - x_m, y_c - y_m)$ . Fig. 6 and Fig. 7 show the centre coordinates dispersion and the centre distance distribution, respectively. Both in the x and y direction the shift is reduced of about six times, passing from an average mean-centre distance  $\Delta$  of 2.5 pixels to a mean distance of 0.45 pixels.

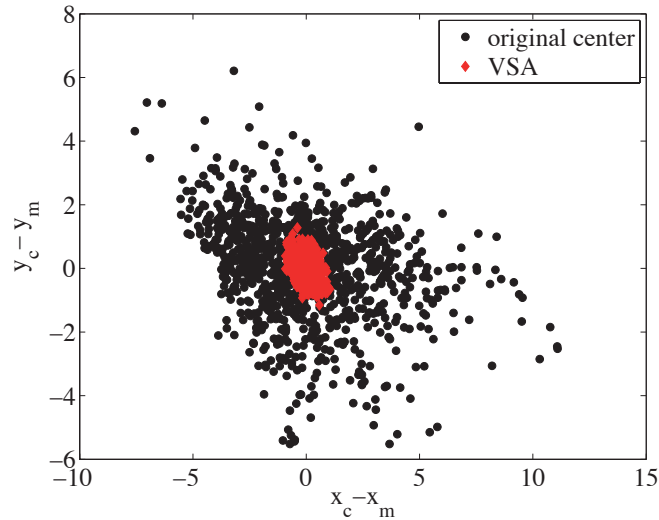


Fig. 6: Image centre coordinate dispersion plot

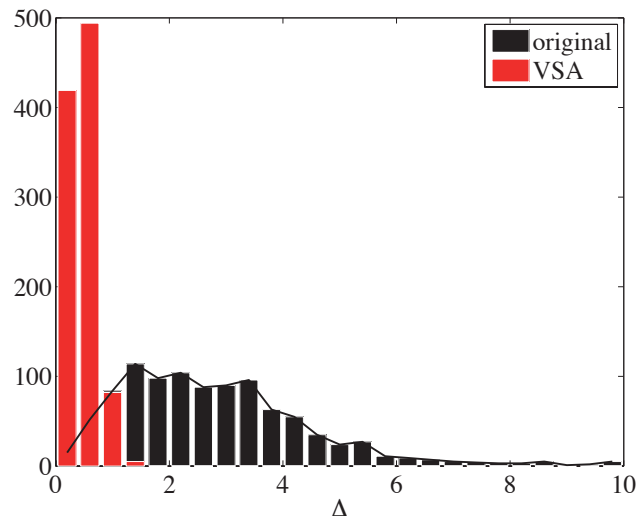


Fig. 7: Mean centre distance distribution

*Shock wave identification algorithm*

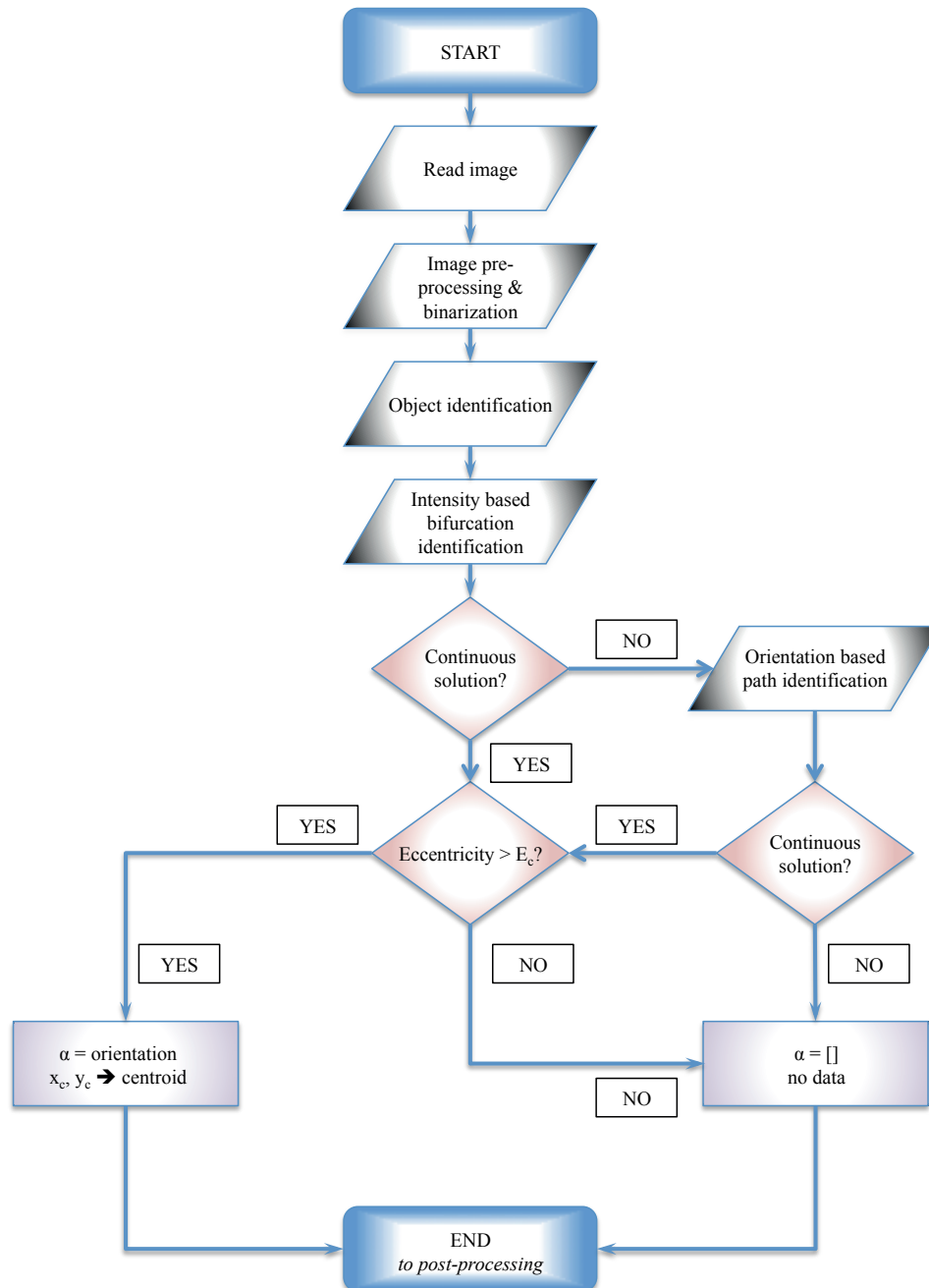
Decision making algorithms find their application in a variety of fields from cancer diagnosis [12] to airbag control [13]. These programs are typically tailored *ad hoc* on the specific problem, since the creation of a “computer-aided” decision procedure requires the transformation of the particular phenomenon properties into measurable quantities.

It is known in fact that even if an image may look confused, more objects are intersecting each other or small branches are interfering with the main path, an experienced person can still identify the principal target among the others. The main goal of this work was to translate the human brain “natural” correlations into mathematical operations in case of shock wave identification. When more shock wave paths are found, due to weak bifurcations or reflections, mathematical, geometrical or logical criteria were implemented to allow the program to take the correct decision.

A Digital Image Processing algorithm was therefore developed with Matlab® to automatically analyse the Schlieren images. The flow chart of the program is shown in Fig. 8 and detailed hereafter.

- Each single image is read and cropped around the area of interest.
- A local background is created and subtracted from the image to compensate for illumination variations. The background is computed row by row, by computing the average columns intensity. The algorithm converts this image portion into a binary image, i.e. a logical array.
- The program labels (*bwlabel*) its connected components providing a label matrix L, where each object is identified with a positive integer number, following the general procedure outlined in [14]:
  1. Run-length encode the input image.
  2. Scan the runs, assigning preliminary labels and recording label equivalences in a local equivalence table.

3. Resolve the equivalence classes.
4. Re-label the runs based on the resolved equivalence classes.



**Fig. 8: Shock wave detection algorithm flow chart**

- The properties of the detected objects are obtained by measuring the characteristics of each labelled component in the label matrix. Both shape properties (e.g. area, centroid, eccentricity, equivalent diameter...) and pixel value measurements (e.g. maximum intensity, pixel values...) are provided by Matlab® built-in function *regionprops*.
- In order to eliminate small bifurcations, minor waves or reflections, only the subset of pixels with the higher intensity is selected among those belonging to the identified objects (Fig. 9).

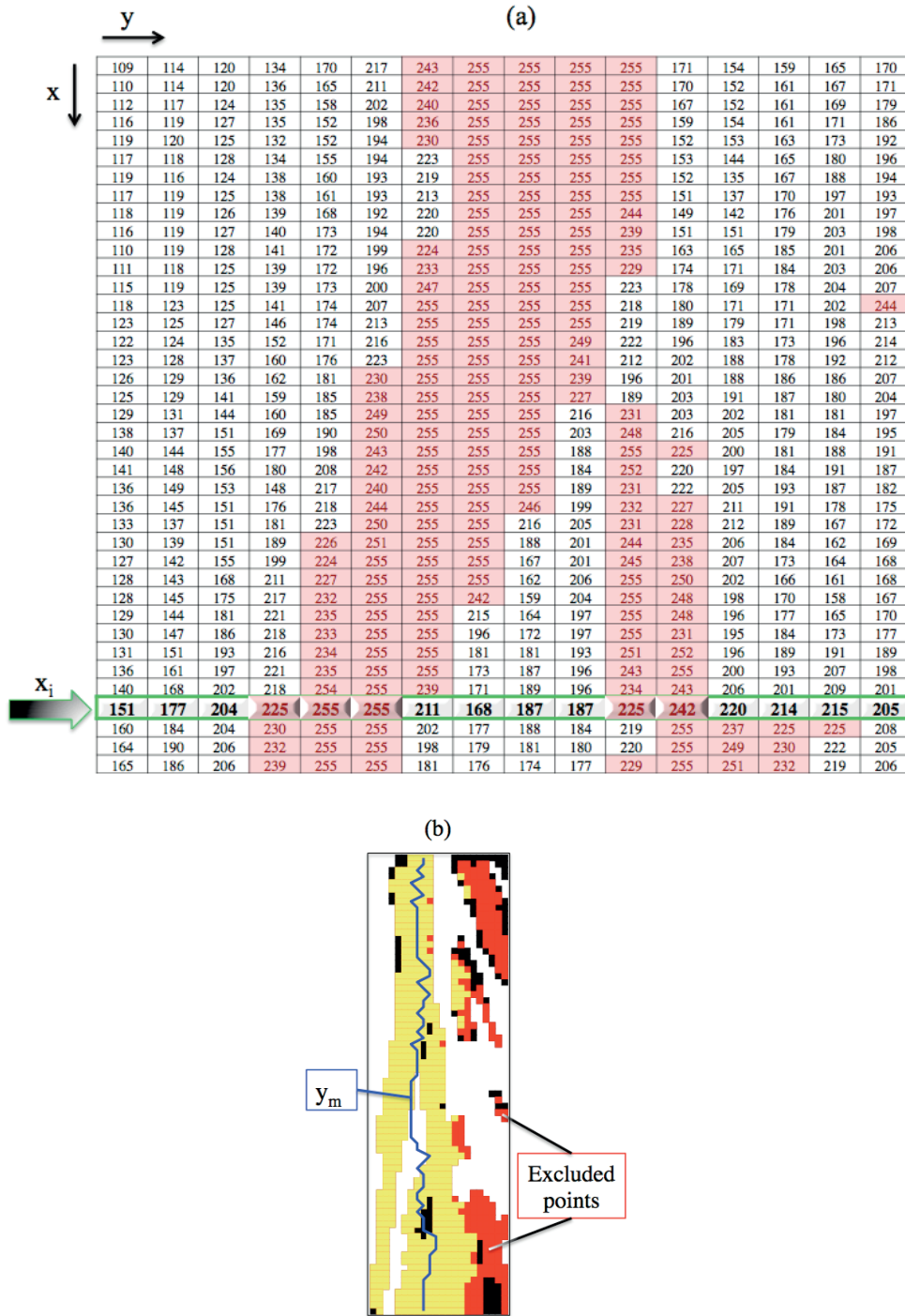


Fig. 9: Intensity based main bifurcation identification: the image as a matrix (a) and outliers exclusion (b)

Since per each row  $x_i$ , more columns  $y_{i,j}^*$  may respect this condition, a mean bifurcation line is computed:

$$y_{m,i}^* = \frac{1}{n} \sum_{j=1}^n y_{i,j}^*$$

and, to exclude outliers, only the points  $y_{i,j}^\#$  that lie within a distance  $\varepsilon$  from  $y_{m,i}^*$  are chosen. The correct mean line is finally re-built row by row:

$$\text{if } |y_{i,j}^* - y_{m,i}^*| \leq \varepsilon \rightarrow y_{m,i}$$

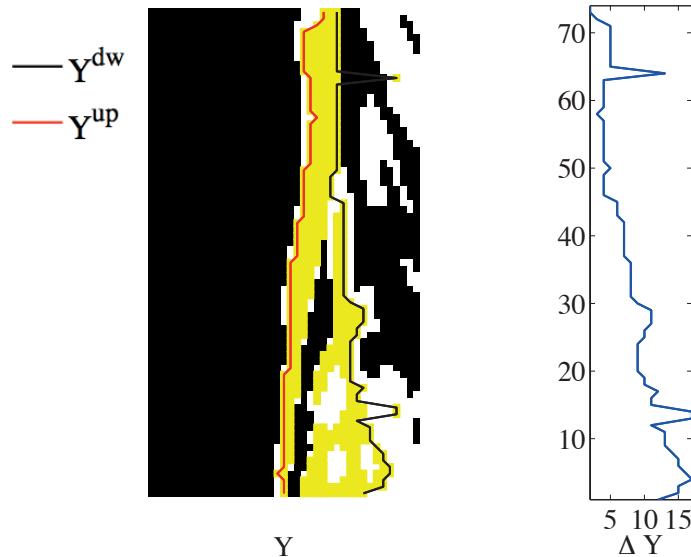
- ✓ Per each coordinate  $x_i$  the upstream and downstream border coordinates ( $Y^{up}$  and  $Y^{dv}$ , Fig. 10 left) are selected from the intensity-identified cloud of points ( $x_i, y_{i,j}^\#$ ). The continuity of the bifurcation line  $y_m$  is verified by evaluating the normalized difference between the two border lines (Fig. 10, right):



$$\Delta Y_i = |Y_i^{up} - Y_i^{dw}|$$

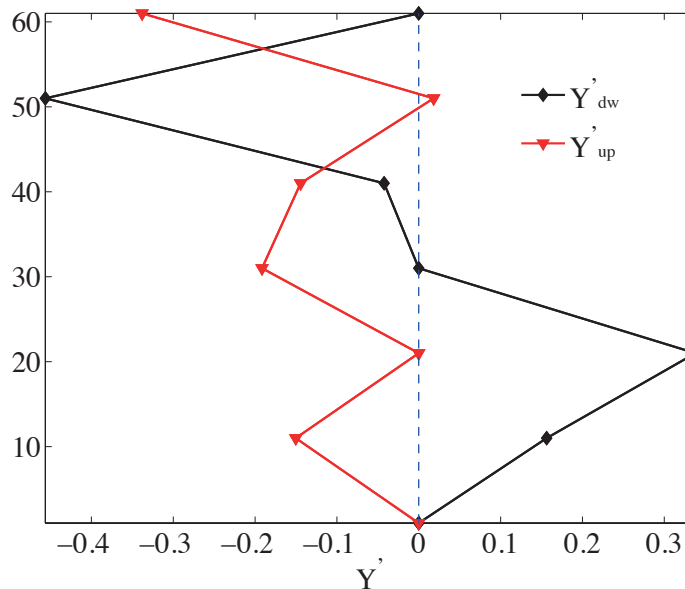
$$d\Delta Y = (\max(\Delta Y) - \min(\Delta Y)) / \text{mean}(\Delta Y) < \varepsilon_b$$

- If the normalized distance difference  $d\Delta Y$  is lower than a threshold value (e.g. 1.5), the coordinates cloud  $(x_i, y_{i,j}^\#)$  is passed to the main program, where it is transformed into a binary image, identified as an object and measured,
- If  $d\Delta Y > \varepsilon_b$  the orientation-based path identification module is called.



**Fig. 10: Solution continuity evaluation:  $Y^{up}$  and  $Y^{dw}$  (left) and their difference  $\Delta Y$  (right)**

- The two lines  $Y^{up}$  and  $Y^{dw}$  are filtered with a low pass filter in order to exclude the higher and sharper peaks.



**Fig. 11: Piecewise derivative of the upstream and downstream border (10 points per piece)**

Their piecewise derivative is then computed (Fig. 11) by solving the least square problem:

$$m_k = V_k \backslash y_{k,j} = [y_{k,j} \ 1_{k,j}] \backslash y_{k,j}$$

$$Y'_k = m_k(1)$$

where  $k$  indicates the  $k^{th}$  piece of points.

The line with the minimal derivative variation (absolute value difference and number of sign inversions) is indicated as the correct shock wave outer border. In the example of Fig. 11, the upstream line  $Y^{up}$  is

therefore the one that represents the wave border  $Y_S^{out}$ . Finally the inner border of the bifurcation is computed (Fig. 12) as it follows:

- per each row  $x_i$ , starting from the selected outer border  $Y_{S,i}^{out}$  and going towards the image centre, the difference between two successive points among  $y_{i,j}^{\#}$  is computed:

$$\Delta y_i = |y_{i,j}^{\#} - y_{i,j-1}^{\#}|$$

- the last point that separates from the previous one of less than 1.5 pixels is selected as the inner border of the shock  $Y_{S,i}^{in}$ .

The coordinate of the points lying within  $Y_S^{in}$  and  $Y_S^{out}$  are passed to the main program, where they are transformed into a binary image, identified as an object and measured.

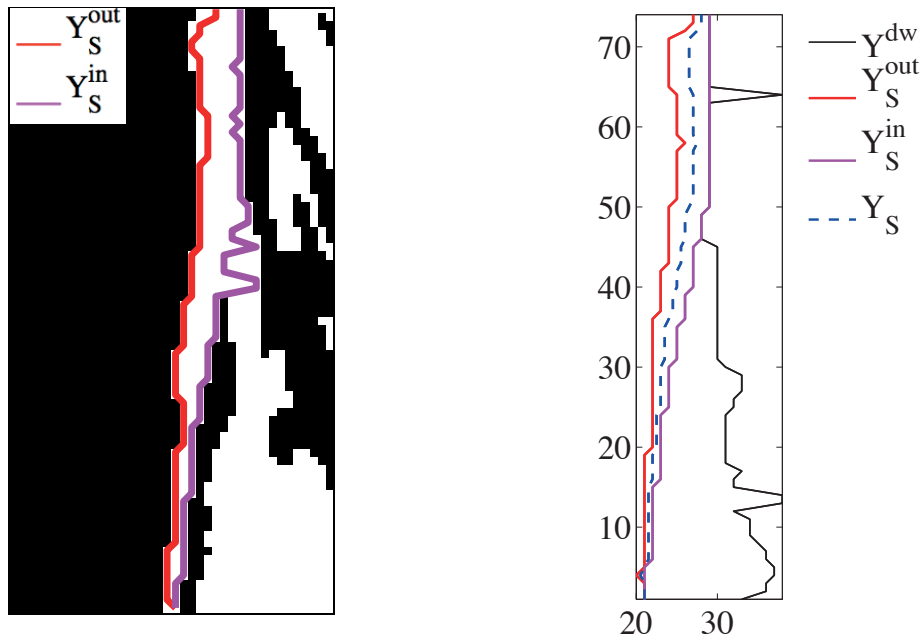


Fig. 12: Shock boundary identification and final shock direction

- ✓ Eccentricity is used as ultimate criterion to select among the detected items the one that corresponds to the compression wave or to verify that the selected object is compatible with a shock wave. If the eccentricity is bigger than the threshold imposed<sup>1</sup>, the centre and orientation of the wave are computed and stored for further analysis, otherwise no data is saved.
- The program loops over all the Schlieren images, providing the time-resolved shock wave angle and centre coordinate.

## RESULTS AND DISCUSSION

In the next sections the capabilities of the algorithm are highlighted and the main achievements obtained with this methodology are described, whereas a more detailed discussion of the experimental results can be found in [4].

### Image analysis

In Fig. 13 an example of how the decision-making algorithm operates is shown, by reporting the crucial phases of the shock wave identification process. Image (a) shows the area around the first shock: the photo reveals one quasi-vertical wave accompanied by several smaller bifurcations/reflections. The binarization of this image leads unfortunately to a unique block (b), whose global orientation does not represent the principal wave angle. The pixels with the higher intensity are then selected (green dots, c) via the intensity-based bifurcation identification module and a mean shock line is computed. By verifying the continuity of the mean shock line, it is found that a bifurcation is still present and the orientation-based path identification module is called: only the final selected line, reported in (d), well represents the principal wave. In order to identify the global wave angle, the identified shock points are finally fitted with a linear fit, which is displayed in Fig. 14.

<sup>1</sup> eccentricity equal to 0 or to 1 corresponds to a circle or a line, respectively

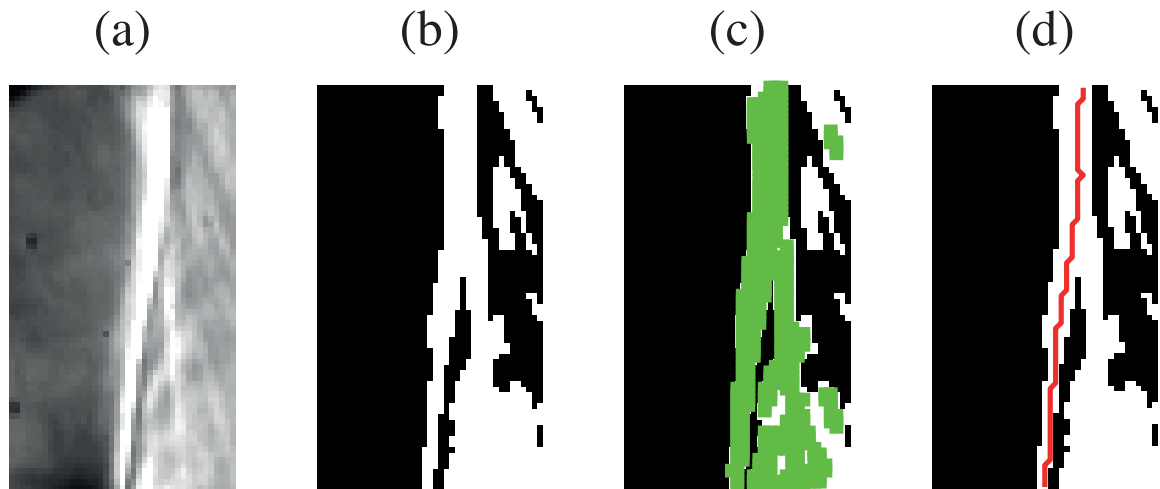


Fig. 13: Decision-making sequence on shock identification

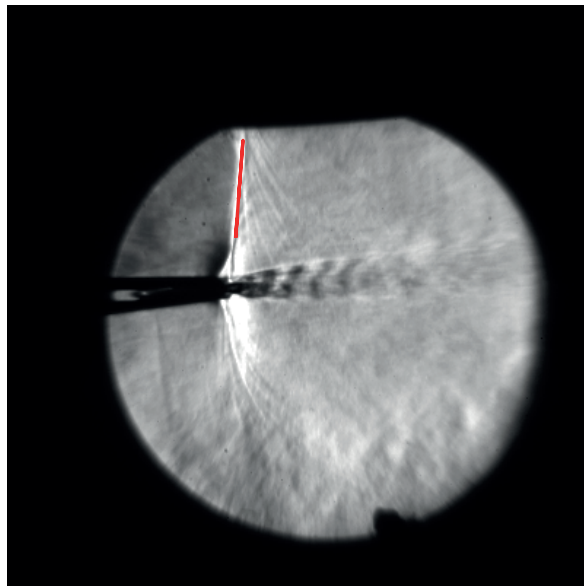


Fig. 14: Original image and shock wave fit

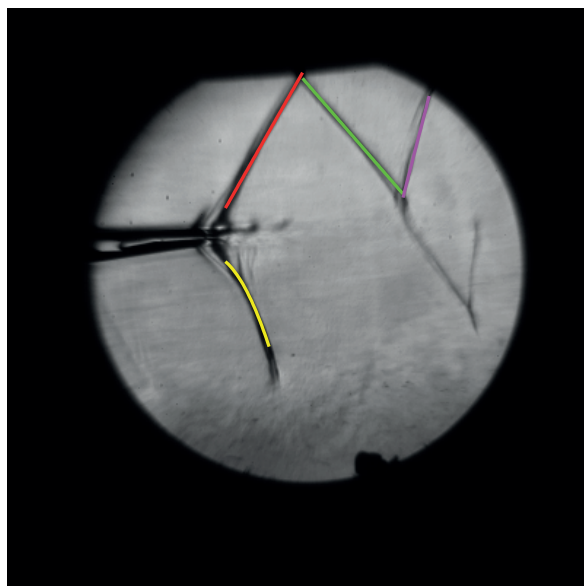
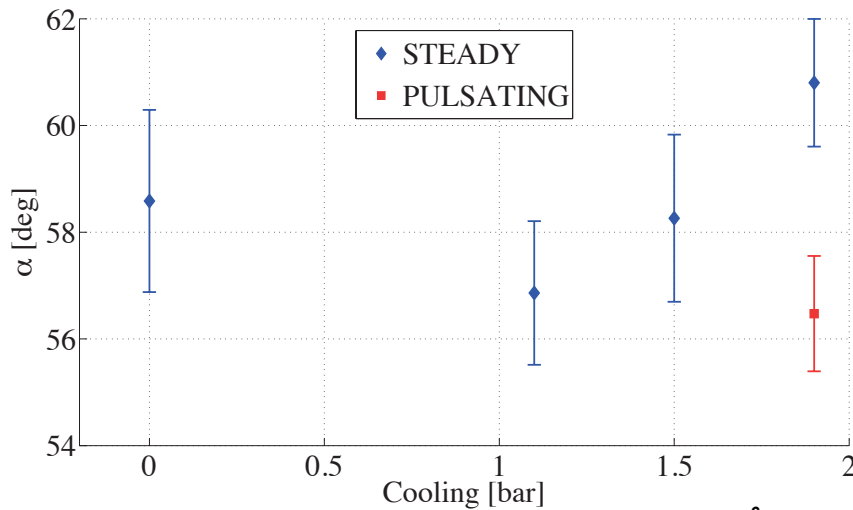


Fig. 15: Multiple waves identification

In case of multiple shock waves, the algorithm can also extract the information regarding shock-wall interaction and wave-wave intersection, storing the coordinates of these points for further analysis (Fig. 15). Per each wave segment, the program choses automatically the equation that fits the data best (linear, parabolic or cubic), plots it accordingly and saves the coefficients together with fit-structure.

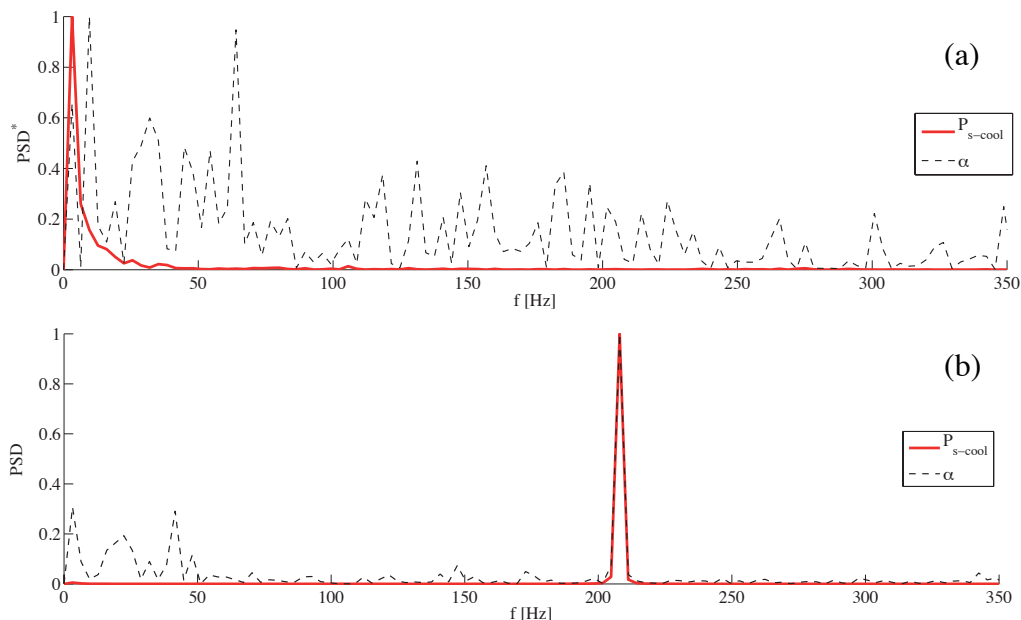
*Parametric study*

In Fig. 16 the average angle variation obtained by the Schlieren images analysis is presented together with the corresponding root mean square (RMS) for a Mach number  $Ma = 1.1$  and a Reynolds number  $Re = 6 \cdot 10^6$ . It is possible to see how steady cooling always reduces the angle fluctuations, but increases the mean shock inclination. Pulsating cooling, on the other hand, reduces both the angle average value and its fluctuations.



**Fig. 16: Schlieren results: average angle at Mach = 1.1 and  $Re = 6 \times 10^6$ . Error bar: RMS**

The time resolved data are also analysed in the frequency domain. From the comparison of the pressure sensor and the primary shock wave angle power spectra (Fig. 17) in case of no cooling (a), it appears that there is no correlation between the two spectra and that at relatively low frequency (i.e. below 350 Hz) the main peak observed is only indicating the signal frequency resolution. In case of pulsating cooling (b), it appears instead that the shock angle variation is in phase with the pulsating cooling (at about 208 Hz), demonstrating therefore that there is a direct connection between the cooling and the shock wave behaviour.



**Fig. 17: Power spectrum comparison: primary shock wave angle (--) and pressure sensor (-). No cooling (a) and pulsating cooling (b).**

## CONCLUSIONS

An original decision-making algorithm was developed to identify shock waves in complex Schlieren images, where reflections and bifurcations were making multiple paths selectable. The principal wave was found basing the search on the original image intensity and local orientation.

The processing of Schlieren pictures acquired at high frequency has been completed to understand the unsteady behavior of the fish tail shock waves that appear at the trailing edge in transonic and supersonic turbomachinery. From this work it was concluded that the coolant ejection results in a shock fluctuations lowering, being the highest reduction achieved with pulsating cooling. Furthermore, it was shown that the shock wave angle is fluttering at the same frequency of the coolant pulsation.

The use of the new decision-making algorithm proved therefore to be extremely effective in the shock wave identification, transforming a flow visualization into a measurement.

## ACKNOWLEDGEMENTS

The authors would like to acknowledge the financial support of U.S. Air Force under the frame of the Project AFOSR FA 8655-08-1-3033. The authors also wish to thank the support of Prof. Bosschaerts and Mr. Christoffels from the Royal Military Academy of Brussels, Belgium.

## REFERENCES

- [1] S. Djouimaa, L. Messaoudi, P.W. Giel, *Transonic turbine blade loading calculations using different turbulence models – effects of reflecting and non-reflecting boundary conditions*, Applied Thermal Engineering 27 (2007) 779-787
- [2] G. Paniagua, T. Yasa, A. de la Loma; L. Castillon, T. Coton, *Unsteady strong shock interactions in a transonic turbine: Experimental and numerical analysis*, Journal of propulsion and Power 24 (2008) 722-731
- [3] R.J. Volino, M.B. Ibrahim, *Separation control on high lift low-pressure turbine airfoils using pulsed vortex generator jets*, Applied Thermal Engineering (2011)
- [4] Paniagua G., Saracoglu B., Tomasoni F., Salvadori S., Miranda A., Martelli F., 2011, *Modulation of Vane Shocks with Pulsating Coolant Flows*. Proceedings of the 47th Joint Propulsion Conference. Paper AIAA-2011-5815. San Diego, USA. July.
- [5] Jones, T. V.; Shultz, D. L.; Hendley, A. D. (1973), *On the Flow in an Isentropic Free Piston Tunnel*, ARC R&M 3731, 1973
- [6] Shultz, D. L.; Jones, T. V.; Oldfield, M. L. G.; Daniels, L. C., (1978), A new transient facility for the measurement of heat transfer rates in *High Temperature Problems in Gas Turbine Engines*. AGARD CP 229, 1978
- [7] Saracoglu B. H., Huang G. P., Paniagua G., *Numerical Study of a Transonic Linear Cascade for Pulsating Trailing Edge Cooling Research*, 10th International Symposium on Experimental and Computational Aerothermodynamics of Internal Flows, Brussels, Belgium, July 2011
- [8] Gonzalez M., Paniagua G., Saracoglu B., Tiseira A., 2010, *Pulsating cooling system for high-pressure turbine blades*. Proceedings of the 5th AIAA Flow Control Conference. Chicago, USA. June.
- [9] G.S. Settles, *Schlieren and Shadowgraph Techniques: Visualizing Phenomena in Transparent Media*, Springer-Verlag, Berlin, 2001
- [10] Otsu, N., *A Threshold Selection Method from Gray-Level Histograms*, IEEE Transactions on Systems, Man, and Cybernetics, Vol. 9, No. 1, 1979, pp.62-66.
- [11] I. Bucher, *Circle fit*, Matlab Central File Exchange, 2004
- [12] Y Wu, M L Giger, K Doi, C J Vyborny, R A Schmidt, C.E.Metz. *Artificial neural networks in mammography: application to decision making in the diagnosis of breast cancer*. Radiology. 1993;187(1):81-87.
- [13] Mahmud, S.M.; Alrabady AI. *A new decision making algorithm for airbag control*. IEE transaction on Vehicular Technology. 1995;44(3):690-697.
- [14] Haralick, Robert M., and Linda G. Shapiro, Computer and Robot Vision, Volume I, Addison-Wesley, 1992, pp. 28-48.

## MEASUREMENT OF THE AERODYNAMICS IN THE PRIMARY ZONE OF A LOW-NO<sub>x</sub> COMBUSTOR AT ATMOSPHERIC AND ISOTHERMAL CONDITIONS

**Christian Faustmann,**

Graz University of Technology,  
Institute for Thermal  
Turbomachinery and  
Machine Dynamics  
Inffeldgasse 25A,  
8010 Graz - Austria

**Andreas Lang**

Andritz Hydro GmbH  
Dr. Karl-Widdmann-Straße 5,  
8160 Weiz - Austria

**Fabrice Giuliani**

Combustion Bay One  
Science Park Graz  
Plüddemangasse 39,  
8010 Graz - Austria

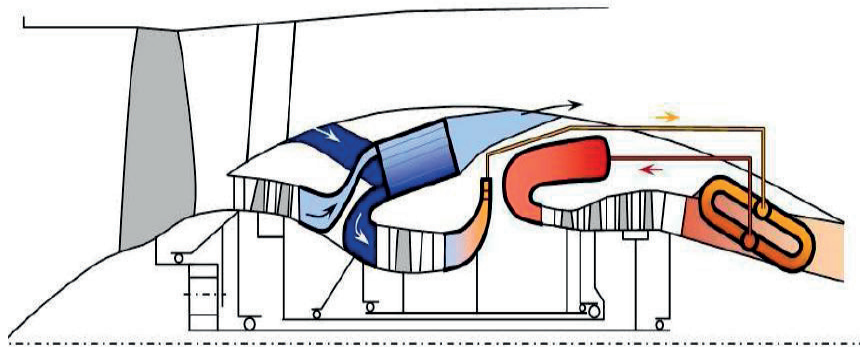
### ABSTRACT

The present paper would complete a lack of information on the aerodynamics of low-NO<sub>x</sub> combustors. The Lean-Premixed-Prevapourized (LPP) technology is theoretically well described, but not a lot of experimental results can be found in literature. In the present paper Laser Doppler Anemometry (LDA) measurements in a test rig modelling a sector of annular reverse flow type combustor chamber are presented. The facility consists of an assembly with two liquid fuelled, low- NO<sub>x</sub> industrial burners as well as a pilot burner. Each burner is separately fed. Three optical accesses allow the use of non-intrusive optical measurement techniques for a description of the primary combustor zone. This contribution refers to the preliminary characterization of the test section, which was already investigated at Graz University of Technology (TU Graz). Experiments were performed at atmospheric conditions without combustion in order to determine the flow dynamics inside the test section. Using a multi component LDA system in two perpendicular directions, the three dimensional flow field, consisting of the coincident mean velocities including most of the Reynolds stresses, was measured. The results show good agreement with what can be found in literature on the LPP technology, in particular no recirculation zone was found and the mean swirl number of  $S=0.32$  is also lower than the critical swirl number of 0.4.

### 1 INTRODUCTION

In the next 20 years Wilfert et al. [1] forecast the expansion rate of the global air traffic with 5% per year. To handle the growth of air pollution caused by this high level of growth in the air traffic, new aero core concepts have to be developed and validated. This research takes place in the NEWAC-Project founded by the European Union under the leadership of MTU Aero Engines. The targets of NEWAC are fully validated new technologies that will reduce CO<sub>2</sub> emissions by 6% and NO<sub>x</sub> by 16% [2]. The Institute of Thermal Turbomachinery and Machine Dynamics (TTM) at TU Graz is one of 40 partners in the NEWAC-program and is participating on subproject 6 (Innovative Combustion). The investigation is focused on the stability of combustion in a test sector combustion chamber equipped with LPP-modules. The combustor is part of the Intercooled Recuperative Aero Engine (IRA) shown in figure 1 and is of the reverse flow type. The test sector under investigation is a sector of this combustor and bends into a planar shape to ease the optical accessibility.

Limited information is available on the LPP-technology (Lean Premixed Prevapourized) in the open literature. Some basics can be found in [3]. More details on overall pressure ratio (OPR) and the risks of auto-ignition and flash-back are given in [1].



**Figure 1. Intercooled Recuperative Aero engine with NEWAC combustion chamber [1].**

Limited information is available on the LPP-technology (Lean Premixed Prevapourized) in the open literature. Some basics can be found in [3]. More details on overall pressure ratio (OPR) and the risks of auto-ignition and flash-back are given in [1].

The aerodynamic phenomena of the LPP-technology were investigated at ambient conditions without any flame. Therefore a test rig was built at the TU Graz, to measure the three velocity components in different planes at the LPP-modules. A 2D-LDA-System (Laser Doppler Anemometry) was used to get 3D information of the aerodynamics in the primary Zone of a Low- $\text{NO}_x$ -Combustor. Measuring data were processed with MathWorks MATLAB..

## 2 EXPERIMENTAL SETUP

The cold flow LDA-tests were performed on a test bench at the Institute for Thermal Turbomachinery and Machine Dynamics at TU Graz. The test rig is designed for the investigation of the cold flow at the combustor primary zone. The test rig itself consists of the following components:

- air supply
- air piping and manual pressure regulation valves
- mass flow meter
- seeding generator
- traversing system
- LDA-System

A separate air supply is used for each LPP-module. The mass flow is metered by V-Cones. The airflow was seeded with oil droplets (di-ethyl-hexyl-sebacat, DEHS), acting as a tracer for the LDA measurements. Each air supply was equipped with a dedicated seeding generator producing an aerosol with a specific particle size of  $0.3\mu\text{m}$ . A two component LDA (DANTEC Fiber-Flow with DANTEC Burst Spectrum Analyzer, DANTEC Dynamics, Roskilde Denmark) fed by an argon ion laser (Coherent Inc., Santa Clara, CA) with wavelengths  $\lambda_{\text{laser}} = 488 \text{ nm}$  and  $514.5 \text{ nm}$  was used. To obtain three dimensional information on the aerodynamics in the primary zone of each LPP-module data was acquired in three perpendicular planes as shown in Fig. 2. There the black circles represent exits of the LPP-modules and the black cube represents the combustion chamber. The x-z- and the x-y-planes are the horizontal and vertical planes located at the center of the LPP-module exits. The blue y-z-plane is located one diameter downstream of the LPP modules.

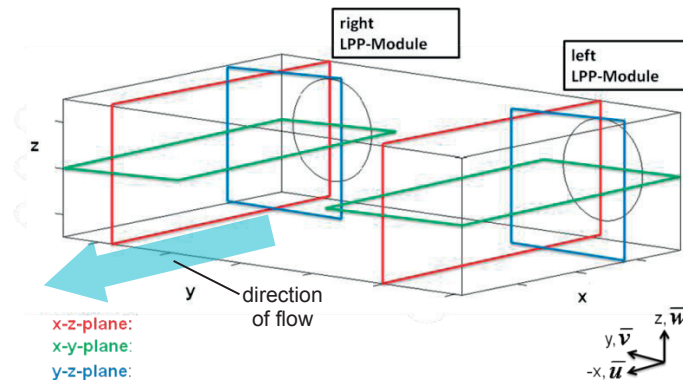


Figure 2. Measurements planes in respect to the LPP injector exits.

Due to the fact that an optical measurement technique is used, optical accessibility to the measurement volume is essential. Two windows frame the vertical sidewalls and a third window is installed at the bottom of the combustor. All windows are made of quartz glass, having a good characteristic concerning refraction of the laser beam. In addition the quartz glass is high temperature resistant, which is essential for tests reaching realistic combustor conditions that took place in the past and can be seen in [8].

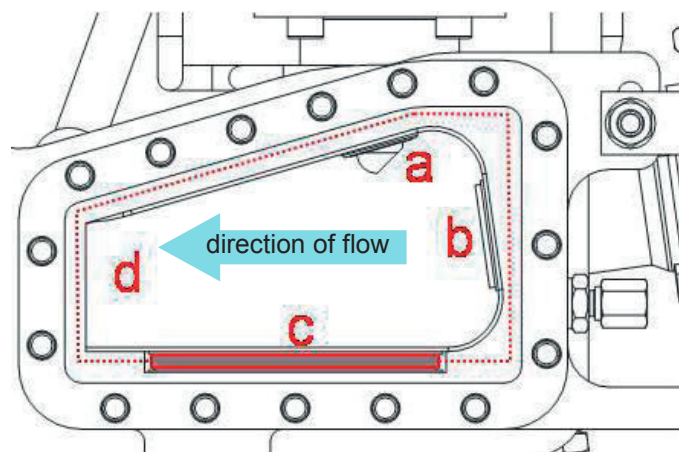
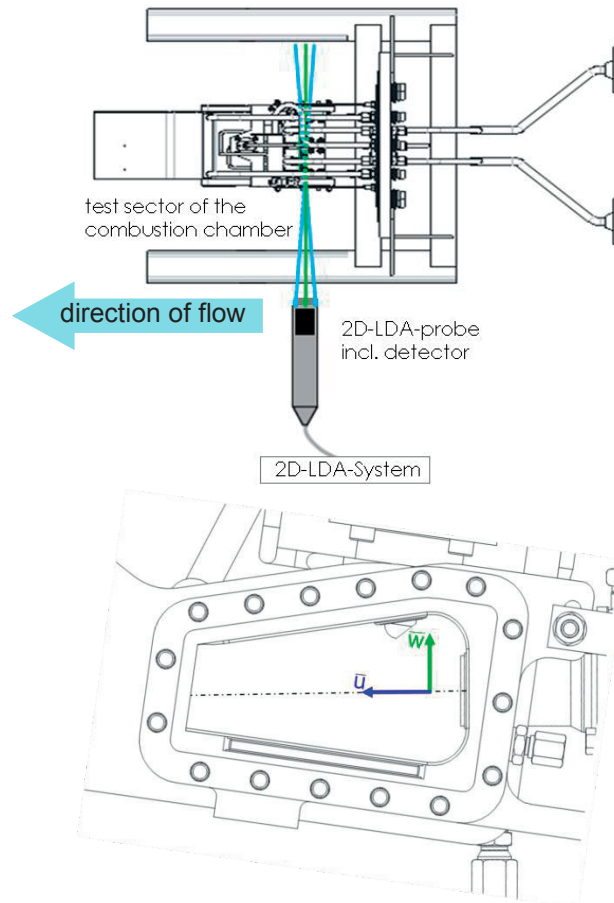


Figure 3. Lateral view of the combustor.

Fig. 3 shows the combustor in a lateral view, where label *a* shows the position of the pilot burner, *b* represents the exit of a LPP-module and the captions *c* and *d* represent the optical accesses on the side walls (dotted line) and bottom.

Besides the three optical accesses two different setups are needed to get a 3D-characteristic of the flow in the combustor with a 2D-LDA-System. Positioning of the optical head was done in both setups with a DANTEC lightweight traverse where the LDA probe was fixed perpendicular to the respective side windows and operated in backscatter mode. The two setups named A and B are shown in Figs. 4 (A) and 5 (B). For ease of operation the change between the setups is achieved by rotating the combustor by 90° such that the respective window was aligned with the LDA probe. In Fig. 4 setup A is shown where the axial and tangential component of velocity and the  $\overline{u^2}$ ,  $\overline{w^2}$ ,  $\overline{u'w'}$  components of the Reynolds tensor can be measured. In Fig. 5, setup B, the axial and the radial components of velocity and the  $\overline{u^2}$ ,  $\overline{v^2}$ ,  $\overline{u'v'}$  correlations are measured. To provide the data with respect to the individual LPP module axis, coordinate transformation was used. A particular problem with seeded flow is the deposition of the seeding on the windows which deteriorates the data rate. Using the DEHS seeding the problem could be overcome by heating the diagnostic window with hot air, such that the seeding evaporated keeping the windows clear.





**Figure 4. Measurement setup A; top: top view of setup, bottom: measured velocities  $\bar{u}$  and  $\bar{w}$  with setup A.**

In addition to the three mean velocities  $\bar{u}$ ,  $\bar{v}$  and  $\bar{w}$  the fluctuations of the measured data can be analyzed. Furthermore the turbulent kinetic energy and the swirl number are evaluated. Each measured data is weighted by the transit time  $\Delta t$ . That is the time a tracer particle needs to pass the measurement volume that is formed by the crossing laser beams [4]. For statistical analysis it is of importance to perform a weighting of the velocities with the transit time, because faster tracer particles are statistically overrepresented as slower ones. Thus weighting with the transit time comes up with a balancing of the faster and the slower tracer particles

Eq. 1-3 show the mathematical formalism for the weighting of the mean velocity, the variance –also known as the velocity fluctuation– and the correlations of the velocity fluctuations respectively. Table 1 shows which quantities can be computed.

$$\bar{u}_i = \frac{\sum_{k=1}^N u_{i,k} \Delta t_k}{\sum_{k=1}^N \Delta t_k}$$

**Eq. 1**

$$\overline{u_i'^2} = \frac{\sum_{k=1}^N (u_{i,k} - \bar{u}_i)^2 \Delta t_k}{\sum_{k=1}^N \Delta t_k}$$

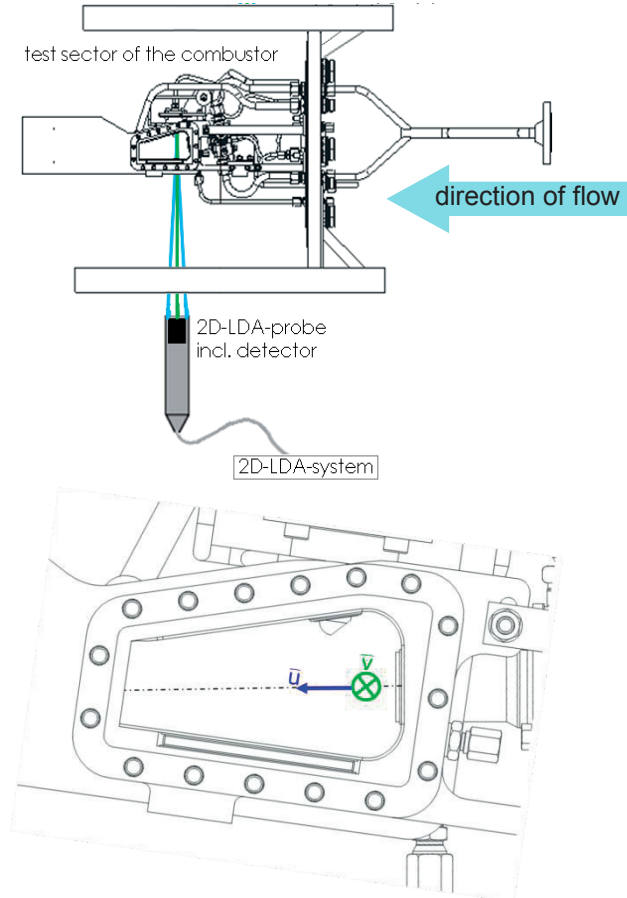
**Eq. 2**

$$\overline{u_i' u_j'} = \frac{\sum_{k=1}^N (u_{i,k} - \bar{u}_i)(u_{j,k} - \bar{u}_j) \Delta t_k}{\sum_{k=1}^N \Delta t_k}$$

**Eq. 3**

Multiplying Eq. 2 and Eq. 3 with the density will lead to the Reynolds' stress tensor. The entries on the principal diagonal are the normal stresses in the respective direction whereas the off-diagonal elements represent the shear stresses.

$$T_t = -\rho \begin{pmatrix} \overline{u'^2} & \overline{u'v'} & \overline{u'w'} \\ \overline{v'u'} & \overline{v'^2} & \overline{v'w'} \\ \overline{w'u'} & \overline{w'v'} & \overline{w'^2} \end{pmatrix} \quad \text{Eq. 4}$$



**Figure 5. Measurement setup B; top: top view of setup, bottom: measured velocities  $\bar{u}$  and  $\bar{w}$  with setup B.**

Furthermore for the characterization of the aerodynamics in the primary zone, the turbulent kinetic energy and the swirl number are of importance.

Assuming isentropic turbulence, Eq. 5 changes into Eq. 6. This assumption was made by reason that it is not possible to measure the diagonal elements of Eq. 4 at the same time with a two component LDA system. But one has to know that this assumption is not valid for every measurement point in the flow field.

$$k = \frac{1}{2} (\overline{u'^2} + \overline{v'^2} + \overline{w'^2}) \quad \text{Eq. 5}$$

$$k = \frac{3}{4} (\overline{u'^2} + \overline{v'^2}) \quad \text{Eq. 6}$$

The swirl number is determined in accordance with Beer and Chigier [5] and adjusted to the present problem:

- atmospheric conditions
- rotationally symmetric
- constant density / incompressibility

The equation of Beer and Chigier will thus be turned into Eq. 7 (expression for x-y-plane).

$$S = \frac{2 \sum_0^{y_{max}} \bar{w} \bar{u} y^2 \Delta y}{D \sum_0^{y_{max}} \bar{u}^2 y \Delta y}$$

Eq. 7

### 3 LDA-PARAMETERS AND TEST CONDITIONS

As shown in Fig. 2 measurements were performed at three different planes per LPP-module. In each plane simultaneous recording of two velocities with a 2D-LDA-System is possible. By measuring with setup A and B a resultant vector out of the three velocity components can be computed. The record length was set to 20,000 samples or a measurement time of 100 seconds. With this setup the turbulence in respect to measurement effort is well enough determined.

The measurements of the aerodynamics in the primary zone of a Low-NO<sub>x</sub> combustor took place at atmospheric and isothermal conditions. The operating conditions were set in accordance with Turbomeca to a reduced air flow representing *take off* conditions ( $\dot{m}_{red} = 0.25 \frac{kg}{s} \frac{\sqrt{k}}{100kPa}$ ).

Table 1. LDA-Parameters

LDA-PARAMETERS		
Number of data points in plane	Averaged data rate	Analyzed quantities
x-z-plane ~180	~250Hz	$\bar{u}, \bar{w}, \frac{TKE_{in}}{u'^2, w'^2, u'w'}$
x-y-plane ~210	~250Hz	$\bar{u}, \bar{v}, \bar{w}, \frac{TKE_{in}}{u'^2, v'^2, w'^2, u'v'}, \frac{TKE_{in}}{u'w'}$
y-z-plane ~150	~100Hz	$\bar{u}, \bar{v}, \bar{w}, \frac{TKE_{in}}{u'^2, v'^2, w'^2, u'v'}, \frac{TKE_{in}}{u'w'}$

### 4 RESULTS

All results shown are non dimensional. Velocities are divided by a reference velocity  $u_0$  (calculated with help of the continuity equation, applied at the premixing tube of the LPP module; Eq. 8 and 9). All dimensions are divided by the diameter of the premixing tube  $D$  (Eq.10).

$$u_0 = \frac{4 \cdot \dot{m} \cdot R \cdot T}{p \cdot D^2 \cdot \pi}$$

Eq. 8

$$u = \frac{\bar{u}}{u_0}$$

Eq. 9

$$l = \frac{\bar{l}}{l_0}$$

Eq. 10

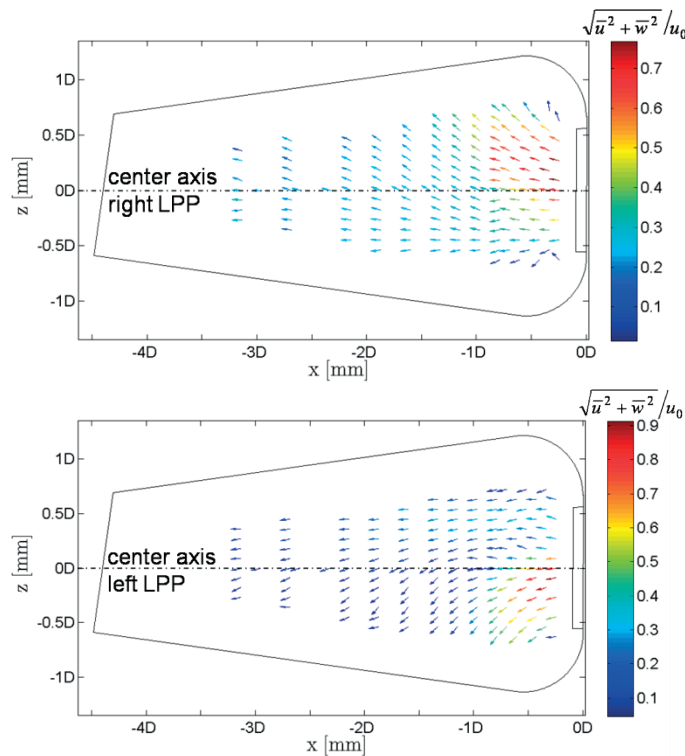
Velocity plots will be shown for both LPP-modules, the velocity fluctuations will be shown at the right LPP-module in the x-y-plane only, although Table 1 indicates that an analysis for both LPP-modules has been performed in each plane.

Fig. 6 shows the velocity plots in the x-z-plane at the right (Fig. 6 top) and left (Fig. 6 bottom) LPP-module. The black rectangle on the right side of the figure sketches the premixing tube of a LPP-module. The liner contours are shown as solid black lines. A vector of mean velocity is plotted at each location where a measurement has been

performed. To reduce measurement effort the grid is spaced fine at the combustor inlet and coarser at the outlet. For the contour plots interpolations with MATLAB's *cubic* and *v4* method were used.

Both plots in Fig. 6 show that no recirculation zone at the center axes of the burners exists. This indicates that the axial impulse in direction to the combustor exit is stronger than the static pressure inside the flow. Fig. 6 further shows an asymmetric flow field of the two LPP-modules. The fluid injected by the right LPP-module tends to flow upwards (maxima of velocity above the center axis) whereas the fluid of the left one flows downwards (maxima of velocity below the center axis). Above the centerline of the right LPP-module and below the center axis of the left LPP-module the flow is nearly axial. The same conditions can be found at the combustor exit. The flow field downstream of the injector is constantly decelerating.

Furthermore the direction of the vectors next to the edges of the combustor indicates the existence of edge vortices. Because of the outer contour of the test sector this area couldn't be measured more detailed without changing the experimental setup, so no detailed investigation of this area has been done.

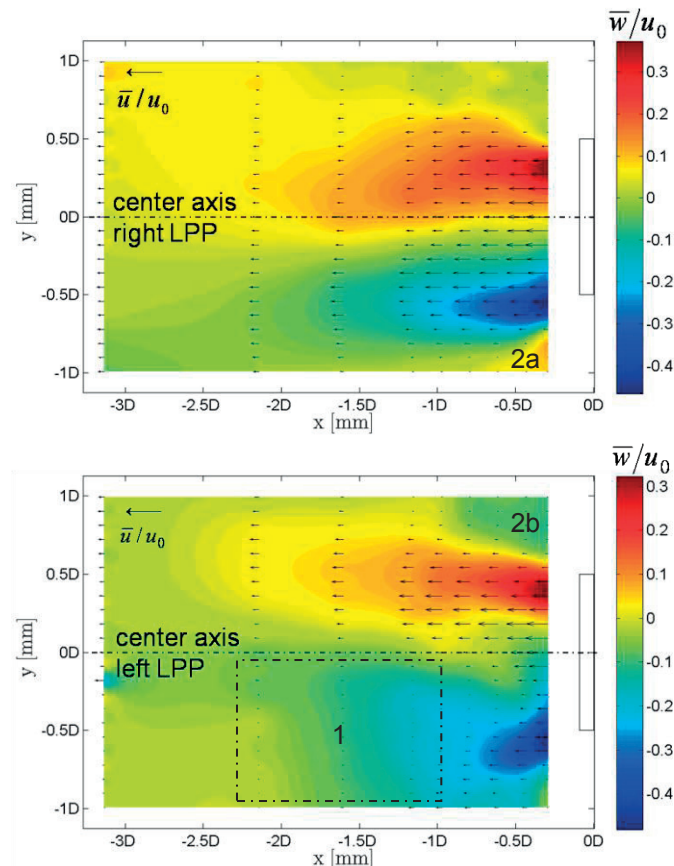


**Figure 6. Absolute velocity plots from the LDA-measurements in the x-z-plane at the right (top) and left (bottom) LPP-module.**

Fig. 7 shows velocity plots at the right and left LPP-module for the x-y plane. Measurements were done at the center axis ( $z/D=0$ ) with a radial expansion of  $1D$  and nearly  $3D$  in axial direction. The axial velocity  $u$  is represented by black vectors and the out of plane component  $w$  as colormap. Like in Fig. 6 the premixing tube of the LPP-modules is sketched as a black rectangle on the right side of both plots. No recirculation zone in the x-y-plane can be found. Below the center axis of the left LPP module (Fig. 7 bottom, labeled as zone I) the flow is drastically decelerating. This can also be found, less pronounced, at the right LPP (Fig. 7 top) above its center axis. However, it can be seen when looking at cross section  $x/D=-1$  that the flow field below the center axis of the left LPP is similar to the one above the center axis of the right one. The axial velocity reaches its maximum near the center of the combustor axis (*LPP right*:  $y/D=-0.5$  ; *LPP left*:  $y/D=0.3$ ) and decelerates towards the combustor walls.

At both LPP-modules the out of plane velocity is in the same order of magnitude. It reaches its maximum near the outlet of the premixing tubes (located at  $x/D=-0.25$ ,  $y/D=\pm 0.5$ ) and slows down towards the combustor exit. This indicates a loss of angular momentum of the swirling flow. The mass flow is rotating anti clock wise at both LPP modules when looking in flow direction. Also of interest in Fig. 7 are the areas labeled with  $2a$  and  $2b$ . These

regions are indicating a third vortex like structure existing between the two swirling flows induced by the LPP modules, which is also rotating anti clock wise. Furthermore there must be some smaller counter rotating vortices due to the balance of angular momentum, which were not detected with this resolution of measurement points.



**Figure 7. Velocity plots from the LDA-measurements in the x-y-plane at the right (top) and the left (bottom) LPP-module; axial velocity shown as vectors, tangential velocity as background color.**

The analysis of the 2D-results is completed with the calculation of velocity fluctuations in the x-y-plane of the right LPP-module. Fig. 8a-d show beside the axial  $\sqrt{\overline{u'^2}}$  and tangential Root Mean Square (RMS) value  $\sqrt{\overline{w'^2}}$  the shear stress  $\overline{u'w'}$  as well as the turbulent kinetic energy  $k_e$ .

Fig. 8 a shows that three regions of higher axial RMS values are developed at  $x/D=-0.25$ . A steep gradient exists at  $y/D=\pm 0.5$  (labeled with 1 and 3 in Fig. 8a). The maximum of the axial RMS value is detected at the center axis next to  $x/D=-0.75$  (label 2). From  $x/D=-1$  to  $x/D=-2$  the three regions (label 1 to 3) are forming a single large area of high level axial RMS value which is nearly expanded to the hole width of the measurement plane. Behind this line the axial RMS value decreases constantly.

Three regions of higher tangential RMS values  $\sqrt{\overline{w'^2}}$  are visible in Fig. 8 b). The regions are formed at the end of the premixing tube. The fluctuation of the third velocity component has its maximum at  $x/D=-0.25$ ,  $y/D=-0.75$  and spreads up to  $y/D=-2$ . In comparison with  $\sqrt{\overline{u'^2}}$ , the high level of tangential RMS values  $\sqrt{\overline{w'^2}}$  of the flow is centered at smaller regions. Fig. 8 c) shows the distribution of the shear stress  $\overline{u'w'}$ . Four areas of high level of shear stress are noticeable. The shear stress in Area 1 and 3 is negative whereas area 2 and 4 are showing a positive shear stress. The maxima are located at area 1 (positive) and 4 (negative) respectively. In these regions of high shear stress not perfectly prevaporized fuel droplets will be ruptured into smaller droplets and vaporized at high temperatures.

In the last plot of Fig. 8 the distribution of the turbulent kinetic energy  $k_e$  (TKE) is shown. Its distribution is similar to the distribution of the normal RMS values  $\sqrt{\overline{u'^2}}$ . Three main regions with high TKE, surrounded by an intermediate level of TKE exist. The maximum itself is located at the center axis next to  $x/D=-1$ . Furthermore

the minimum of  $k_e$  is at the same position as the minimum of both RMS values in the upper right edge of the measurement plane. In Fig. 8 d) it can be seen that the production of turbulence depends on the axial velocity component mainly and area 2 is where the biggest amount of energy dissipates.

Dividing the turbulent kinetic energy by the axial component of the mean velocity gives the intensity of turbulence, reaching a maximum of 26%.

As said before two setups were used in combination with a 2D LDA system. As a consequence a three dimensional analysis of the flow field can be done for distinctive points in the measurement volume of the combustor. The results are shown in the x-y-plane in Fig. 9. The absolute velocity in the x-y-plane  $\sqrt{u^2 + w^2}$  was computed by using measurements from setup B. The out of plane velocity component  $w$  was derived from setup A. Thus the colored contour plots of  $w$  are qualitatively the same as shown in Fig. 7 but with different color axis.

Furthermore the measurable area in setup B is smaller than in setup A (compare Fig. 37 and Fig. 9), so that the effective vector plot of absolute velocity in Fig. 9 is smaller than the colored contour plot representing the out of plane velocity. However by using the available data an expansion of the jet can clearly be seen. At  $x/D=-1$  it is computed with 10 degrees to the center axis (labeled with 1 in Fig. 9).

In region 2 the axial component is dominating the flow direction. At the center of the combustor (area 3) the flow is decelerated to quasi zero. Velocities below a certain threshold (given by the manufacturer) or even a back flow should be avoided to prevent flashback into the injection modules.

The flow field behind  $x/D=-2$  seems to be very turbulent because no direction of flow is dominant.

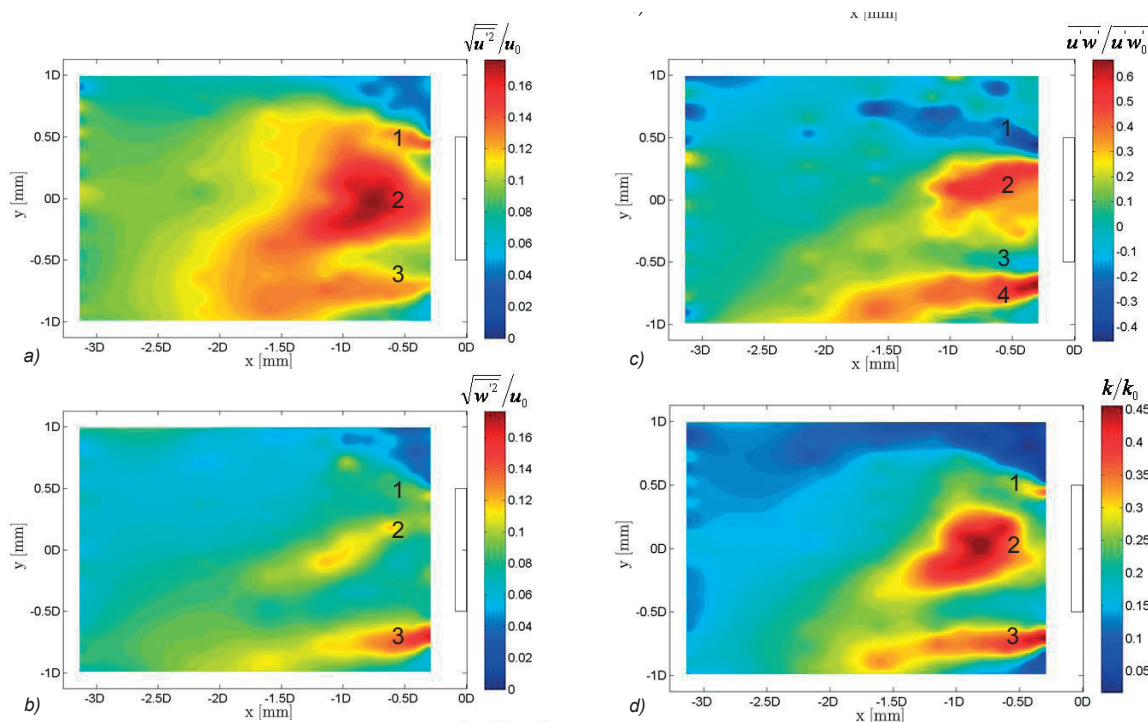


Figure 8. Colored contour plots of the distribution of a) axial RMS value  $\sqrt{u^2}$ , b) tangential RMS value  $\sqrt{w^2}$ , c) shear stress  $u'w'$  and d) turbulent kinetic energy  $k_e$

The calculation of the swirl number is given in Eq. 7 and is an indicator of a reverse flow in a swirling jet. If the swirl number exceeds a value of 0.4 the flow on the center axis begins to stream backwards and forms a recirculation zone [6]. Overall eight swirl numbers, at distance  $x/D=-1$  downstream the injectors were computed in the x-y- and x-z-measurement plane. A mean of these eight values results in an averaged swirl number of  $S=0.32$ . This calculation confirms the results of the vector plot that no flow is recirculated in the primary combustion zone.

## 5 CONCLUSION AND OUTLOOK

A set of LDA-measurements were performed to characterize the aerodynamics in the primary zone of a Low- $\text{NO}_x$ -combustor at ambient conditions. By using two different experimental setups, three dimensional information of the flow field in the combustor could be gathered. Measurements were performed in three different planes per LPP-module. The results of the Laser-Doppler-Anemometry are in accordance with the information which can be found in the literature about the technology of LPP-combustion, meaning that no recirculation zone was found and the mean swirl number of  $S=0.32$  is also lower than the characteristically critical swirl number of 0.4. Forming a recirculation zone should be avoided because of the danger of flashback for this type of injector.

Furthermore an asymmetry of the flow in the x-z-plane was found.

The analysis of the flow field also showed the presence of two main vortices (one at each LPP-module) and a smaller vortex between the two burners (Fig. 7 areas 2a and 2b). All three vortices rotate in the same direction, clock wise when looking upstream (Fig. 10). This phenomenon can also be seen in the y-z-plane which is located at a distance of  $x/D=-1$  to the front wall of the combustor but is not part of the result presented.

In addition a widening of the jet of approximately 10 degrees at the exit of the LPP-modules was computed.

As the test sector is designed for operation at reactive conditions at elevated pressures and temperatures further research especially in terms of combustion stability will be performed in the future at the Institute for Thermal Turbomachinery and Machine Dynamics (TTM) at Graz University of Technology. The robustness of the combustion is investigated at steady-state operating condition as well as when being perturbed by a modulation on the air or on the fuel supply. For forced excitation of the air flow the reader is referred to [7] for a detailed description of the new type of flow exciter used.

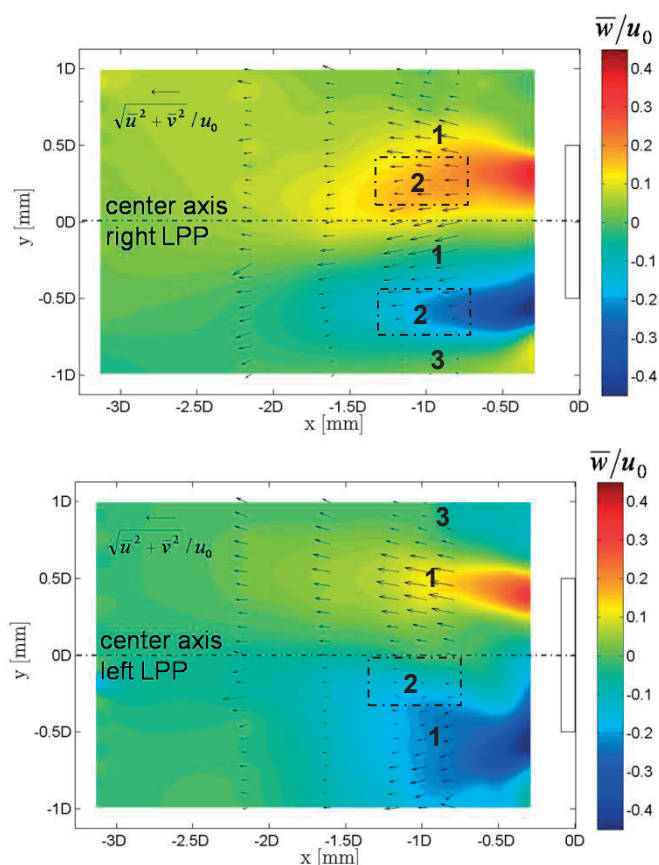


Figure 9. Velocity plot of LDA-measurement by combining measurements of setup A and B (3D flow field); top: right LPP-module, bottom: left LPP-module.

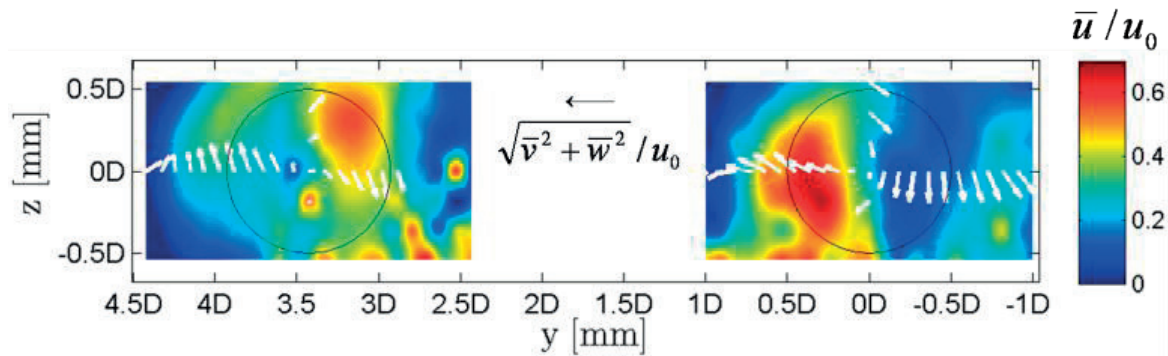


Figure 10. Velocity plot from LDA-measurement with setup B in the y-z-plane at  $x/D=-1$ , when looking against the flow direction.

## NOMENCLATURE

NEWAC	New Aero Engine Core Concepts
TTM	Institute for Thermal Turbomachinery and Machine Dynamics of Graz University of Technology
TU	Graz Graz University of Technology
LPP	Lean Premixed Prevaporized
IRA	Intercooled Recuperative Aero engine
OPR	Overall Pressure Ratio
LDA	Laser Doppler Anemometry
S	Swirl number
RMS	Root mean square

## ACKNOWLEDGMENTS

The test rig at TU Graz was supported by the European Commission as part of the Integrated Project "New Aero Engine Core Concepts" (NEWAC, AIP5-CT-2006-030876), which is gratefully acknowledged.

## REFERENCES

- [1] Wilfert G., Sieber J., Rolt A., Baker N., Touyeras A., Colantuoni S., "New Environmental Friendly Aero Engine Core Concepts", ISABE-2007-1120, 2007
- [2] Bock S., Horn W., Wilfert G., Sieber J., "Active Technology within the NEWAC Research Program for cleaner and more efficient Aero engines", CEAS-2007-1235, 2007
- [3] Joos F., "Technische Verbrennung", 1. Auflage, Springer, 2006
- [4] Ruck B., „Lasermethoden in der Strömungsmess-technik“, 1. Auflage, AT-Fachverlag GmbH Stuttgart, 1990
- [5] Beer J.M., Chigier N.H., "Combustion Aerodynamics", Applied Science, London, 1972
- [6] Lefebvre A.H., "Gas Turbine Combustion", 2nd Edition, Taylor & Francis Group New York, 1999
- [7] Giuliani F., Lang A., Gradl K., Siebenhofer P., "Flow modulation for refined control of the combustion dynamics using a novel actuator", ASME Conf. Proc. 2011, GT-2011-4507
- [8] Lang A, Unsteady Combustion Phenomena in Current and Future Aero Engines, Phd Thesis, Graz, 2011





# CHARACTERIZATION OF A HIGH SUBSONIC WIND TUNNEL TEST SECTION TO DEVELOP A STUDY APPROACH TO SOLVE THE INVERSE HEAT CONDUCTION PROBLEM

Ir. F. Baldani\* , Ir. Dr. Prof. W. Bosschaerts , Ing. R. Wagemakers  
 Royal Military School of Belgium  
 30 Avenue de la Renaissance, 1000 Brussels, Belgium

\*Corresponding author: francesco.baldani@rma.ac.be.

## ABSTRACT

Aim of the project is to propose a methodology to retrieve the heat flux through a finned heat exchanger placed downstream the fan of a turbine jet engine. The core of the Ph.D. study is the solution of the so called Inverse Heat Conduction Problem (IHCP). To solve the IHCP the surface temperature of the heat conducting body has to be used as boundary condition of the problem. The Infra Red thermography is used to measure the heat exchanger surface temperature. The experiments are performed at low speed and at high subsonic speed. These latter are performed in a blow-down wind tunnel capable to reach Mach numbers of the order of 0.75. The flow field in the blow-down wind tunnel test section is characterized exploiting the Constant Temperature Anemometry (C.T.A.) technique. To be able to perform multi-point measurements an 'ad-hoc' hot-wire probes support has been conceived and manufactured.

**Keywords:** Inverse Heat Conduction Problem, High Subsonic Speed, Infra Red Thermography, Constant Temperature Anemometry, hot-wire probes support

## 1 INTRODUCTION

The improvements in the manufacturing techniques as well as in the available materials push the aerothermal engineers to find better solutions in order to improve engine performances. Indeed, improving turbine engine performances for military and civil purposes has a deep impact on thermal efficiency, fuel consumption, life-time and consequently on the achievement of the working standards required by the new laws in matter of environment such as noise and pollutant emissions. Aim of the project is to study the heat transfer from a hot surface to a cold flow under conditions similar to those encountered by aircraft turbine engines, hence using the main flow of the engine to study a heat exchanger placed just downstream the fan. The main part of the research project deals with the solution of the "inverse heat conduction problem" which consists in imposing the object surface temperature as boundary condition and computing via numerical methods the resulting heat flux. The heat transfer coefficient is to be studied both locally and globally, since a global study of  $h$  is fundamental in the preliminary design phase while a local study of  $h$  is useful to understand the effects of the geometry on the local flow conditions (i.e. the turbulence intensity level) and on the achievable heat exchange. We should remind that in a forced convection the flow is influenced by the amount of heat injected and that the flow rate versus the heat power injected is one of the major triggers for the flow that develops. On top of this the conduction within the plate adds up with the heat convection from the surface.

It should also be clear that to deepen the understanding of the heat transfer occurring in installations as finned heat exchangers one has always to consider that a simple superposition of the heat exchange phenomena is not enough. Indeed one should rather talk of "conjugate" heat transfer this latter being the actual coupled interaction of conduction and convection. For instance neglecting the effect of the wall conduction which greatly affects the

temperature distribution will result in imposing unrealistic thermal boundary conditions at the solid-fluid interface leading to wrong heat transfer rates and coefficients.

For all these reasons the characterization of the wind tunnel test section flow field is a crucial issue. This is why the C.T.A. technique is chosen to characterize the flow field obtainable in the wind tunnel. The scheme in Figure 1 shows and summarizes the approach proposed to study the problem under analysis.

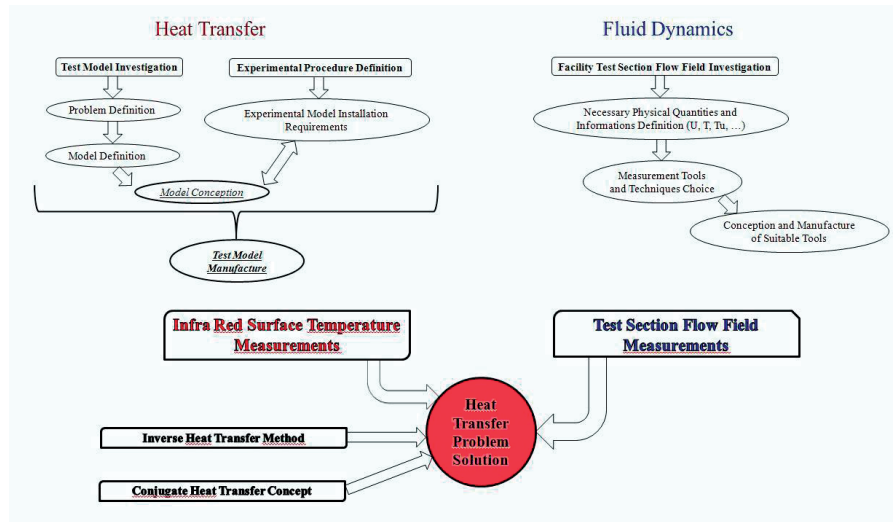


Figure 1. Proposed Study Approach.

## 1 CONJUGATE HEAT TRANSFER CONCEPT

Since the studies conducted by Perelman[16] it is well known the importance of imposing correct boundary conditions when dealing with heat transfer problems involving a solid submerged in a flowing fluid. Indeed it is proven that in presence of large thermal gradient (in space) and if the fluid encounters obstacles (rib, fin, etc..) the thermal boundary conditions imposed (uniform  $T_{surf}$ , uniform heat flux) in the classical study (purely convective) are unrealistic. For this it is of crucial importance impose the correct boundary conditions at the solid-fluid interface. Therefore the conjugate heat transfer theory is the one to be used, being based on the concept that the effects of the solid domain conduction have to be coupled with the convection phenomenon happening over the solid surface. The idea is to perform surface temperature measurements of the finned heat exchanger under analysis with the I.R. thermography technique after having characterized the wind tunnel test section flow field exploiting the C.T.A. technique and/or the P.I.V. technique in order to be able to impose the correct boundary conditions for computing the surface heat flux distribution (via commercial FEM solvers or as proposed hereafter via a numerical solution of the so obtained Inverse Heat Conduction Problem)[10, 12, 15].

Furthermore for the characterization of the aerodynamics in the primary zone, the turbulent kinetic energy and the swirl number are of importance.

Assuming isentropic turbulence, Eq. 5 changes into Eq. 6. This assumption was made by reason that it is not possible to measure the diagonal elements of Eq. 4 at the same time with a two component LDA system. But one has to know that this assumption is not valid for every measurement point in the flow field.

The swirl number is determined in accordance with Beer and Chigier [5] and adjusted to the present problem:

- atmospheric conditions
- rotationally symmetric
- constant density / incompressibility

## 2 TRANSIENT INVERSE HEAT CONDUCTION PROBLEM

Determining local convection coefficients accurately or perform accurate local heat flux measurements is a hard and expensive task but for many cases the heat flux distribution is an indispensable parameter. For finned heat exchangers this task is particularly challenging [9, 11, 19]. Indeed heat transfer measurements at the fin base would introduce a thermal resistance between the primary surface and the fin due to the presence of the measurement device. Therefore the heat fluxes at the fin base have to be determined indirectly by measuring the heat fluxes through the extended surface and the primary surface. Among the available techniques to perform such measurements (heat flux sensors, local temperature measurements) the inverse heat conduction technique is probably the most suitable for our study. It is mainly used to estimate temperatures or heat fluxes at surfaces that are inaccessible for measurements. The advantage of this method is that the experimental studies can be performed under similar conditions and environment as during the operation. To solve an inverse heat conduction problem, a mathematical optimization method is required, which uses temperature measurements as input. Based on surface temperatures of a solid object, heat fluxes on one or more surfaces of the object can be estimated. So the need for internal temperature measurements can be omitted. Depending on the temperature measurement technique, the disturbance of the local temperature fields and heat flux distribution is limited or even absent. It also has the advantage that the temperature field in the whole object can be reconstructed based on surface temperature measurements, together with the coupled heat flux distribution. The proposed code allows the determination of the local convective heat exchange coefficient  $h(x,y,t)$ , taking into account for the conductive flux in the heated plate. In general the heat flux can rise and fall abruptly and can be both positive and negative where negative values indicate heat losses from the surface. According to Beck, Blackwell and St.Clair [6] the source of heating is immaterial to the IHCP procedures. Mathematically the IHCP (for the 1-D case) can be described as in the set of equations 1 to 4.

$$\frac{\partial}{\partial x} \left( k \frac{\partial T}{\partial x} \right) = \rho c \frac{\partial T}{\partial t}$$

Eq. 1

Where the thermal conductivity  $k$ , the density  $\rho$  and the specific heat  $c$  are postulated to be known functions of temperature.

$$T(x, 0) = T_0(x) \quad \frac{\partial T}{\partial x} = 0 \text{ at } x = L \quad T(x_1, t_i) = Y_i$$

Eq. 2

Eq. 3

Eq. 4

The objective is to estimate the surface heat flux at discrete times,  $t_p$ , from

$$q(t_i) = -k \left. \frac{\partial T(x, t_i)}{\partial x} \right|_{x=0}$$

Eq. 5

After the paper by Beck, Blackwell and Haji-Sheikh [5] where can be found a review of some inverse heat conduction methods the method chosen to solve the IHCP is the so called 'function specification method' (FSM). The FSM has the advantage to be simple in concept and to not change the physics of the problem since the intrinsic parabolic nature of the problem is unchanged. The FSM is sequential in nature and thus computationally efficient and moreover the measurements in the distant future do not affect the 'present' estimates as for other methods [5]. The FSM can be used for linear and nonlinear problems and finite differences, finite elements or numerical convolution can be used. The method itself consists in minimizing, with respect to the heat flux  $q_M$  the sum of squares function as described by Eq. 6[5]. The equations 6 to 11 refer to measurements acquired by one sensor over multiple time steps.

$$S_M = \sum_{i=1}^r = (Y_{M+i-1} - T_{M+i-1})^2$$

**Eq. 6**

which involves the times  $t_M, t_{M+1}, \dots, t_{M+r-1}$ . Hence 'future' information is used to obtain  $q_M$ . Some functional form for  $q(t)$  for  $t_M$  to  $t_{M+r-1}$  is selected, the simplest being

$$q_{M+1} = q_M, \quad i = 1, 2, \dots, r$$

**Eq. 7**

The calculated temperature  $T_{M+i}$ , is expanded in a Taylor series for  $q_M$  obtaining

$$T_{M+i-1} = T_{M+i-1}|_{\hat{q}_M} + X_{M+i-1,M} (q_M - \hat{q}_M)$$

**Eq. 8**

where  $X_{M+i-1,M}$  is the sensitivity coefficient defined by

$$X_{M+i-1,M} = \frac{\partial T_{M+i-1,M}}{\partial q_M}$$

**Eq. 9**

the resulting algorithm after minimizing Eq. 6 with respect to  $q_M$  is

$$\hat{q}_M = \hat{q}_{M-1} + \frac{\sum_{i=1}^r [Y_{M+i-1} - T_{M+i-1}|_{q_M=\dots=\hat{q}_M}] X_{M+i-1,M}}{\sum_{i=1}^r X_{M+i-1,M}^2}$$

**Eq. 10**

Only  $\hat{q}_M$  is retained for time  $t_M$  and  $M$  is increased by one and the procedure is repeated. The iterative regularization method minimizes the whole domain function

$$S_M = \sum_{i=1}^I = (Y_i - T_i)^2$$

**Eq. 11**

where  $I$  is the total number of measurements. It should be noticed that in our analysis we use multiple sensors (i.e. surface temperature cartography  $T(x, y, t)$  measured by the I.R. camera). Anyway this does not affect the exposed solution methodology but just the mathematical formalism.

## 2.1 IHCP Solution Validation

One can validate the proposed solution methodology for a flat plate of very thin thickness in a laminar flow. The validity of the proposed solution can be checked solving twice the direct model via a CFD software (*Fluent*<sup>®</sup> in our case). We compute first the heating phase with equations 17 to 22. In Eq. 17 the heat transfer coefficient  $h$  is computed from the Nusselt correlation (see equations 12 to 16).

$$Nu = 0.332 \cdot Re^{1/2} \cdot Pr^{1/3}$$

**Eq. 12**

Equation 12 can be rewritten as follows to take into account for the Nusselt number evolution along the plate:

$$Nu(x) = \frac{0.332 \cdot Re(x)^{1/2} \cdot Pr^{1/3}}{\left[1 - \left(\frac{x_0}{x}\right)^{3/4}\right]^{1/3}}$$

**Eq. 13**

If we take  $x_0 = 0$  then the equation 13 reduces to:

$$Nu(x) = 0.332 \cdot Re(x)^{1/2} \cdot Pr^{1/3}$$

**Eq. 14**

Since fluid properties (such as viscosity, diffusivity, etc.) can vary significantly with temperature, there can be some ambiguity as to which temperature one should use to select property values. The recommended approach is the use of the average of the wall and free-stream temperatures, defined as the film temperature  $T_{film} = (T_{surface} + T_{air})/2$

Now recalling that the Nusselt number can be also expressed as reported in equation 15 we will be able, once  $Nu(x)$  is known, to compute  $h(x)$  as from equation 16.

$$Nu(x) = \frac{h(x) \cdot x}{k_{air}} \quad \text{Eq. 15}$$

$$h(x) = \frac{Nu(x) \cdot k_{air}}{x} \quad \text{Eq. 16}$$

The equation 12 holds for a laminar, isothermal, local situation with  $Pr > 0.6$  which is the situation we will deal with imposing a flow velocity ( $U_{\infty}$ ) of 10 m/s and a flow bulk temperature ( $T_{\infty}$ ) of 18 °C.

$$(dzdxdy) \lambda \left( \frac{\partial^2 T}{\partial x^2} + \frac{\partial^2 T}{\partial y^2} \right) + P (dzdxdy) = \rho c_p \frac{\partial T}{\partial t} (dzdxdy) + hdxdy (T - T_{\infty})$$

Eq. 17

with as initial condition

$$T(x, y, 0) = T_0 \quad \text{Eq. 18}$$

and as boundary conditions

$$-\lambda \frac{\partial T}{\partial x} \Big|_{x=0} = 0 \quad \text{Eq. 19}$$

$$-\lambda \frac{\partial T}{\partial x} \Big|_{x=L} = 0 \quad \text{Eq. 20}$$

$$-\lambda \frac{\partial T}{\partial y} \Big|_{y=0} = 0 \quad \text{Eq. 21}$$

$$-\lambda \frac{\partial T}{\partial y} \Big|_{y=H} = 0 \quad \text{Eq. 22}$$

The result of this first direct simulation is the surface 'hot' reference temperature cartography  $T(x, y, t_1) = T_1$ . The second direct simulation is performed to compute the cooling phase and therefore retrieve the surface 'cold' reference temperature cartography  $T(x, y, t_2) = T_2$  (exploiting Eq. 23 and equations 18 to 22).

$$(dzdxdy) \lambda \left( \frac{\partial^2 T}{\partial x^2} + \frac{\partial^2 T}{\partial y^2} \right) = \rho c_p \frac{\partial T}{\partial t} (dzdxdy) + hdxdy (T - T_{\infty})$$

Eq. 23

It is now possible to use  $T_1$  and  $T_2$  as boundary conditions for the solution of the IHCP. The obtained result is reported in Figure 2.

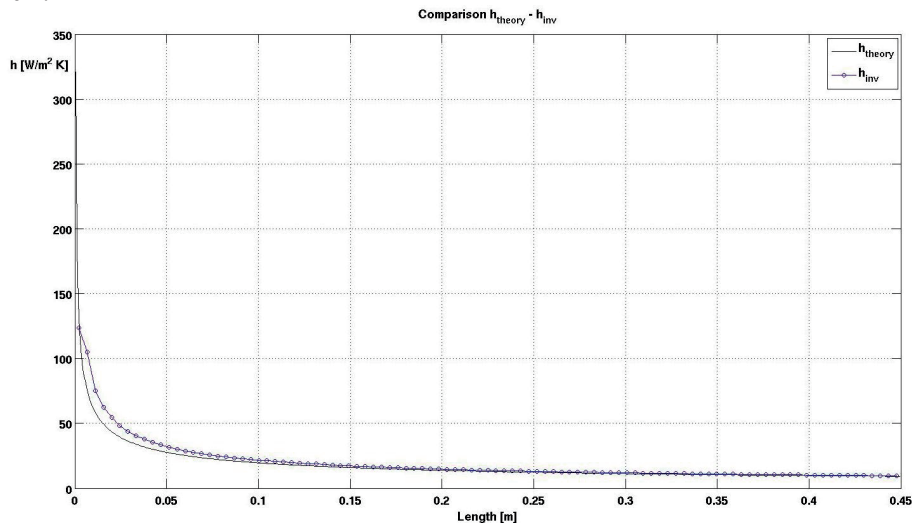


Figure 2. Theory - IHCP solution Comparison.

### 3 EXPERIMENTAL FACILITIES AND SET-UP

The facility used for the high speed experiments is a blow-down wind tunnel where the air coming from a pressurized tank can be heated.

A velocity  $U_{mean} \approx 30\text{-}230\text{ m/s}$  with a flow temperature  $T_{mean} \approx 290\text{-}320\text{ K}$  are flow conditions that can be considered satisfying the similarity rules to those appearing at the inlet of an aircraft engine during various flight conditions. See Figure 3 for the working scheme of the installation. The test section sketch and the installation of the measuring tools are sketched in Figure 4.

The experimental set-up for the low speed experiments is pictured in Figure 5. In the picture it is possible to see the I.R. camera used to acquire the surface thermographs, a hot-wire rake used to check the test section velocity and the heating resistance together with its power supply.

### 4 EXPERIMENTAL CAMPAIGNS AND DATA ANALYSIS

The following sections summarize the sets of experimental campaigns that have been conducted in order to characterize the high speed wind tunnel test section flow field and to validate the inverse heat conduction problem solution method.

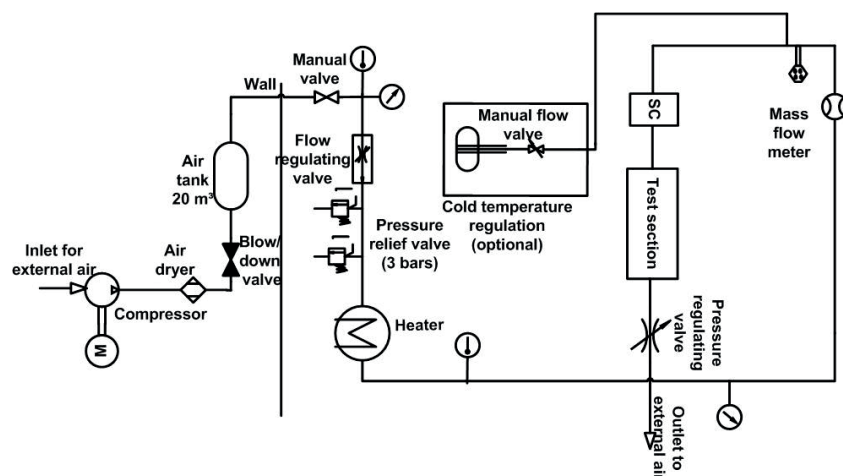


Figure 3. Facility Working Principle Diagram (Courtesy of ULB).

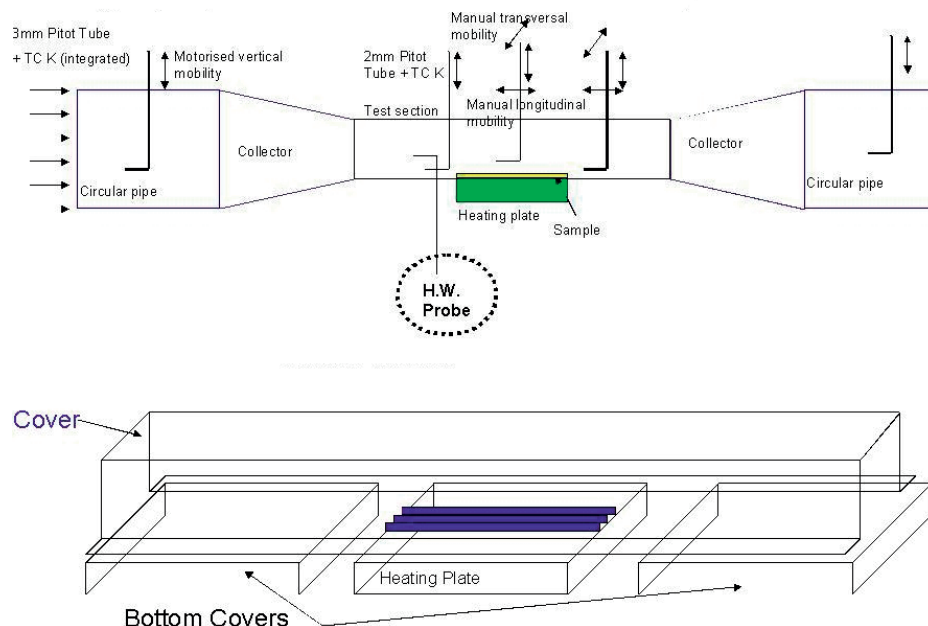


Figure 4. Test Section and Measuring Tools Installation Sketch (Courtesy of ULB).

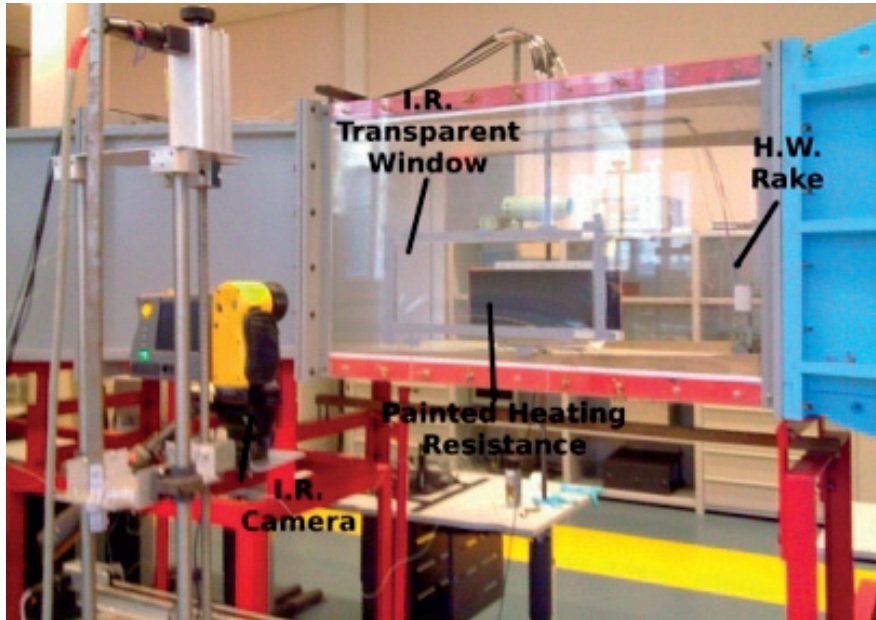


Figure 5. I.R. Low Speed Experiments Set-up.

#### 4.1 High Speed Experimental Campaign

Aim of the high speed experimental campaign is to characterize the blow-down wind tunnel flow field via the C.T.A. technique. Using hot-wire probes five different regimes of interest are investigated. A second experimental campaign is performed to measure the velocity profile and the effect of the presence of a finned heat exchanger in the section. A third series of experiments is performed to test the capabilities of a manufactured hot-wire probes rake.

##### 4.1.1 Mean Flow Field Measurements

The tests are performed with a plane bottom wall. The five investigated regimes classified according to the velocity and the mean total temperature of the fluid in the test section are summarized in table 1.

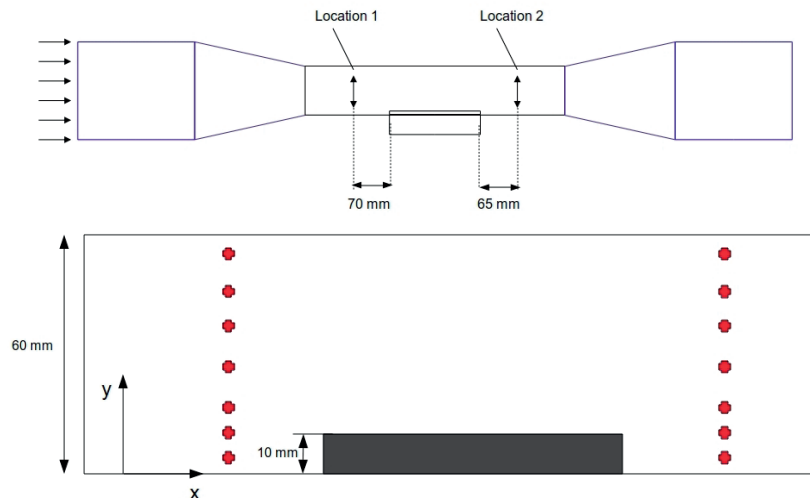
Table 1. Tested Regimes

Regime #	$U_{mean}$	$T_{total}$
1	230 m/s	315 K
2	160 m/s	305 K
3	130 m/s	300 K
4	60 m/s	295 K
5	30 m/s	295 K

##### 4.1.2 Traverses Experiments

This experimental campaign is performed with the finned heat exchanger placed in the test section but with no heat injection (i.e. no heat exchange between the finned surface and the flow) during the measurements. The experiments consist in hot-wire probe traverses in order to measure the velocity profiles before and after the prototype. The sketch in Figure 6 shows the positions and the locations where the experiments are performed.





**Figure 6. H-W. Traverses Experiments.**

According to the frame of reference shown in Figure 6 the positions analyzed for the two locations are:  $y = 6-11-16-26-36-46-56 \text{ mm}$ . The measurements in the two locations are performed during two different experiments.

#### 4.1.3 Hot-wire Rakes

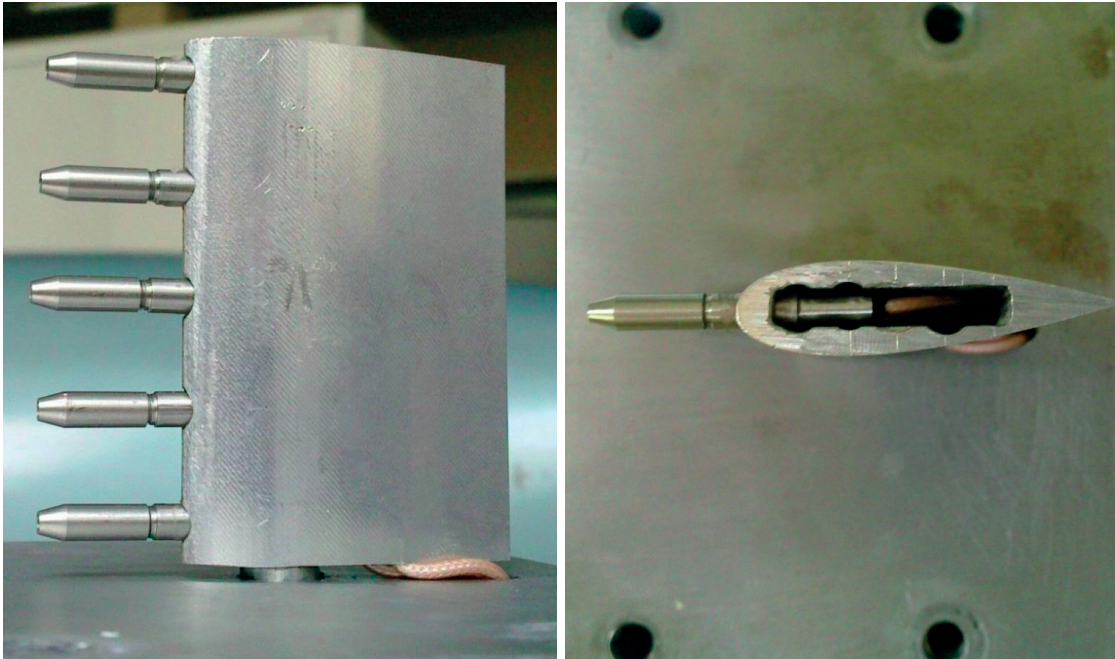
A major issue while performing the traverses experiments is to keep perfectly constant the flow conditions in order to let the moving probe facing the same flow field. To overcome this problem a design for a hot-wire probes rake is proposed, so that the velocity could be measured in different positions at once. The designed support is based on a well known NACA 4 digits symmetrical wing. The manufactured 3 probes support installed in the test section can be seen in Figure 7.



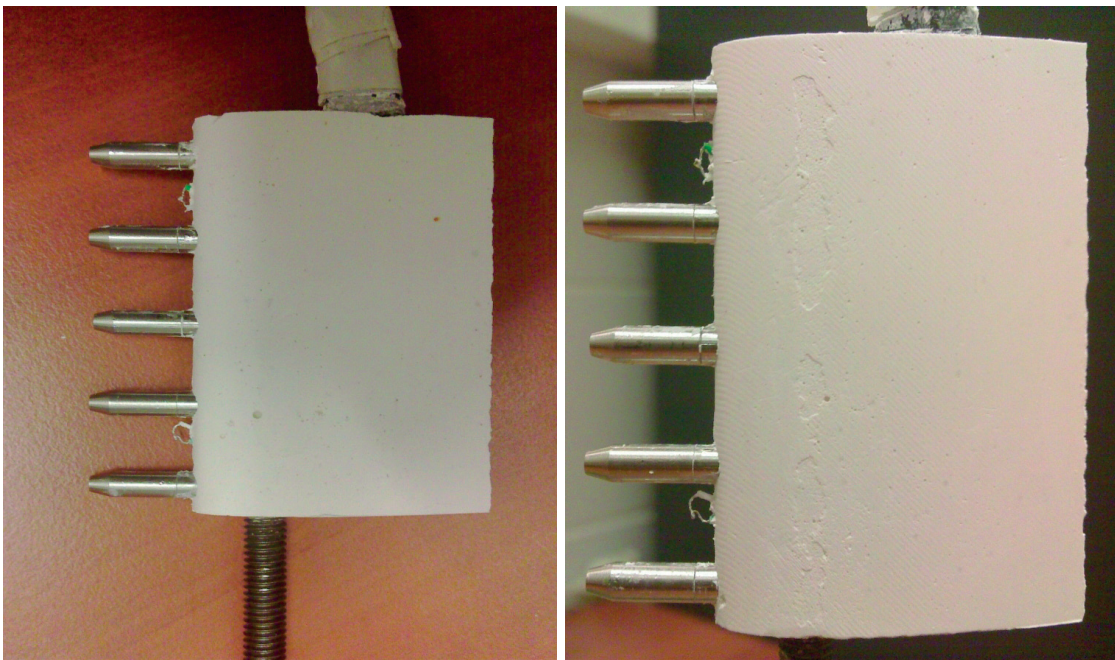
**Figure 7. Manufactured 3 Probes Support.**

The reasons why after some preliminary studies a symmetrical wing based on a NACA-0025 airfoil is chosen are reported next. The support has to be inserted in a high velocity environment this means that big forces could occur. Therefore to greatly reduce the forces acting on the rake and consequently the need for stout holders any kind of shape creating important drag forces should be avoided. The area facing the flow should be as little as possible to

reduce the blockage and consequently the interference with the free flow. Additionally when dealing with velocities of the order of  $230\text{ m/s}$  reducing the vibrations of the support becomes also very important. The adopted solution besides satisfying the abovementioned requirements allows also to minimize the wake size drastically reducing the interference effects on other measuring tools installed behind the rake itself. After the validation of the 3 probes support we decided to manufacture a 5 probes support that could grant the vertical velocity profile measurement of the whole test section at once. The rake is pictured in Figure 8, the probes are installed at a distance of  $12.5\text{ mm}$  from each other. In Figure 9 we can see the last version of the H.W. rake, prepared with molding plaster and where two thermocouples have been embedded in the support. This probe support has been tested only at low speed.



**Figure 8. Manufactured 5 Probes Support.**



**Figure 9. Manufactured 5 Probes Support (Plaster).**

#### 4.2 C.T.A. Data Analysis

When dealing with signals like those obtainable with the C.T.A. one can perform mainly three kind of analysis:

1. Descriptive static statistic analysis:
  - averaged values
  - skewness, kurtosis
  - variance, standard deviation
2. Spectral analysis
3. Signal correlation analysis
  - autocorrelation
  - cross-correlation

Since the C.T.A. technique is an indirect measurement technique a calibration law is required. Calibration units are available for this purpose, letting us associate to a known velocity the voltage measured by the hot-wire probe [18]. But this procedure cannot be exploited to analyze the data when the temperature varies during the measurements. Since the environment in which the hot-wire probe is placed is characterized by rather significant temperature variations, 6/7 K during the same regime and from 320 K to 295 K from the beginning to the end of a complete run, rather than a calibration curve a calibration surface with the temperature as additional variable would be required. The biggest issue to obtain such a calibration surface is that a dedicated wind tunnel is needed, where both the velocity and the flow temperature can be controlled. The one available at the Royal Military School can reach a maximum velocity of 30 m/s under controlled temperature conditions but during the experiments the velocity ranges between 40 m/s and 230 m/s. Therefore an alternative calibration procedure is needed. The "in-situ" calibration proposed consists in extracting the measured voltage, velocity and temperature for each investigated flow regime. The raw voltages are then corrected in temperature according to equation 25 and an iterative procedure implemented in *Matlab*<sup>®</sup> computes simultaneously the "reference King's Law coefficients". The basic idea is to retrieve a "unique" calibration law that can be used even if the temperature is changing, the scheme in Figure 10 summarizes the strategy to obtain the proposed calibration curve.

In this way it is possible to perform experiments and exploit the acquired data to obtain a calibration law that is corrected in temperature. Equation 24 shows the King's Law while in equation 25 is reported the correction applied prior to linearize the data [14].

$$E_{corr}^2 = A_{ref} + B_{ref} \cdot U^{n_{ref}} \quad E_{corr} = E_{meas} \cdot \left( \frac{T_w - T_{ref}}{T_w - T_a} \right)^{0.5 \cdot (1 \pm m)}$$

Eq. 24 Eq. 25

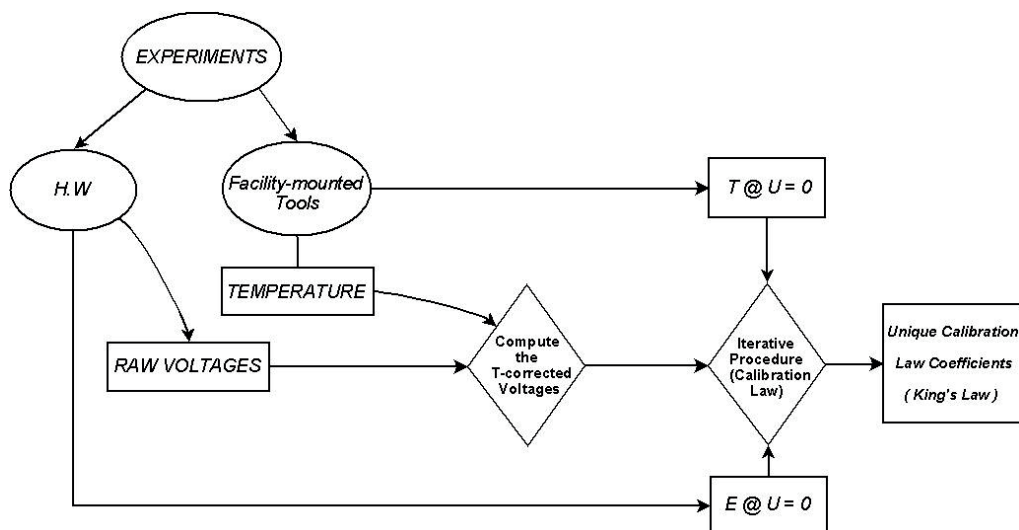


Figure 10. Unique Calibration Law Procedure Logical Scheme.

where  $T_w$  is the wire temperature,  $T_{ref}$  is the reference temperature (in this case the temperature in the test section immediately before the experiment),  $T_a$  is the ambient temperature, measured by the facility mounted instrumentation. The parameter  $m$  is called "Temperature Loading Factor" and is suggested by Dantec for temperature correction purposes, it should be kept between 0.2 and 0.3 and added or subtracted depending on whether  $T_a$  is bigger or smaller than  $T_{ref}$  respectively. An example of the resulting "unique" calibration law is reported in Figure 11.

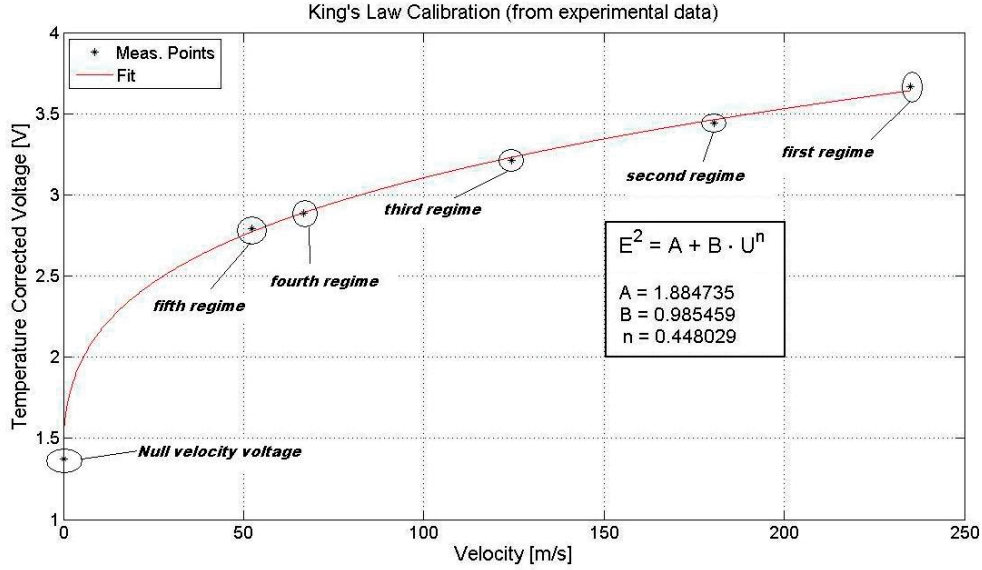


Figure 11. Unique Calibration Law Example.

#### 4.2.1 Correction for Fluid Temperature Drift

To obtain the actual velocities the reference King's law coefficients are "tuned" accordingly to the measured fluid temperature. The corrected King's law coefficients are computed as described by the set of equations 26.

$$\left\{ \begin{array}{l} A_{corr} = \left( \frac{T_w - T_a}{T_w - T_0} \right)^{(1 \pm m)} \cdot \frac{K_{fa}}{K_{f_0}} \cdot \left( \frac{Pr_{fa}}{Pr_{f_0}} \right)^{0.2} \cdot A_{ref} \\ B_{corr} = \left( \frac{T_w - T_a}{T_w - T_0} \right)^{(1 \pm m)} \cdot \frac{K_{fa}}{K_{f_0}} \cdot \left( \frac{Pr_{fa}}{Pr_{f_0}} \right)^{0.33} \\ \cdot \left( \frac{\rho_{fa}}{\rho_{f_0}} \right)^n \cdot \left( \frac{\mu_{fa}}{\mu_{f_0}} \right)^{-n} B_{ref} \end{array} \right.$$

**Eq. 26**

The air physical properties in equation 26 are computed at the temperatures  $T_{fa}$  and  $T_{f_0}$  respectively the ambient and reference film temperatures obtainable as follows:

$$\left\{ \begin{array}{l} T_{fa} = \frac{T_w + T_a}{2} \\ T_{f_{ref}} = \frac{T_w + T_{ref}}{2} \end{array} \right.$$

**Eq. 27**

So after the correction the King's calibration law should be rewritten as follows:

$$E^2 = A_{corr} + B_{corr} \cdot U^n$$

**Eq. 28**

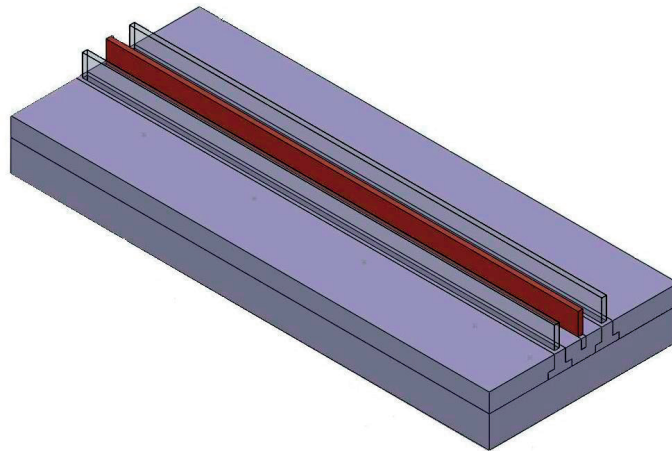
Eventually the velocity in the wind tunnel test section is computed as reported by the expression in equation 29.

$$U = \left( \frac{E^2 - A_{corr}}{B_{corr}} \right)^{\frac{1}{n}}$$

**Eq. 29**

### 4.3 Low Speed Experimental Campaign: I.R. Analysis

Aim of the low speed experimental campaign is to validate the methodology and the tools to be used to solve the IHCP. In a low speed wind tunnel a quasi-2D heating resistance has been placed in the test section and surface thermographs are recorded ([8]) in order to exploit a numerical procedure capable to compute the heat conduction coefficient. The analysis of the requirements and of the constraints led to the conception of the experimental model as sketched in Figure 12.



**Figure 12. Experimental Model Conception Sketch.**

The real heat exchanger is reproduced by means of a central fin, made of copper and acting as heating resistance. On the two sides of this central fin is placed a set of two fins made of I.R. transparent material ( $CaF_2$  for instance). The idea is to exploit the prototype symmetry in order to simplify its testing model. Additionally using a heating resistance as central fin allows us to know and control the heat injected.

According to the mentioned needs the proposed procedure to perform the experiments can be summarized as follows:

1. Heat the central fin up to the maximum allowed temperature
2. Open the facility valve in order to reach a stabilized velocity
3. Increase the heating power injected in the fin accordingly to the velocity increase in order to keep the heating resistance at a constant temperature
4. Once the velocity and the fin  $T_{surf}$  are stabilized acquire a reference surface thermograph (hot surface)
5. Switch off the heating resistance
6. Record the fin  $T_{surf}$  evolution with the I.R. camera (cold surface)
7. Solve the IHCP via the numerical calculation

For what concerns the experiments presented in this work one should remind that the configuration proposed in Figure 12 has been replaced by a stand alone very thin ( $0.25\text{ mm}$ ) but with a bigger surface ( $170 \times 450\text{ mm}$ ) heating resistance for a sake of simplicity. The heating resistance is of the order of  $20\Omega$  and it is fed with  $12\text{ Volts}$ . The flow velocity in the wind tunnel test section is  $10\text{ m/s}$ . The above mentioned procedure is then applied as described.

#### 4.4 I.R. Experiments Data Analysis

The code exploited to solve the IHCP needs to be fed with a matrix of data representing the thermograph acquired by the I.R. camera. Therefore once recorded, the images must be prepared in order to be used as boundary conditions for the numerical method proposed. The rebuilding procedure could be summarized as follows:

1. An I.R. image where the color map palette is present is needed in order to be able to know the color levels to be linked to the temperature levels (see Figure 13).
2. Retrieve a vector able to translate the R(ed)-G(reen)- B(lue) data contained in the I.R. images into a matrix containing the surface temperature.
3. Pick up conveniently a frame from the recorded I.R. video, this will be the cold surface and fix the time step for the numerical solution (see Figure 14).
4. Translate the image into a *Matlab*® exploitable matrix.
5. Crop the image in order to contain only the surface of interest (i.e. only the flat plate and not the supports, etc. ...), see Figure 15

Once prepared the I.R. images for the analysis one should just insert the right surface dimensions, time step and material characteristics in the script and feed the script with the hot surface and the cold surface informations matrices [4].

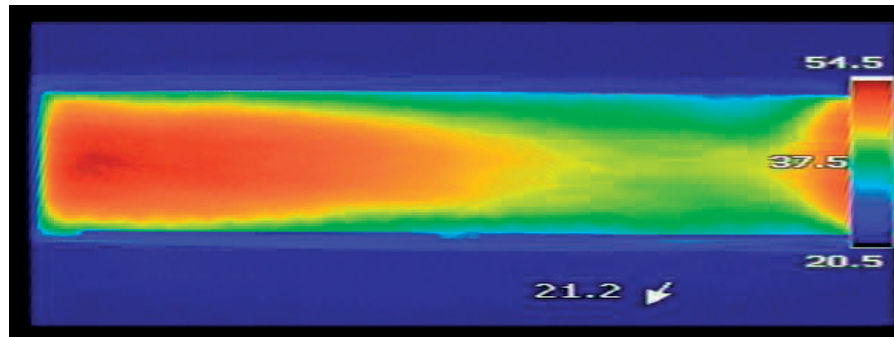


Figure 13. Color vs. Temperature Levels.

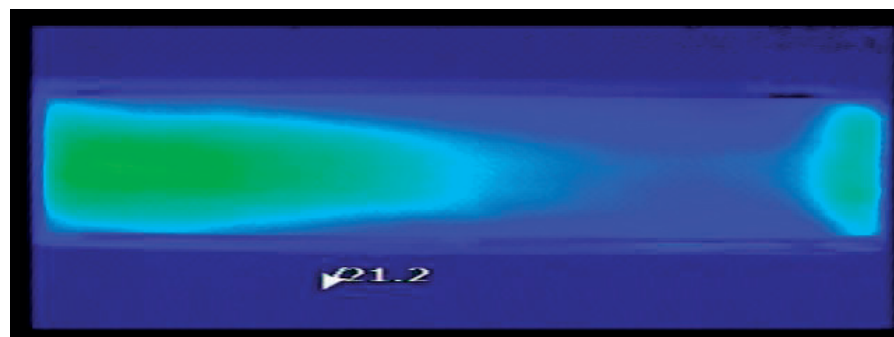


Figure 14. Cold Surface I.R. Image.

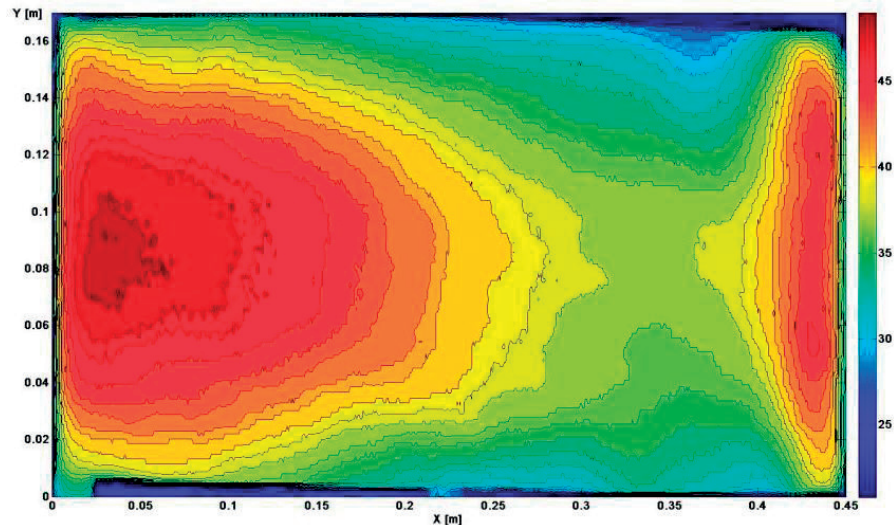


Figure 15. Cropped and Translated Image Example.

## 5 CFD LOW SPEED SIMULATION

The purpose of these simulations is to check the behavior of the hot-wire probes support when inserted in the flow field. For this work the calculations have been used also to define the distance at which should be placed the heating resistance used for the I.R. experimental campaign. Indeed it is important to reduce at the maximum the influence of the wake released by the probe rake so that the recorded I.R. images depict the actual situation of a “hot” object submerged by an undisturbed “cold” flow. In Figure 16 is reported the geometry used to perform the simulations, it is possible to notice that the probe prongs and the wires are not modeled.

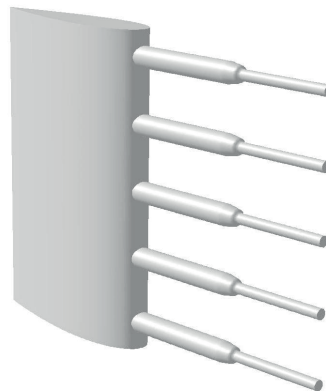


Figure 16. H.W. Rake Model.

The model is created with the open source software K-3D (<http://www.k-3d.org>) while the mesh is produced with the automatic mesher HEXPRESS<sup>TM</sup>/Hybrid. The calculations have been performed with the commercial solver *Fluent*<sup>®</sup>. The domain reproducing the R.M.A. wind tunnel test section (60 cm x 60 cm x 120 cm) is of about two millions cells. The 3-D steady state simulations have been performed using a standard *k - ε* turbulence model and the *Fluent*<sup>®</sup> enhanced wall treatment option enabled. The discretization schemes used are the *Fluent* c standard scheme for the pressure and the first order upwind scheme for the momentum, the turbulent kinetic energy and the turbulent dissipation rate. The velocity used for the simulation is the same as the one used for the I.R. test, 10 m/s.

## 6 RESULTS

In this section are presented the obtained results. The flow field analysis of the blow-down wind tunnel are presented first. The low speed I.R. analysis experiment are only partially presented as they are performed for validation purposes and the whole methodology could not be fully discussed in this article. Eventually are presented the numerical simulations of the H.W. rake behavior performed at low speed.

## 6.1 Mean Flow Field Results

It is of crucial importance to characterize the turbulence in the testing chamber, the size of the turbulent scales and the frequency content. In Table 2 are summarized the results of the static statistic analysis and of the autocorrelation analysis for each flow regime [1, 2, 7, 13, 17].

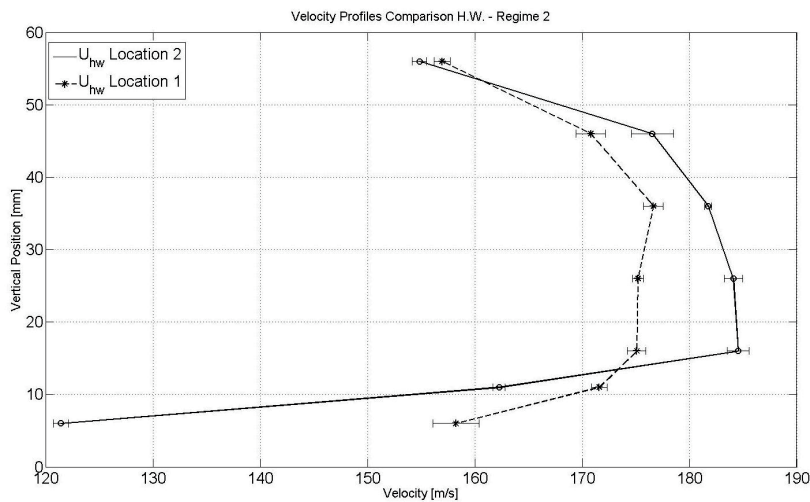
**Table 2. Experimental Campaign Results.**

<i>Regime</i>	<i>1</i>	<i>2</i>	<i>3</i>	<i>4</i>	<i>5</i>
$U_{meas}$ [m/s] (Pitot)	226.29	180.65	126.35	72.33	45.33
$U_{comp}$ [m/s] (H.W.)	234.19	170.57	123.10	71.04	47.26
Uncertainty [m/s]	$\pm 4.47$	$\pm 4.44$	$\pm 4.08$	$\pm 0.99$	$\pm 0.35$
Uncertainty %	1.91	2.60	3.32	1.39	0.74
$Re_d$	42.25	31.25	22.81	13.31	8.91
<i>Mach</i> number	0.66	0.49	0.35	0.21	0.14
$T_{mean}$ [K]	$\approx 315$	$\approx 307$	$\approx 301$	$\approx 296$	$\approx 293$
R.M.S.	5.615	3.398	2.846	1.753	1.267
Variance	31.523	11.549	8.098	3.072	1.604
Turbulence Intensity %	2.397	1.992	2.312	2.467	2.680
Skewness	-0.695	-0.506	-0.320	-0.314	-0.286
Kurtosis	3.655	3.791	3.483	3.565	3.512
Int. Length Scale [mm]	37.897	38.572	41.617	20.740	19.330
Taylor Micro Scale $\lambda$ [mm]	6.795	4.855	4.163	2.739	2.468
Dissipation Rate $\epsilon$ [ $m^2/s^3$ ]	283.83	200.56	189.11	163.86	104.82
Kolmogorov Length Scale $\eta$ [mm]	0.0931	0.1003	0.1010	0.1038	0.1155

The frequency analysis is performed exploiting the F.F.T. (Fast Fourier Transform) algorithm of Matlab which uses a special version of the discrete Fourier transform to filter the data. The error analysis for the presented results is performed according to the error propagation theory (the Kline-McClintock approach) always using a confidence interval of the 95%.

## 6.2 Hot-wire Traverses Results

The measures, coupled with pressure measurements, allow computing the pressure losses caused by the presence of the heat exchange. The test conditions repeatability being one of the main issues the results presented cannot be retained quantitatively precise. Especially since the traverses at the two locations have been performed during two different test. However the experimental campaign gives meaningful information about the general flow field behavior [3].



**Figure 17. Velocity Profiles - H.W. Measures.**



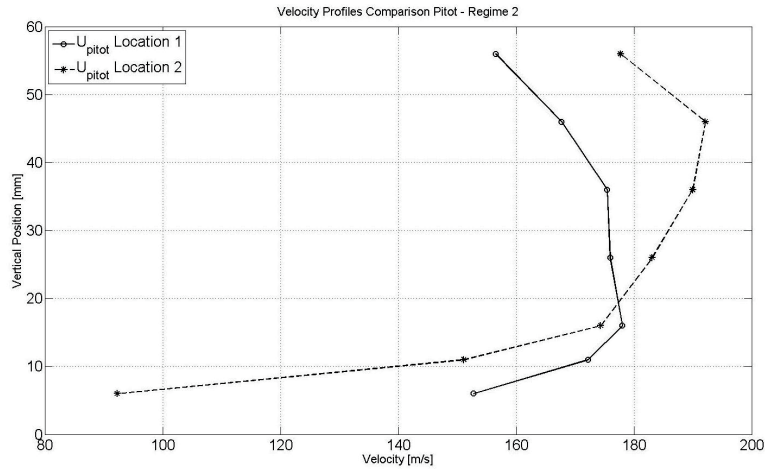


Figure 18. Velocity Profiles - Pitot Measures.

From Figure 19 and Figure 20 we can notice a discrepancy between the measurements performed with the hotwire and the Pitot tube that seems to be mainly due to the fact that the wind tunnel is a blow-down facility. In fact with such facilities one of the biggest issues is to be certain to have exactly the same flow conditions for enough time to perform a full traverse analysis. If we compare these results with the results in table 3 it is clear as performing multi-point measurements gives much more reliable measurements since we are certain that the flow conditions will be the same.

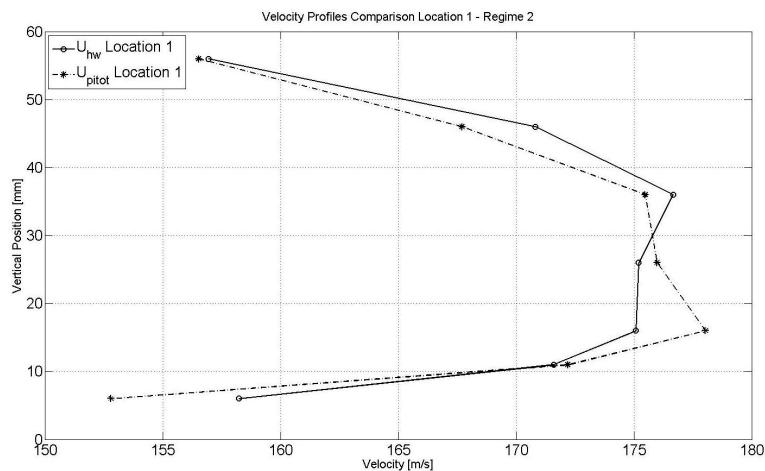


Figure 19. Velocity Profiles - Location 1, H.W. - Pitot Comparison.

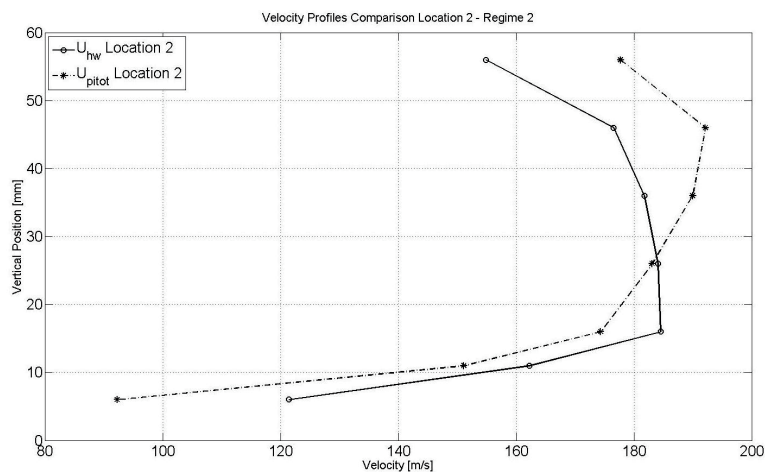


Figure 20. Velocity Profiles - Location 2, H.W. - Pitot Comparison.

### 6.3 Hot-wire Rake Results

Since the wind tunnel is exploited in parallel by ULB and some modifications have been performed on it the results obtained with the hot-wire rakes should not be compared with above reported results. The main purpose of the performed experiments is to validate the manufactured rakes.

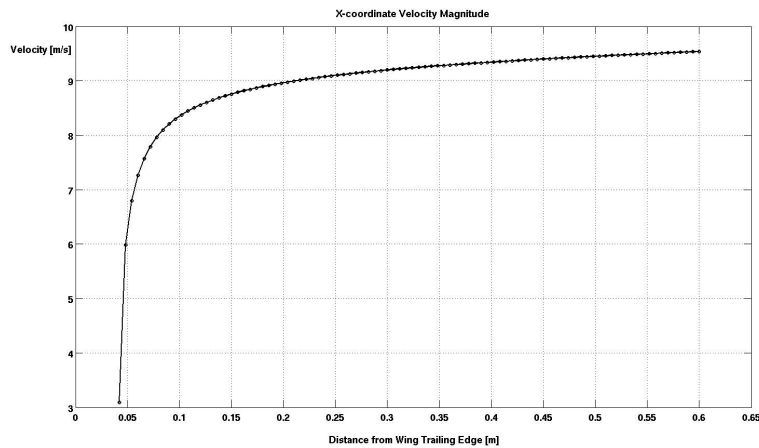
**Table 3. H.W. Rake 3 Probes vs. Pitot.**

<i>Regime</i>	<i>Position</i>	$U_{meas}$ Pitot	$U_{meas}$ H.W.
1	1	$\approx 205.04 \text{ m/s}$	$\approx 205.64 \text{ m/s}$
	2	$\approx 207.01 \text{ m/s}$	$\approx 207.95 \text{ m/s}$
	3	$\approx 201.64 \text{ m/s}$	$\approx 203.40 \text{ m/s}$
2	1	$\approx 177.59 \text{ m/s}$	$\approx 171.01 \text{ m/s}$
	2	$\approx 173.34 \text{ m/s}$	$\approx 173.70 \text{ m/s}$
	3	$\approx 169.77 \text{ m/s}$	$\approx 170.78 \text{ m/s}$
3	1	$\approx 120.89 \text{ m/s}$	$\approx 121.88 \text{ m/s}$
	2	$\approx 124.40 \text{ m/s}$	$\approx 125.97 \text{ m/s}$
	3	$\approx 119.61 \text{ m/s}$	$\approx 124.54 \text{ m/s}$

In table 3 are reported the velocities measured with the 3-probes support and a Pitot tube at the same positions but at a different distance from the test section inlet during the same test. It is easy to understand as the possibility to simultaneously measure the whole velocity profile drastically reduce the uncertainty linked to the capacity of maintaining exactly the same flow conditions for a long period of time. Therefore the accuracy of the velocity profiles measured with the rake is much higher and the profile shape gives indications on the actual test section flow field being not linked to the wind tunnel working parameters controlled by the operator

### 6.4 CFD Simulation Results

In Figure 21 is plotted the computed velocity profile along the x-axis extracted from the wing trailing edge to the end of the numerical domain.



**Figure 21. X-coordinate Velocity Plot.**

It is possible to notice that after 35 cm the influence of the rake wake starts being negligible, this why the heating resistance used for the I.R. experiment has been placed at about 40 cm from the probe support.

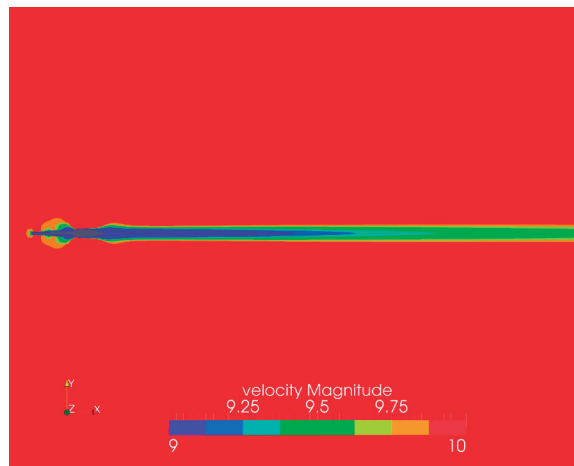


Figure 22 CFD-computed Velocity Contour Plot.

From the contour plot reported in Figure 22 it is possible to see the influence of the presence of the rake in the whole domain. The results obtained could be used for comparison with oil flow visualization. This will be more interesting when moving to the high velocity case as the oil visualization allows to clearly see if the transition to supersonic occurs and where the flow in case detach from the wing surface.

### 6.5 IHCP Solution Results

Hereafter, in Figure 23, we can see a cartography of the convective heat transfer coefficient obtained exploiting the numerical solution of the IHCP. The results refer to the experiments performed with a time step of 5 seconds between two I.R. images and the flow is coming from the right side. The reason why the highest value of  $h$  is not located where the flow first impact the heated plate is due to the fact that the plate itself is installed on thick support in order to respect the boundary conditions (see equations 19 to 22) required by the IHCP solution. One should also notice that a regularization method is applied for the results presented.

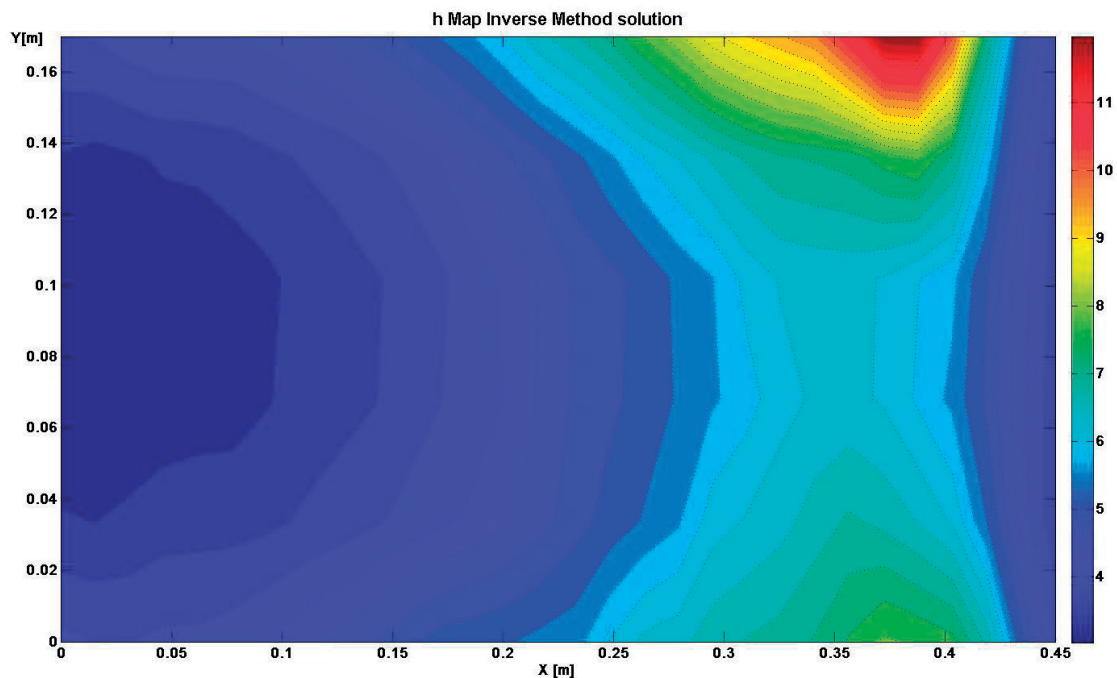


Figure 23.  $h_{surf}$  Cartography.

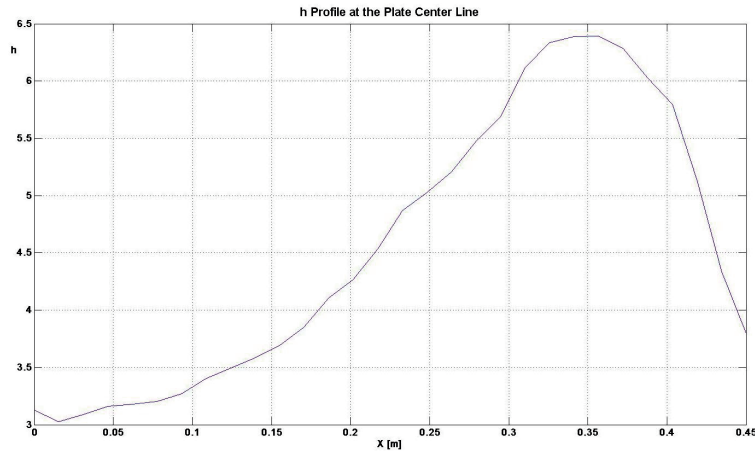


Figure 24.  $h_{surf}$  Plot at the Plate Center Line.

## 7 CONCLUSIONS

The analysis performed to check the flow field quality makes us assume that modifications should be performed on the wind tunnel. Indeed the very low turbulence level, together with the almost parabolic velocity profiles measured, let us assume that flow could probably not be fully developed when entering the test section. Though the absence of spectral peaks lets us deduce that the turbulence in the flow field is homogeneous and no frequency correlated structures are present (no vortex shedding or other phenomena). This leading to the conviction that performing minor modifications should be enough to improve the flow field quality. The coupling of Pitot tube and hot-wire probe traverse measurements shows that the general behavior of the flow field is maintained almost constant. Nevertheless it also testifies that the wind tunnel is not able to reproduce exactly the same conditions ( $p_{tot}$  profile,  $U$  profile, etc..) for two consecutive tests. The test performed with the hot-wire probes rake show the goodness of the support chosen design in order to overcome the main issue affecting a blow-down facility: maintain exactly the same working conditions for a long period of time. Indeed the rake allowed us to measure the velocity at five different positions instantaneously without affecting significantly the flow field itself. The obtained results have been taken into account by the U.L.B. engineers while conceiving a revised version of the facility that is now under construction. The flow field of this new wind tunnel will be investigated in the next months. For what concerns the numerical solution of the IHCP the validation test performed gave encouraging results. The lesson learned from the preliminary test performed is that one has to carefully prepare the experimental set-up in order to reduce as much as possible the heat losses (very high thermal insulation on the sides and on the back face of the fin). Furthermore prepare the experimental set-up to work with a finned heat exchanger at high subsonic velocity will be even more challenging. Nevertheless the task to validate the methodology and develop a consistent approach to this kind of analysis can be considered as accomplished. The simulations performed over the H.W. probe rake have been very helpful to correctly prepare the I.R. low velocity experimental set-up. Additionally the geometry and the meshing procedure are now well established so that it will be easier to move to the high subsonic velocity case.

## 8 FUTURE DEVELOPMENTS

One of the main and more imminent task will be to check the flow field quality in the revised version of the blow-down wind tunnel. Besides this task the capabilities of the H.W. rake made in plaster should be validate, indeed CFD simulations and flow oil visualization at high speed are scheduled in order to accomplish the task. The set-up for the I.R. experiments should be modified in order to let a flat velocity profile reach the heated plated. An enhanced regularization parameter based on the variation of the heat flux gradient is under validation and should be included in the proposed algorithm to solve the IHCP. Additionally the whole procedure should be optimized for a flow reaching  $M \approx 0.7$  where possible issues could be the very small amount of time to grab I.R. images, the flow stabilization and the fin temperature stabilization

## ACKNOWLEDGMENTS

I would like to thankfully acknowledge the “TEMPO Laboratory“ of the University of Valenciennes guided by Professor Souad Harmand for giving me the opportunity to exploit their knowledge on the IHCP.

I also would like to sincerely thank the ULB research engineer Nicolas Heintz for the months of work performed together and the availability he showed..

## REFERENCES

- [1] AIAA. *Preliminary Measurements of Velocity, Density and Total Temperature Fluctuations in Compressible Subsonic Flow*, Reno, NV, January 1983. AIAA.
- [2] AIAA. *Turbulence in Complex Flows: A Selected Review*, Reno, NV, January 1992. AIAA.
- [3] F. Baldani and W. Bosschaerts. Turbulence measurements in a high subsonic non-isothermal flow field. turbine engines inlet conditions analysis. *Conference Proceedings*, (ISABE-2011-1815), Gothenburg - September 2011.
- [4] F. Baldani, W. Bosschaerts, and R. Wagemakers. High velocities wind tunnel flow field investigation and heat exchanger infra-red analysis. part 1: Experimental set-up, experiments and first results. *Conference Proceedings*, (ISAIF10-11), Brussels - July 2011.
- [5] J. Beck, B. Blackwell, and A. Hoji-Sheikh. Comparison of some inverse heat conduction methods using experimental data. *International Journal of Heat Mass Transfer*, (Vol. 39, pp. 3649-3657), 1996.
- [6] J. Beck, B. Blackwell, and C. S. C. Jr. *INVERSE HEAT CONDUCTION - Ill-posed Problems*. International Text Books in Mechanical Engineering. Wiley Interscience Publication, first edition edition, 1985.
- [7] H. Bruun. *Hot-wire Anemometry, Principles and Signal Processing*. Oxford University Press Inc., 1995.
- [8] G. Cardone, T. Astarita, and G. Carlomagno. Wall heat transfer in static and rotating 180 degrees turn channels by quantitative infrared thermography. *Re. Gén. Therm.*, (37, 644-652), 1998.
- [9] F. Coletti. *Coupled Flow Field and Heat Transfer in an Advanced Internal Cooling Scheme*. PhD thesis, 2010.
- [10] F. Coletti, A. Armellini, T. Arts, and C. Scholtes. Aero-thermal investigation of a rib-roughened trailing edge channel with crossing jets - part ii: Heat transfer analysis. *ASME paper No. GT2008 - 50695*, 2008.
- [11] B. Cukurel, T. Arts, and C. Selcan. Conjugate heat transfer characterization in a ribbed cooling channel. *Conference Proceedings*, (ISAIF10-161), Brussels - July 2011.
- [12] P. H. Groeber and D. S. Erk. *Fundamentals of Heat Transfer*. McGraw-Hill Series in Mechanical Engineering. McGraw-Hill Book Company, INC., third revised edition by dr. u. grigull edition, 1962.
- [13] D. Hanson and K. Horan. Turbulence/cascade inter action: spectra of inflow, cascade response and noise. (A98-30871), 1998.
- [14] F. E. Jorgensen. *How to measure turbulence with hot-wire anemometers*. Dantec Dynamics, Tonsbakke 16-18, DK-2740 Skovlunde, Denmark, 2005.
- [15] F. Kreith. *Principles of Heat Transfer*. International Text Books in Mechanical Engineering. International Textbook Company Ltd, 158 Buckingham Palace Road London, second revised edition edition, 1965.
- [16] T. Perelman. On conjugated problems of heat transfer. *International Journal of Heat Mass Transfer*, (Vol. 3, pp. 293-303), 1961.

- [17] P. Stainback and K. Nagabushana. Review of hotwire anemometry techniques and the range of their applicability for various flows. *Electronic Journal of Fluids Engineering, Transactions of the ASME*.
- [18] Various. *Measurement Techniques in Fluid Dynamics - An Introduction*. VKI Lecture Series. von Karman Institute, second revised edition edition, 2001.
- [19] A. Willockx. *Using the Inverse Heat Conduction Problem and Thermography for the Determination of Local Heat Transfer Coefficients and Fin Effectiveness for Longitudinal Fins*. PhD thesis, 2009.



## A NEW LINEAR CASCADE TEST FACILITY FOR USE IN ENGINEERING EDUCATION

**Monaco, L.**

The Royal Institute of Technology  
Chair of Heat and Power  
Technology  
Stockholm, Sweden  
lucio@kth.se

**Vogt, D. M.**

The Royal Institute of Technology  
Chair of Heat and Power  
Technology  
Stockholm, Sweden  
damian.vogt@energy.kth.se

**Fransson, T. H.**

The Royal Institute of Technology  
Chair of Heat and Power  
Technology  
Stockholm, Sweden  
torsten.fransson@energy.kth.se

### ABSTRACT

A new low-speed air-operated linear cascade test facility has been developed at the Heat and Power Technology Division at KTH, Sweden. The rig has fully remote operability and is used as an educational tool for the students in engineering courses on turbomachinery. Both on campus and distant students are involved in experimental activities with the rig in the form of laboratory exercises. The current setup allows determination of profile losses through a low pressure turbine blade row at low subsonic flow conditions. The present paper contains a description of test rig design and its commissioning and introduces the concepts for future applications of the facility in investigation of additional flow phenomena in turbomachinery. Findings of the first field experience with the linear cascade are here reported..

### INTRODUCTION

Despite the increasing application of computational fluid dynamics (CFD) tools in turbomachinery related research, experimental testing still plays a key role in the investigation of a wide branch of aerodynamic and aeromechanical phenomena. Blade and engine tests are performed before the final design [1] and no power plant or propulsion system can enter the market before having passed very severe testing campaigns. While the familiarization of engineering students with CFD tools is relatively widespread and easy to include in their educational path, the possibility to give them experience on experimental testing is rather limited, especially in the case of distant students. The department of Energy Technology at KTH has been one of the pioneers in the introduction of remote laboratory activities for distance education. Examples are the work carried out by Navarathna [2] on a linear cascade and the newly deployed remote pump laboratory [3]. The existing linear cascade needed to be strongly refurbished and a complete redesign of the facility for an enhanced laboratory activity has been undertaken..

From an investigation on current research in turbomachinery, it has appeared that linear cascades are still of particular interest for the analysis of twodimensional flow fields and in the preliminary design phase of axial flow machines. Of technical relevance is the straight cascade tunnel Göttingen (EGG) at DLR [4], and the linear cascade rig at Chalmers University [5]. Applications of linear cascades in research include blade film cooling studies [6], tip clearance effects [7], effect of incoming wakes on blade rows [8], [9] and end wall heat transfer of nozzle guide vanes [10].

While keeping the concept of the linear cascade, the design of the present test facility has been addressed towards a versatile solution easy to adapt to new experiments and remotely controlled for use in on campus as well as distance education.



**NOMENCLATURE**

$c$	chord, m
$p$	pressure, Pa
$s$	span, m
$\gamma$	blade stagger angle, ° ratio of specific heats, -
$\xi$	kinematic loss coefficient

2-D	two-dimensional
3-D	three-dimensional
CFD	Computational Fluid Dynamics
DAQ	Data Acquisition System
HPT	Heat and Power Technology
KTH	Royal Institute of Technology, Sweden
PML	Pressure Measurement Lab
RCL	Remote Cascade Lab

**Subscripts**

ax	axial
0	total
1	inlet
2	outlet

**DESCRIPTION OF THE TEST FACILITY**

The new aerodynamic test facility at the HPT Division at KTH is shown in Figure 1. The rig is connected to an air supply system delivering up to 2.5 kg/s for an estimated maximum outlet Mach number of about 0.4. At present the rig is equipped with instrumentation for the analysis of the aerodynamic performances of a linear cascade of low pressure turbine blades. The main operating parameters are included in Table 1.



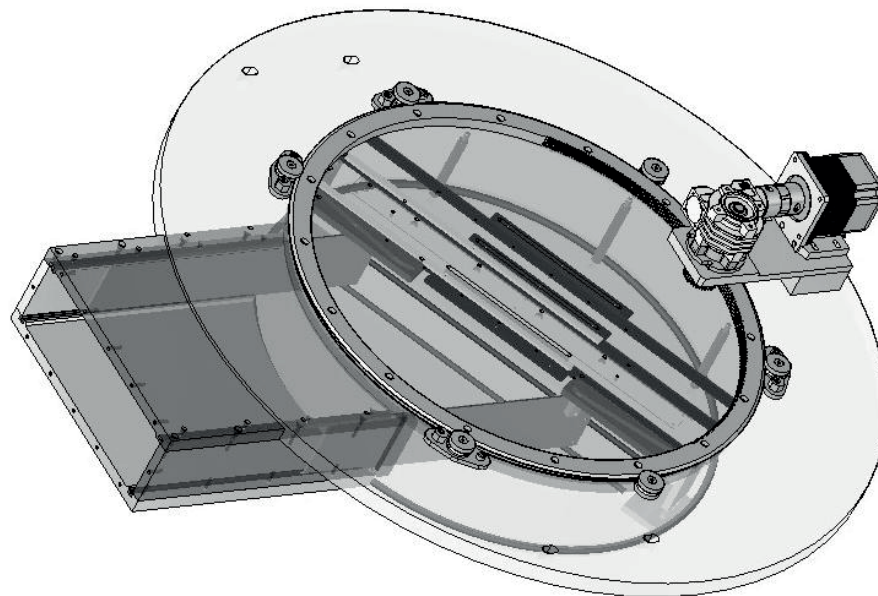
**Figure 1. RCL test facility.**

**Table 1. Main operating parameters.**

Parameter	Unit	Range
Inlet flow angle	°	-45 ÷ +45
Inlet Mach number	-	0.05 ÷ 0.3

The core of the system is shown in Figure 2 and consists of a central disc supporting all the instrumentation for the measurements (1). A second circular disc (2), made of Plexiglas, is maintained at 100 mm distance and constitutes the outer wall. The main disc is mounted on a ring slide (3) and can be rotated to allow variation of the inflow angle between  $-45^\circ$  and  $+45^\circ$ . Two sidewalls (4) slide vertically following the rotation of the disc by means of a cam follower system. The cross section of the channel measures 300 mm x 100 mm.

During the design of the facility, major effort has been put to extend the flexibility of the system. An opening of 530 mm x 80 mm (5) at the center of the Plexiglas disc allows introduction in the test section of different test objects. For the experimental investigation on linear cascades, the blades are mounted between parallel plates in the form of an interchangeable module.

**Figure 2. Rotation system.**

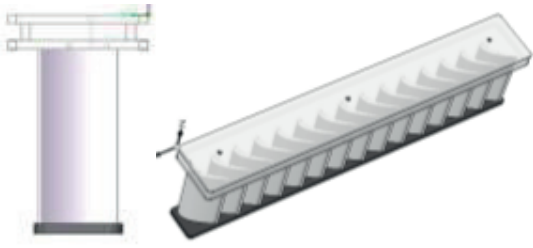
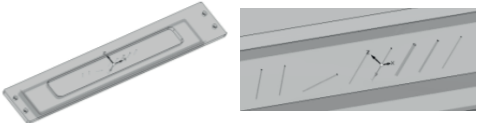
### Interchangeable Module

Different blade profiles as well as blades with variable tip leakage can be tested in the RCL. The test rig has been designed such that each set of blades is assembled as a dedicated interchangeable module. The module is pulled out from the test section after having removed two retaining plates fastened to the Plexiglas disk, visible in Figure 1.



Table 2 and Table 3 show the modules currently available and the ones that have already been designed. Results presented in this paper refer to the RCL equipped with the RCL-AETR module with 15 prismatic blades whose specifications are included in Table 4. The blades have been manufactured with SLA (Stereolithography Prototype) process. The same technique will be employed for the realization of blades instrumented with pressure taps on the surface for the determination of the aerodynamic loading at discrete span sections.

An additional module consists of a single plate with several pressure taps – shown in Table 5 - to be used in the PML exercise where the study on the influence of pressure tappings on the measurement values is addressed.

**Table 2. Currently available modules.**

Name	CAD Model	Use / Description
RCL-AETR		RCL Exercise (used e.g. in MJ2244 [11] and MJ 2340 [12]) Prismatic blades
PML		PML Exercise 9 different pressure tappings

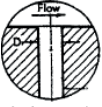
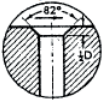

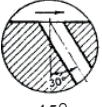
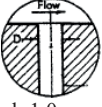
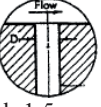

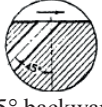
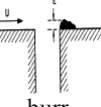
**Table 2. Modules designed for further investigation of flow phenomena in linear cascades.**

Name	CAD Model	Use / Description
RCL-AETR CS20		RCL Exercise (MJ2244, MJ2430) Compound sweep: maximum 20% of $C_{ax}$
PML		RCL Exercise (MJ2244, MJ2430) Variable tip clearance (motor driven)

**Table 4. Blade profile characteristics for RCL-AETR Module.**

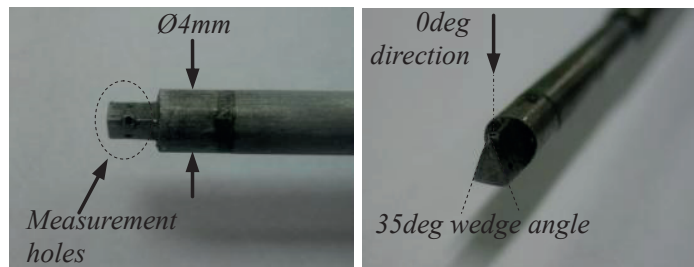
Parameter	Symbol	Unit	Value
Real chord	$C$	mm	54
Axial chord	$C_{ax}$	mm	47
Span	$S$	mm	100
Aspect ratio	$S/C_{ax}$	-	2,1
Stagger angle	$\gamma$	°	-23
TE metal angle	$\alpha_{TE}$	°	-60
Blade pitch	$\vartheta$	mm	34,2

**Table 5. Pressure tappings used in the PML.**

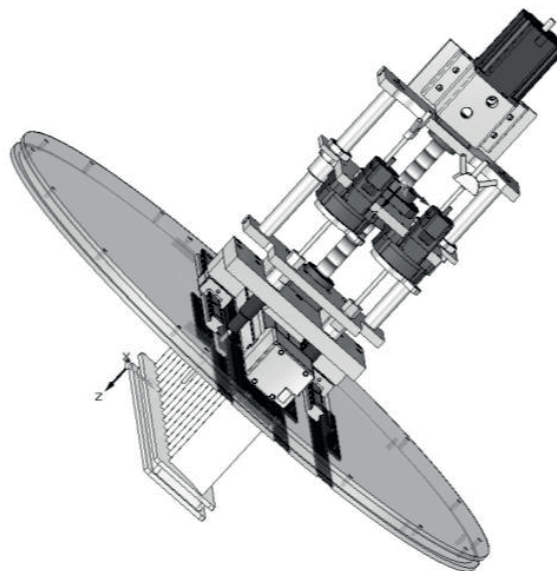
 d=0.6 mm (ref)	 Counter-sink 82°	 30°
 45°	 d=1.0 mm	 d=1,5 mm
 30° backward	 45° backward	 burr

### Probe Traversing System

For the experimental investigation of blade profile losses, two aerodynamic 3-hole wedge probes have been used. The probes – detailed view in Figure 3 - are mounted on the bi-directional traversing system shown in Figure 4. Main specifications are included in Table 6. Along with the pitchwise and spanwise positioning, the probes (1) can be automatically rotated around their spin axis for being aligned with the flow at the location of the measurement. The probes pass across the central disc through dedicated slots (5) where sliding plates of low friction plastic material ensure a proper sealing of the test section from the surroundings. A slot for a third pressure probe has been included for future wake evolution studies.



**Figure 3. Aerodynamic 3-hole wedge probe.**



**Figure 4. Probes traversing system.**

**Table 6. Probe traversing system specifications.**

Motion	System	Range	Accuracy
Pitchwise	Linear guide (2)	170 mm	±0,05 mm
Spanwise	Spindle and stepper motor (3)	0 ÷ 98 %	±0,02 mm
Probe rotation	Hollow shaft stepper motor (4)	0÷360°	±0,02°

The choice of 3-hole wedge probes has been driven by the possibility of limiting the complexity of the system while ensuring good readings within a range of  $\pm 20^\circ$  pitch angle. The probes have been extensively used in other arrangements, including an annularshaped sector cascade. For the future, the adoption of 4- hole or greater multiple hole probes has been considered in order to better capture the 3-D flow phenomena closed to the endwalls.

### Data Acquisition System

The laboratory activities to be conducted on the RCL test rig are based on pressure measurements. Two PSI 9116<sup>1</sup> high accuracy pressure scanners have been included in the facility for a 32-channels capability. Specifications for the PSI9116 are included in Table 7.

**Table 7. Main specifications of the PSI 9116 pressure scanner.**

Parameter	Unit	Value
Channels	-	16
Pressure range	psi	0÷5, 0÷15
Accuracy	% FS	±0,05
Acquisition rate	Hz	up to 500

### REMOTE OPERABILITY

The new linear cascade at KTH has been designed to be fully operated on distance by non-expert users. This has addressed the choice of the control system and the programming language for the development of the user interface.

The automation system for the rotation of the cascade and for the positioning of the probes is based on stepper motors controlled with two National Instruments NI7334 motion cards for up to 8 axis motion capability. The control interface has been realized in LabView<sup>2</sup> and the Remote Panels Technology<sup>3</sup> has been used to make it accessible on the network..

### User Interface

The graphical interface for the operation of the RCL is shown in Figure 6 as it appears when accessed through the web browser at the specified public IP address. What follows in the present description refers to the use of the facility for the RCL exercise where measurements are based on probes traversing.

All controls are arranged on the left side of the page. These include operation of the fan for the air supply to the test rig (frequency control), rotation of the cascade, positioning of the traversing system, data storage and forwarding to the final user.

The central block is dominated by the graphical representation of the cascade including the real-time motion of the probes for a direct association of the pitchwise and spanwise coordinates with the acquired data which are plotted in the graphs underneath. Focus is put on the  $0^\circ$ -direction pressure (refer to Figure 3 ) upstream and downstream of the cascade – which represent the approximate values of total pressure - and on the side pressures

1 Pressure Systems Inc., www.pressuresystems.com.

2 LabView 2010 SP1 Professional Development System.

3 LabView Remote Panels. Created using the Web Publishing Tool. The host user needs to install the LabView Run-Time Engine - downloadable from www.ni.com - compatible with the operating system of his/her machine.

on the downstream probe. The former allows fast identification of the wakes behind the blades while the latter allows rough estimation of the alignment of the probe with the flow at the outlet. By selecting the ‘traverse results’ tab the view switches to a second window where the current distribution of each of the relevant flow quantities is compared with the distributions from the previous measurements. This allows, for example, a rapid identification of the occurrence of 3D flow phenomena when moving towards the blade tip.

The right-hand part of the interface condensates all the aerodynamic and thermodynamic data acquired. These include the 32 pressures from the two pressure scanners, the total temperature in the inlet pipe and the atmospheric pressure read from the barometer system installed in the department. The graphical representation in the lower corner facilitates the identification and the understanding of the pressures values detected by the two probes.

### Network cameras

The room in which the RCL facility is installed is equipped with a set of network cameras<sup>4</sup>. The cameras are fully controllable in pan, tilt and zoom<sup>5</sup>, and the user can also choose among a selection of preset views. The cameras are easily accessible also with smartphones and tablets<sup>6</sup>. Free apps such as Netcamviewer can be used which require only typing the IP address [13], the brand of the camera and the credentials. All aforementioned controls and preset views are automatically operable.



Figure 5. Network cameras in web browser.

4 Contact the authors for access information.

5 During the first use, it might be necessary for the user to download and install the Axis Media Control Active X, which can also be downloaded for free from [www.axis.com](http://www.axis.com).

6 Tests performed with smartphones and tablets running Apple and Android operating systems.

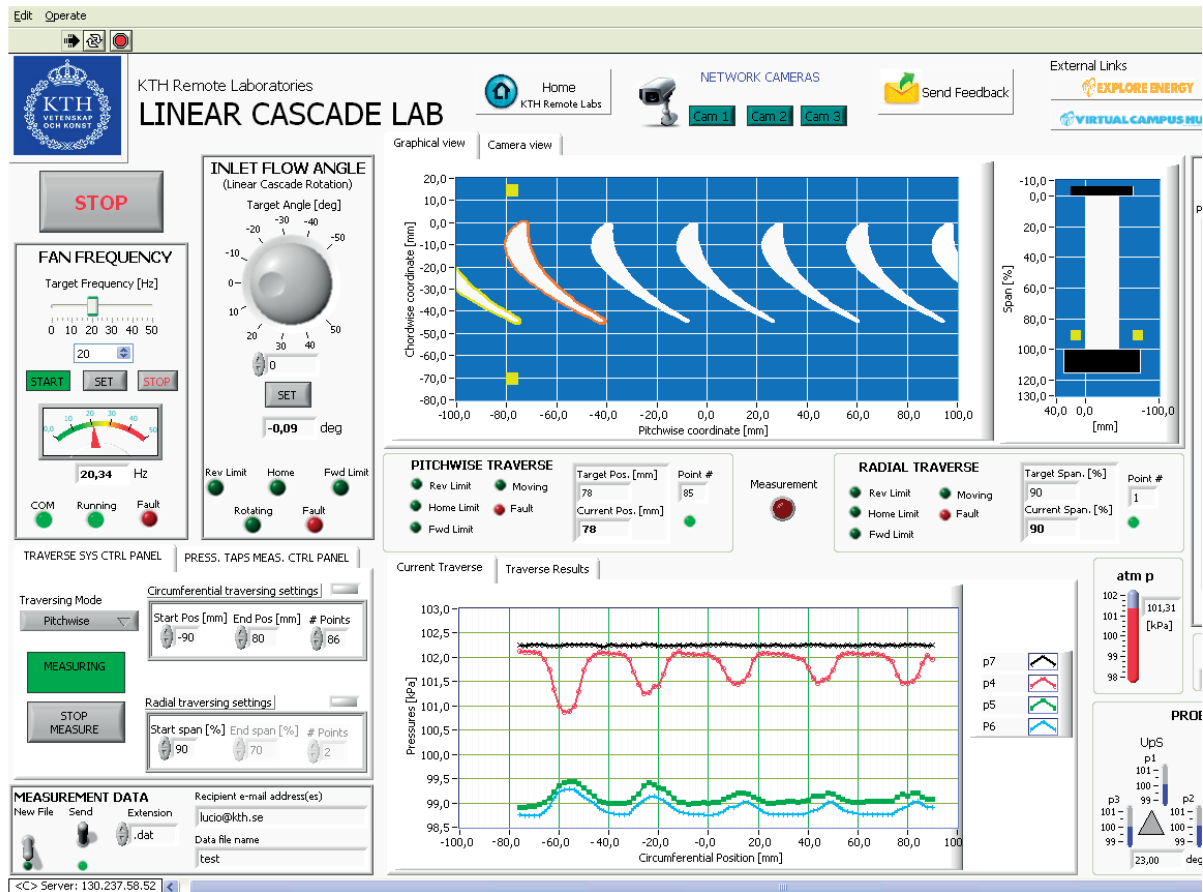


Figure 6. User interface of the RCL accessed through the browser.

## FIRST FIELD EXPERIENCE

The first application of the linear cascade test facility has regarded the investigation of the downstream flow field distribution and of the profile losses through a low pressure turbine blade row. The cascade performance is determined in terms of the mass averaged value of the kinematic loss coefficient, defined as.

$$\xi = \frac{\left(\frac{p_2}{p_{02}}\right)^{\frac{\gamma-1}{\gamma}} - \left(\frac{p_2}{p_{01}}\right)^{\frac{\gamma-1}{\gamma}}}{1 - \left(\frac{p_2}{p_{02}}\right)^{\frac{\gamma-1}{\gamma}}}$$

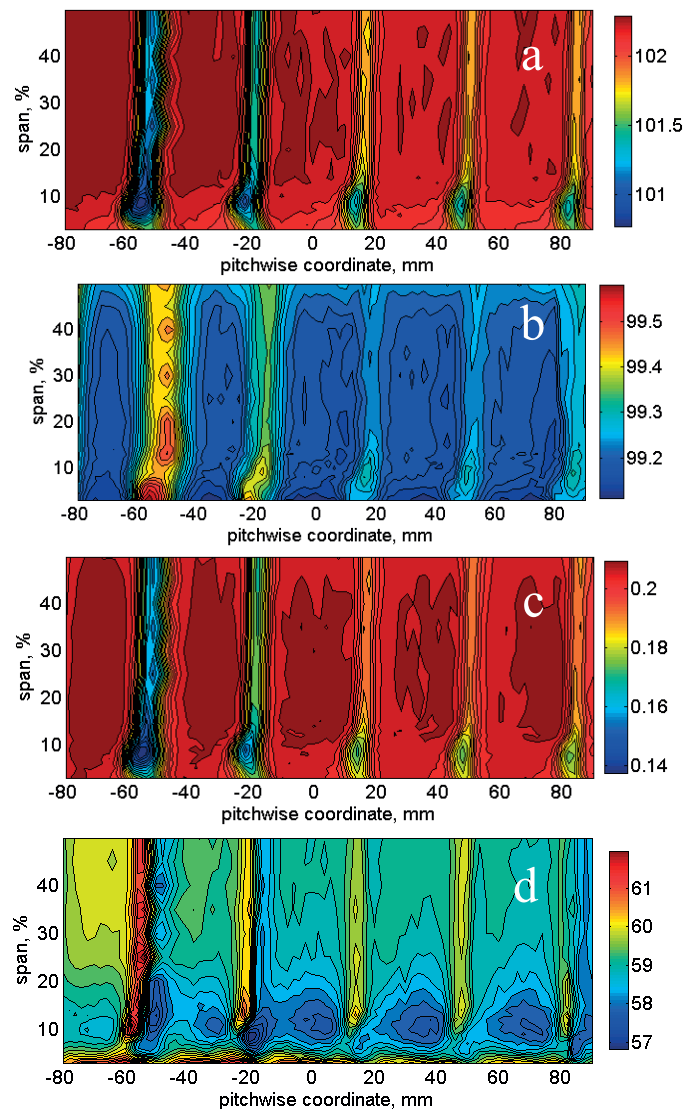
Eq. 1.

where the subscripts 0,1 and 2 for the pressure  $p$  refer to total, inlet and outlet respectively and  $\gamma$  is the ratio of specific heats.

Data presented here result from the collection of the measurements taken together with the engineering students of the Thermal Turbomachinery and Airbreathing Propulsion II courses in the Academic Year 2012. For the laboratory exercise, the RCL-AETR module has been modified so to include an investigation on the effect of the surface roughness on the steady performances. As visible in the snapshot from the network camera in Figure 5 and underlined in the graphical representation of the module in the user interface in Figure 6, two of the blades within the test section have been covered with sand paper. ISO/FEPA P320 – the brown one – and ISO/FEPA P60 – the yellow one – have been glued on the surface of blade 4 and 5 respectively.

Different inflow angles and different fan frequencies have been tested. Pitchwise and 2D traverses over five passages have been performed at various span locations. Figure 7 shows the downstream distribution of total pressure, static pressure, Mach number and flow angle for a representative case: 20 Hz fan frequency and  $0^\circ$  angle of the cascade. The first set or runs of the linear cascade rig highlights the achievement of a pretty good level of periodicity among the different passages within the positioning range of the pitchwise traversing system. The RCL-AETR module with prismatic blades shows a fairly uniform flow field in the central span sections while rather intense 3D phenomena are detected in the regions closed to the endwalls in complete agreement with the expectations.

Particular interest has aroused from the investigation of the effect of the roughness of the blade surface here reported. This has shown a strong impact on the static pressure, total pressure and flow angle distributions, especially for blade 5. The increased thickness deriving from the application of the sand paper should be accounted for, though very closed to the value of thickness of the P320 the effect of which, instead, is rather moderate.



**Figure 7. Downstream distributions of (a) total pressure [kPa]; (b) static pressure [kPa]; (c) Mach number; (d) flow angle [deg].**

Figure 8 shows the loss coefficient versus the spanwise coordinate for the five blades in the range -80 to 90 mm pitchwise coordinate. These values are obtained from mass average of the flow quantities at a given span location. The periodicity in the results among the first three passages (blades without sand paper) is here confirmed. With increasing roughness of the surface, the loss coefficient increases at all span positions. In the mid passage values move from 5% to up to 9% and closed to the blade tip from 12% to 18%.



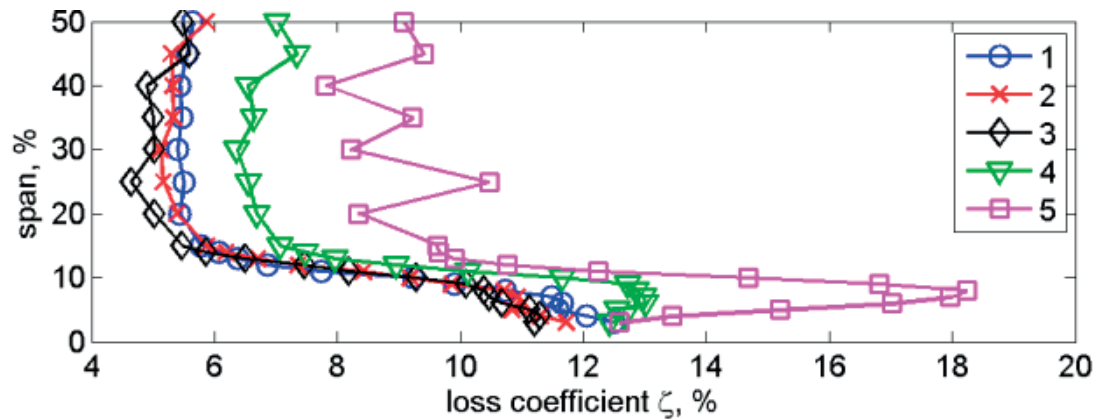


Figure 8. Spanwise loss coefficient. Blade count is the same as in the user interface.

## CONCLUSIONS

A new aerodynamic test facility for use in engineering education has been realized at the Heat and Power Technology Division at KTH. The test section is equipped with a linear cascade of low pressure turbine blades operated at low subsonic flow conditions. The major element of uniqueness of the facility is represented by its capability of fully remote operation, particularly suitable for use in courses with distant students. Great attention has been spent on the design of a highly flexible system for an easy and fast setup of different laboratory experiments. The most relevant solution regards the arrangement of blades in interchangeable and cost-effective modules. Considerable effort has been reserved for the development of an attractive and user friendly graphical interface including real-time plot of the quantities of major interest for the experiment.

First field experience has shown a good behavior of the test facility. Great periodicity of the flow among the passages has been reached as well as good and reliable operation of the measuring equipment obtained.

On the technical side, further development of the rig includes utilization of instrumented blades, 4-hole aerodynamic probes and the realization of a setup with free vibration of the blades in the travelling wave mode.

On the educational side, laboratory instructions, video tutorials, self-assessments and virtual laboratory exercises are currently being developed in order to offer a complete and comprehensive educational tool. Further experience with the students is required, and teachers and researchers interested in using the remote cascade laboratory are invited to contact the authors for additional information.

## ACKNOWLEDGMENTS

The realization of the present test facility has been performed within the framework of continuous improvement of educational material and technology financially supported by the HPT Division at the Department of Energy Technology, KTH. Part of the work has been financed within the EU funded Erasmus Mundus Master programme THRUST (Turbomachinery Aeromechanical University Training, [www.explorethrust.eu](http://www.explorethrust.eu)) under the grant agreement number 2010-2459/001-001-EM II-EMMC and the framework partnership agreement Nr 2010-0134, the EIT KIC InnoEnergy initiative ([www.kic-innoenergy.com](http://www.kic-innoenergy.com)) as part of developing Learning Modules, and within the EU funded Virtual Campus project ([www.exploreenergy.eu/Partners/VirtualCampusHu](http://www.exploreenergy.eu/Partners/VirtualCampusHu)) under the grant agreement number 283746. The authors gratefully acknowledge the financial support from these sources.

A special thank goes to Alessio Contran who contributed to the design of the laboratory before he decided to meet new challenges in industry.

## REFERENCES

- [1] Seinturier, E., 2008, "Forced Response Computation for Bladed Disks. Industrial Practices and Advanced Methods", Lecture Series 2008-05: Structural Design of Aircraft Engines: Key Objectives and Techniques. Von Karman Institute for Fluid Dynamics.

- [2] Navarathna, N., Fedulov, V., Martin, A., Fransson, T.H., 2004, "Web-based, Interactive Laboratory Experiments in Turbomachine Aerodynamics.", Proceedings of the ASME Turbo Expo 2004, June 14-17, 2004, Vienna, Austria
- [3] Monaco, L., Vogt, D., M., Fransson, T., H., "Implementation of a Remote Pump Laboratory Exercise in the Training of Engineering Students", ASME Paper GT2012-69983 to be presented in ASME Turbo Expo 2012
- [4] The Straight Cascade Tunnel 'Göttingen' at the German Aerospace Center, Germany, [http://www.dlr.de/at/en/desktopdefault.aspx/tabid-1565/2433\\_read-3789/](http://www.dlr.de/at/en/desktopdefault.aspx/tabid-1565/2433_read-3789/), accessed on Feb 29, 2012
- [5] Chalmers' Linear Cascade Rig at Chalmers University of Technology, Sweden, <http://www.chalmers.se/am/EN/research/research-resources/chalmers-windtunnels/chalmers-8217-linear>, accessed on Feb 29, 2012
- [6] Gehrler, A., Woisetschläger, J., Jericha, H., "Blade Film Cooling by Underexpanded Transonic Jet Layers". ASME Paper 97-GT-246
- [7] Williams, R., Gregory-Smith, D., He, L., Ingram, G., 2010, "Experiments and Computations on Large Tip Clearance Effects in a Linear Cascade", ASME J. Turbomach, 132, Issue 2, 021018
- [8] Coton, T., Arts, T., Lefebvre, M., Liamis, N., 2003, "Unsteady and Calming Effects Investigation on a Very High-Lift LP Turbine Blade—Part I: Experimental Analysis", ASME J. Turbomach. 125, pp. 281
- [9] Volino, R. J., 2012, "Effect of Unsteady Wakes on Boundary Layer Separation on a Very High Lift Low Pressure Turbine Airfoil", J. Turbomach. 134, 011011
- [10] Rubensdörffer, F., Fransson, T. H., "A new test facility for evaluation of parameters defining nozzle guide vane endwall heat transfer", The 17th Symposium on Measuring Techniques in Transonic and Supersonic Flow in Cascades and Turbomachines, Stockholm, Sweden, September 2004
- [11] MJ2244 Airbreathing Propulsion II course, <http://www.kth.se/student/kurser/kurs/MJ2244>, accessed on Feb 26, 2012
- [12] MJ2430 Thermal Turbomachinery course, <http://www.kth.se/student/kurser/kurs/MJ2430>, accessed on Feb 26, 2012
- [13] Network cameras IP addresses are: 130.237.58.71 and 130.237.58.53

ISBN 978-84-8363-966-5



## XXI Biennial Symposium on Measuring Techniques in Turbomachinery

Transonic and Supersonic Flow in Cascades and Turbomachines

[ EDITORS ]

J.M. Desantes | CMT-Motores Térmicos, Universitat Politècnica de València, Spain

G. Paniagua | Von Karman Institute for Fluid Dynamics, Belgium

J.R. Serrano | CMT-Motores Térmicos, Universitat Politècnica de València, Spain

### Aknowlegements:

The editors would like to thank the authors Pavel Safarik, Martin Luxa, Helena Picmausova and David Šimurda, for the cession of the cover image.

The publication of these proceedings has been supported by a grant from the Generalitat Valenciana (reference AORG/2012/026)